



**HAL**  
open science

# Metrology of scanning microwave microscopy applied to transport measurement for semiconductors

Damien Richert

► **To cite this version:**

Damien Richert. Metrology of scanning microwave microscopy applied to transport measurement for semiconductors. Physics [physics]. Insa lyon, 2024. English. NNT : . tel-04748080v1

**HAL Id: tel-04748080**

**<https://hal.science/tel-04748080v1>**

Submitted on 22 Oct 2024 (v1), last revised 19 Dec 2024 (v2)

**HAL** is a multi-disciplinary open access archive for the deposit and dissemination of scientific research documents, whether they are published or not. The documents may come from teaching and research institutions in France or abroad, or from public or private research centers.

L'archive ouverte pluridisciplinaire **HAL**, est destinée au dépôt et à la diffusion de documents scientifiques de niveau recherche, publiés ou non, émanant des établissements d'enseignement et de recherche français ou étrangers, des laboratoires publics ou privés.



N°d'ordre

NNT : xxx

**THESE de DOCTORAT DE L'INSA LYON,  
membre de l'Université de Lyon**

**Ecole Doctorale N°160  
(Electronique, Electrotechnique, Automatique)**

**Spécialité/ discipline de doctorat :**  
Electronique, micro et nanoélectronique, optique et laser

Soutenue publiquement le 08/07/2024, par :  
**Damien Richert**

---

**Métrologie des techniques de  
microscopie à sonde locale micro-onde  
appliquées aux mesures de transport  
dans le domaine des semiconducteurs**

**Metrology of scanning microwave  
microscopy applied to transport  
measurement for semiconductors**

---

Devant le jury composé de :

Theron, Didier, Directeur de recherche, Université de Lille

**Président**

Bourillot, Eric MCF-HDR, Université de Bourgogne  
Coq Germanicus, Rosine Professeur des Universités, Université de Caen  
Klapetek, Petr Docteur, Czech Metrology Institute (CMI)

**Rapporteur  
Rapporteuse  
Examineur**

Gautier, Brice Professeur des Universités, INSA Lyon  
Piquemal, François Docteur HDR, LNE

**Directeur de thèse  
Co-directeur de thèse**

Département FEDORA – INSA Lyon - Ecoles Doctorales

SIGLE	ECOLE DOCTORALE	NOM ET COORDONNEES DU RESPONSABLE
ED 206 CHIMIE	<u>CHIMIE DE LYON</u> <a href="https://www.edchimie-lyon.fr">https://www.edchimie-lyon.fr</a> Sec. : Renée EL MELHEM Bât. Blaise PASCAL, 3e étage <a href="mailto:secretariat@edchimie-lyon.fr">secretariat@edchimie-lyon.fr</a>	M. Stéphane DANIELE C2P2-CPE LYON-UMR 5265 Bâtiment F308, BP 2077 43 Boulevard du 11 novembre 1918 69616 Villeurbanne <a href="mailto:directeur@edchimie-lyon.fr">directeur@edchimie-lyon.fr</a>
ED 341 E2M2	<u>ÉVOLUTION, ÉCOSYSTÈME, MICROBIOLOGIE, MODÉLISATION</u> <a href="http://e2m2.universite-lyon.fr">http://e2m2.universite-lyon.fr</a> Sec. : Bénédicte LANZA Bât. Atrium, UCB Lyon 1 Tél : 04.72.44.83.62 <a href="mailto:secretariat.e2m2@univ-lyon1.fr">secretariat.e2m2@univ-lyon1.fr</a>	Mme Sandrine CHARLES Université Claude Bernard Lyon 1 UFR Biosciences Bâtiment Mendel 43, boulevard du 11 Novembre 1918 69622 Villeurbanne CEDEX <a href="mailto:e2m2.codir@listes.univ-lyon1.fr">e2m2.codir@listes.univ-lyon1.fr</a>
ED 205 EDISS	<u>INTERDISCIPLINAIRE SCIENCES-SANTÉ</u> <a href="http://ediss.universite-lyon.fr">http://ediss.universite-lyon.fr</a> Sec. : Bénédicte LANZA Bât. Atrium, UCB Lyon 1 Tél : 04.72.44.83.62 <a href="mailto:secretariat.ediss@univ-lyon1.fr">secretariat.ediss@univ-lyon1.fr</a>	Mme Sylvie RICARD-BLUM Laboratoire ICBMS - UMR 5246 CNRS - Université Lyon 1 Bâtiment Raulin - 2ème étage Nord 43 Boulevard du 11 novembre 1918 69622 Villeurbanne Cedex Tél : +33(0)4 72 44 82 32 <a href="mailto:sylvie.ricard-blum@univ-lyon1.fr">sylvie.ricard-blum@univ-lyon1.fr</a>
ED 34 EDML	<u>MATÉRIAUX DE LYON</u> <a href="http://ed34.universite-lyon.fr">http://ed34.universite-lyon.fr</a> Sec. : Yann DE ORDENANA Tél : 04.72.18.62.44 <a href="mailto:yann.de-ordenana@ec-lyon.fr">yann.de-ordenana@ec-lyon.fr</a>	M. Stéphane BENAYOUN Ecole Centrale de Lyon Laboratoire LTDS 36 avenue Guy de Collongue 69134 Ecully CEDEX Tél : 04.72.18.64.37 <a href="mailto:stephane.benayoun@ec-lyon.fr">stephane.benayoun@ec-lyon.fr</a>
ED 160 EEA	<u>ÉLECTRONIQUE, ÉLECTROTECHNIQUE, AUTOMATIQUE</u> <a href="https://eдея.universite-lyon.fr">https://eдея.universite-lyon.fr</a> Sec. : Philomène TRECOURT Bâtiment Direction INSA Lyon Tél : 04.72.43.71.70 <a href="mailto:secretariat.eдея@insa-lyon.fr">secretariat.eдея@insa-lyon.fr</a>	M. Philippe DELACHARTRE INSA LYON Laboratoire CREATIS Bâtiment Blaise Pascal, 7 avenue Jean Capelle 69621 Villeurbanne CEDEX Tél : 04.72.43.88.63 <a href="mailto:philippe.delachartre@insa-lyon.fr">philippe.delachartre@insa-lyon.fr</a>
ED 512 INFOMATHS	<u>INFORMATIQUE ET MATHÉMATIQUES</u> <a href="http://edinfomaths.universite-lyon.fr">http://edinfomaths.universite-lyon.fr</a> Sec. : Renée EL MELHEM Bât. Blaise PASCAL, 3e étage Tél : 04.72.43.80.46 <a href="mailto:infomaths@univ-lyon1.fr">infomaths@univ-lyon1.fr</a>	M. Hamamache KHEDDOUCI Université Claude Bernard Lyon 1 Bât. Nautibus 43, Boulevard du 11 novembre 1918 69 622 Villeurbanne Cedex France Tél : 04.72.44.83.69 <a href="mailto:direction.infomaths@listes.univ-lyon1.fr">direction.infomaths@listes.univ-lyon1.fr</a>
ED 162 MEGA	<u>MÉCANIQUE, ÉNERGÉTIQUE, GÉNIE CIVIL, ACOUSTIQUE</u> <a href="http://edmega.universite-lyon.fr">http://edmega.universite-lyon.fr</a> Sec. : Philomène TRECOURT Tél : 04.72.43.71.70 Bâtiment Direction INSA Lyon <a href="mailto:mega@insa-lyon.fr">mega@insa-lyon.fr</a>	M. Etienne PARIZET INSA Lyon Laboratoire LVA Bâtiment St. Exupéry 25 bis av. Jean Capelle 69621 Villeurbanne CEDEX <a href="mailto:etienne.parizet@insa-lyon.fr">etienne.parizet@insa-lyon.fr</a>
ED 483 ScSo	<u>ScSo<sup>1</sup></u> <a href="https://edsciencessociales.universite-lyon.fr">https://edsciencessociales.universite-lyon.fr</a> Sec. : Mélina FAVETON Tél : 04.78.69.77.79 <a href="mailto:melina.faveton@univ-lyon2.fr">melina.faveton@univ-lyon2.fr</a>	M. Bruno MILLY (INSA : J.Y. TOUSSAINT) Univ. Lyon 2 Campus Berges du Rhône 18, quai Claude Bernard 69365 LYON CEDEX 07 Bureau BEL 319 <a href="mailto:bruno.milly@univ-lyon2.fr">bruno.milly@univ-lyon2.fr</a>

<sup>1</sup> ScSo : Histoire, Géographie, Aménagement, Urbanisme, Archéologie, Science politique, Sociologie, Anthropologie

## Résumé

Cette thèse se focalise sur l'établissement d'une métrologie des mesures de propriétés électriques à l'échelle submicrométrique. La technique Scanning Microwave Microscopy (SMM), qui permet d'accéder aux propriétés électriques d'un échantillon (impédance, permittivité électrique, et concentration de dopants), répond à ces critères. Il s'agit d'un microscope à force atomique interfacé à un analyseur de réseaux vectoriel (VNA). Si la métrologie associée au VNA est bien établie, ce n'est pas le cas pour les configurations SMM. Un VNA permet, s'il est étalonné, d'extraire des propriétés électriques à partir de la mesure du paramètre de réflexion. Pour une configuration SMM, la méthode la plus commune est dérivée de la méthode d'étalonnage Short-Open-Load utilisant trois impédances connues sur un échantillon de référence. L'un des résultats clés de cette thèse est l'établissement du bilan d'incertitude associé à la mesure d'impédance par SMM. Pour ce faire, une caractérisation de l'échantillon de référence démontre que l'incertitude associée aux valeurs des impédances présentes (0,3 fF – 9,8 fF) est inférieure à 2,8%. Fort de ce bilan d'incertitude, un second échantillon de référence est proposé et caractérisé avec une incertitude associée inférieure à 1,9%. L'incertitude sur la mesure des capacités de référence par le SMM étalonné est inférieure à 3%. Un cas d'application est proposé : l'extraction de la permittivité d'échantillons piézoélectriques avec une incertitude inférieure à 11%. L'incertitude due à l'humidité relative (RH) sur l'étalonnage du SMM a été étudiée empiriquement et par simulation numérique. Cette dernière impacte la calibration à hauteur de 0,4% pour les capacités de 0,3 fF et devient négligeable pour les capacités au-dessus de 4 fF. Enfin, des courbes  $dC/dz$  ont été acquises par microscopie à force électrostatique (EFM) sur un diélectrique connu afin d'assurer la traçabilité de la mesure de constante de raideur de la sonde employée.



Cette partie présente un résumé de synthèse en français du contenu du manuscrit.

# 1 Introduction générale

Le XX siècle a été marqué par l'apparition des circuits logiques pour automatiser le traitement de l'information. Au début, les composants étaient analogiques et de tailles imposantes comme l'emblématique transistor à lampe. Le secteur a subi une transformation majeure avec l'arrivée des semi-conducteurs. Avec les progrès techniques, en particulier, les améliorations dans la résolution de gravure, les composants sont devenus de plus en plus petits. Gordon Moore, l'un des co-créateurs d'Intel a émis l'observation que le nombre de transistors doublerait tous les deux ans. Pour continuer sur cette tendance, de nouvelles architectures telles que les FinFETs et Gates-all-around (GAA) sont apparues en même temps que la diminution constante de la taille des composants avec des dimensions critiques qui avoisinent aujourd'hui les 2 nm ainsi que l'exploration de matériaux 2D avec la possibilité de composant en simple plan atomique.

Afin d'accompagner le développement de ces composants, il devient critique de pouvoir mesurer les impédances, les permittivités diélectriques, les densités de dopants et les courants de fuite à l'échelle submicrométrique. En raison de sa polyvalence, le microscope à force atomique (AFM) est un bon candidat. Parmi les nombreux modes électriques, cette thèse se concentre sur le scanning microwave microscope (SMM). Un SMM est un AFM travaillant en mode contact interfacé à un analyseur de réseaux vectoriel (VNA). En mesurant le paramètre de réflexion, il est possible de remonter aux propriétés électriques de l'échantillon.

Si la métrologie des mesures électriques reposant sur le VNA est bien établie, ce n'est pas le cas pour le SMM. Cela est dû au manque de structures étalons, d'homogénéisation des méthodes d'étalonnage de l'instrument et aux considérations spécifiques à l'AFM. Comme toutes les mesures AFM, le revêtement de la pointe ainsi que sa forme impactent de façon importante la mesure. D'autres paramètres d'importance sont la forme du contact pointe-échantillon, la présence du ménisque d'eau à l'interface, l'état chimique de la surface de l'échantillon ainsi que sa rugosité. Enfin des phénomènes électrochimiques, l'échauffement par effet Joule ainsi que l'injection et la diffusion d'espèces chargées peuvent impacter la mesure.

Il existe deux principales techniques d'étalonnage, l'une fondée sur un échantillon de référence, l'autre sur l'acquisition d'une courbe  $dC/dz$ .

Le premier chapitre de cette thèse établit l'état de l'art des mesures de permittivité électrique et d'impédance, tant à l'échelle macro- que sub-micrométrique.

Le second chapitre traite des différentes structures de référence capacitives et de l'établissement du bilan d'incertitude associé aux valeurs des capacités en présence. Une seconde version de l'échantillon de référence est proposée puis fabriquée et caractérisée afin de réduire l'incertitude associée aux valeurs capacitives.

Le troisième chapitre est focalisé sur la première méthode d'étalonnage. Le dispositif expérimental en place au LNE est détaillé. Le bilan d'incertitude associé aux mesures de capacité sur l'échantillon de référence est établi. L'impact sur l'étalonnage de différents paramètres expérimentaux y est détaillé à la fois de manière empirique et en se reposant sur un modèle numérique. La méthode de substitution y est également évaluée par des mesures avec une pointe blindée. Enfin, une application est présentée à travers la mesure de la constante diélectrique d'échantillon inconnu à forte constante diélectrique.

Le quatrième et dernier chapitre se concentre sur la seconde méthode d'étalonnage. La méthode est décrite. Elle est ensuite appliquée sur une terrasse d'oxyde de silicium. Une comparaison avec la

première méthode a été envisagée, mais fut infructueuse. Des perspectives sont présentées pour résoudre le problème rencontré. Une seconde partie de ce chapitre traite de la mesure traçable au SI de la constante diélectrique du levier.

## 2 État de l'art

Dans ce chapitre, les points nécessaires à la bonne compréhension du travail effectué sont abordés. Tout d'abord, un rappel est fait sur la définition et l'origine physique de l'impédance électrique et de la permittivité électrique. Le principe fondamental d'une mesure de capacité  $y$  est présenté ainsi que les différentes considérations à prendre en compte en fonction du type de capacité mesurée. Le lien entre la capacité et la constante diélectrique de l'échantillon sondé est souligné. Dans la Figure 1, les principales sources d'erreurs sur la mesure de capacité, à savoir la température, le niveau de potentiel électrique continu et alternatif appliqué, le choix de la fréquence d'excitation, et le niveau de bruit sont décrites.

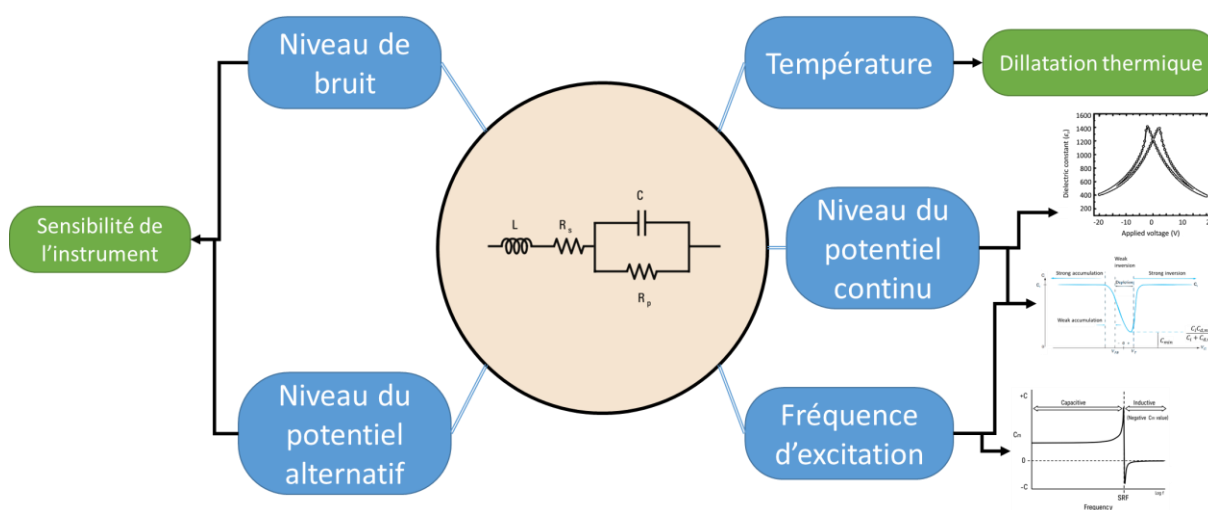


Figure 1. Principales influences sur la mesure d'impédance, [1]–[3]

Les principales techniques de mesures d'impédance à l'échelle macroscopique sont décrites pour les basses fréquences (inférieures à la centaine de MHz) et les radios fréquences (RF, entre 0,3 GHz et 300 GHz). Les méthodes pour les basses fréquences incluent les mesures de courbe d'intensité en fonction de la tension appliquée (I-V), ainsi que les ponts d'impédance (simple et auto-équilibré) utilisés dans les LCRmètres. Les mesures RF abordées comprennent les dispositifs expérimentaux pour les mesures RF I-V dans le cas d'impédance faible (inférieure à 1 k $\Omega$ ) et forte (supérieure à 100 k $\Omega$ ). Une attention particulière est portée aux mesures par analyseur de réseaux vectoriel (VNA). L'instrument est décrit dans la Figure 2. Le signal micro-onde généré par la source voit sa puissance réglée par l'amplificateur intégré dans une boucle de rétroaction (ALC). Il est ensuite dirigé vers l'un des ports du VNA par un commutateur. Un diviseur de signal dirige une partie de l'onde vers un mélangeur de fréquence pour être converti en un signal à fréquence intermédiaire (IF) lisible par un ordinateur, tandis que la seconde partie du signal est envoyée dans un coupleur directionnel avant d'atteindre le port du VNA. Le signal renvoyé par l'échantillon est collecté par le port du VNA, passe par le coupleur directionnel et lui aussi est transformé en signal IF par un mélangeur de fréquence. Le paramètre de réflexion  $S_{11}$  est alors mesuré en prenant le ratio du signal réfléchi sur le signal envoyé. La mesure d'impédance par le VNA repose sur le  $S_{11}$  comme le montre l'Équation 1.

$$S_{11} = \frac{Z_S - Z_0}{Z_S + Z_0} \quad \text{Équation 1. [4]}$$

où  $Z_S$  est l'impédance de l'échantillon et  $Z_0$  est l'impédance de référence (typiquement 50  $\Omega$ ).

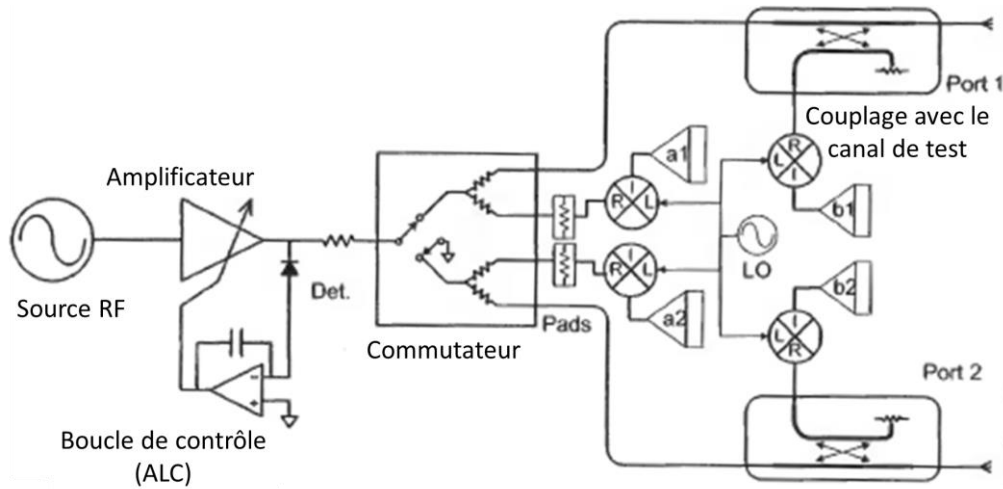


Figure 2. Diagramme de bloc d'un VNA, [4]

Dues aux différents éléments en charge de l'acheminement et de la lecture du signal RF à l'échantillon, des erreurs sont générées lors de la mesure du paramètre  $S_{11}$  créant une différence significative entre le  $S_{11}$  à l'interface de l'échantillon et celui lu par le VNA. Un étalonnage de la mesure est dès lors nécessaire pour compenser ces erreurs [5]. Le paramètre de réflexion non étalonné est désormais noté  $S_{11,m}$ . L'une des premières méthodes déployées fut l'étalonnage Short-Open-Load (SOL) où une fonction de correction utilisant trois paramètres d'erreur est établie en mesurant trois étalons d'impédance (un court-circuit, un circuit ouvert et une charge d'impédance connue). La fonction de correction est donnée par l'Équation 2.

$$S_{11} = \frac{S_{11,m} - e_{00}}{e_{01} + e_{11}(S_{11,m} - e_{00})} \quad \text{Équation 2.}$$

Une fois l'étalonnage du VNA effectué, le bilan d'incertitude associé à la mesure d'impédance par ce VNA peut être établi [6].

Tableau 1. Bilan d'incertitude sur la mesure de la partie réelle de  $S_{11}$  par le VNA sur une charge adaptée.

Contribution	Type	$f = 0,46$ GHz
Étalon de charge	B	0,00200
Étalon de circuit ouvert	B	0,00000
Étalon de court-circuit	B	0,00000
Répétabilité des connections	A	0,00045
Dérive du VNA	A	0,00002
Linéarité du VNA	A	0,00001
Niveau de bruit	A	0,00002
Incertitude combinée		0,0205



La plus grande contribution au bilan d'incertitude vient de l'échantillon de référence de charge et sera abordée en détail dans le second chapitre. Ensuite, vient la répétabilité des connexions. Elle est évaluée en déconnectant et reconnectant plusieurs fois les connectiques. La dérive du VNA est due aux changements de température modifiant le chemin électrique du signal et affectant les performances du VNA. La non-linéarité du VNA est source de défaut dans la lecture des signaux incident et réfléchi, mais peut être réduite en ajustant la puissance du signal émis. Enfin, le bruit du VNA est caractérisé par le bruit ajouté à la mesure par les instruments (Trace noise) et le bruit présent lors d'une mesure à vide par le VNA (bruit de plancher) [4], [6]. Ces niveaux de bruit peuvent être réduits en moyennant et réduisant la fréquence de bande passante.

Les principaux équipements permettant d'interfacer le VNA avec l'échantillon sont présentés. Une attention particulière est portée sur les résonateurs diélectriques (SPDR) et la ligne coaxiale ouverte en contact direct avec l'échantillon qui sont présentés (Figure 3).

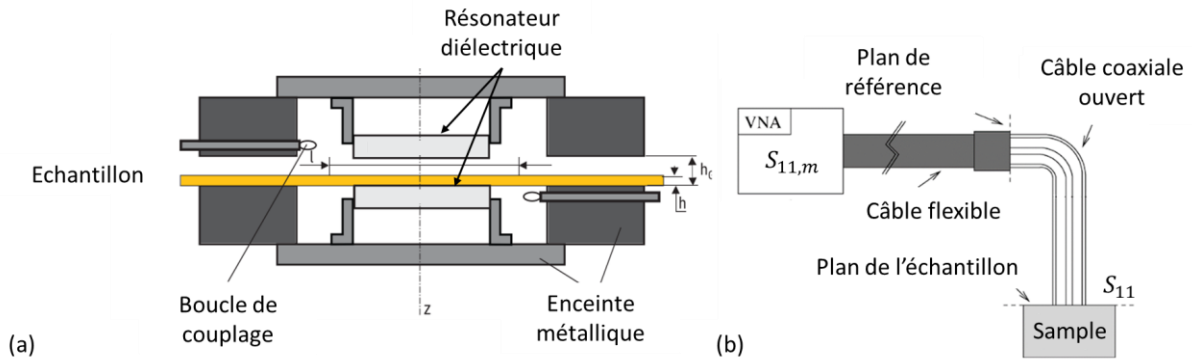


Figure 3. (a) Résonateur diélectrique [7], (b) ligne coaxiale ouverte [8]

Dans le cas du SPDR (Figure 3.a), l'échantillon est placé entre les 2 résonateurs diélectriques, chacun relié à un port différent du VNA. La fréquence de résonance ( $f_0$ ) et le facteur de qualité ( $Q$ ) sont évalués pour la cavité à vide et sous charge. Le changement de ces deux quantités peut être relié à la constante diélectrique et tangente d'angle de perte de l'échantillon par l'Équation 3.

$$\epsilon_r = \frac{1 + f_0 - f_s}{hf_0K_S} \quad \text{Équation 3.a}$$

$$\tan(\delta) = \frac{Q_0^{-1} - Q_S^{-1}}{h\epsilon_r K_S} \quad \text{Équation 3.b}$$

où  $h$  est l'épaisseur de l'échantillon et  $K_S$  est une propriété propre du SPDR. Pour la méthode de ligne coaxiale ouverte, le signal micro-onde est guidé jusqu'à l'échantillon par la ligne puis est réfléchi jusqu'au VNA où le  $S_{11}$  est évalué. Après étalonnage, le  $S_{11}$  peut être lié à l'admittance et donc l'impédance de l'échantillon. Il existe d'autres méthodes de mesure fondées sur les mesures de lignes coplanaires ou de capacités déposées sur l'échantillon. Les incertitudes associées aux différentes méthodes sont présentées dans le Tableau 2.

Tableau 2. Incertitude associées au mesure de  $\epsilon_r$  et de  $\tan(\delta)$  par les différentes méthodes [9].

Technique	Incertitude sur $\epsilon_r$	Incertitude sur $\tan(\delta)$
SPDR	$\pm 0,5\%$	$\pm 5 \cdot 10^{-5} \%$
Sonde coaxial	$\pm 2\% - 10\%$	$\pm 2 \cdot 10^{-2} \%$
Ligne de transmission	$\pm 1\% - 10\%$	$\pm 5 \cdot 10^{-3} \%$
Capacité	$\pm 1\%$	$\pm 5 \cdot 10^{-4} \%$

Les techniques de microscopie à force atomique (AFM) sont ensuite présentées. Une configuration type est montrée Figure 4. L'échantillon ou la pointe, ou dans certaines configurations, les deux sont montés sur un scanner piézoélectrique. Un laser est focalisé sur le levier de la pointe AFM puis est réfléchi sur un photodétecteur à quatre quadrants. La lecture de celui-ci permet de remonter aux informations de déflexion et de friction. La Figure 4.b montre le potentiel d'interaction entre la pointe et l'échantillon en fonction de la distance. Cette courbe est similaire à un potentiel de Lennard-Jones décrivant la force d'interaction entre deux atomes et peut être expliquée de manière similaire. Lorsque la pointe est loin de la surface, la force d'interaction peut être considérée nulle. La déflexion du levier lue à cette position est alors enregistrée comme point de référence ( $D_0$ ). Lorsque la pointe s'approche de l'échantillon, elle entre dans le régime attractif de la force électrostatique. Enfin pour les faibles distances, c'est le régime répulsif de la force électrostatique qui s'impose à la pointe AFM. Selon le régime d'interaction, l'instrument travaille en plusieurs modes. Si la force d'interaction est constante au cours du balayage, alors l'AFM travaille en mode constant. De plus, si cette force est répulsive, l'apex de la pointe est en contact physique avec la surface de l'échantillon et on parle alors de mode contact. La force d'interaction est liée à la variation de la déflexion par rapport au point de référence par la loi d'Hooke Équation 4

$$F_{ts} = k\Delta D$$

Équation 4

où  $k$  [ $\text{N}\cdot\text{m}^{-1}$ ] est la constante de raideur du levier et  $S$  [ $\text{m}\cdot\text{V}^{-1}$ ] est la sensibilité de la lecture, c'est-à-dire le déplacement sur l'axe  $z$  du levier correspondant à un  $\Delta D$  de 1 V [10].

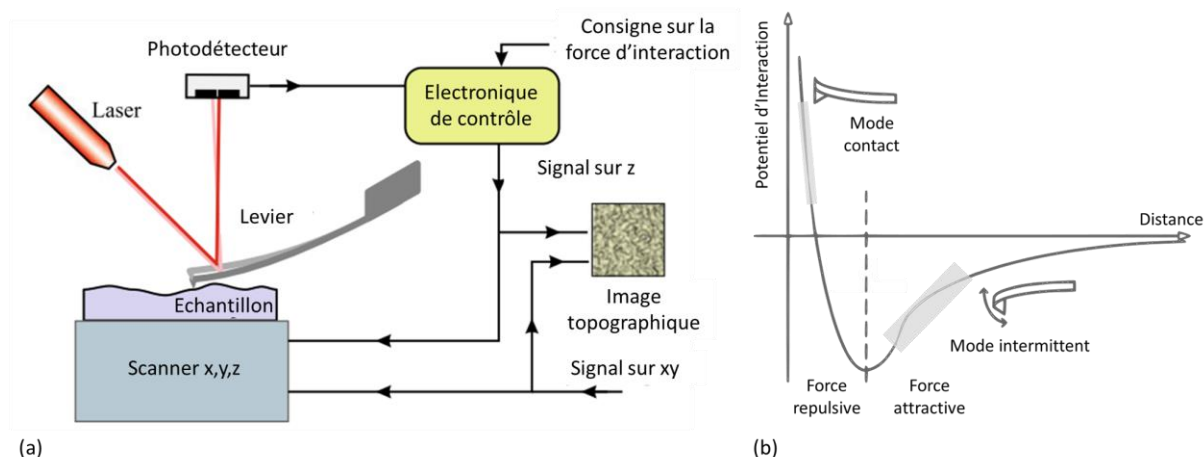


Figure 4. (a) Dispositif AFM typique. (b) Courbe de potentiel entre une pointe AFM et l'échantillon [10], [11]

Au cours de ce mode, la force d'interaction est typiquement de quelques dizaines de nanonewton. Le mode contact a une résolution latérale limitée par la convolution entre la pointe et l'échantillon. Il reste néanmoins la clef pour effectuer des mesures électriques, car il assure un contact pointe-échantillon inchangé sur l'ensemble de la mesure. Cependant l'aire de contact entre les deux éléments est susceptible de changer due à l'érosion de la pointe au cours du balayage [12]. Ce mode peut également être utilisé pour acquérir des courbes de force de manière ponctuelle [10].

Le dernier mode à être mentionné est le mode dynamique, où l'interaction pointe-échantillon change au cours du balayage [13]. Dans ce mode, un élément piézoélectrique met la pointe en oscillation à une pulsation ( $\omega$ ) proche de la résonance ( $\omega_0$ ). Le système pointe-échantillon peut alors être assimilé à un oscillateur harmonique amorti [10]. Le système est alors modélisé par deux ressorts : le premier représentant le levier de la pointe avec une constante de raideur ( $k$ ) et le second correspondant à la

force d'interaction entre la pointe et l'échantillon ( $k'$ ). Pour de petites amplitudes, l'interaction est linéaire et  $k'$  est considéré constant. Lorsque la pointe est approchée de la surface de l'échantillon, l'amortissement génère un décalage dans la fréquence d'oscillation de la pointe ( $\Delta\omega$ ). La force d'interaction peut être retrouvée à partir de ce décalage et de la constante de raideur du levier (Équation 5).

$$\Delta\omega = -\frac{\omega_0}{2k} \left. \frac{\partial F_{ts}}{\partial z} \right|_{z=0} \quad \text{Équation 5.}$$

Quel que soit le mode utilisé, les images AFM sont sensibles aux artefacts de mesure prenant ses origines dans la pointe, le scanner, l'électronique de contrôle, le bruit extérieur, la dérive thermique et les interférences dues au laser [10], [14]. Le dispositif présent au LNE étant dans un environnement contrôlé avec des variations de température inférieures à 0,1 °C et utilisant un levier relativement large, les deux dernières contributions peuvent être négligées. Les autres contributions sont résumées dans la Figure 5. La convolution entre la pointe et l'échantillon peut créer des zones mortes où l'apex de la pointe n'arrive pas à accéder rendant les éléments de surface invisible à l'imagerie AFM. D'autres artefacts peuvent apparaître, pour des raisons similaires dans le cas d'une pointe endommagée. Une pointe plus effilée peut réduire cet effet de convolution [10], [15]. Les effets non-linéaires du déplacement du scanner piézoélectrique peuvent créer des déformations de l'image comme montrées Figure 5.b et c. Celles-ci peuvent être atténuées par une boucle de rétroaction sur le scanner. Cette boucle de rétroaction doit être étalonnée par un échantillon de référence, qui est lui caractérisé par un AFM métrologique [16]–[18]. Des déformations de l'image sur l'axe lent du balayage peuvent apparaître, notamment au début de l'acquisition d'une nouvelle image. Cela est dû au déplacement important effectué par l'élément piézoélectrique pour atteindre la position demandée. Cet effet peut être réduit en relançant l'acquisition de l'image après quelques lignes. Finalement, si la boucle de rétroaction est mal réglée, des surcompensations d'arrêtes peuvent être générées créant des artefacts (Figure 5.e).

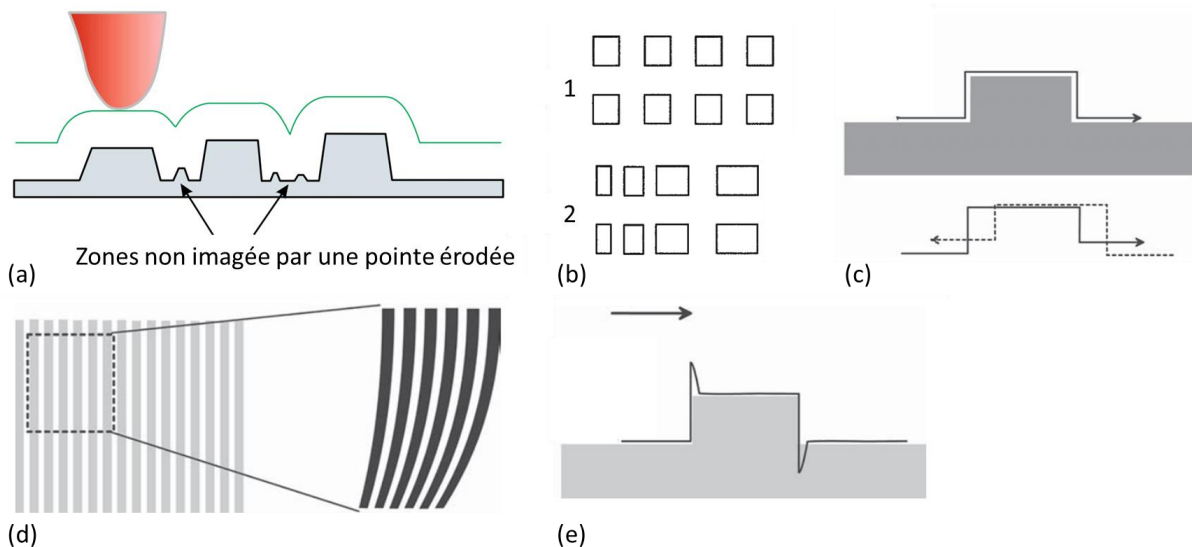


Figure 5. (a) Convolution pointe échantillon, (b) Non-linéarité du scanner xy, (c) Hystérésis du scanner z, (d) creep du scanner xy, (e) Surcompensation des arrêtes, [10], [14]

L'AFM dispose d'une bibliothèque de modes électriques comprenant notamment le scanning capacitance microscope (SCM), le microscope à force électrostatique (EFM) et le scanning microwave

microscope (SMM). Le SMM est un AFM travaillant en mode contact interfacé avec un VNA. La sonde SMM transmet et reçoit le signal micro-onde à l'échantillon. Pour atteindre des résolutions submicrométriques, le SMM opère dans le régime en champ-proche [19]. Différentes sondes SMM sont présentées en Figure 6.

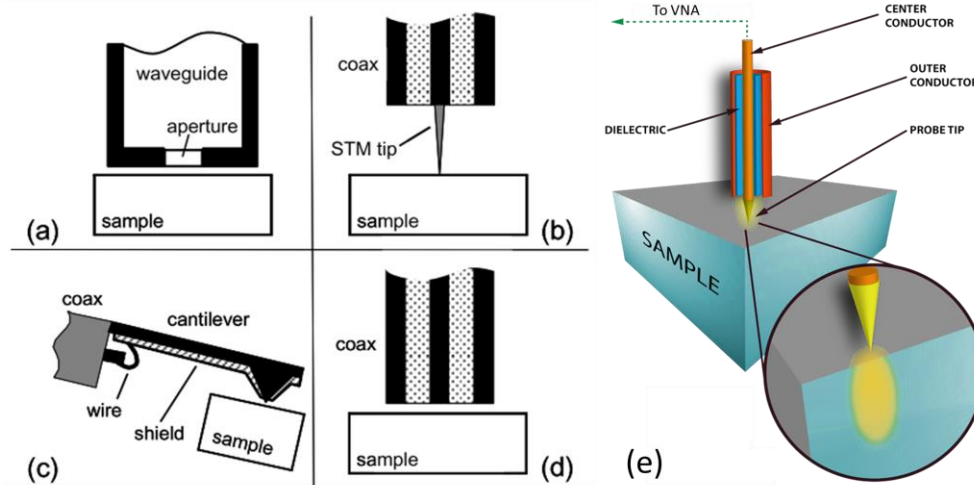


Figure 6. Différentes pointes SMM. (a) ouverture dans un guide d'onde, (b) : Pointe STM, (c). Pointe AFM blindée [20], (d). câble coaxiale ouvert [19], (e) distribution du champ électrique autour d'une sonde SMM [21].

Le travail présenté dans cette thèse se focalise exclusivement sur les sondes SMM fondées sur les pointes AFM.

### 3 Structure de référence

Comme toutes les techniques de mesure impliquant un VNA, le SMM doit être étalonné avant toute mesure. À ce jour, les procédures d'étalonnage ont été mentionnées dans la littérature :

- La méthode de résonance [22], [23] ;
- Une méthode fondée sur des courbes d'approche-retrait  $dC/dz$  issues de mesure EFM [24], [25] ;
- Une méthode à deux paramètres [26] ;
- Une méthode Short-Open-Load modifiée (mSOL) [27].

Les deux premières méthodes sont effectuées sur des diélectriques d'épaisseur connue, mais ne demandent pas d'échantillon présentant des impédances bien définies, ce qui n'est pas le cas pour les deux dernières méthodes. Dans ce chapitre, les structures d'étalonnage présentant des impédances définies sont détaillées. Historiquement, les premières structures de référence capacitive pour le SMM ont été développées par A. Karbassi [28] puis étendues aux valeurs inférieures à 1 fF [26]. Celles-ci servent de base pour les kits d'étalonnage capacitifs commercialisés par MC2 Technologies.

Ces structures sont composées de 144 motifs identiques présentant 4 zones de 48 micro-condensateurs Métal-Oxyde-Semiconducteur (MOS). Chaque zone présente un escalier de  $\text{SiO}_2$  composé de 4 marches sur lesquels 12 plots d'or sont déposés afin de former les électrodes supérieures des condensateurs. Afin de déterminer les valeurs de capacité présentes sur la structure, les dimensions des plots d'or et des couches diélectriques sont déterminées ainsi que la constante diélectrique du  $\text{SiO}_2$ . Ces mesures assurent la traçabilité au SI.

Les mesures d'épaisseur sont effectuées par un AFM étalonné (Nanoman V de Veeco) travaillant en mode tapping avec une pointe à faible rayon d'apex (OTESPA-R3, Bruker,  $R_{\text{apex}} = 7 \text{ nm}$ ) et une vitesse de balayage de  $6 \mu\text{m/s}$ . L'étalonnage de l'AFM a été fait sur un échantillon de référence dimensionnel

(P900H60, [29]) caractérisé par l'AFM métrologique du LNE [30]. Quatre images topographiques ont été acquises sur l'échantillon de référence de capacité (A61) (Figure 7).

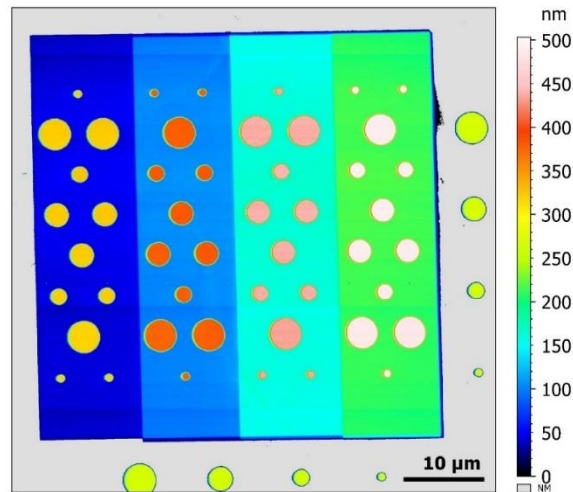


Figure 7. Image AFM de l'échantillon A61 après traitement avec le logiciel MountainLab

Le bilan d'incertitude associé à la mesure d'épaisseur est présenté dans le Tableau 3.

Tableau 3. Bilan d'incertitude associé à la mesure d'épaisseur par AFM sur chacune des terrasses (1 à 4) et sur les plots

Bilan d'incertitude (nm)	Type	1	2	3	4	Plots
Répétabilité	A	0,6	0,4	0,4	0,3	0,2
Étalonnage de l'AFM	B	0,3	0,7	1,1	1,5	1,9
Incertitude combinée		0,7	0,8	1,2	1,5	1,9
$h$ (nm)		$49,8 \pm 0,7$	$100,8 \pm 0,8$	$160,2 \pm 1,2$	$214,8 \pm 1,5$	$275,1 \pm 1,9$

L'incertitude due à l'étalonnage de l'AFM est définie par l'Équation 6 où  $h_{cal}$  est l'épaisseur de marche sur l'échantillon de étalonnage (70,7 nm) et  $u_{\text{épaisseur, cal}}$  est l'incertitude associée (0,5 nm).

$$u_{\text{épaisseur}} = \frac{u_{\text{épaisseur, cal}}}{h_{cal}} \quad \text{Équation 6.}$$

Les mesures d'aire sont, quant à elles, assurées par un microscope électronique à balayage (MEB) (Zeiss ULTRA-Plus) utilisant un détecteur à l'intérieur de la colonne (in-lens detector) afin d'accroître la sensibilité aux éléments topographiques. Deux séries d'images ont été acquises, la première avec un potentiel d'accélération de 3 kV et la seconde avec un potentiel d'accélération de 10 kV. Une vue globale, ainsi que deux zooms sur un plot de diamètre de 1 µm sont montrés en Figure 8.

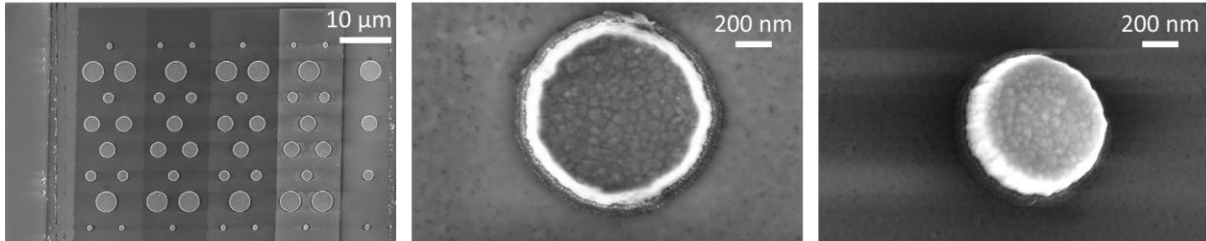


Figure 8. Image en mode électrons secondaires sur l'échantillon A61. (gauche) : vue globale, (centre) : zoom sur un plot de diamètre 1  $\mu\text{m}$ , (droite) : vue incliné du même plot.

Deux couronnes sont présentes autour du plot de 1  $\mu\text{m}$ . La première est due à l'inclinaison du flanc du plot confirmée par image AFM. L'angle du flanc est estimé à  $(19,5 \pm 1,5)^\circ$ . La seconde couronne est localisée en bas du plot. Des analyses par energy dispersive X-ray (EDX) ont montré que cette seconde couronne est composée de titane qui est la couche d'accroche entre l'or et le  $\text{SiO}_2$ . Une analyse plus poussée par AFM montre que la largeur de cette couronne est de  $(40,3 \pm 3,6)$  nm. Deux hypothèses peuvent expliquer cela, soit la résine utilisée dans la lithographie électronique (PMMA) a été érodée avant l'étape de lithographie du plot d'or, soit la résine a étiré la couche de titane.

Ces deux couronnes rendent difficile l'extraction de l'aire des plots à partir des images MEB. Une autre approche fut alors adoptée. L'AFM fut utilisé en mode tapping comme dans la section précédente et les aires de chaque plot furent évaluées à différentes hauteurs (10%, 30%, 50%, 70%, 90 %) relativement au substrat. Puis l'aire à la hauteur maximale du plot est extrapolée. Cette approche permet de s'affranchir de la convolution de la pointe avec l'échantillon. Le bilan d'incertitude des mesures d'aire par AFM est présenté Tableau 4.

Tableau 4. Bilan d'incertitude associé aux mesures d'aire par AFM sur l'échantillon A61

Bilan d'incertitude ( $\mu\text{m}^2$ )	Type	$C_{13}$	$C_{02}$	$C_{19}$	$C_{40}$
Répétabilité	A	$4,0 \cdot 10^{-3}$	$3,0 \cdot 10^{-3}$	$3,6 \cdot 10^{-3}$	$6,6 \cdot 10^{-3}$
Résolution de l'image	B	$102,6 \cdot 10^{-3}$	$74,7 \cdot 10^{-3}$	$50,2 \cdot 10^{-3}$	$22,6 \cdot 10^{-3}$
Étalonnage AFM	B	$28,0 \cdot 10^{-3}$	$14,9 \cdot 10^{-3}$	$6,9 \cdot 10^{-3}$	$1,7 \cdot 10^{-3}$
Correction de la couronne	B	$0,4 \cdot 10^{-3}$	$0,4 \cdot 10^{-3}$	$0,3 \cdot 10^{-3}$	$0,4 \cdot 10^{-3}$
Correction du cône	B	$30,7 \cdot 10^{-3}$	$23,2 \cdot 10^{-3}$	$15,9 \cdot 10^{-3}$	$28,1 \cdot 10^{-3}$
Incertainité combinée		$110,6 \cdot 10^{-3}$	$79,9 \cdot 10^{-3}$	$53,1 \cdot 10^{-3}$	$25,0 \cdot 10^{-3}$
Aire ( $\mu\text{m}^2$ )		13,33	7,47	3,61	0,99
$R_{\text{pad}}$ ( $\mu\text{m}$ )		2,06	1,54	1,07	0,56

Finalement, la capacité de déplétion est évaluée à partir de la concentration de dopants dans le substrat de silicium [31]. La concentration de dopants est donnée par une mesure de résistivité avec la station sous pointe. Les pointes sont mises en contact avec les plots Schottky. Un potentiel continu est appliqué à l'ensemble de la structure pour s'assurer du caractère conducteur des diodes Schottky. La concentration de dopants ainsi mesurée est de  $(8,2 \pm 0,3) \cdot 10^{18}$  atomes/ $\text{cm}^3$ . La capacité de déplétion en série contribue à la capacité totale par 0,25% à 8,64%.

À cause du faible ratio entre l'épaisseur du diélectrique et le rayon des plots, les effets de bord ne sont plus négligeables dans le calcul de la capacité et l'équation de capacité plan-plan n'est plus valide. Il est alors nécessaire de recourir à une simulation numérique pour extraire les capacités des mesures précédemment exposées. Un modèle est conçu à l'aide du logiciel Comsol Multiphysics en utilisant le

module AC/DC. L'équation de Poisson est utilisée pour déterminer la distribution du potentiel électrique ( $V$ ) dans l'ensemble de la boîte de simulation. La capacité est alors évaluée par l'Équation 7.

$$C = - \frac{\iint_{top\ electrode} \vec{\nabla} \cdot (\epsilon \vec{\nabla} V) \cdot d\vec{s}}{\Delta V} \quad \text{Équation 7.}$$

où  $\vec{s}$  est le vecteur normal à la surface. À partir de ces données de simulation et de la littérature [32], une formule empirique est trouvée afin de propager les incertitudes sur la valeur de capacité. Un accord à 2% est trouvé entre les valeurs simulées et celles retournées par l'équation empirique.

Le bilan d'incertitude associé aux différentes capacités est alors établi (Tableau 5, [33]).

Tableau 5. Bilan d'incertitude associé à l'échantillon de référence capacitif (A61)

Bilan d'incertitude	Type	$C_{13}$	$C_{37}$	$C_{48}$
$C_{tot}$ (fF)		9,472	2,528	0,272
$u_{Cox}$ (aF)		181,9	37,7	7,4
$u_A$ ( $\mu\text{m}^2$ )	(A, B)	0,110	0,111	0,025
$u_h$ (nm)	(A,B)	0,7	1,5	1,5
$u_{\text{permittivité}}$	B	0,039	0,039	0,039
$u_{Cd}$ (aF)	B	188,7	14,5	2,1
$u_{\text{model}}$ (aF)	B	1,9	0,5	0,1
$u_{\text{Combinée}}$ (aF)		262,6	63,1	9,2
$u_{\text{Combinée}}$ (%)		2,77	1,60	2,84

Ce bilan d'incertitude permet de souligner l'importance des mesures dimensionnelles et de la capacité de déplétion dans la détermination des capacités de la structure. Une nouvelle version de l'échantillon de référence capacitif est proposée afin de réduire l'incertitude associée aux valeurs capacitives. Pour réduire l'incertitude associée aux mesures d'aire, l'épaisseur des plots a été diminuée (de 275 nm à 100 nm) permettant l'obtention d'un flanc vertical. La composition de la couche d'accroche passa du titane au chrome afin de s'assurer de l'absence d'épaulement à la base des plots. Ces deux modifications permettent l'extraction des aires à partir des images MEB assurant une meilleure incertitude. De plus, l'aire des plots et l'épaisseur des couches diélectriques furent augmentées afin de diminuer l'incertitude relative.

Le substrat de silicium fut choisi avec une concentration de dopant plus élevée réduisant l'impact de la capacité de déplétion.

Après mesure des aires par MEB, des épaisseurs par AFM et de la concentration de dopant par la station sous pointe, le bilan d'incertitude fut établi pour cette nouvelle version d'échantillon de étalonnage capacitif Tableau 6.

Tableau 6. Bilan d'incertitude associé à l'échantillon de référence capacitif, seconde version (B03)

Bilan d'incertitude	Type	$C_{13}$	$C_{37}$	$C_{48}$
$C_{tot}$ (fF)		39,381	11,112	0,298
$u_{Cox}$ (aF)		463,2	122,5	5,6
$u_A$ ( $\mu\text{m}^2$ )	(A, B)	0,00142	0,00142	0,00134
$u_h$ (nm)	(A,B)	4,6	11,2	11,2
$u_{\text{permittivité}}$	B	0,039	0,039	0,039
$u_{Cd}$ (aF)	B	29,3	2,3	0,1
$u_{\text{model}}$ (aF)	B	39,4	11,1	0,3
$u_{\text{Combinée}}$ (aF)		465,5	123,0	5,6
$u_{\text{Combinée}}$ (%)		1,18	1,11	1,88

## 4 Méthode d'étalonnage du SMM sur structure de référence

Le système en place au LNE est un AFM 5600 LS (Keysight Technology) interfacé avec un VNA N5230C (Keysight Technology). L'ensemble est dans une salle blindée pour s'affranchir des champs électromagnétiques extérieurs. L'AFM est placé dans une boîte à gants sous atmosphère contrôlée (température, pression, humidité relative) d'azote. Un système interférométrique est implémenté entre le VNA et l'AFM pour augmenter le nombre de pics disponibles et la sensibilité de l'instrument [34] comme montré en Figure 9. Pour l'ensemble des mesures de ce chapitre, sauf mention contraire, la pointe utilisée est une pointe en platine massif (300PT12 B, Rocky Mountain Nanotechnology).

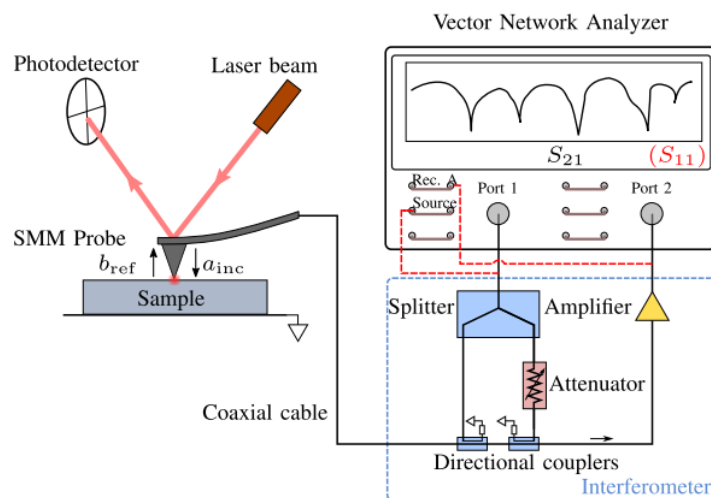


Figure 9. Schéma du setup SMM avec système interférométrique, [35]



Le VNA utilisé a été caractérisé avec un niveau de bruit inférieur à -93,9 dB et un niveau de bruit pour le SMM interférométrique inférieur à 59,6 dB sur la gamme 2,13 GHz à 18,94 GHz [35].

L'étalonnage mSOL de l'instrument fut caractérisé sur la première et seconde version de l'échantillon de référence capacitif. Le paramètre  $S_{11,m}$  a été mesuré sur l'ensemble du motif de 48 plots, puis redressé par le logiciel Gwyddion [36]. Pour chaque plot, plusieurs valeurs de  $S_{11,m}$  sont enregistrées et un histogramme est tracé. La valeur la plus représentative du plot est extraite à partir d'un ajustement de fonction gaussienne par Matlab en utilisant supprimant les points aberrants [37].

La Figure 10 montre la projection de la pointe SMM sur l'échantillon (a) ainsi que les capacités pointe-échantillon en jeu dans différentes configurations.

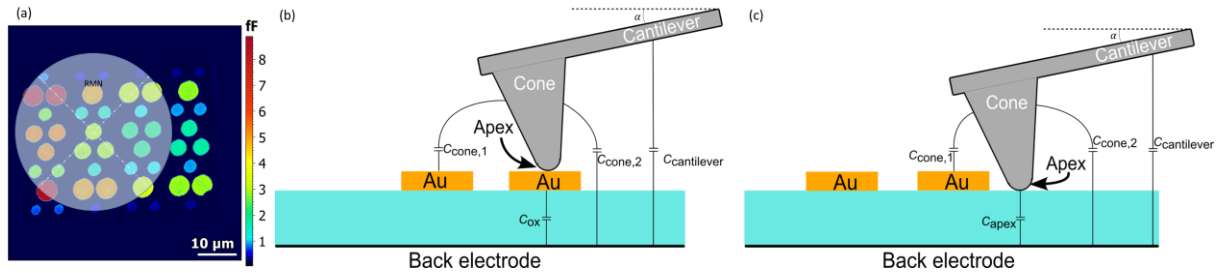


Figure 10. (a) Projection du cône de la sonde AFM; Capacité en jeu dans le cas (b) d'une pointe sur un plot d'or, (c) d'une pointe dans le voisinage d'un plot d'or.

La Figure 10.b montre bien la contribution non-locale des capacités sondées par la pointe sur un plot d'or. Pour s'en affranchir, une solution est la méthode par substitution. En effet, à cause de l'importante différence d'échelle entre les plots capacitifs et le cône et le levier de la pointe, les contributions des capacités cône-échantillon et levier-échantillon ne varient pas de manière significative lorsque la pointe est sur un plot d'or et dans son voisinage immédiat. On peut alors considérer la différence de  $S_{11,m}$  pour ces deux configurations comme correspondant à la différence entre la capacité du plot et la capacité entre l'apex et la couche diélectrique ( $\Delta S_{11,m} = C_{ox} - C_{apex}$ ). Comme la capacité de l'apex sur la couche diélectrique est faible, on peut approximer  $\Delta S_{11,m}$  à  $C_{ox}$ . Dans la pratique, cela est fait en enlevant la valeur moyenne du fond de chaque terrasse (mean background subtraction). Cette méthode fut reportée dans la littérature pour la première fois par [26].

Le bilan d'incertitude pour la étalonnage mSOL est reporté dans le Tableau 7.

Tableau 7. Bilan d'incertitude associé à la mesure de capacité par le SMM calibré sur la première version de l'échantillon de référence (A64), [33]

	$C_{05}$	$C_{23}$	$C_{32}$
Capacitance (fF)	$(8,79 \pm 0,19)$	$(1,36 \pm 0,04)$	$(0,33 \pm 0,01)$
Incertitude, Type A (%)	0,5	1,3	2,1
$u_{hist,i}$	0,1	0,6	2,1
$u_{rép,i}$	0,5	1,1	0,2
Incertitude, Type B (%)	2,1	2,9	2,6
$u_{SMM,i}$	2,1	2,9	2,5
$u_{parasite}$	0,02	0,18	0,72
$u_{humidité}$	0,2	0,2	0,2
$u_{combinée} (%)$	2,2	3,2	3,3

Les incertitudes d'histogramme correspondent à l'écart-type associé à chaque histogramme, celles de répétabilité sont évaluées à partir de 3 séries de mesure. Les incertitudes  $u_{SMM,i}$  prennent leur origine dans l'incertitude associée aux valeurs des capacités de la structure de référence. Elles sont évaluées

en changeant les valeurs du triplet de référence par les incertitudes de chacune des capacités considérées. Le triplet de référence prend alors 27 valeurs différentes et  $u_{SMM,i}$  prend alors pour valeur l'écart-type de l'ensemble des étalonnages effectués avec ces triplets. Les capacités parasites sont estimées à partir des expressions analytiques de capacité pointe-échantillons [38]–[40] en prenant les valeurs nominales de géométrie de la pointe. Enfin, les effets d'humidité ont été étudiés en effectuant l'étalonnage à quatre valeurs d'humidité relative (RH) différentes et en comparant les résultats des étalonnages à RH plus élevée (RH = 2%, RH = 2,9% et RH = 4%) avec celle à plus faible RH (RH = 0,9 %). Après ces mesures, une valeur conservatrice de 0,2% a été considérée pour l'incertitude due à l'humidité.

L'impact de la position du motif étudié a été évalué par des mesures en aller-retour sur 5 motifs différents. Pour s'affranchir des possibles dérives temporelles le motif central (de référence) fut scanné avant et après le motif test (excentré). Le SMM fut étalonné sur le motif de référence et l'étalonnage fut appliqué au motif test. Un bon accord (à 2%) est trouvé entre les valeurs attendues et les valeurs mesurées sur les différents motifs tests soulignant ainsi l'homogénéité de la capacité de déplétion et du bruit électromagnétique au-dessus de l'échantillon A64.

La même expérience fut conduite entre deux échantillons de la première version d'étalonnage (A64 et A61). L'A64 a servi d'échantillon de référence tandis que l'A61 est l'échantillon test. Des écarts pouvant aller jusqu'à 20% entre les valeurs attendues et mesurées furent observés.

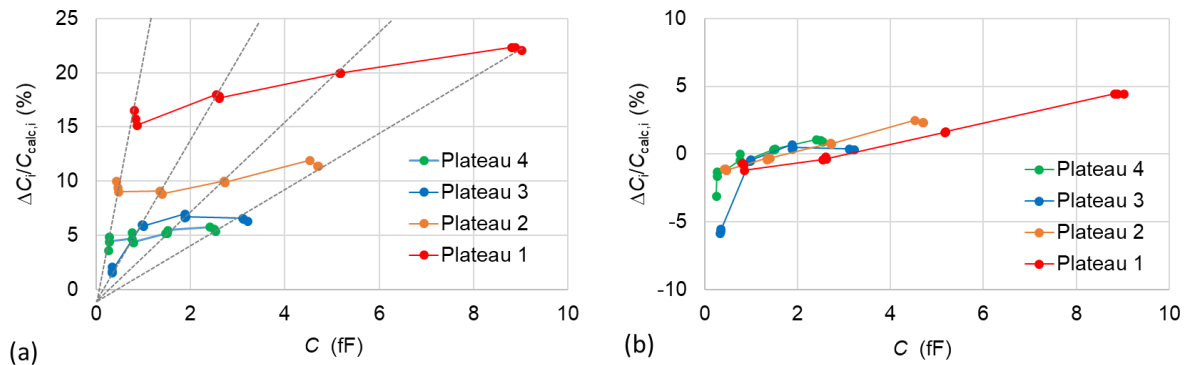


Figure 11. Différences de capacité attendues et mesurées en % sur A61, SMM Calibré sur l'A64 (a) : différence brute, (b) différence corrigées par une capacité en série C'

La Figure 11 reporte ces écarts relatifs plateau par plateau. En Figure 11.a, une tendance linéaire est visible dans l'écart relatif entre plots de même diamètre. Cela peut s'expliquer par un condensateur plan en série ( $C' = \epsilon \frac{A}{l}$ ) où A est l'aire des plots et l est l'épaisseur de la couche parasite variant entre les échantillons. Considérant que la couche parasite est l'oxyde natif (SiO<sub>2</sub>) présent à l'arrière de la structure, la différence d'épaisseur est alors de 7,61 nm. Cela semble important pour un oxyde natif. Une autre explication pourrait être la différence de constante diélectrique du SiO<sub>2</sub> entre les deux structures ou une combinaison de ces deux phénomènes.

La nouvelle version de l'échantillon d'étalonnage (MC2, v2 ici B03) fut également évaluée. L'auto-étalonnage du SMM montra un bon accord avec des erreurs relatives inférieures à 1,2%. Une comparaison entre les deux versions de l'étalon de référence fut effectuée (Figure 12).

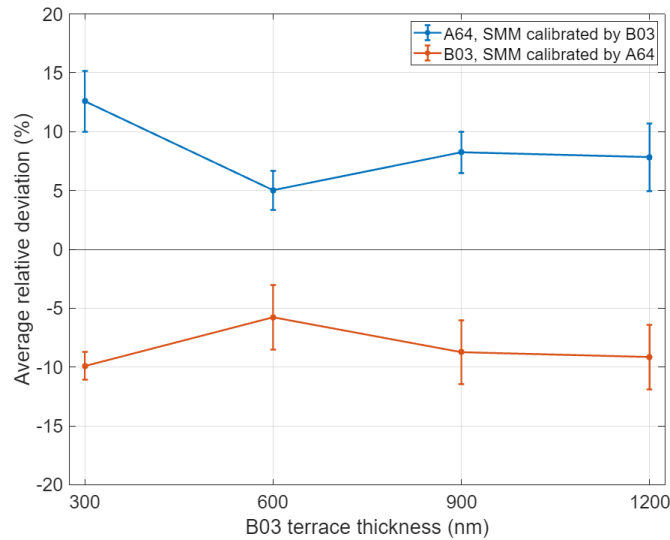


Figure 12. Moyenne des écarts relatifs en % entre les valeurs mesurées et attendues sur l'échantillon test.

Un bon accord est trouvé entre les valeurs attendues et mesurées avec des écart-types inférieurs à 6,6%. Cependant, un écart systémique et symétrique semble être présent à hauteur de 7% entre les deux structures. Une comparaison plus poussée entre les deux échantillons est à prévoir pour mieux comprendre l'origine de cet écart.

La robustesse de la méthode de substitution fut évaluée en utilisant une pointe présentant un levier blindée (sMIM, PrimeNano [41]). Pour prendre en compte la géométrie particulière de la sonde, un porte pointe adapté fut fabriqué par C&K Dole. La pointe fut ensuite utilisée pour acquérir une image  $S_{11,m}$  sur l'échantillon de référence A64. Le SMM fut étalonné avec les données redressées avec et sans la méthode de substitution.

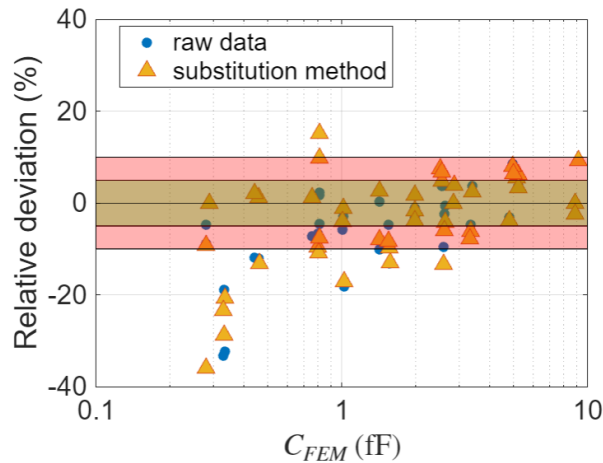


Figure 13. Ecarts relatifs entre les valeurs mesurées et attendues des capacités pour les données traitées (triangle) ou non (rond) par la méthode de substitution.

La Figure 13 présente les écarts relatifs entre les capacités mesurées et attendues dans le cas du traitement avec et sans méthode de substitution. Il n'y a pas d'écart significatif dans les tendances entre ces deux traitements, montrant ainsi la fiabilité de la méthode de substitution qui est comparable à l'usage d'une pointe blindée.

L'impact du revêtement de la pointe est également étudié. Les performances de l'étalonnage obtenues avec une pointe RMN étalon et une revêtue de graphène sont comparées. L'écart-type des écarts relatifs est de 80 aF pour la pointe RMN simple et de 61 aF pour la pointe revêtue de graphène. L'origine de cette amélioration peut être double, la nature hydrophobique de la couche de graphène,

diminuant l'impact du RH ou la meilleure stabilité mécanique de la pointe apportée par le revêtement graphène. Des expériences supplémentaires sont à prévoir en changeant le RH et en augmentant la vitesse de scan pour discriminer entre ces deux hypothèses.

Finalement, des simulations en résolvant l'équation de propagation d'une onde électromagnétique dans une configuration SMM sont conduites pour évaluer plus finement l'impact du ménisque d'eau sur l'étalonnage mSOL. La boîte de simulation comprend une pointe SMM sur une capacité MOS de valeur connue Figure 14.

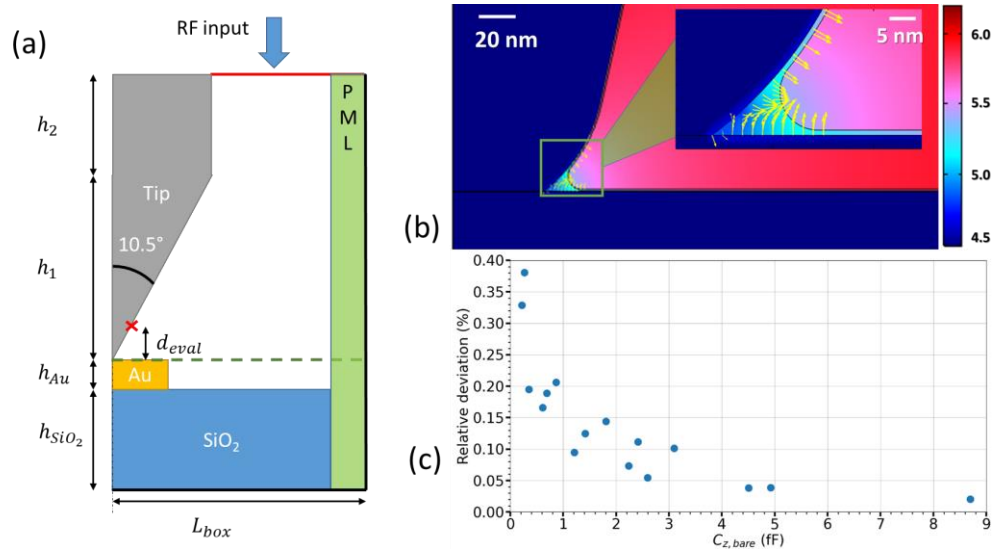


Figure 14. (a) Boîte de simulation. ligne verte pointillée: ligne de contrôle pour l'intégration du potentiel électrique; Croix rouge : Point de contrôle pour l'intégration du champ magnétique ; PML : Perfectly Matched Layer ; Frontière noire en gras, condition Perfect Electric Conductor (PEC) ; Frontière rouge : condition de port, (b) Distribution du champ électrique ( $\log_{10}E$ ) à l'interface pointe échantillon dans le cas d'un ménisque d'eau présent. (c) Ecart relatif entre les valeurs attendues et résultant de la mesure simulée dans le cas d'un étalonnage sans ménisque d'eau appliquée à une configuration avec ménisque d'eau.

Le signal micro onde est injecté par la condition de port au sommet de la boîte de simulation, puis est transmis à l'échantillon par le guide d'onde formé par la pointe et la frontière droite de la boîte de simulation. L'étalonnage mSOL est effectué puis évalué sur 13 autres capacités. L'écart relatif associé à cet étalonnage est inférieur à 1%. Les paramètres d'étalonnage sont ensuite appliqués à la configuration avec un ménisque d'eau (Figure 14.b). Les écarts relatifs entre les valeurs attendues et résultant de la simulation de la mesure sont reportés en Figure 14.c. Conformément aux valeurs obtenues expérimentalement, les écarts relatifs sont négligeables ( $< 0,05\%$ ) pour les fortes valeurs de capacité ( $> 4$  fF) puis augmentent jusqu'à quelques dixièmes de pourcent (0,4%).

Enfin, nous avons traité un cas d'application sous la forme de l'extraction de la constante diélectrique de matériaux piézoélectrique à forte constante diélectrique (PZT et PMN-PT) sur lesquels des plots capacitifs ont été déposés [42]. Le SMM est étalonné sur l'échantillon de référence A64, puis une mesure de  $S_{11,m}$  est acquise sur l'échantillon test, enfin un second balayage est effectué sur l'A64 pour contrôler toute dérive temporelle. L'étude est détaillée ici uniquement sur le PZT, le même principe s'appliquant à la mesure du PMN-PT.

Le SMM étalonné a servi pour extraire les valeurs capacitives des plots sur le PZT. Connaissant les caractéristiques dimensionnelles de l'échantillon (aire des plots, hauteurs des plots et du diélectrique), des simulations numériques ont été conduites. Pour chaque plot mesuré, la constante diélectrique de la couche PZT fut ajustée afin de faire correspondre la valeur calculée à la valeur obtenue expérimentalement.

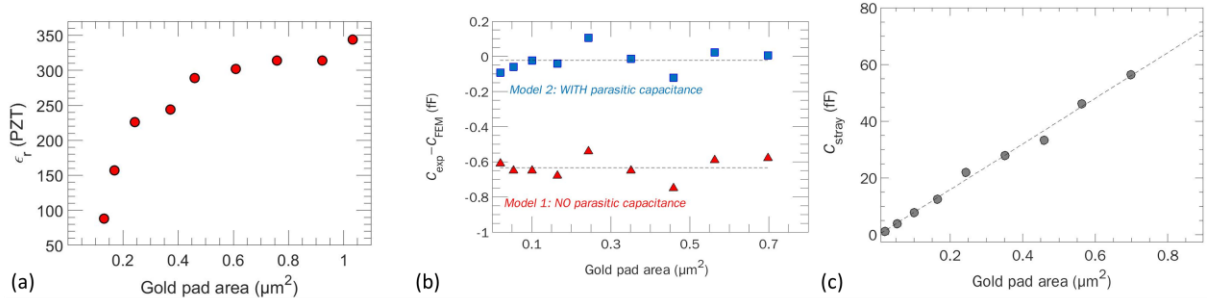


Figure 15. (a) Evolution de la constante diélectrique évaluée plot par plot sur le PZT en fonction de l'aire des plots ; (b) : Constante diélectrique évaluée sur l'ensemble des plots sans et avec une capacité parasite en série; (c) capacité parasite en fonction de l'aire des plots.

La constante diélectrique ainsi obtenue augmente de manière significative avec l'aire des plots ce qui n'est pas attendu et ne peut pas être expliqué par la configuration de l'échantillon. Cependant, si l'on considère une capacité parasite en série des plots, il est possible de trouver une constante diélectrique inchangée pour l'ensemble de la structure correspondant à un écart absolu constant entre les valeurs calculées et mesurées. La capacité en série à rajouter pour retrouver un écart nul est alors calculée pour chaque plot. En traçant sa valeur en fonction de l'aire des plots, un comportement correspondant à un condensateur plan est trouvé. Par calcul, une couche d'épaisseur comprise entre 2 nm et 10 nm avec une constante diélectrique comprise entre 30 et 80 correspond aux valeurs trouvées. Cette constante diélectrique fait penser à celle de l'eau confinée sur une dimension [43], [44]. L'épaisseur correspondante est en accord avec les images en coupe au MEB acquise à l'interface PZT-Plot d'or [42].

## 5 Méthode d'étalonnage du SMM à partir des courbes d'approche retrait $dC/dz$

La seconde méthode d'étalonnage repose sur des courbes d'approche retrait en mode EFM. Un potentiel alternatif est appliqué à la pointe. Lorsque celle-ci approche la surface de l'échantillon, la force électrostatique exercée sur la pointe la met en oscillation mécanique. Une détection synchrone est mise en place pour extraire le second harmonique de l'oscillation mécanique tout en conservant constante la fréquence d'amplitude au cours de l'expérience. Cette oscillation peut être convertie en force électrostatique par l'Équation 8.a, où  $S$  est la sensibilité du photodétecteur [m/V] et  $G$  est le gain de la détection synchrone. Il existe une relation entre le second harmonique de la force électrostatique et le gradient de capacité Équation 8.b, [45].

$$F_{2\omega} = A_{p,2\omega} \frac{kS}{G} \quad \text{Équation 8.a}$$

$$F_{2\omega} = -\frac{V_{AC}^2 \cos(\omega t)}{4} \frac{dC}{dz} \quad \text{Équation 8.b}$$

La pointe utilisée dans ce chapitre a une constante de raideur nominale de 18 N/m (300Pt12B, RMN). La pointe est amenée sur un motif de l'échantillon de référence capacitif (A64) au-dessus de la terrasse de  $\text{SiO}_2$  de 100 nm. Trois séries de 10 courbes approche retrait sont acquises. Les deux premières servent à la stabilisation de l'élément piézoélectrique  $z$  et la dernière est utilisée pour la mesure. Le paramètre  $S_{11,m}$  est acquis simultanément.

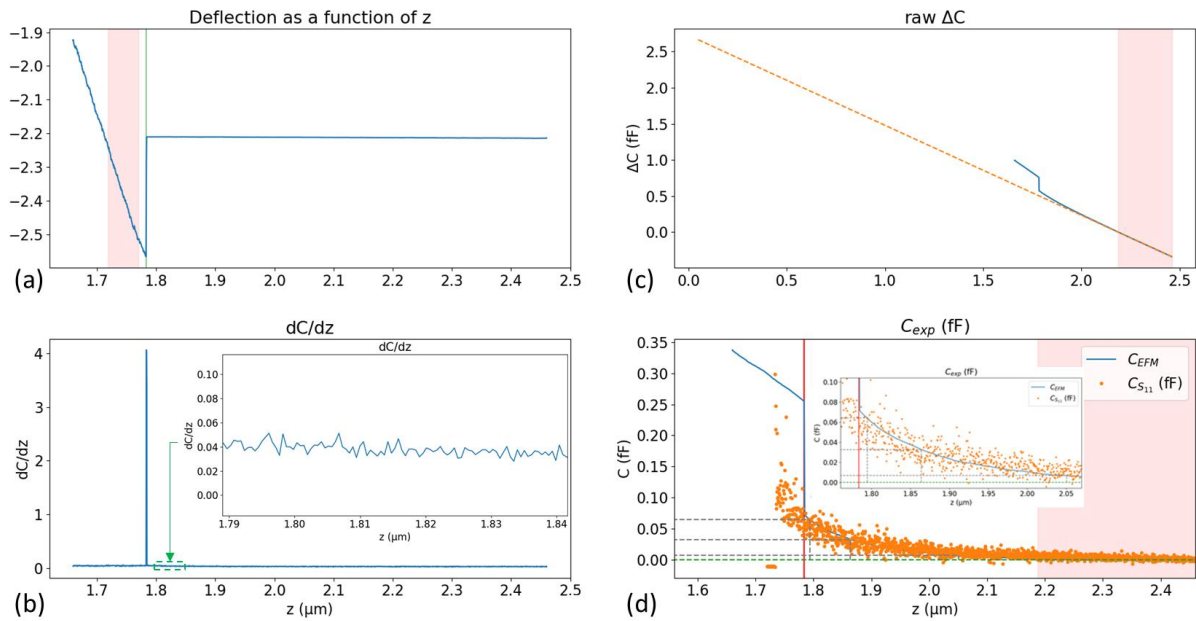


Figure 16. Interprétation de la courbe de retrait sur le SiO<sub>2</sub> ( $h=100$  nm). (a) : Déflexion ; (b) : Signal  $dC/dz$  en considérant la constante de raideur nominale ( $k=18$  N/m). (c)  $\Delta C$  brut ; (d) :  $\Delta C$  redressé de la pente lointaine (suppression de la contribution du levier).

La Figure 16 présente le traitement effectué sur les courbes d'approche retrait sur le diélectrique. En sélectionnant 3 points de référence, il est possible d'étalonner le SMM comme le montre le bon accord obtenu entre la courbe EFM et la courbe de capacité issue de l'étalonnage du SMM.

Il peut être intéressant de comparer les performances d'étalonnage du chapitre 3 et celles issues des courbes EFM. Cependant, les valeurs maximales obtenues sur le diélectrique sont de quelques centaines d'attofarad. Il n'y a pas de recouvrement des plages de capacité couverte par ces deux méthodes, rendant impossible la comparaison. Une approche naïve serait d'effectuer la mesure EFM au-dessus des plots capacitifs afin de prendre avantage de la capacité définie par le plot d'or. L'impédance sondée est alors la capacité de l'oxide en série avec la capacité formée entre la pointe et le plot d'or ( $C_{air}$ ). Celle-ci ayant un ordre de grandeur de 2 à 3 fois plus faible que celle définie par le plot capacitif. Les impédances étant en série, l'impédance total vue par la pointe est alors dominée par  $C_{air}$ .

$$\frac{1}{C} = \frac{1}{C_{ox}} + \frac{1}{C_{Air}} \quad \text{Équation 9}$$

Le signal associé à la capacité entre le plot d'or et l'électrode inférieure de l'échantillon est alors sous le niveau de bruit de la technique EFM. Une autre approche serait d'effectuer les deux mesures sur un échantillon présentant des capacités plus faibles (inférieures à 100 aF). Cela permettrait un recouvrement des plages couvertes par les deux techniques.

La méthode EFM peut également être utilisée afin d'établir une mesure traçable au SI de la constante de raideur du levier. Dans ce cas, une courbe  $dC/dz$  est acquise sur un échantillon de constante diélectrique connue. Connaissant la géométrie de la pointe, il est possible d'estimer la capacité pointe-échantillon en jeu [46]. La constante de raideur du levier peut alors être ajustée pour faire correspondre la courbe de capacité obtenue expérimentalement avec celle attendue de la géométrie de la pointe et constante diélectrique de l'échantillon. Un exemple est présenté en Figure 17. Le modèle est représenté par la courbe continue en noire et l'incertitude générée par l'incertitude sur le rayon de l'apex est représentée en rouge. Les données expérimentales sont quant à elles représentées en vert avec l'incertitude de répétabilité. Une constante de raideur de 1 N/m assure une bonne correspondance entre les deux courbes. Cela est à mettre en comparaison avec la valeur nominale de 0,8 N/m.

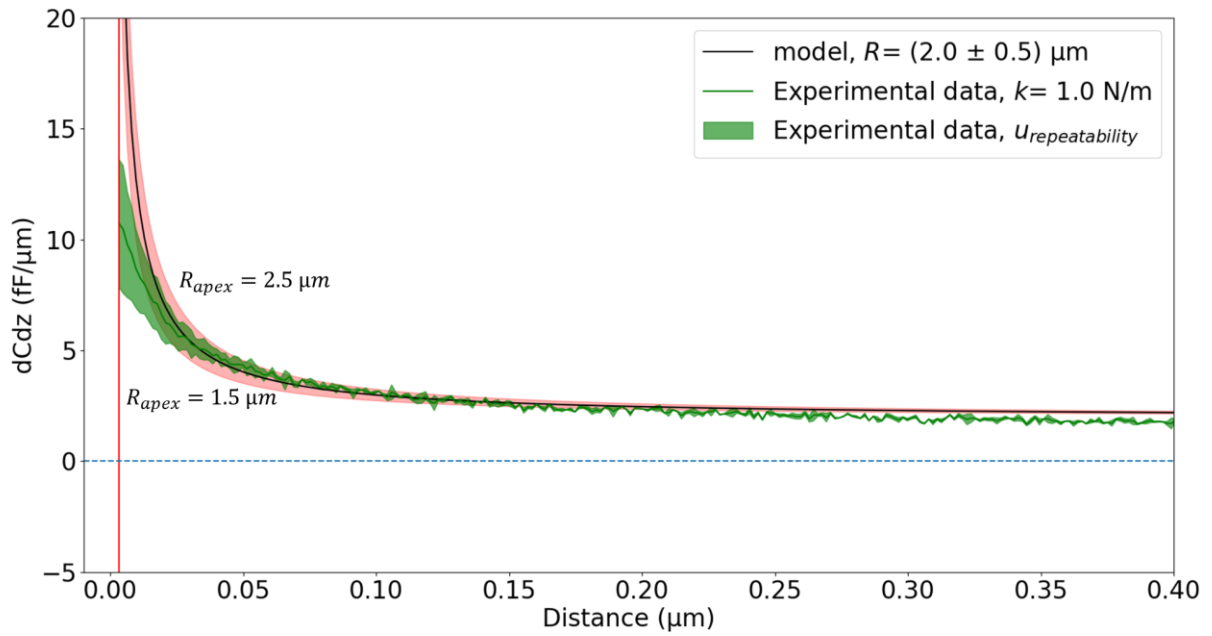


Figure 17. Détermination de la constante de raideur de la pointe à partir de courbe  $dC/dz$ .

Des travaux futurs sont à prévoir pour caractériser la constante de raideur pointe avec les méthodes traditionnelles (bruit thermique, méthode de Sader) afin d'avoir des points de comparaison.

# Conclusion

Cette thèse traite de l'établissement d'une métrologie des mesures de propriétés électriques à l'échelle submicrométrique. La technique Scanning Microwave Microscopy (SMM), qui permet d'accéder aux propriétés électriques d'un échantillon (impédance, permittivité électrique, et concentration de dopants), répond à ces critères. Il s'agit d'un microscope à force atomique interfacé à un analyseur de réseaux vectoriel (VNA). Si la métrologie associée au VNA est bien établie, ce n'est pas le cas pour les configurations SMM. Un VNA permet, s'il est étalonné, d'extraire des propriétés électriques à partir de la mesure du paramètre de réflexion. Pour une configuration SMM, la méthode la plus commune est dérivée de l'étalonnage Short-Open-Load utilisant trois impédances connues sur un échantillon de référence. L'un des résultats clés de cette thèse est l'établissement du bilan d'incertitude associé à la mesure d'impédance par SMM. Pour ce faire, une caractérisation de l'échantillon de référence démontre que l'incertitude associée aux valeurs des impédances présentes (0,3 fF – 9,8 fF) est inférieure à 2,8 %. Fort de ce bilan d'incertitude, un second échantillon de référence est proposé et caractérisé avec une incertitude associée inférieure à 1,9%. L'incertitude sur la mesure des capacités de référence par le SMM étalonné est inférieure à 3%. Un cas d'application est proposé : l'extraction de la permittivité d'échantillons piézoélectriques avec une incertitude inférieure à 6.9%. L'incertitude due à l'humidité relative (RH) sur l'étalonnage du SMM a été étudiée empiriquement et par simulation numérique. Cette dernière impacte l'étalonnage à hauteur de 0,4 % pour les capacités de 0,3 fF et devient négligeable pour les capacités au-dessus de 4 fF. Enfin, des courbes  $dC/dz$  ont été acquises par microscopie à force électrostatique (EFM) sur un diélectrique connu afin d'assurer la traçabilité de la mesure de constante de raideur de la sonde employée.



- [1] Keysight Technologies, "Impedance Measurement Handbook," *Agilent*, p. 140, 2009, [Online]. Available: [www.keysight.com](http://www.keysight.com).
- [2] J.-S. Yang *et al.*, "Piezoelectric and Pyroelectric Properties of Pb(Zr,Ti)O<sub>3</sub> Films for Micro-Sensors and Actuators," *Integr. Ferroelectr.*, vol. 54, no. 1, pp. 515–525, 2003, doi: 10.1080/714040701.
- [3] B. G. Streetman and S. K. Banerjee, *Solid state electronic devices*, 7th ed. 2016.
- [4] J. P. Dunsmore, *Handbook of Microwave Component Measurements: With Advanced VNA Techniques*. Wiley, 2012.
- [5] A. Rumiantsev and N. Ridler, "VNA calibration," *IEEE Microw. Mag.*, vol. 9, no. 3, pp. 86–99, 2008, doi: 10.1109/MMM.2008.919925.
- [6] EURAMET, "Guidelines on the Evaluation of Vector Network Analysers," 2018.
- [7] K. Technologies, "Application Note Keysight Technologies Split Post Dielectric Resonators for Dielectric Measurements of Substrates."
- [8] D. Popovic *et al.*, "Precision open-ended coaxial probes for in vivo and ex vivo dielectric spectroscopy of biological tissues at microwave frequencies," *IEEE Trans. Microw. Theory Tech.*, vol. 53, no. 5, pp. 1713–1721, 2005, doi: 10.1109/TMTT.2005.847111.
- [9] J. B. Jarvis *et al.*, "Measuring the Permittivity and Permeability of Lossy Materials: Solids, Liquids, Metals, Building Materials, and Negative-Index Materials," Boulder, CO, 2005.
- [10] P. Avouris, B. Bhushan, D. Bimberg, K. von Klitzing, C.-Z. Ning, and R. Wiesendanger, *Atomic Force Microscopy*. 2019.
- [11] T.-T. Nguyen, "Synthèse et contrôle de la taille de nanocristaux de silicium par plasma froid. Application dans les domaines de l'optoélectronique et de la nanoélectronique," no. January 2008, 2010.
- [12] B. Gautier *et al.*, "Techniques de mesure de grandeurs électriques adaptées aux nanocircuits Techniques de mesure de grandeurs électriques adaptées aux nanocircuits par," *Tech. l'Ingénieur*, vol. 33, no. 0, 2016.
- [13] J. Rivoal and C. Fr, "Microscopie à force atomique ( AFM )," vol. 33, no. 0, 2005.
- [14] D. Ricci and P. C. Braga, "Recognizing and avoiding artifacts in AFM imaging.," *Methods Mol. Biol.*, vol. 242, pp. 25–37, 2004, doi: 10.1385/1-59259-647-9:25.
- [15] J. Canet-Ferrer, E. Coronado, A. Forment-Aliaga, and E. Pinilla-Cienfuegos, "Correction of the tip convolution effects in the imaging of nanostructures studied through scanning force microscopy," *Nanotechnology*, vol. 25, no. 39, 2014, doi: 10.1088/0957-4484/25/39/395703.
- [16] E. Heaps *et al.*, "Bringing real-time traceability to high-speed atomic force microscopy," *Meas. Sci. Technol.*, vol. 31, no. 7, p. 74005, 2020, doi: 10.1088/1361-6501/ab7ca9.
- [17] A. Delvallée, N. Feltin, S. Ducourtieux, M. Trabelsi, and J. F. Hochepped, "Toward an uncertainty budget for measuring nanoparticles by AFM," *Metrologia*, vol. 53, no. 1, pp. 41–50, 2015, doi: 10.1088/0026-1394/53/1/41.
- [18] A. J. Fleming, "A review of nanometer resolution position sensors: Operation and performance," *Sensors Actuators, A Phys.*, vol. 190, pp. 106–126, 2013, doi: 10.1016/j.sna.2012.10.016.
- [19] S. M. Anlage, V. V. Talanov, and A. R. Schwartz, *Principles of near-field microwave microscopy*, vol. 2. 2007.
- [20] D. W. Van Der Weide, "Localized picosecond resolution with a near-field microwave/scanning-force microscope," *Appl. Phys. Lett.*, vol. 70, no. 6, pp. 677–679, 1997, doi: 10.1063/1.118272.
- [21] C. Boutin and P. Kabos, "Near-Field Scanning Microwave Microscope: Big at the Nanoscale," *Analytical Science*, 2012.
- [22] C. Gao, T. Wei, F. Duewer, Y. Lu, and X. D. Xiang, "High spatial resolution quantitative microwave impedance microscopy by a scanning tip microwave near-field microscope," *Appl. Phys. Lett.*, vol. 71, no. 13, pp. 1872–1874, 1997, doi: 10.1063/1.120444.
- [23] C. Gao, F. Duewer, and X. D. Xiang, "Quantitative microwave evanescent microscopy," *Appl. Phys. Lett.*, vol. 75, no. 19, pp. 3005–3007, 1999, doi: 10.1063/1.125216.
- [24] G. Gramse, I. Casuso, J. Toset, L. Fumagalli, and G. Gomila, "Quantitative dielectric constant

- measurement of thin films by DC electrostatic force microscopy," *Nanotechnology*, vol. 20, no. 39, 2009, doi: 10.1088/0957-4484/20/39/395702.
- [25] G. Gramse, M. Kasper, L. Fumagalli, G. Gomila, P. Hinterdorfer, and F. Kienberger, "Calibrated complex impedance and permittivity measurements with scanning microwave microscopy," *Nanotechnology*, vol. 25, no. 14, 2014, doi: 10.1088/0957-4484/25/14/145703.
- [26] H. P. Huber *et al.*, "Calibrated nanoscale capacitance measurements using a scanning microwave microscope," *Rev. Sci. Instrum.*, vol. 81, no. 11, 2010, doi: 10.1063/1.3491926.
- [27] J. Hoffmann, M. Wollensack, M. Zeier, J. Niegemann, H. P. Huber, and F. Kienberger, "A calibration algorithm for nearfield scanning microwave microscopes," *Proc. IEEE Conf. Nanotechnol.*, pp. 1–4, 2012, doi: 10.1109/NANO.2012.6322116.
- [28] A. Karbassi, D. Ruf, A. D. Bettermann, C. A. Paulson, and D. W. Van Der Weide, "Quantitative scanning near-field microwave microscopy for thin film dielectric constant measurement," *Rev. Sci. Instrum.*, vol. 76, 2008, doi: 10.1063/1.2953095.
- [29] L. Crouzier *et al.*, "Development of a new hybrid approach combining AFM and SEM for the nanoparticle dimensional metrology," *Beilstein J. Nanotechnol.*, vol. 10, pp. 1523–1536, 2019, doi: 10.3762/bjnano.10.150.
- [30] S. Ducourtieux and B. Poyet, "Development of a metrological atomic force microscope with minimized Abbe error and differential interferometer-based real-time position control," *Meas. Sci. Technol.*, vol. 22, no. 9, 2011, doi: 10.1088/0957-0233/22/9/094010.
- [31] S. M. Sze and K. K. Ng, *Physics of Semiconductor Devices*, 3rd ed. John Wiley & Sons, Inc., 2007.
- [32] G. J. Sloggett, N. G. Barton, and S. J. Spencer, "Fringing fields in disc capacitors," *J. Phys. A. Math. Gen.*, vol. 19, no. 14, pp. 2725–2736, 1986, doi: 10.1088/0305-4470/19/14/012.
- [33] **F. Piquemal, J. Morán-Meza, A. Delvallée, D. Richert, and K. Kaja, "Progress in Traceable Nanoscale Capacitance Measurements Using Scanning Microwave Microscopy," *Nanomaterials*, vol. 11, no. 820, 2021, doi: doi.org/10.3390/nano11030820.**
- [34] T. Dargent *et al.*, "An interferometric scanning microwave microscope and calibration method for sub-fF microwave measurements," *Rev. Sci. Instrum.*, vol. 84, no. 12, 2013, doi: 10.1063/1.4848995.
- [35] **J. Hoffmann *et al.*, "Comparison of Impedance Matching Networks for Scanning Microwave Microscopy," *IEEE Trans. Instrum. Meas.*, 2024, doi: 10.1109/TIM.2024.3378310.**
- [36] P. Klapetek, D. Nečas, and C. Anderson, "Gwyddion User Guide (gwyddion.net/documentation/user-guide-en)," 2021, [Online]. Available: gwyddion.net/documentation/user-guide-en.
- [37] B. Rosner, "Percentage points for a generalized esd many-outlier procedure," *Technometrics*, vol. 25, no. 2, pp. 165–172, 1983, doi: 10.1080/00401706.1983.10487848.
- [38] L. Fumagalli *et al.*, "Nanoscale capacitance imaging with attofarad resolution using ac current sensing atomic force microscopy," *Nanotechnology*, vol. 17, no. 18, pp. 4581–4587, 2006, doi: 10.1088/0957-4484/17/18/009.
- [39] L. Fumagalli, G. Ferrari, M. Sampietro, and G. Gomila, "Dielectric-constant measurement of thin insulating films at low frequency by nanoscale capacitance microscopy," *Appl. Phys. Lett.*, vol. 91, no. 24, 2007, doi: 10.1063/1.2821119.
- [40] G. Gomila, G. Gramse, and L. Fumagalli, "Finite-size effects and analytical modeling of electrostatic force microscopy applied to dielectric films," *Nanotechnology*, vol. 25, no. 25, 2014, doi: 10.1088/0957-4484/25/25/255702.
- [41] K. Lai, W. Kundhikanjana, M. A. Kelly, and Z. X. Shen, "Nanoscale microwave microscopy using shielded cantilever probes," *Appl. Nanosci.*, vol. 1, no. 1, pp. 13–18, 2011, doi: 10.1007/s13204-011-0002-7.
- [42] **D. Richert *et al.*, "Traceable nanoscale measurements of high dielectric constant by scanning microwave microscopy," *Nanomaterials*, vol. 11, no. 11, 2021, doi: 10.3390/nano11113104.**
- [43] L. Fumagalli *et al.*, "Anomalously low dielectric constant of confined water," *Science (80-. )*, vol. 360, no. 6395, pp. 1339–1342, 2018, doi: 10.1126/science.aat4191.

- [44] T. Dufils, C. Schran, J. Chen, A. K. Geim, L. Fumagalli, and A. Michaelides, "Origin of dielectric polarization suppression in confined water from first principles," *Chem. Sci.*, vol. 15, no. 2, pp. 516–527, 2023, doi: 10.1039/d3sc04740g.
- [45] P. Girard, "Electrostatic force microscopy: Principles and some applications to semiconductors," *Nanotechnology*, vol. 12, no. 4, pp. 485–490, 2001, doi: 10.1088/0957-4484/12/4/321.
- [46] G. Gramse, M. Kasper, L. Fumagalli, G. Gomila, P. Hinterdorfer, and F. Kienberger, "Corrigendum: Calibrated complex impedance and permittivity measurements with scanning microwave microscopy (2014 Nanotechnology)," *Nanotechnology*, vol. 26, no. 14, 2015, doi: 10.1088/0957-4484/26/14/149501.



<b>Introduction .....</b>	<b>30</b>
<b>Chapter 1 State of the art on impedance measurement at the nanoscale .....</b>	<b>33</b>
1 <i>Physic recall on electric impedance</i> .....	34
1.1 Impedance .....	34
1.2 Dielectric constant and loss tangent .....	35
1.3 Capacitor measurement .....	36
1.4 Macroscale measurement .....	38
2 <i>Microwave measurement</i> .....	39
2.1 Theory .....	39
2.2 Measurement by vector network analyzer .....	41
2.2.1 Vector Network Analyzer (VNA) .....	41
2.2.2 Test fixture.....	42
2.3 Smith Chart .....	44
3 <i>Atomic Force Microscopy</i> .....	45
3.1 System description – Mode.....	45
3.1.1 Contact mode.....	46
3.1.2 Dynamic mode.....	47
3.2 Instrument artifact and calibration .....	48
4 <i>Modes for AFM electric imaging</i> .....	50
5 <i>Conclusion</i> .....	52
<b>Chapter 2 Reference standards .....</b>	<b>56</b>
1 <i>Needs and samples description</i> .....	57
1.1 Need for calibration sample .....	57
1.2 History of capacitance standards for nanoscale measurements .....	57
1.2.1 Parallel plate structure .....	58
1.2.2 Membrane structure.....	59
2 <i>Structure characterization</i> .....	60
2.1 Dimensional measurement .....	61
2.1.1 Thickness evaluation.....	61
2.1.2 Area of the electrodes .....	62
2.2 Electrical measurement .....	66
2.2.1 Dopant concentration .....	66
2.2.2 Relative permittivity .....	67
3 <i>Estimation of capacitance values</i> .....	68
3.1 Simulation .....	68
3.1.1 Need for simulation .....	68
3.1.2 Solving Poisson’s equation by Comsol Multiphysics.....	68
3.1.3 Using an open-source solution – FeniCS python library .....	71
3.2 Empirical formula .....	71
4 <i>Evaluation of the uncertainty associated with capacitance</i> .....	72
5 <i>Second version of the calibration structure</i> .....	73
5.1 Parallel plate architecture.....	73
5.2 Membrane structure.....	75
6 <i>Conclusion</i> .....	76
<b>Chapter 3 Modified Short Open Load calibration .....</b>	<b>79</b>
1 <i>System description</i> .....	80
1.1 Probe holder .....	80
1.2 Interferometric system .....	81
1.3 VNA characterization .....	82

2	<i>Self-calibration</i> .....	83
2.1	Method description .....	83
2.2	Far parts contribution .....	86
2.3	Uncertainty budget.....	87
3	<i>Calibration robustness</i> .....	89
3.1	System of coordinate .....	89
3.2	Impact of location .....	90
3.3	Comparison between the two reference structures .....	91
3.4	Tip shape contribution .....	95
3.4.1	Shielded probe .....	95
3.4.2	Tip geometries .....	97
3.4.3	Tip coating .....	98
3.5	Simulation.....	98
3.5.1	Configuration .....	99
3.5.2	Self-calibration .....	101
3.5.3	Water meniscus evaluation .....	101
4	<i>Application – measurement on high-k sample</i> .....	104
4.1	Sample description .....	104
4.2	Dielectric constant evaluation.....	106
5	<i>Conclusion</i> .....	110
<b>Chapter 4 Electrostatic Force Microscopy based calibration .....</b>		<b>114</b>
1	<i>Principle</i> .....	115
1.1	Operating mode far from the resonance frequency.....	117
2	<i>Comparison with the mSOL calibration</i> .....	117
2.1	Capacitance gradient on the dielectric.....	118
3	<i>Estimation of the cantilever spring constant</i> .....	120
3.1	Common methods for spring constant evaluation .....	120
3.1.1	Thermal noise.....	120
3.1.2	Sader method.....	121
3.1.3	Ion milling method .....	122
3.1.4	Force sensor.....	123
3.2	Electrostatic method .....	124
4	<i>Conclusion</i> .....	128
<b>Conclusion.....</b>		<b>132</b>

## Introduction

The twenty century was marked by the emergence of logic circuit to automatize the treatment of information. At the beginning, the components were analogic and quite large as the emblematic lamp transistor. The sector went through major transformation with the invention of solid state electronics. Starting from a germanium wafer, then latter a silicon wafer, the components are manufactured and connected between each other directly on the wafer. As the technology progresses, the fabrication technology, in particular the etching resolution, improved allowing to make smaller and smaller component. The cost of logic board started decreasing as it was possible to put the same number of component using less material. Gordon Moore, one of the co-fonder of Intel was able to come up with his law stating that the number of transistors in an integrated circuit doubles about every two years. To keep up with this trend, we have seen the apparition of novel architure such as FinFETs and Gates all around (GAA) <sup>1</sup>, as well as the continuous decrease in the dimension of the component, now down to 2 nm <sup>2</sup>. exploration of 2D nanomaterials nanostructure with the possibility of atomically flat component.

To support the development of such small scale electronic, there is a need for accessing the impedance, dielectric constant, dopant density and leakage current at the sub-micrometric scale. These quantities translate to the speed of transistors and processors, read/write memory access, secured data storage, and telecommunication applications, or to failure analysis. It must satisfy the requirement of information technology (IT), communication, health system (lab-on-chip, biosensor) and energy industry (renewable energy) as well as expectation from standardization effort such as IEC/TC113. Due to the small size of the considered component, random variation and in the amount and variation of molecules can affects those parameters. For 2D materials, atomic defect characterization is key for their integration in 3D chips. Moreover the novel architectures have a small target to background volume ratio leading to low signal-to-noise ratio. Another visible trend is the switch from Si to Ge as channel material <sup>3</sup>. Those differents points make it necessary to develop a metrology for electrical measurement at sub-micrometric resolution.

In reason of the versatility of its modes, the atomic force microscope (AFM) is a tool that could fill this need. By sweeping a tip with submicrometric apex radius over a sample, the AFM can give knowledge on the sample topography. If this tip is conductive, it can access the electrical properties of a sample such as current or resistance (CAFM), electric field distribution (EFM), surface potential (KPFM) and dopant density (SSRM).

Another technique gained interest over the past years, the scanning microwave microscopy (SMM). It relies on a well known electrical characterization method at GHz frequency in which a microwave is sent by a vector network alayser (VNA) to the sample and its reflection parameter ( $S_{11}$ ) is collected. There is a relationship between the electrical impedance and the  $S_{11}$ . Nevertheless, due to perturbation along the transmission line, the  $S_{11}$  at the sample interface differs from the  $S_{11}$  measured at the VNA interface. This can be compensated by the calibration of the instrument using three standard in a procedure called Short-Open-Load (SOL) calibration. When interfaced with an AFM using a conductive probe, this measurement method can satisfy the requirement for electrical measurement at sub-micrometric scale. Such a experiment is called a SMM. This method can access the impedance, electrical permittivity and dopant concentration on surface and buried structures <sup>4</sup>. Accessing to the properties of buried structures is key to characterize 3D integrated circuits. An example of application is the detection of hole inside through silicon via by SMM. Contrarily to other methods (FIB/SEM, AFM tomography), this technique is nondestructive.

The IRDS also highlights the importance of metrology for carriers mobilibility in for stack on stressed silicon, silicon on isolator, germanium on isolator, and III-V heterostructures. There is also a need to characterize the resistances in play inside transistors as those determine the maximal operating frequency of the transistor.

Although the metrology of electrical measurement using a VNA is already well established, it is not the case for SMM measurements due to lack of calibration structure, standardization of the calibration method, and specific consideration due to the AFM itself. Indeed, as all AFM techniques, several parameters affects the SMM measure. The main ones are the coating and shape of the AFM probe, the tip-sample contact type and water meniscus formed at the interface between the two, the chemical state of the sample's surface as well as its roughness. Finally because it is an electric imaging mode, there is other consideration such as the electrochemistry (for example oxide growth due to relative humidity and application of an electric field), joule heating, injection and diffusion of charged species, and parasitic capacitance from other part of the AFM probe that can harm the spatial resolution of the measurement.

Establishing traceable SMM measurement and uncertainty budget associated can provide a roadmap for future development of SMM and stimulate standardization and international comparison. Reliable metrology at the nanoscale will also enable faster route to the market of critical low-carbon industrial technologies, including energy efficient electronics, solar energy, and more efficient power electronics. Possible application could be found in the new mobility concepts (autonomous driving, electromobility, Hydrogen technology) which have needs for new data processing devices in the on-board electronics of all vehicles. A novel class of electronic nanodevices with lower power consumption and improved robustness will be an important support for autonomous driving cars. Such technologies will have significant impact in reduction of greenhouse gas emissions. It will also help fortify the europe position in the semiconductor industry.

It exists two main calibration techniques. The first one is based on a calibration standard composed of at least three known impedances. By adapting a modified SOL calibration, the measurement acquired on the sample can be use to establish a mapping function from the measured  $S_{11}$  to the calibrated one. The second calibration methode is based on the acquisition of a  $dC/dz$  approach retract curve at lower frequency (typically a few kHz). By integrating this curve, the tip-sample capacitance can be known at any distance. It is then possible to select three different capacitance to establish the calibration of the instrument providing that the capacitance doesn't change significantly from low to high frequency. This translate in an unchanged dielectric constant for the whole frequency range, limiting the available material. For the first method, the main uncertainty originates from the calibration standard itself while the second method is limited by the spring constant of the cantilever ( $k$ ).

The first chapter of this thesis will be focused on the physical recall on the electrical impedance and properties (dielectric constant and loss tangent), then attention will be drawn on the measurement techniques for impedance at low and radio frequency (RF). Finally, the operating principle of AFM will be detailed as well as its principal mode for electric measurement.

The second chapter will deal with the reference standards for the first method of SMM calibration. The pre-existing standard was characterize dimensionnaly and electrically. Numerical simulations were conducted from those properties to have knowledge of the values of the different capacitors. A comprehensive uncertainty budget on those value was produced. Knowing the major source of uncertainty, a second version of the calibration standard was designed and manufactured. It was fully characterize and a significant improvement in the uncertainty on the capacitance value is shown.

The third chapter is focused on the first calibration method. The experimental setup is described and the associated noise level of the VNA measurement using is characterized. Then, the SMM setup is calibrated over the calibration standards and the uncertainty budget is established. The impact of various parameters (choice of AFM probe, location on the standards, relative humidity) on the calibration performance are studied both empirically and by use of numerical simulation for the water meniscus. The substitution method used to allow sub-micrometric measurement with an unshield tip is validated by experiment using a shielded tip. The calibrated instrument is finally used to extract the dielectric constant of high- $\kappa$  piezoelectric material over the 0.5 GHz to 6 GHz range as well as the



associated uncertainty budget. The work presented in this chapter could help disseminate the good practice for instrument calibration and capacitance measurement by SMM.

The fourth and last chapter draws attention to the second calibration method, the use of the approach retract EFM curve. The method is described and used to calibrate the SMM. A first attempt to compare the two calibration method is made but was unsuccessful. Perspectives are presented to solve the issue. A second part of this chapter focuses on the necessity of knowing the spring constant of the used cantilever. A short state of the art on the different available techniques is provided and a novel technique using the EFM approach-retract curve is presented. The preliminary results are within the expected values and future work are described to establish the associated uncertainty budget. A modification of the method is also presented to improve the uncertainty associated with the tip-sample distance evaluation during the experiment.

---

<sup>1</sup> International Roadmap for Devices and System, IEEE, 2023

<sup>2</sup> Pi. S. et al., Memristor crossbar arrays with 6-nm half-pitch and 2-nm critical dimension, Nature Nanotechnology, 2019

<sup>3</sup> Bunday, B. et al., X. Metrology capabilities and needs for 7nm and 5nm logic nodes, SPIE advanced lithography, 2017

<sup>4</sup> Kopanski J. et al., Characterization of buried interfaces with scanning probe microscopy, ECS Meeting abstracts, 2016

# Chapter 1 State of the art on impedance measurement at the nanoscale

## Chapter 1 State of the art on impedance measurement at the nanoscale 33

1	<i>Physic recall on electric impedance</i> .....	34
1.1	Impedance .....	34
1.2	Dielectric constant and loss tangent .....	35
1.3	Capacitor measurement.....	36
1.4	Macroscale measurement .....	38
2	<i>Microwave measurement</i> .....	39
2.1	Theory .....	39
2.2	Measurement by vector network analyzer.....	41
2.2.1	Vector Network Analyzer (VNA) .....	41
2.2.2	Test fixture.....	42
2.3	Smith Chart .....	44
3	<i>Atomic Force Microscopy</i> .....	45
3.1	System description – Mode.....	45
3.1.1	Contact mode.....	46
3.1.2	Dynamic mode.....	47
3.2	Instrument artifact and calibration .....	48
4	<i>Modes for AFM electric imaging</i> .....	50
5	<i>Conclusion</i> .....	52

# 1 Physic recall on electric impedance

## 1.1 Impedance

As mentioned in the introduction, there is a growing need to characterize the electrical properties of electronic devices at the nanoscale. One key element that can be measured is the complex impedance ( $Z$ ). It is defined as the opposition a component offers to the flow of an alternative current at a frequency  $f$  as defined in Equation 1-1

$$Z_x = \frac{U}{I} \quad \text{Equation 1-1,}$$

where  $U$  is the complex potential drop inside the impedance and  $I$  is the complex current. The real part of the impedance is the resistance ( $R$ ) and its imaginary part is the reactance ( $X$ ). At room temperature, the electrical resistance is present in any component, there is no purely imaginary impedance. A positive reactance is said inductive while a negative one is capacitive. By definition, the impedance of an inductance can be written as in Equation 1-2

$$Z_x = R + j\omega L \quad \text{Equation 1-2,}$$

and the impedance of a capacitance is defined by Equation 1-3

$$Z_x = R - j\frac{1}{\omega C} \quad \text{Equation 1-3,}$$

where  $\omega$  is the angular frequency ( $\omega = 2\pi f$ ). From an electromagnetic point of view, an inductance is the magnetic flow to current ratio. Using the Lenz law, the inductance can be written as in Equation 1-4.

$$U = -L \frac{\partial I}{\partial t} \quad \text{Equation 1-4.}$$

The capacitance is defined as the stored charge ( $Q$ ) to voltage ratio as reported in Equation 1-5.

$$C = \frac{Q}{|U|} \quad \text{Equation 1-5.}$$

Figure 1-1 shows a perfect parallel plate capacitor.

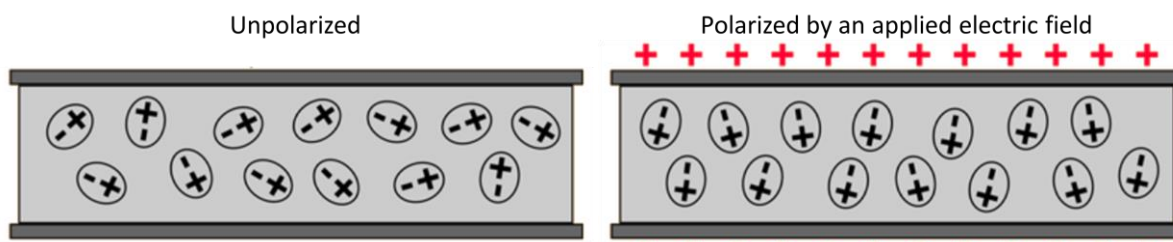


Figure 1-1, Parallel plate capacitor unpolarized and under an electric field excitation.

Applying Gauss' law to the polarized configuration, the surface charge density  $\sigma$  is given by Equation 1-6.

$$\sigma = \epsilon_0 \epsilon_r' \frac{V}{d} \quad \text{Equation 1-6.}$$

$$C = A \frac{\sigma}{V} \quad \text{Equation 1-7.}$$

where  $d$  is the plate separation distance,  $\epsilon_0$  is the electrical permittivity of the vacuum, and  $\epsilon_r'$  is the relative electrical permittivity of the medium. The capacitance is then given by Equation 1-7.

## 1.2 Dielectric constant and loss tangent

The relative electrical permittivity of the medium is a complex quantity. Its real part ( $\epsilon_r'$ ) is called the dielectric constant and represents the electrical field screening occurring in a dielectric medium under an electric field excitation. Its imaginary part ( $\epsilon_r''$ ) is referred to as the dielectric loss factor. This screening is dependent on the frequency of the incident electric field. It is due to the polarization occurring inside the dielectric medium. This polarization can be divided into three contributions: dipolar, ionic, and electronics [1]. Figure 1-2 shows the frequency dependence of those contributions.

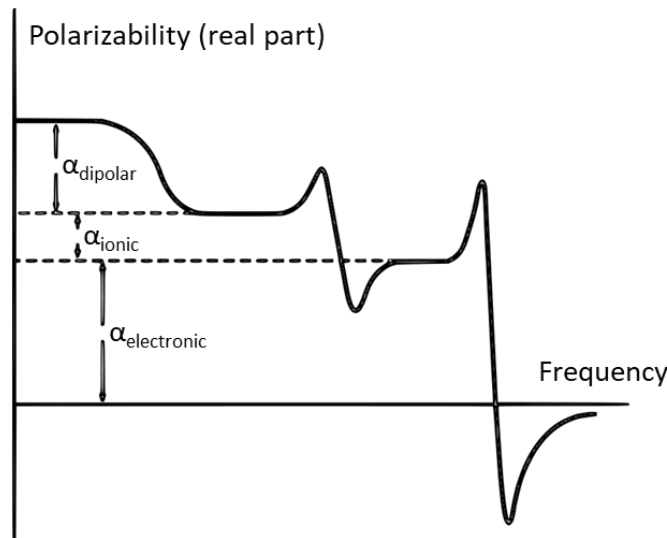


Figure 1-2, Frequency dependence of the polarizability, [1]

The dipolar contribution arises from molecules' orientation inside the electric field and is the first to vanish because of the inertia of the molecules. The ionic contribution comes from the displacement of ions relative to each other. Finally, the electronic contribution emanates from the displacement of the electron shell with respect to the nucleus. This contribution is the last one to vanish thanks to the low inertia of electrons. The nucleus-electron interaction can be modeled as a harmonic oscillator by the Drude-Lorentz model. Focusing only on the electronic consideration, the dielectric function can be described by Equation 1-8.

$$\epsilon_r(\omega) = 1 + \frac{\omega_p^2}{\omega_0^2 - \omega^2 - j\omega\gamma} \quad \text{Equation 1-8.}$$

where  $\omega_0$  is the oscillator resonant pulsation,  $\omega_p$  is the plasma pulsation and  $\gamma$  is the damping coefficient. The behavior of the real part and imaginary part of the dielectric function can be better understood by rewriting Equation 1-8 in Equation 1-9.

$$\epsilon_r(\omega) = 1 + \omega_p^2 \frac{\omega_0^2 - \omega^2 + j\omega\gamma}{(\omega_0^2 - \omega^2)^2 + (\omega\gamma)^2} \quad \text{Equation 1-9.}$$

For frequencies far below  $\omega_0$ , the dielectric function is constant. In this thesis work, silicon oxide was extensively used, and its resonant pulsation is around 5.2 THz as shown in Figure 1-3 [2].

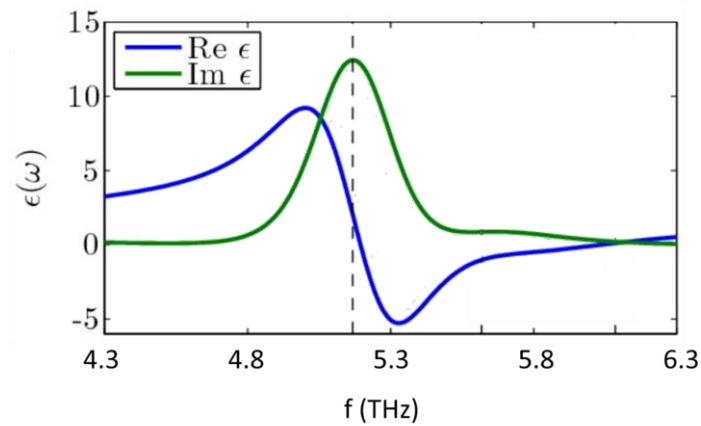


Figure 1-3. Dielectric function of thin film SiO<sub>2</sub> layer, [2]

As we work in the microwave regime, this frequency is quite far from our working frequency. We can then consider the dielectric function of SiO<sub>2</sub> to be constant. Finally, the loss tangent is widely used in the semiconductor industry to characterize the lossy behavior of dielectric medium. It is defined by Equation 1-10.

$$\tan(\delta) = \frac{\omega\epsilon_r'' + \sigma}{\omega\epsilon_r'} \quad \text{Equation 1-10.}$$

where  $\sigma$  is the medium electrical conductivity and  $\tan(\delta)$  is the loss tangent. It can be seen as the ratio of dielectric loss to the energy stored in the dielectric. The dielectric loss is the sum of loss due to bound charge, dipole relaxation, and free charge conduction.

### 1.3 Capacitor measurement

As mentioned in 1.1, the dielectric constant is directly linked to the capacitance value. Hence, it can be assessed by measuring the impedance of a capacitor. Independently from the measurement method, the measured value ( $Z_m$ ) differs from the real impedance value ( $Z_r$ ). For example, Figure 1-4 represents the real and measured impedance value of a capacitor. The real-world capacitor is a combination of the ideal capacitor ( $C$ ) and the parasitic component from the capacitor itself ( $R_p$ ) and the cables ( $R_s, L$ ). Then, the test fixture has its own impedance due to internal components and cables. We have access to the measured value and the objective is to have this value as close as possible to the real impedance value. For this, we need to know the real impedance value and it is one prime reason for the calibration sample in which the  $Z_r$  can be known with a controlled uncertainty.

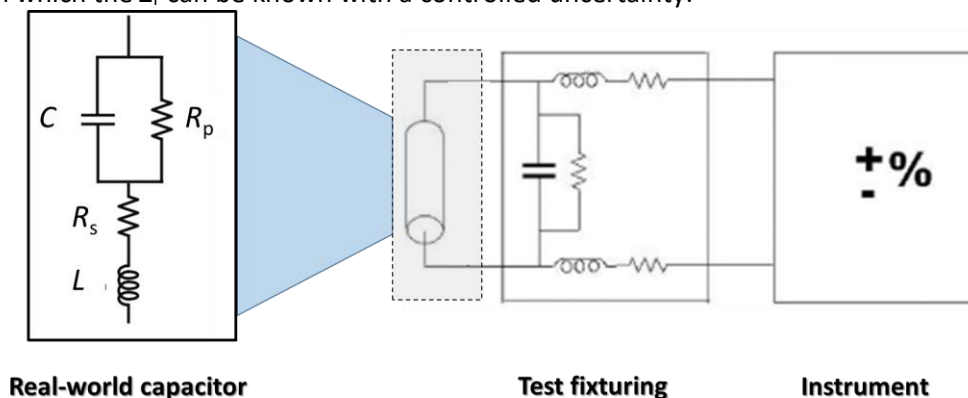


Figure 1-4. Real and measured impedance values, from [3]

Various parameters affect the measured impedance value. The most common ones are the test frequency, the test signal level, DC bias, the temperature, and the noise level. As shown in Figure 1-2,

the polarizability, and the dielectric constant, of a medium are frequency-dependent. Moreover, the complex impedance of the real-world capacitor is given by Equation 1-11.

$$Z_r = R_s + \frac{R_p}{1 + \omega^2 R_p^2 C^2} + j\omega \frac{L - R_p^2 C + \omega^2 R_p^2 C^2 L}{1 + \omega^2 R_p^2 C^2} \quad \text{Equation 1-11.}$$

Hence, the component will switch from a capacitive behavior to an inductive behavior. The test signal level plays a role in the signal-to-noise ratio (SNR). A high SNR confers better accuracy and stability to the measurement. The impedance also changes with the temperature due to the thermal expansion. Finally, depending on the nature of the studied capacitors, several physical phenomena affect the capacitor value and are DC bias dependent. There are several types of capacitors, the two of interest for us, the Metal-Oxide-Semiconductor (MOS) capacitor and the Metal-Insulator-Metal capacitor (MIM), are shown in Figure 1-5.

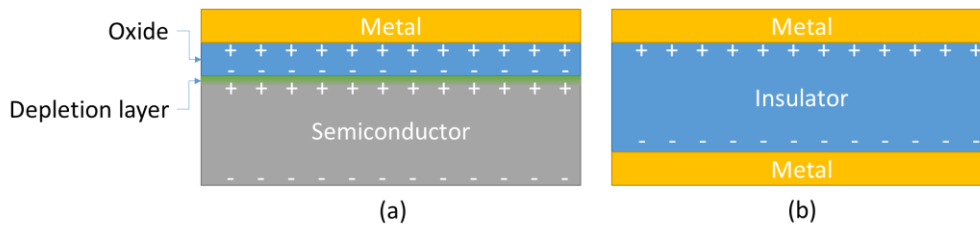


Figure 1-5. (a) MOS capacitor, (b) MIM capacitor

In a MOS capacitor, a depletion layer is formed in the semiconductor [4] according to Equation 1-12.

$$C_d = \epsilon A \sqrt{\frac{e^2 N_a}{kT\epsilon} (V_b - V)} \quad \text{Equation 1-12.}$$

where  $A$  is the area of the electrode,  $k$  is the Boltzmann constant,  $e$  is the fundamental charge,  $T$  is the temperature,  $V_b$  is the built-in voltage and  $V$  is the DC bias. The capacitance of the structure ( $C$ ) is then given by

Equation 1-13.

$$\frac{1}{C} = \frac{1}{C_{ox}} + \frac{1}{C_d} \quad \text{Equation 1-13.}$$

where  $C_{ox}$  is the capacitance of the oxide layer. Hence, the DC bias voltage has an impact on the measured capacitance.

For the MIM capacitor, the insulator of interest for us was a piezoelectric with a high dielectric constant. The ionic contribution to polarizability needs to be considered in addition to the electronic contribution. Indeed, most piezoelectric have a perovskite structure (Figure 1-6) composed of a lattice of divalent metal ions and one single tetravalent metal ion.

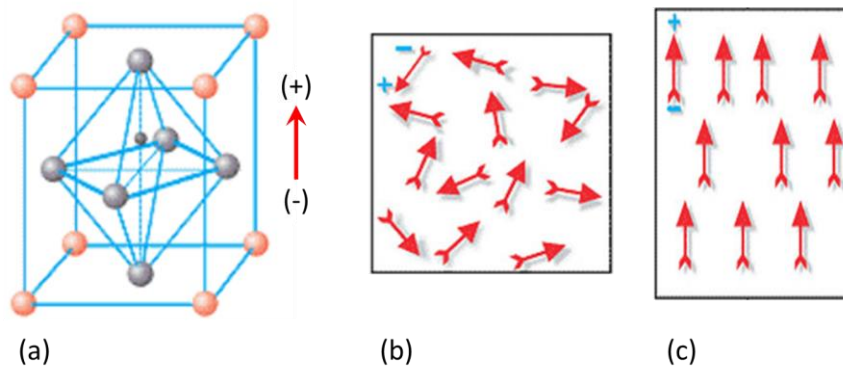


Figure 1-6. (a) Perovskite crystal at temperatures below curie point, Large orange sphere: Large divalent metal ion, Large gray sphere:  $O^{2+}$ , small gray sphere: small tetravalent metal ion; (b): piezoelectric before electrical excitation, (c) and under electrical excitation, the red arrows are the orientation of the electric dipoles [5]

These ions generate a dipole moment. For thin film piezoelectric, the orientation is either up or down. Adjacent perovskite tends to align their moment, forming domains with a net dipole moment. Hence, the overall polarization of the piezoelectric is null as shown in Figure 1-5. b. However, under DC bias, the domains align their moment with that of the applied electric field. The piezoelectric element is then extended or compressed in the direction of the electric field (Figure 1-6. b, c). Moreover, this alignment of the different domains also changes the dielectric constant of the piezoelectric [6]. Those two mechanisms change the impedance of the sample. Figure 1-7 summarizes the main contribution on the measured impedance.

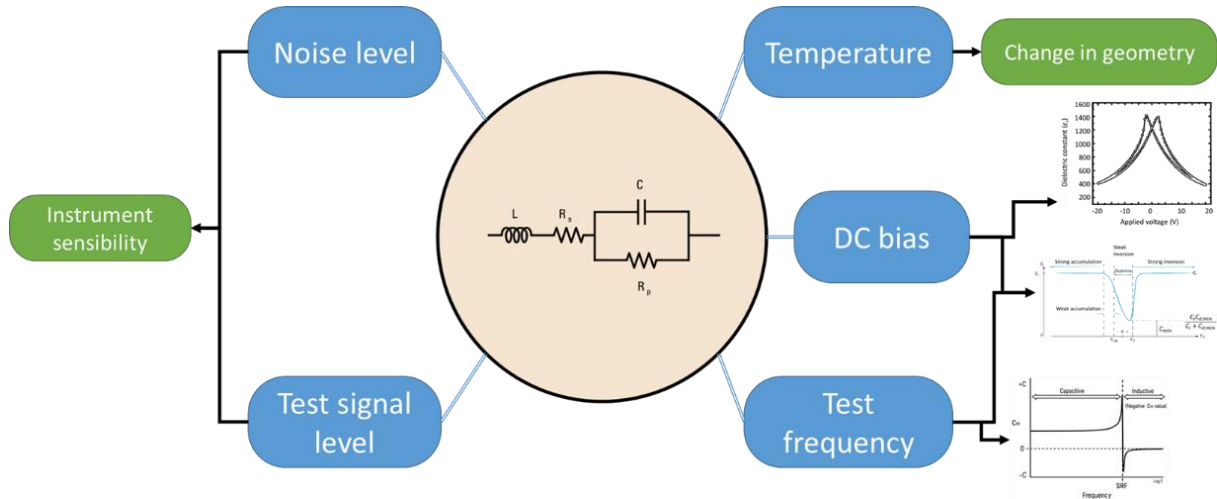


Figure 1-7. Main influences on the measured impedance, [3], [6], [7]

Now that we have reviewed the main parameters impacting the impedance measurement impedance and its uncertainty, let us explore the existing measurement methods.

## 1.4 Macroscale measurement

Several impedance measurement setups have been developed over the years. The most common setups are the I-V method and the bridge method as shown in Figure 1-8.

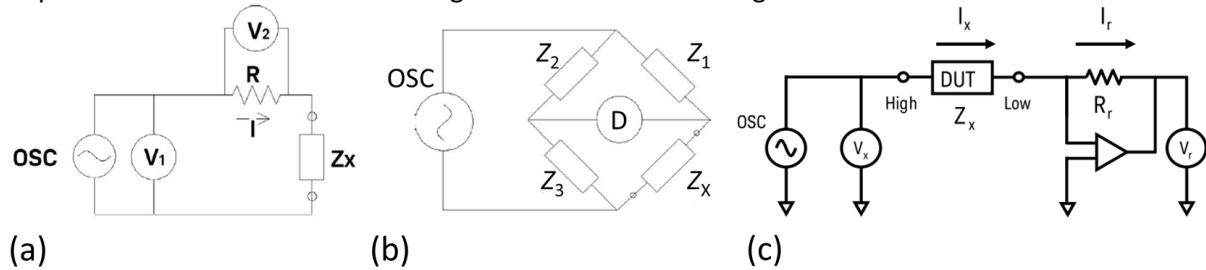


Figure 1-8. (a) I-V setup, (b) Bridge setup, (c) Auto-balancing bridge [3]

In the I-V method, the complex impedance is measured by applying an alternative potential and measuring the current and voltage drop at the component. The current is assessed by a voltmeter at a known resistance  $R$ .  $Z_x$  is defined by Equation 1-14.

$$Z_x = \frac{V_1}{V_2} R \quad \text{Equation 1-14.}$$

In the bridge configuration, the impedances  $Z_i$  are adjusted to obtain a null current in the detector  $D$ .  $Z_x$  is obtained by Equation 1-15.

$$Z_x = \frac{Z_1}{Z_2} Z_3 \quad \text{Equation 1-15.}$$

The same principle is applied in the auto-balancing bridge but the impedance  $Z_i$  is replaced by an I-V converter. The objective is to balance the current ( $I_x$ ) flowing in the device under test (DUT) by the

current in the ranging resistance ( $I_r$ ). Because the two currents are equal, the impedance of the DUT is then given by Equation 1-16.

$$Z_x = R_r \frac{V_x}{V_r} \quad \text{Equation 1-16.}$$

All those methods allow for macroscale measurement of impedance at frequencies up to a few hundreds of MHz. It is interesting to extend the measurement to microwave frequency, as this part of the spectrum is highly sensitive to charge distribution and displacement [8]. In the next section, impedance measurement techniques applicable to GHz frequency will be detailed.

## 2 Microwave measurement

### 2.1 Theory

Historically, the electromagnetic spectrum has been divided into subsections by wavelength. The subsection of the wavelength ranging from one millimeter to one meter is named microwave. Therefore, the corresponding frequencies range from 0.3 to 300 GHz. Many electronic components use those frequencies in their daily operation. To limit the loss in signal transmission, microwave circuits relied on transmission lines to propagate the signal. The solution to Maxwell's equation in a lossless, uniform, and isotropic transmission line is given by a pair of waves propagating in opposite directions [9]. These pairs of waves are referred to as modes. By an adequate choice of the transmission line geometry and frequency of the signal, a single mode can be observed. The work described in this thesis is restricted to this last case. As the electromagnetic wave exits the transmission line, a part of the signal is reflected as illustrated in Figure 1-9.

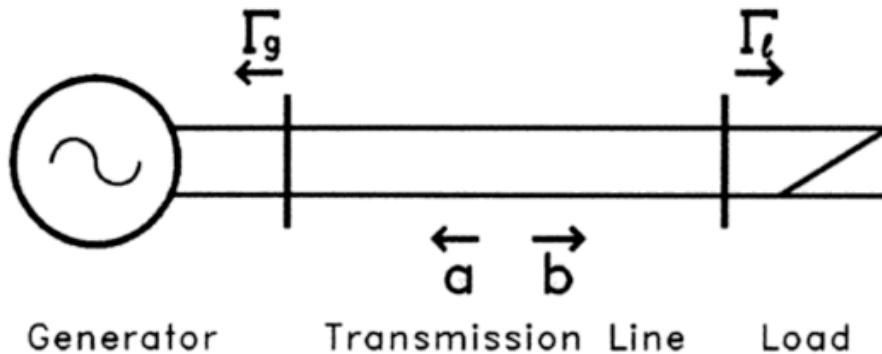


Figure 1-9. Excitation of an impedance by a generator linked by a transmission line, [9]

The ratio of the reflected to incident signal is called the reflection coefficient ( $S_{11}$ ) and is a function of the impedance mismatch between the transmission line and the load. This ratio is written in Equation 1-17.

$$S_{11} = \frac{Z_s - Z_0}{Z_s + Z_0} \quad \text{Equation 1-17.}$$

where  $Z_s$  is the load impedance and  $Z_0$  is the transmission line impedance. The typical  $Z_0$  is typically set to 50  $\Omega$ . Therefore, additional precautions must be taken to limit the reflection of the probing microwave signal before it reaches the DUT.



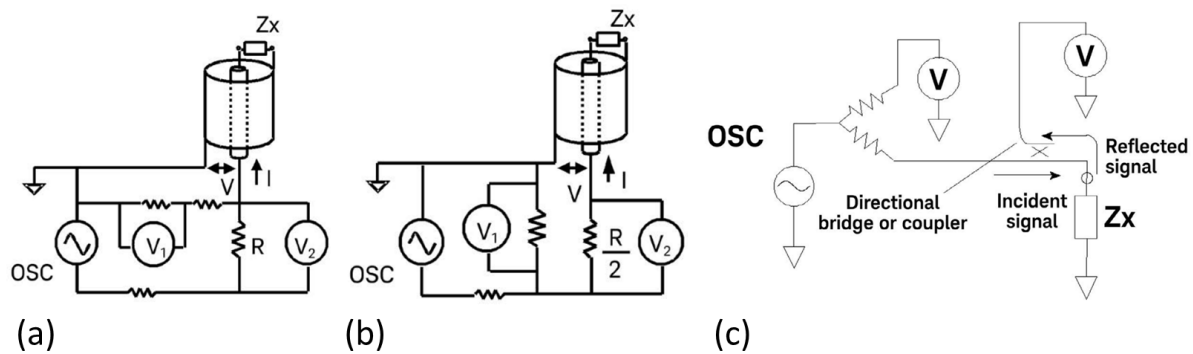


Figure 1-10. RF I-V for (a) low impedance, (b) high impedance, (c) Network analysis method, [3]

The previously seen I-V method can be adapted to limit the reflections in the microwave circuit of measurement as illustrated in Figure 1-10. a,b. The measurement circuit impedance is matched to the one of the coaxial waveguide. The DUT ( $Z_x$ ) is measured by the potential to electrical ratio and is given by Equation 1-18.a (.b) for the low (high) impedance configuration.

$$Z_x = \frac{2R}{\frac{V_2}{V_1} - 1} \quad \text{Equation 1-18.a}$$

$$Z_x = \frac{R}{2} \left( \frac{V_1}{V_2} - 1 \right) \quad \text{Equation 1-18.b}$$

This adaptation can reach an operating frequency of 3 GHz. If higher frequencies are to be measured, a different method, namely the reflection coefficient measurement method must be used. The DUT is connected to a vector network analyzer (VNA) that sends and receives a microwave. It then measures the  $S_{11}$ , and using equation 13 finds the impedance of the DUT. The details of the experimental setup will be further explained in the instrumentation section. A comparison of the impedance sensitivity of the two methods is presented in Figure 1-11.

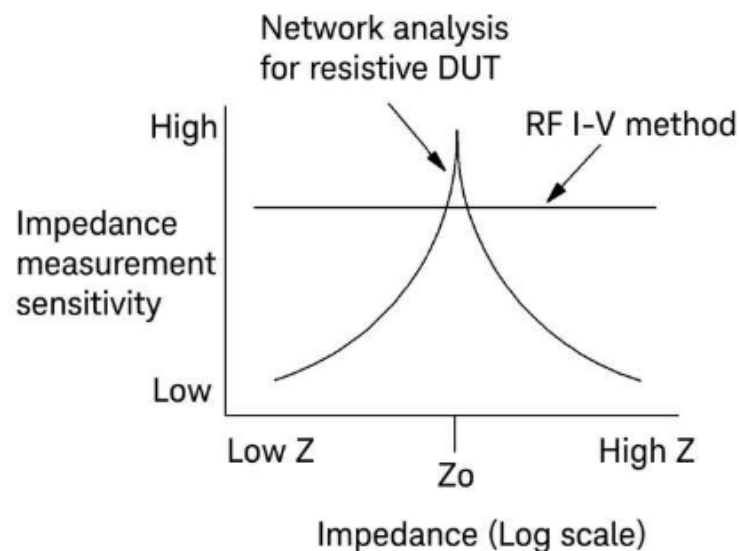


Figure 1-11. Impedance measurement sensitivity of the RF I-V and network analysis methods, [3]

The  $S_{11}$  measurement technique has a low sensitivity to impedance far from the characteristic impedance ( $Z_0$ ) but shows outstanding performance for impedance near  $Z_0$ . Therefore, it might be necessary to add a matching element on the transmission line to the DUT to ensure good sensitivity. On the other hand, the sensitivity of the RF I-V method is constant, as it measures the current-to-potential ratio.

## 2.2 Measurement by vector network analyzer

In this section, the experimental setup required to implement the  $S_{11}$  measurement techniques will be detailed.

### 2.2.1 Vector Network Analyzer (VNA)

A VNA is a complex instrument that sends and measures microwave signals. It is composed of three main components, namely the source, the test set, and the receiver [10]. The block diagram of a typical VNA is presented in Figure 1-12.

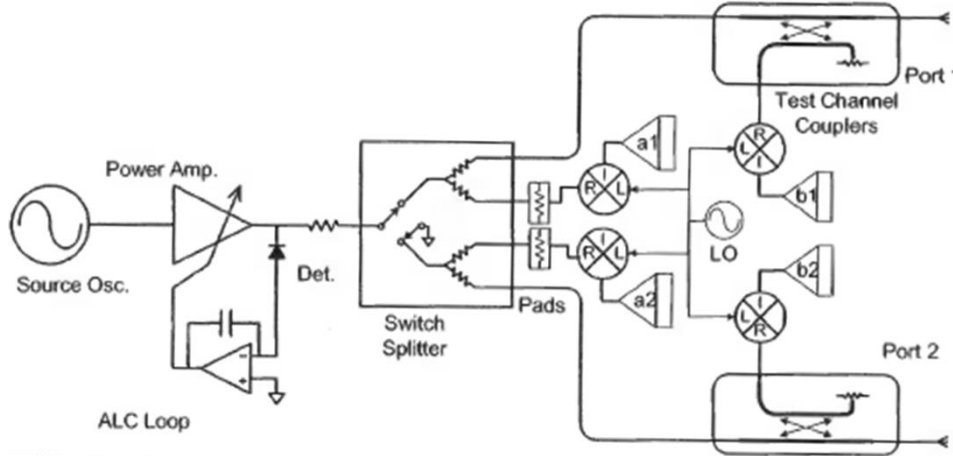


Figure 1-12. Block diagram of a VNA, [10]

The microwave is generated by the source and goes through the automated loop control (ALC) allowing it to set the power level. It is then directed to one of the ports of the VNA. A splitter will divide the signal into two parts, one goes directly to a mixer and is converted into an intermediate frequency (IF) signal readable by a computer ( $a_i$ ,  $i$  can be equal to either 1 or 2). The IF is controlled by a local oscillator (LO). The second part of the microwave signal passes through a directional device and reaches the port. The signal returned by the sample comes inside the port and passes through the directional device. It is directed to a second mixer and recorded as  $b_i$ , where  $i$  can be equal to either 1 or 2. The  $S_{ij}$  ( $i, j$  can be 1 or 2) parameter is then computed by Equation 1-19.

$$S_{ij} = \left. \frac{b_j}{a_i} \right|_{a_k=0} \quad \text{Equation 1-19,}$$

where  $k$  is 2 (1) if  $i$  is 1 (2) to be sure no signal is sent by the probing port. The VNA doesn't output the incident and reflected signal but their readings through a complex system, yet not perfect. Hence, a calibration is required to obtain the true  $S_{11}$  parameter [11]. From now on, the measured reflection coefficient will be noted  $S_{11,m}$  and the calibrated one will be noted  $S_{11}$ . Several calibration methods have been developed. One of the first methods includes the Short-Open-Load calibration where a three-term error model (Equation 1-20) is found by measuring different reflection standards.

$$S_{11} = \frac{S_{11,m} - e_{00}}{e_{01} + e_{11}(S_{11,m} - e_{00})} \quad \text{Equation 1-20.}$$

The three-term solution for the error coefficients is given by Equation 1-21 [10]

$$\begin{bmatrix} e_{00} \\ e_{01} - e_{00}e_{11} \\ e_{11} \end{bmatrix} = \begin{bmatrix} 1 & S_{11}^{open} & S_{11}^{open} S_{11,m}^{open} \\ 1 & S_{11}^{short} & S_{11}^{short} S_{11,m}^{short} \\ 1 & S_{11}^{load} & S_{11}^{load} S_{11,m}^{load} \end{bmatrix}^{-1} \begin{bmatrix} S_{11,m}^{open} \\ S_{11,m}^{short} \\ S_{11,m}^{load} \end{bmatrix} \quad \text{Equation 1-21.}$$

It is clear that this calibration method requires full knowledge of the reflection standards. Another family of calibrations is based on transmission line standards and requires only a partial knowledge of

the standards. It uses the redundancy of measurement results ( $S_{12,m}=S_{21,m}$ ) and is sometimes called self-calibration. The calibration of the  $S_{11}$  is then given by Equation 1-22.

$$S_{11} = e_{00} + \frac{e_{01} \left( S_{11} + \frac{e_{LF} S_{21}^2}{1 - e_{LF} S_{22}} \right)}{1 - e_{11} \left( S_{11} + \frac{e_{LF} S_{21}^2}{1 - e_{LF} S_{22}} \right)} \quad \text{Equation 1-22}$$

This calibration requires the knowledge of the full  $S$  matrix and relies on four different error coefficients. Once the VNA has been calibrated, we can express the uncertainty budget associated with its measurement (table 1) [12].

Table 1. Uncertainty budget of  $Re[S_{11}]$ , of a matched load at 0.46 GHz [12]

Contribution	Type	$f = 0.46$ GHz
Calibration load	B	0.00200
Calibration open	B	0.00000
Calibration short	B	0.00000
Connection repeatability	A	0.00045
VNA Drift	A	0.00002
VNA Linearity	A	0.00001
VNA Noise	A	0.00002
Combined		0.0205

The largest contribution to the uncertainty budget of VNA measurement comes from the calibration standards and will be reviewed extensively later on. The connection repeatability impacts the microwave signal transmission to the DUT and needs to be taken into account in the uncertainty budget. It is measured by fully disconnecting and reconnecting several times the connectors. The VNA drift changes the measured signals and is due to temperature changes. This variation leads to modification in the electric paths of the signal and changes in the performances of the VNA's components. The VNA non-linearity leads to measurement error in the detection of  $a_i$  and  $b_i$  signals but can be significantly reduced by lowering the source power level. The VNA trace noise is the quantity of random noise generated by the VNA that is added to the measurement. Finally, the VNA is characterized by its noise floor [10], [12]. The noise floor is the random fluctuation in  $b_1$  in the absence of a reflected signal. It corresponds to the lowest signal measurable by the VNA. Both noise levels can be reduced by averaging and smaller IF bandwidth.

### 2.2.2 Test fixture

To measure the DUT's electrical properties ( $\epsilon_r$ ,  $\tan(\delta)$ ), a test fixture must be used to connect the DUT to the VNA. Four categories of test fixtures have been identified, namely the resonator, the waveguide, the capacitor, and the transmission line [13]. Examples of measurements using these test fixtures are shown in Figure 1-13. In Figure 1-13.a, a specific resonator fixture, the split post-dielectric resonator (SPDR) is shown. The DUT is located between two dielectric resonators, each connected to a different VNA. The transmission parameters ( $S_{12}$ ,  $S_{21}$ ) are measured for a frequency sweep. The resonance frequency ( $f_0$ ) and quality factor ( $Q$ ) are evaluated for the empty and loaded cavity. The frequency shift and change in the quality factor can be linked to the electric properties of the sample by Equation 1-23.

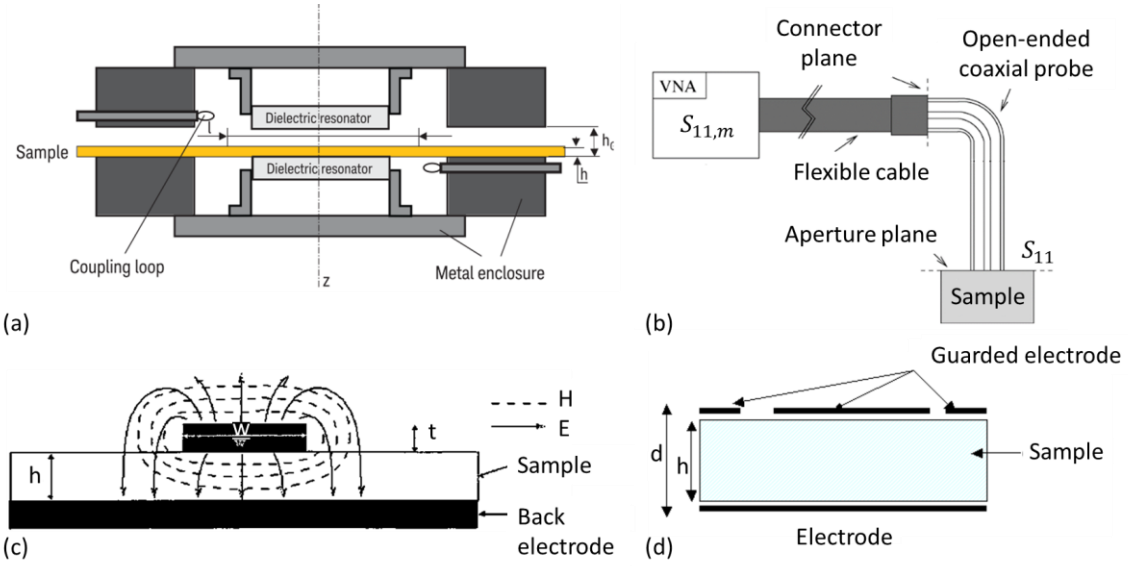


Figure 1-13. (a) Split post dielectric resonator fixture [14], (b) Open-ended coaxial probe dielectric measurement [15], (c) microstrip transmission line, (d) micro capacitor [13]

$$\epsilon_r = \frac{1 + f_0 - f_s}{hf_0 K_s} \quad \text{Equation 1-23.a}$$

$$\tan(\delta) \approx \frac{Q_0^{-1} - Q_s^{-1}}{h\epsilon_r K_s} \quad \text{Equation 1-23.b}$$

In the resonator, the propagation mode is  $TE_{011}$ , hence, the electric field is tangential to the sample. This reduces the influence of the air gap in the measurement therefore leading to lower uncertainty [13], [16]. The open-end coaxial probe method (Figure 1-13.b) guides the wave toward the sample surface and the  $S_{11}$  is evaluated. After calibration, the  $S_{11,m}$  can be linked to the admittance of the probe-sample system ( $Y$ ). Equation 1-24 expresses the relationship between the admittance and the dielectric constant [17]

$$Y(\epsilon) = Y_0 \frac{ik_0^2}{k_c \ln(b/a)} \int_0^\infty \frac{[J_0(\zeta a) - J_0(\zeta b)]^2}{\zeta \sqrt{\zeta^2 - k_0^2}} d\zeta \quad \text{Equation 1-24.a}$$

$$k = \frac{2\pi}{\lambda} = \frac{2\pi\sqrt{\mu_r \epsilon_r}}{\lambda_0} \quad \text{Equation 1-24.b}$$

where  $Y_0$  is the characteristic admittance of the probe,  $a$  and  $b$  are the inner and outer conductors of the coaxial waveguide,  $k_0$ , and  $k_c$  are the wavenumber of the coaxial waveguide and the sample and  $J_0$  is the first-order Bessel function. Due to the discontinuity between the waveguide and the sample, a parasitic impedance is present due to the non-perfect contact. This adds uncertainty to the measurements [13]. Nevertheless, this technique does not require any sample preparation and is therefore non-destructive. In the transmission line method, the microwave is sent in the transmission line. The Nicolson-Ross-Weir (NRW) algorithm [18], [19] allows for the computation of the electrical permittivity ( $\epsilon_r$ ) and magnetic permeability ( $\mu_r$ ) from the reflection and transmission ( $S_{21}$ ) coefficients (Equation 1-25).

$$\epsilon_r = \frac{\lambda_0^2}{\mu_r \left[ \frac{1}{\lambda_c^2} - \left( \frac{j}{2\pi L} \ln(T) \right)^2 \right]} \quad \text{Equation 1-25.a}$$

$$\mu_r = \left( \frac{j}{2\pi L} \ln(T) \right)^{-1} \frac{1 + \Gamma}{(1 - \Gamma) \sqrt{\frac{1}{\lambda_0^2} - \frac{1}{\lambda_c^2}}} \quad \text{Equation 1-25.b}$$

$$\Gamma = \frac{S_{11}^2 - S_{21}^2 + 1}{2S_{11}} \pm \sqrt{\left( \frac{S_{11}^2 - S_{21}^2 + 1}{2S_{11}} \right)^2 - 1} \quad \text{Equation 1-25.c}$$

$$T = \exp(-\gamma L) = \frac{S_{11} + S_{21} - \Gamma}{1 - (S_{11} + S_{21})\Gamma} \quad \text{Equation 1-25.d}$$

Where  $L$  is the transmission line length,  $\gamma$  its propagation constant,  $\lambda_0$  and  $\lambda_c$  are the wavelengths in the vacuum and in the transmission line. In the last configuration, the capacitor measurement, the sample is sandwiched between two electrodes, and the impedance is measured. Using the parallel plate approximation and the formula for conductance ( $G = \omega \epsilon'' A/d$ ) at low frequency, the relative electric permittivity can be extracted from capacitance and conductance measurements (Equation 1-26) [13].

$$\epsilon_r = \frac{C - jG/\omega}{C_{\text{air}} - jG_{\text{air}}/\omega} \quad \text{Equation 1-26}$$

In Figure 1-13.d, guarded electrodes are implemented to minimize the impact of the fringing field. Table 2 recaps the different test fixtures.

Table 2. Uncertainty associated  $\epsilon_r$  and  $\tan(\delta)$  as a function of the different test fixtures, [13]

Technique	Field	Uncertainty on $\epsilon_r$	Uncertainty on $\tan(\delta)$
Resonator	TE <sub>011</sub>	± 0.5%	± 5 10 <sup>-5</sup> %
Coaxial probe	TEM, TM <sub>01</sub>	± 2% – 10%	± 2 10 <sup>-2</sup> %
Transmission line	TEM, TE <sub>01</sub>	± 1% – 10%	± 5 10 <sup>-3</sup> %
Capacitor	Normal E-field	± 1%	± 5 10 <sup>-4</sup> %

## 2.3 Smith Chart

One convenient way to represent the reflection coefficient is to plot its imaginary part as a function of its real part. This representation is called a Smith chart and one of its main perks is that it allows for graphical reading of the impedance associated with a given value of  $S_{11}$  as shown in Figure 1-14.

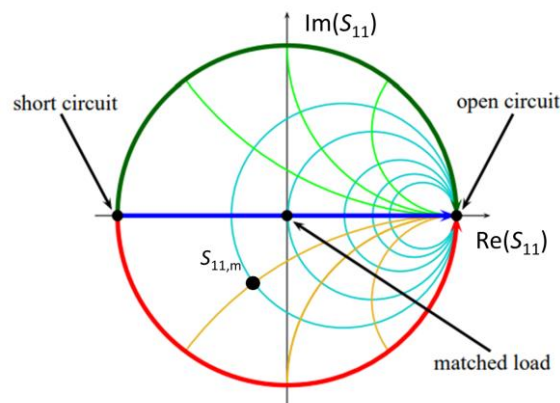


Figure 1-14. Simplify Smith chart. Blue bold line: purely resistive device; Red bold line: purely capacitive devices; Green bold line: purely inductive devices; Blue thin circle: constant resistance value; Orange thin line: constant capacitive value; Green thin line: constant inductive value, [20]

Considering the constant impedance circle (thin line in Figure 1-14), the resistance and reactance can be geometrically determined (Equation 1-27) [21].

$$\left( \operatorname{Re}(S_{11,m}) - \frac{R}{R+1} \right)^2 + \operatorname{Im}(S_{11,m})^2 = \frac{1}{(1+R)^2} \quad \text{Equation 1-27.a}$$

$$\left( \operatorname{Re}(S_{11,m}) - 1 \right)^2 + \left( \operatorname{Im}(S_{11,m}) - \frac{1}{X} \right)^2 = \frac{1}{X^2} \quad \text{Equation 1-27.b}$$

A DUT of resistance  $R$  will have a  $S_{11,m}$  belonging to a circle of center  $\left(\frac{R}{R+1}, 0\right)$  with a radius of  $\frac{1}{R+1}$ . Similarly, the  $S_{11,m}$  associated to a DUT with a reactance  $X$ , will belong to a circle of center  $\left(1, \frac{1}{X}\right)$  with a radius of  $\frac{1}{X}$ .

### 3 Atomic Force Microscopy

In 1982, Binnig and Rohrer showed the possibility of controlling a tunneling current between a sharp tungsten tip and a conductive surface in a vacuum environment [22]. They use their setup to acquire an image of the sample's topography, hence giving birth to Scanning Tunneling Microscopy (STM). In the original setup, the tip was mounted on a piezoelectric actuator. A closed-loop controller was set to keep the tunneling current between the tip and the surface constant. Using this principle, they were able to reach atomic resolution on the z-axis. Nevertheless, the very principle of STM limits the imaging capability to conductive surfaces. To overcome this limitation, Atomic Force Microscopy (AFM) was developed in 1985 and relies on the sensing of the interaction force between the probe and the sample's surface. In this section, a description of the AFM will be given.

#### 3.1 System description – Mode

The AFM configuration is close to the one of STM and is described in Figure 1-15.a. The probe or the sample is mounted on a piezo actuator. A laser is shot on the cantilever of the AFM probe and is reflected to a four-quadrant photodetector. The photodetectors array holds the information on the deflection and friction. Figure 1-15.b shows the interaction between the probe and the surface as a function of the distance.

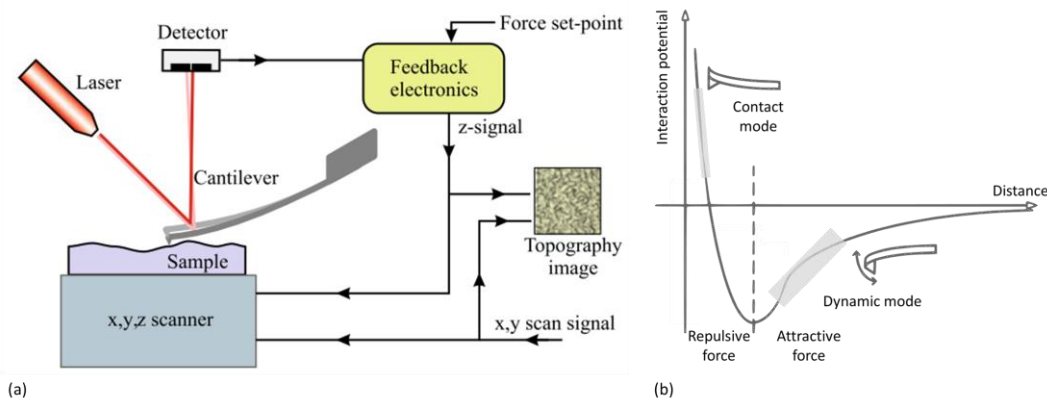


Figure 1-15. (a) Typical AFM scanner setup, (b) Interaction potential between the AFM tip and the sample, [23], [24]

This curve is similar to a Lennard-Jones potential describing the interaction force between two atoms and can be explained similarly. When the tip is far from the surface, the overall sensed force is null. The deflection associated with this position is recorded as a reference point ( $D_0$ ). As it approaches, it starts sensing the long-range attractive electrostatic force. Then, it feels the repulsive force. Different imaging modes exist depending on the nature of the interaction force. If the interaction force is kept constant over the scan, the AFM works in static mode. Moreover, if the overall interaction force is repulsive, the apex of the tip physically touches the sample's surface and we are in contact mode. When the tip-sample interaction changes over the scan, the AFM is in dynamic mode [25].

### 3.1.1 Contact mode

In the contact mode, the tip-sample interaction force is kept at a constant repulsive value during the whole scan. In this mode, the tip-sample interaction force can be expressed as a function of the deflection deviation from the reference point ( $\Delta D = D - D_0$ ) using Hooke's law (Equation 1-28)

$$F_{ts} = kS\Delta D \quad \text{Equation 1-28,}$$

where  $k$  [ $\text{N}\cdot\text{m}^{-1}$ ] is the spring constant of the cantilever and  $S$  [ $\text{m}\cdot\text{V}^{-1}$ ] is the sensitivity of the reading, *i.e.* the displacement of the laser on the array corresponding to a reading of one volt [23]. Practically, the interaction is controlled by a feedback loop maintaining the  $\Delta D$  at a constant set-point defined by the user. The z-displacement output of the feedback loop is recorded for the whole scan and corresponds to the topography channel of the image. During this mode, the atoms of the tip's apex are in contact with those of the sample's surface. This introduces a non-negligible friction force that can be responsible for tip and/or sample damage if the interaction force is too high [23]. The typical interaction force is in the order of tens of nanonewtons. Let's focus on the achievable resolution of the contact mode. Figure 1-16 shows the topography profile returned by an AFM tip scanning a step in contact mode.

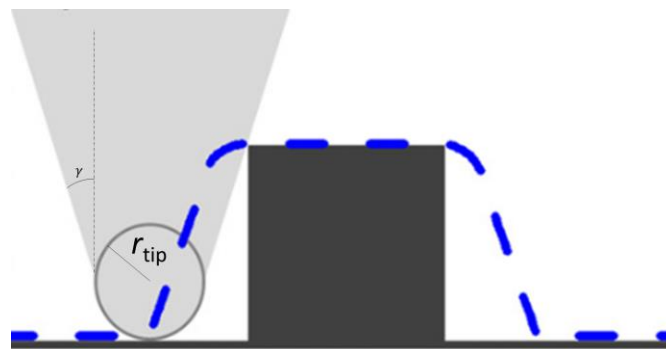


Figure 1-16. Topography profile obtained from a step scan by an AFM tip in contact mode, [26].

One can notice that the convolution between the tip and the feature to be scanned creates an imaging artifact. This is due to the non-null values of the apex radius ( $r_{\text{tip}}$ ) and the cone angle ( $\gamma$ ). Due to this convolution, the features are enlarged in AFM measurement. Despite this drawback, the contact mode is essential if we want to image the electrical properties of the sample. Indeed, all impedance measurement technique depends on the contact resistance between the probe and the sample [3]. Hence, it is critical to ensure that the contact doesn't evolve with time, which is precisely what the AFM does in contact mode as it operates at a constant interaction force. Nevertheless, due to the similar dimensions of the apex (tens of nanometers) and the sample roughness, the contact area may change during the scan and it is challenging to evaluate it [27]. One can also use the contact mode to punctual force-distance curves at giving points [23]. A schematic of a force-distance curve is shown Figure 1-17.

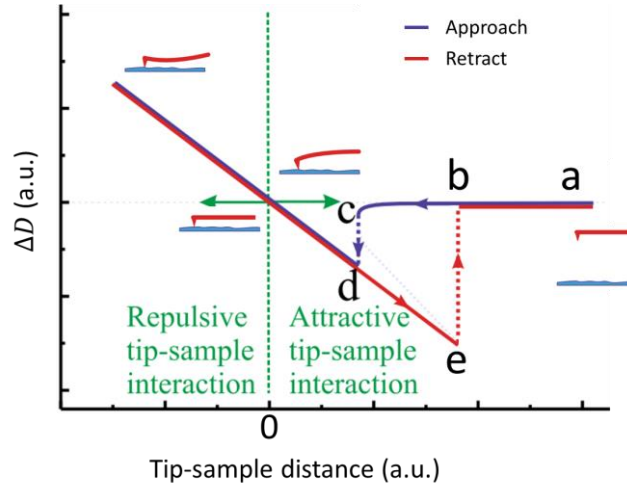


Figure 1-17. Deflection deviation from the rest value ( $D_0$ ) as a function of the tip-sample distance. A schematic of the tip-sample system is shown at different  $Z_{\text{sample}}$  (red: tip; blue sample's surface) [23]

As the tip is far from the sample's surface (point a), the cantilever is at its rest position (i) reading a deflection  $D_0$ . The probe is approaching the surface up to a point where the gradient of  $F_{ts}$  equals the spring constant of the cantilever (point c). This leads to a tipping point where the tip jumps to contact with the sample surface. The  $\Delta D$  is then negative (attractive interaction force) as the cantilever bends downward. Then, as the tip distance keeps reducing, the sample's surface pushes on the tip to redress the cantilever back to its original bend. This is the point of reference for the tip-sample distance. Passed this point, the cantilever is bent upward and the  $\Delta D$  is positive. If the tip-sample distance starts increasing again, the repulsive interaction force will decrease up to a point where it becomes attractive again. If we continue, we will reach another tipping point (e) leading to a snap out of contact of the AFM tip.

### 3.1.2 Dynamic mode

In the resonant mode, the AFM tip is mechanically excited to an angular frequency ( $\omega_{\text{drive}}$ ) close to its resonance angular frequency ( $\omega_0$ ) at a given amplitude ( $A_{\text{drive}}$ ). The system AFM probe-sample's surface can then be assimilated to a driven damped harmonic oscillator model [23]. Its  $\omega_0$  and quality factor ( $Q$ ) are defined by the cantilever. The tip-sample interaction force as well as the surrounding medium of the AFM probe dampens the harmonic oscillator. The system can then be modeled by two springs, one for the cantilever with a spring constant  $k$  and the other representing the tip-sample interaction force with a spring constant  $k'(z)$ . For small amplitudes, the interaction force is linear and the  $k'$  can be considered constant. When the tip is far from the sample's surface, the oscillation of the AFM tip is free at the full amplitude. As the tip is brought closer to the sample's surface, a shift ( $\Delta\omega = \omega_0|_{\text{close}} - \omega_0|_{\text{far}}$ ) in  $\omega_0$  is observed due to the damping. This result in a shift in  $\omega$  by the same quantity defined by Equation 1-29.

$$\Delta\omega = -\frac{\omega_0}{2k} \frac{\partial F_{ts}}{\partial z} \Big|_{z=0} \quad \text{Equation 1-29.}$$

Figure 1-18.a) shows the resonance frequency dependence in the tip-sample distance. It assumes a Lennard-Jones potential for the  $F_{ts}$ . Figure 1-18.b) represents the oscillation amplitude as a function of the oscillation frequency.



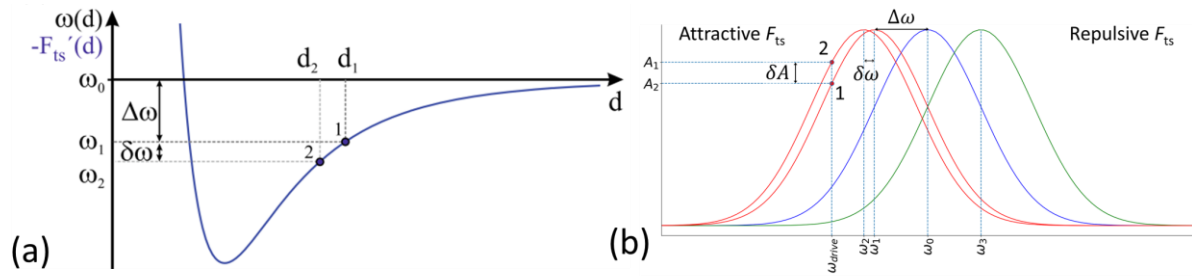


Figure 1-18. (a) Resonance frequency as a function of the tip-sample distance assuming a Lennard-Jones potential. (b) Measured amplitude as a function of oscillation frequency. The blue (red) curve is obtained for an AFM probe located far (near, attractive  $F_{ts}$ ) on the sample's surface, from [23]

When working in the dynamic mode, the driving frequency is chosen near the resonance frequency. A  $\delta\omega$  is observed as the tip-sample's distance varies. A feedback loop is set to maintain the measured amplitude of the cantilever oscillation constant to  $A_1$  by adjusting the tip-sample distance. This is called the amplitude-modulated AFM (AM AFM). The sign of  $\omega$  change depends on the interaction regime. If the  $F_{ts}$  is repulsive, then the frequency shift is toward higher values. It is toward lower value if the  $F_{ts}$  is attractive. This can be understood from Equation 20 and Figure 1-15.b. In the AM mode, the tip is not always in contact with the sample's surface which helps save both the sample and the probe [23]. It also reduces the tip-sample convolution, therefore reducing the dimension uncertainty associated with in-plane measurements [28].

### 3.2 Instrument artifact and calibration

Artifacts in AFM imaging can come from the tip, the scanner, and the feedback control, external periodic noise, thermal drift, and laser interference [23], [29]. The last two are neglected in this work as the AFM setup is in a controlled environment with temperature variation below  $0.1^\circ\text{C}$  and the cantilever used is quite large, shading an important part of the laser spot. Indeed, the laser interference artifact occurs when the laser beam reflected by the sample surface forms an interference pattern with the beam reflected by the AFM cantilever. Hence if the cantilever shades an important part of the laser, the reflected intensity to incident intensity ratio becomes negligible in everyday operation. The effects of the other artifacts on the AFM image are shown in Figure 1-19. The AFM tip convolves with the sample surface. This leads to a topography deformation and creates a dead zone at the bottom of the trench where the features are not seen by the AFM tip. Other artifacts may occur when a damaged tip is employed [29]. This convolution can be mitigated by using a sharper tip with a high factor ratio[23], [26].

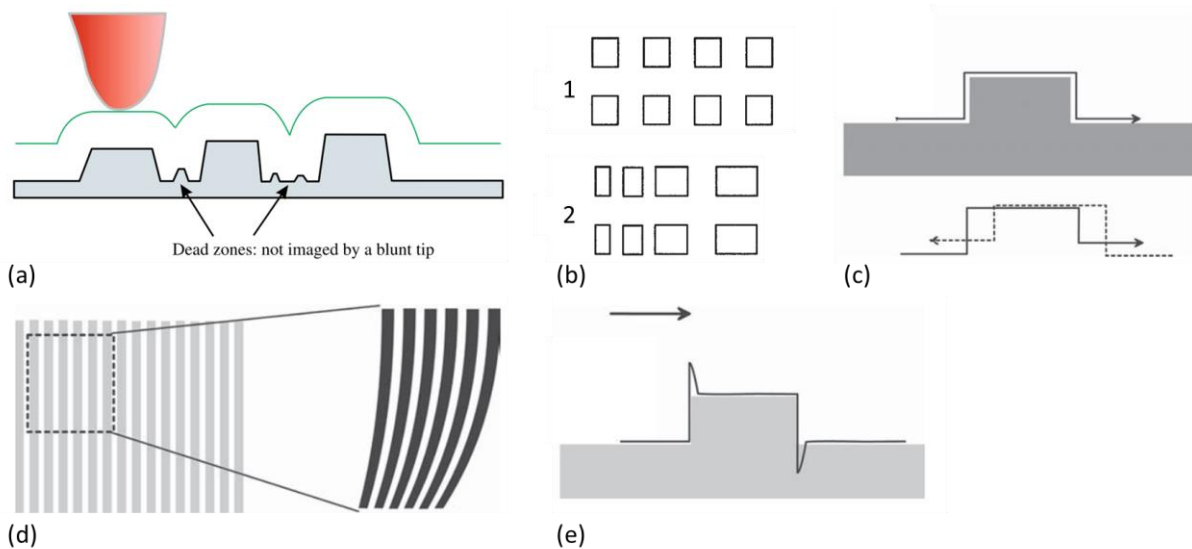


Figure 1-19. (a) Tip-sample convolution and dead zone, (b) Scanner xy nonlinearity, (c) Scanner z hysteresis, (d) Scanner creep xy, (e) Edge overshooting [23], [29]

Nonlinearity in the scanner displacement piezoelectric actuators as a function of the driving signal can lead to image deformation (Figure 1-19.b and c). This nonlinearity can be corrected by using a closed-loop scanner, which after calibration, can read the actual displacement of the scanner. The parameter of control is then the piezo displacement and not the driving voltage. It is typically done by a capacitive sensor [30] which requires calibration to accurately convert the sensor reading into capacitance. Dimensional calibration samples are characterized by a metrological AFM with an interferometric system to ensure the traceability to the international system of units (SI) [31]. Figure 1-20 shows the traceability route of AFM measurement [32].

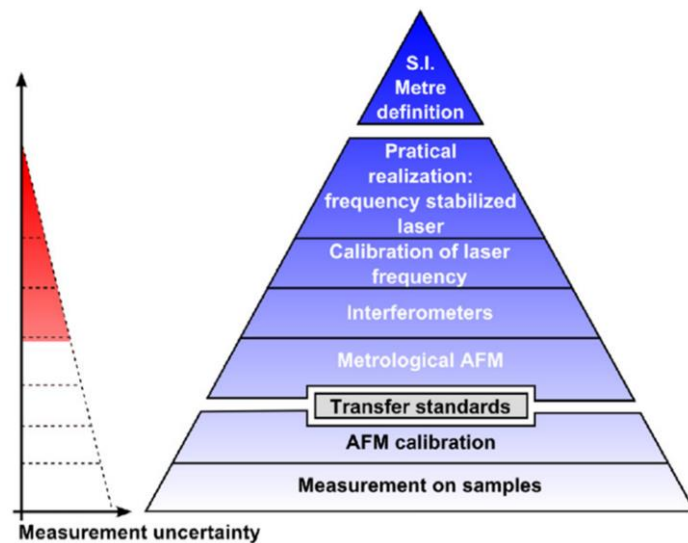


Figure 1-20. Traceability pyramid of dimensional measurement with AFM, [32]

That system can be used to give a reference measurement and uncertainty to calibration samples for the most common capacitor sensor-based AFM. A xy scanner creep can be observed when the piezo actuator has not reached its final position before moving to the next one [23]. This occurs often at the beginning of a new scan and can be mitigated by restarting the scan after a few lines. It is due to the large piezo displacement occurring at the scan beginning in order to reach the starting location. Independently from the chosen technology, precautions must be taken in the closed-loop controller. A too-short response time may lead to overcompensation in the control of z displacement creating the defect observed at the edge in Figure 1-19.e. Careful calibration can solve the scanner nonlinearity and

hysteresis [33], [34]. A good compromise between the scan speed and PID gains must be done to prevent these edge overshooting.

## 4 Modes for AFM electric imaging

As previously mentioned, the need for imaging electric properties with a nanoscale spatial resolution has arisen these past years following the progress in the semiconductor industry. For capacitance measurement, several modes have been developed. In this section, a focus will be shined on the scanning capacitance microscopy (SCM), the electrostatic force microscopy (EFM), and the scanning microwave microscopy (SMM).

The SCM relies on resonance measurements.

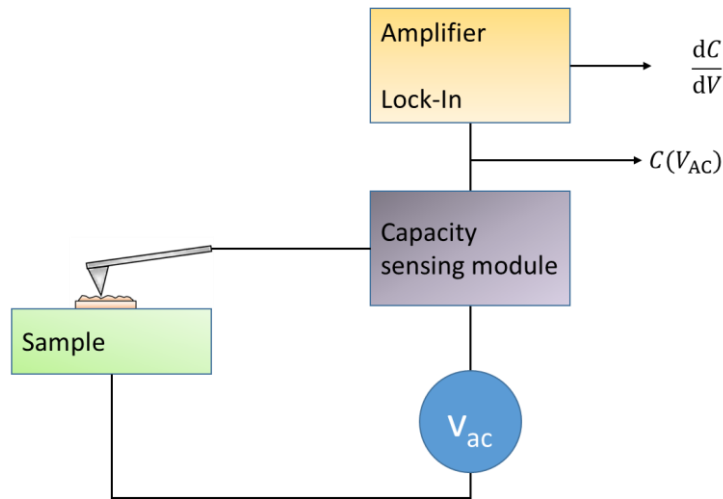


Figure 1-21. Schematic for SCM setup, from [35]

A schematic of the SCM setup is shown in Figure 1-21. An alternative signal with a frequency of a few tens of kHz is applied to the AFM tip through a capacitance sensing module. This module is a resonator including the tip-sample capacitance which changes with the applied voltage  $C(V_{AC})$ . The frequency resonance of the module changes as a function of the capacitance. If we send a signal at the native  $f_0$  of the resonator, its output amplitude changes as a function of the tip-sample capacitance. The reader can refer to [36] for further explanation.

For EFM setup, an alternative voltage of a few kHz is applied between the AFM probe and the sample. The potential difference between the sample's surface and the tip can be seen as the contribution of the local contact potential ( $V_{cp}$ ), the continuous ( $V_{DC}$ ) and alternative ( $V_{AC}$ ) part of the applied voltage, and the induced voltage ( $V_{ind}$ ) (Equation 1-30) [37].

$$V = (V_{cp} + V_{ind} + V_{DC}) + V_{AC}\sin(\omega t) \quad \text{Equation 1-30.}$$

This potential difference creates an electrostatic force operating with two harmonics (equation 22).

$$F_{es} = F_{DC} + F_{\omega} + F_{2\omega} \quad \text{Equation 1-31.a}$$

$$F_{DC} = \frac{(V_{cp} + V_{ind} + V_{DC})^2 + V_{AC}/2}{2} \frac{dC}{dz} \quad \text{Equation 1-31.b}$$

$$F_{\omega} = (V_{cp} + V_{ind} + V_{DC})V_{AC}\sin(\omega t) \frac{dC}{dz} \quad \text{Equation 1-31.c}$$

$$F_{2\omega} = -\frac{V_{AC}^2 \cos(2\omega t)}{4} \frac{dC}{dz} \quad \text{Equation 1-31.d}$$

Using a lock-in to isolate the signal at a specific frequency, this imaging mode can be used to extract the tip-sample capacitance variation as a function of the  $d_{ts}$  or the local charge of the sample [37]. This mode is used in this work to extract local capacitance gradient at low frequency.

The last mode to be mentioned is the SMM, in which a VNA is interfaced with an AFM working in contact mode. The AFM tip radiates microwaves inside the DUT and collects reflected signals. In its macroscale setup, the VNA measurement results are averaged over the wavelength scale [38], [39]. To reach nanoscale resolution, the SMM is working in a near-field regime. Figure 1-22 shows the same surface feature imaged by far-field and near-field microwaves. An important change in resolution can be observed.

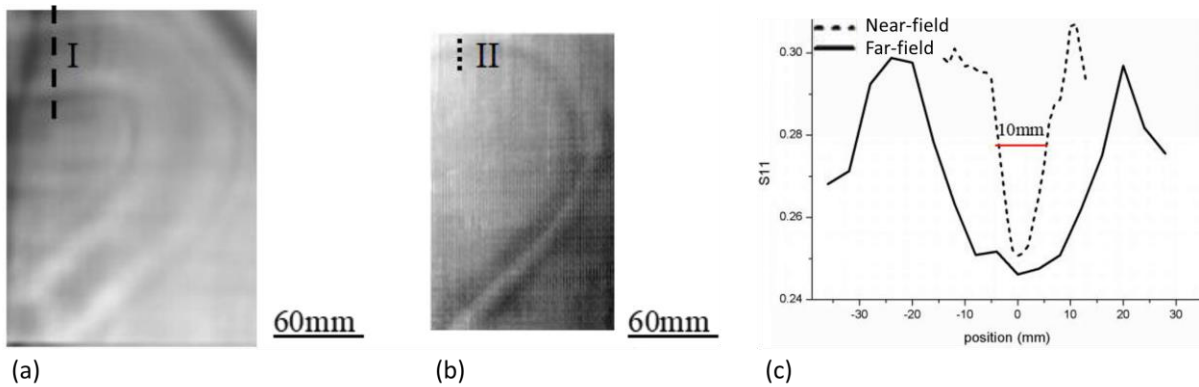


Figure 1-22. Comparison between far-field (a) and near-field (b) imaging of the same indentation defect on a glass fiber cloth in a matrix of vinyl ester resin. (c).  $S_{11,m}$  amplitude along the profile I (far-field) and II (near-field), [39]

In near-field microwave imaging, the electromagnetic field doesn't propagate and depends on the tip geometry and local electromagnetic properties of the neighborhood of the tip's apex [40]. Equation 1-32 must be satisfied to enable the near-field imaging

$$r_{apex} \leq d_{ts} \ll \lambda \quad \text{Equation 1-32.a}$$

$$d_{ts} \ll \frac{\lambda}{2\pi} (\epsilon_r \mu_r)^{-1} \quad \text{Equation 1-32.b}$$

where  $d_{ts}$  is the tip-sample distance and  $r_{apex}$  is the radius of the tip's apex. Those conditions are satisfied by a micrometer or less apex's radius operating in contact mode AFM for gigahertz VNA frequency on a high permittivity sample ( $f_{VNA} = 20 \text{ GHz}$ ,  $\epsilon_r = 1000$ ,  $d_{ts} \ll 75.4 \text{ } \mu\text{m}$ ). Several types of SMM probes have been developed over the years (Figure 1-23). They can be divided into two categories, the probe with a tip and those without. The best spatial resolution is achieved with the STM tip geometry with spatial resolution below 10 nm [41]. It is explained by the geometry of the tip with a small apex radius, small cone opening, and absence of a cantilever which contribute to the widening of the electromagnetic field.

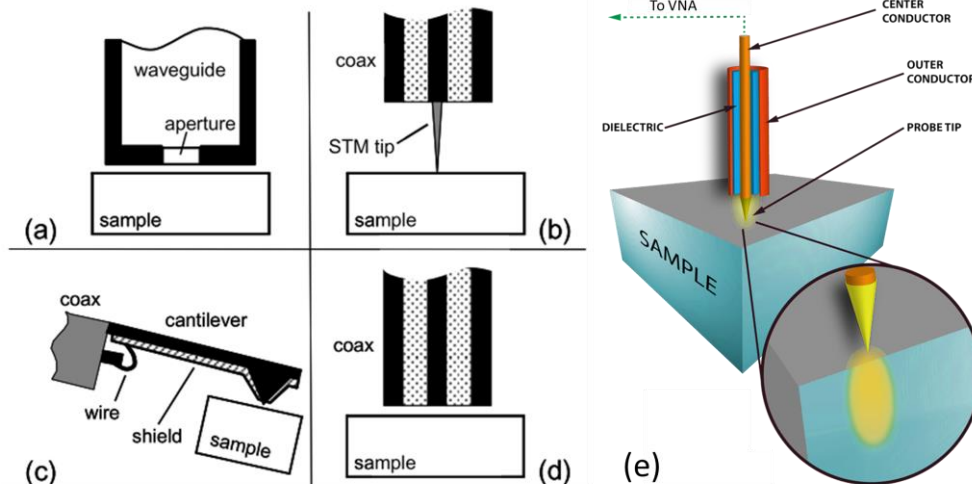


*Figure 1-23.* Different types of near-field microwave probes: (a): aperture in a waveguide, (b) STM tip, (c) AFM tip, (d) open-ended coaxial line, [40]; e: Electric field distribution around the SMM probe, [42]

The work described in this thesis focused exclusively on SMM probes based on AFM tip design. In a typical SMM experiment, the  $S_{11}$  parameter is measured and, after calibration, the quantity of interest is extracted. The SMM can be used to measure the impedance of surface [43]–[45] and buried [46] structure, dielectric constant, loss tangent [47], [48], dopant concentration [49], and field distribution [50]. Despite all those different applications, no comprehensive study on the uncertainty associated with those measurements has been conducted before this work. It will allow for identification of the systematic errors, their reductions, and, if required their compensation by post-measurement correction.

## 5 Conclusion

In this chapter, the electrical impedance and the physical principle behind it are addressed. The link between the polarizability of the different electrical carriers and the dielectric constant is established, explaining the frequency dependence of these two quantities. Then, an overview of the different techniques for impedance measurement at low and high frequencies is given. Their operations and limitations are described. A particular highlight was put on the reflection measurement by VNA as it is the main technique used in this thesis work. The need for VNA calibration is raised and different calibration methods are shown. The most commonly available test fixtures for this method are mentioned. The key feature is the typical uncertainty on  $\epsilon_r$  measurement by VNA is below 0.5% for the resonator and 1% for the capacitor-based measurement. Then the principle of AFM is explained. Contact and dynamic imaging modes are described as well as the acquisition of force distance curve. The contact mode ensures a constant contact force between the tip and the sample which makes it a well-suited mode for imaging the electrical properties of the sample. Nevertheless, because of the important friction forces, the apex of the tip and the sample are prone to degradation. On the other hand, the dynamic mode befits the topographical image as the tip-sample convolution is reduced in this mode. Finally, the most relevant techniques for imaging electrical quantities by AFM are listed. The EFM and SMM principles are detailed and the measurements interpretation is touched on.

- [1] C. Kittel, *Introduction to Solid State Physics*, 8th Editio., vol. 35, no. 6. 2005.
- [2] L. M. Zhang *et al.*, "Near-field spectroscopy of silicon dioxide thin films," *Phys. Rev. B - Condens. Matter Mater. Phys.*, vol. 85, no. 7, 2012, doi: 10.1103/PhysRevB.85.075419.
- [3] Keysight Technologies, "Impedance Measurement Handbook," *Agilent*, p. 140, 2009, [Online]. Available: [www.keysight.com](http://www.keysight.com).
- [4] S. M. Sze and K. K. Ng, *Physics of Semiconductor Devices*, 3rd ed. John Wiley & Sons, Inc., 2007.
- [5] I. Patel, "Ceramic Based Intelligent Piezoelectric Energy Harvesting Device," in *Advances in Ceramics – Electric and Magnetic Ceramics, Bioceramics, Ceramics and Environment*, S. Costas, Ed. 2011.
- [6] J.-S. Yang *et al.*, "Piezoelectric and Pyroelectric Properties of Pb(Zr,Ti)O<sub>3</sub> Films for Micro-Sensors and Actuators," *Integr. Ferroelectr.*, vol. 54, no. 1, pp. 515–525, 2003, doi: 10.1080/714040701.
- [7] B. G. Streetman and S. K. Banerjee, *Solid state electronic devices*, 7th ed. 2016.
- [8] P. H. Siegel, "Microwaves Are Everywhere: 'SMM: Nano-Microwaves,'" *IEEE J. Microwaves*, vol. 1, no. 4, pp. 838–852, 2021, doi: 10.1109/jmw.2021.3106936.
- [9] G. F. Engen, *Microwave circuit theory and foundations of microwave metrology*. IEEE Measurement Series 9, 1992.
- [10] J. P. Dunsmore, *Handbook of Microwave Component Measurements: With Advanced VNA Techniques*. Wiley, 2012.
- [11] A. Rumiantsev and N. Ridler, "VNA calibration," *IEEE Microw. Mag.*, vol. 9, no. 3, pp. 86–99, 2008, doi: 10.1109/MMM.2008.919925.
- [12] EURAMET, "Guidelines on the Evaluation of Vector Network Analysers," 2018.
- [13] J. B. Jarvis *et al.*, "Measuring the Permittivity and Permeability of Lossy Materials: Solids, Liquids, Metals, Building Materials, and Negative-Index Materials," Boulder, CO, 2005.
- [14] K. Technologies, "Application Note Keysight Technologies Split Post Dielectric Resonators for Dielectric Measurements of Substrates."
- [15] D. Popovic *et al.*, "Precision open-ended coaxial probes for in vivo and ex vivo dielectric spectroscopy of biological tissues at microwave frequencies," *IEEE Trans. Microw. Theory Tech.*, vol. 53, no. 5, pp. 1713–1721, 2005, doi: 10.1109/TMTT.2005.847111.
- [16] R. G. Geyer, M. D. Janezic, and E. J. Vanzura, "The NIST 60-millimeter diameter cylindrical cavity resonator: Performance Evaluation for Permittivity Measurements," 1993, [Online]. Available: <https://nvlpubs.nist.gov/nistpubs/Legacy/TN/nbstechnicalnote1354.pdf>.
- [17] I. Dilmann, M. N. Akinci, T. Yilmaz, M. Cayoren, and I. Akduman, "A Method to Measure Complex Dielectric Permittivity with Open-Ended Coaxial Probes," *IEEE Trans. Instrum. Meas.*, vol. 71, pp. 1–7, 2022, doi: 10.1109/TIM.2022.3147878.
- [18] W. B. Weir, "Automatic Measurement of Complex Dielectric Constant and Permeability at Microwave Frequencies," *Proc. IEEE*, vol. 62, no. 1, pp. 33–36, 1974, doi: 10.1109/PROC.1974.9382.
- [19] J. Baker-Jarvis, E. J. Vanzura, and W. A. Kissick, "Improved technique for determining complex permittivity with the transmission/reflection method," *IEEE Trans. Microw. Theory Tech.*, vol. 38, no. 8, pp. 1096–1103, 1990, doi: 10.1109/22.57336.
- [20] F. Caspers, "RF engineering basic concepts: the Smith chart," in *CAS 2010 - CERN Accelerator School: RF for Accelerators, Proceedings*, 2011, no. 2, pp. 95–116.
- [21] K.-C. Chan and A. Harter, "Impedance matching and Smith Chart : Basic Considerations," no. July, pp. 1–23, 2000.
- [22] G. Binnig, H. Rohrer, C. Gerber, and E. Weibel, "Surface Studies by Scanning Tunneling Microscopy," *Phys. Rev. Lett.*, vol. 49, no. 1, pp. 57–61, 1982.
- [23] P. Avouris, B. Bhushan, D. Bimberg, K. von Klitzing, C.-Z. Ning, and R. Wiesendanger, *Atomic Force Microscopy*. 2019.
- [24] T.-T. Nguyen, "Synthèse et contrôle de la taille de nanocristaux de silicium par plasma froid. Application dans les domaine de l'optoélectronique et de la nanoélectronique," no. January 2008, 2010.

- [25] J. Rivoal and C. Fr, "Microscopie à force atomique ( AFM )," vol. 33, no. 0, 2005.
- [26] J. Canet-Ferrer, E. Coronado, A. Forment-Aliaga, and E. Pinilla-Cienfuegos, "Correction of the tip convolution effects in the imaging of nanostructures studied through scanning force microscopy," *Nanotechnology*, vol. 25, no. 39, 2014, doi: 10.1088/0957-4484/25/39/395703.
- [27] B. Gautier *et al.*, "Techniques de mesure de grandeurs électriques adaptées aux nanocircuits Techniques de mesure de grandeurs ´ lectriques adapte ´ es e aux nanocircuits par," *Tech. l'Ingénieur*, vol. 33, no. 0, 2016.
- [28] U. of Cambridge, "Atomic Force Microscopy," 2009. <https://www.doitpoms.ac.uk/tlplib/afm/index.php> (accessed Feb. 12, 2024).
- [29] D. Ricci and P. C. Braga, "Recognizing and avoiding artifacts in AFM imaging.," *Methods Mol. Biol.*, vol. 242, pp. 25–37, 2004, doi: 10.1385/1-59259-647-9:25.
- [30] A. J. Fleming, "A review of nanometer resolution position sensors: Operation and performance," *Sensors Actuators, A Phys.*, vol. 190, pp. 106–126, 2013, doi: 10.1016/j.sna.2012.10.016.
- [31] E. Heaps *et al.*, "Bringing real-time traceability to high-speed atomic force microscopy," *Meas. Sci. Technol.*, vol. 31, no. 7, p. 74005, 2020, doi: 10.1088/1361-6501/ab7ca9.
- [32] A. Delvallée, N. Feltin, S. Ducourtieux, M. Trabelsi, and J. F. Hochepped, "Toward an uncertainty budget for measuring nanoparticles by AFM," *Metrologia*, vol. 53, no. 1, pp. 41–50, 2015, doi: 10.1088/0026-1394/53/1/41.
- [33] LNE, "Dimensional standard 2D network sample - Calibration certificate," 2020.
- [34] A. Technologies, "Agilent Technologies 5500 Scanning Probe Microscope User's Guide," *Agil. SPM*, p. 215, 2008, [Online]. Available: [http://www.charfac.umn.edu/instruments/5500\\_Users\\_Guide.pdf](http://www.charfac.umn.edu/instruments/5500_Users_Guide.pdf).
- [35] I. Estevez, "DEVELOPPEMENT D'UNE TECHNIQUE D'IMAGERIE D'IMPEDANCE ELECTRIQUE LOCALE A PARTIR D'UN MICROSCOPE A FORCE ATOMIQUE," Université Paris-sud 11, 2010.
- [36] J. R. Matey and J. Blanc, "Scanning capacitance microscopy," *J. Appl. Phys.*, vol. 57, no. 5, pp. 1437–1444, 1985, doi: 10.1063/1.334506.
- [37] P. Girard, "Electrostatic force microscopy: Principles and some applications to semiconductors," *Nanotechnology*, vol. 12, no. 4, pp. 485–490, 2001, doi: 10.1088/0957-4484/12/4/321.
- [38] Z. Chu, L. Zheng, and K. Lai, "Microwave Microscopy and Its Applications," *Annu. Rev. Mater. Res.*, vol. 50, pp. 105–130, 2020, doi: 10.1146/annurev-matsci-081519-011844.
- [39] Z. Li, L. Zhou, H. Lei, and Y. Pei, "Microwave near-field and far-field imaging of composite plate with hat stiffeners," *Compos. Part B Eng.*, vol. 161, no. May 2018, pp. 87–95, 2019, doi: 10.1016/j.compositesb.2018.10.058.
- [40] S. M. Anlage, V. V. Talanov, and A. R. Schwartz, *Principles of near-field microwave microscopy*, vol. 2. 2007.
- [41] A. Imtiaz and S. M. Anlage, "A novel STM-assisted microwave microscope with capacitance and loss imaging capability," *Ultramicroscopy*, vol. 94, no. 3–4, pp. 209–216, 2003, doi: 10.1016/S0304-3991(02)00291-7.
- [42] C. Boutin and P. Kabos, "Near-Field Scanning Microwave Microscope: Big at the Nanoscale," *Analytical Science*, 2012.
- [43] F. Wang *et al.*, "Quantitative impedance characterization of sub-10 nm scale capacitors and tunnel junctions with an interferometric scanning microwave microscope," *Nanotechnology*, vol. 25, no. 40, 2014, doi: 10.1088/0957-4484/25/40/405703.
- [44] S. S. Tuca *et al.*, "Calibrated complex impedance of CHO cells and E. coli bacteria at GHz frequencies using scanning microwave microscopy," *Nanotechnology*, vol. 27, no. 13, 2016, doi: 10.1088/0957-4484/27/13/135702.
- [45] T. Le Quang, D. Vasyukov, J. Hoffmann, A. Buchter, and M. Zeier, "Fabrication and Measurements of Inductive Devices for Scanning Microwave Microscopy," pp. 1–5.
- [46] G. Gramse *et al.*, "Nondestructive imaging of atomically thin nanostructures buried in silicon," *Sci. Adv.*, vol. 3, no. 6, pp. 1–9, 2017, doi: 10.1126/sciadv.1602586.
- [47] M. C. Biagi *et al.*, "Nanoscale electric permittivity of single bacterial cells at gigahertz

- frequencies by scanning microwave microscopy," *ACS Nano*, vol. 10, no. 1, pp. 280–288, 2016, doi: 10.1021/acsnano.5b04279.
- [48] H. Bakli, K. Haddadi, and T. Lasri, "Modeling and Calibration in Near-Field Microwave Microscopy for Dielectric Constant and Loss Tangent Measurement," *IEEE Sens. J.*, vol. 16, no. 12, pp. 4667–4668, 2016, doi: 10.1109/JSEN.2016.2533608.
- [49] A. Buchter *et al.*, "Scanning microwave microscopy applied to semiconducting GaAs structures," *Rev. Sci. Instrum.*, vol. 89, no. 2, 2018, doi: 10.1063/1.5015966.
- [50] F. Cheng *et al.*, "Imaging microwave field of chip surfaces based on scanning microwave microscopy," *Phys. Scr.*, 2023, doi: 10.1088/1402-4896/acd81f.



## Chapter 2 Reference standards

### Chapter 2 Reference standards 56

1	<i>Needs and samples description</i>	57
1.1	Need for calibration sample	57
1.2	History of capacitance standards for nanoscale measurements	57
1.2.1	Parallel plate structure	58
1.2.2	Membrane structure	59
2	<i>Structure characterization</i>	60
2.1	Dimensional measurement	61
2.1.1	Thickness evaluation	61
2.1.2	Area of the electrodes	62
2.2	Electrical measurement	66
2.2.1	Dopant concentration	66
2.2.2	Relative permittivity	67
3	<i>Estimation of capacitance values</i>	68
3.1	Simulation	68
3.1.1	Need for simulation	68
3.1.2	Solving Poisson's equation by Comsol Multiphysics	68
3.1.3	Using an open-source solution – FeniCS python library	71
3.2	Empirical formula	71
4	<i>Evaluation of the uncertainty associated with capacitance</i>	72
5	<i>Second version of the calibration structure</i>	73
5.1	Parallel plate architecture	73
5.2	Membrane structure	75
6	<i>Conclusion</i>	76

# 1 Needs and samples description

## 1.1 Need for calibration sample

---

As mentioned in the first chapter, the VNA needs to be calibrated before any impedance measurement. The objective of the calibration is to bring the reference plane to the interface between the SMM tip and the sample. Because of the particular AFM configuration, there is a need for microscale calibration samples and specific calibration methods. So far, the following calibration methods have been reported in the literature:

- The resonance method [1][2];
- A method based on EFM measurement [3][4];
- A two-parameter calibration [5];
- A modified Short Open Load [6].

The first two calibration techniques are performed on a dielectric of known thickness but do not require any impedance defined by the sample contrary to the last two methods. Those rely on the measurement of known impedance by the SMM. A mapping function ( $f$ ) is established between the measured value of the  $S_{11}$  and the  $S_{11}$  associated with the actual sample capacitances ( $S_{11,m} \xrightarrow{f} S_{11}$ ).

Calibration samples are the subject of this chapter. As the scope of this thesis is on the measurements of dielectric properties ( $\epsilon_r$ ,  $\tan(\delta)$ ) which can be achieved by measuring capacitance, only the capacitance standards will be developed here. Inductance, resistance, or dopant concentration standards can be found elsewhere in the literature [7], [8].

## 1.2 History of capacitance standards for nanoscale measurements

---

Capacitance measurements by the mean of SMM were first reported in 1999 [2]. A sample was mounted and the capacitance between the AFM probe and the back electrode was evaluated at different tip-sample distances. It relies on a resonant method where the capacitance is deduced from the resonance frequency shift created by the sample. For tip-sample distance below a tenth of the apex's radius, an empirical formula can be used to compute the z-gradient of the tip-sample capacitance as a function of the apex's radius and tip-sample distance. There also exists a relationship between the resonant frequency shift and the z-gradient of the capacitance. The frequency shift derivation with respect to the tip-sample distance is measured. With accurate knowledge of the tip and sample geometry, the local dielectric constant can be determined using an empirical equation. The second method also relies on measuring the z-gradient of the tip-sample capacitance and uses computed capacitance to extract the dielectric constant and capacitance of the sample. The prime difference resides in the method used for measuring this gradient. The second method is based on EFM experiment and is detailed in Chapter 4. In both methods, the measurement is highly sensitive to the tip geometry. This latter is difficult to characterize and is prone to change during the scanning process as the SMM operates in contact mode.

The last two calibration methods rely on measurements of capacitance standard structures where the impedance of interest is defined by the sample itself. The tip geometry is therefore a less sensitive data as its impact on the total capacitance is significantly reduced. This topic will be largely explored in Chapter 3. The first capacitance standard structures for SMM calibration were introduced by A. Karbassi [9]. It was later extended to a lower capacitance range (below 1 fF) by H. Huber et al [5] and is presented in the next paragraph (1.2.1).

### 1.2.1 Parallel plate structure

The capacitance standard for SMM used by Huber adopts a parallel plate geometry as shown in Figure 2-1. This structure is composed of several patterns, each containing 48 metal oxide semiconductor (MOS) capacitors. A SiO<sub>2</sub> layer of 200 nm is grown by plasma-enhanced chemical vapor deposition (PE CVD) on a highly p-doped silicon substrate. Then, it went under a lithography process to define a sequence of steps of 50 nm. A SiO<sub>2</sub> staircase of four 50 nm steps is then obtained. The top electrode is a circular gold pad fabricated by electron beam evaporation of a 200 nm gold layer which then was submitted to lift-off lithography. To ensure good adhesion between the dielectric layer and the gold pad, a 20 nm titanium layer was first deposited on the SiO<sub>2</sub> staircase [5], [10].

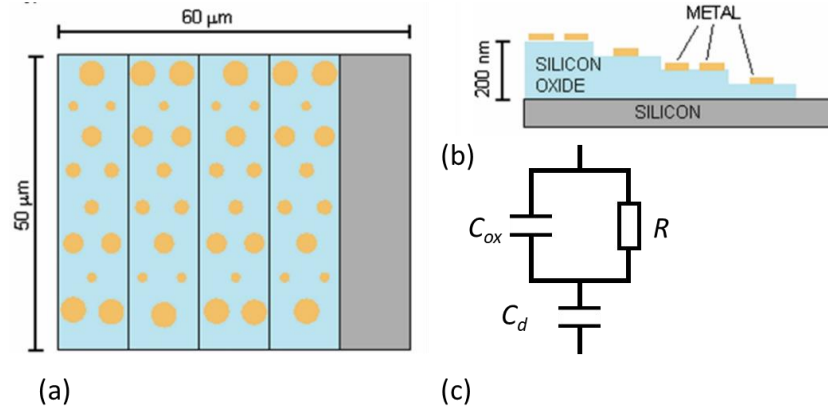


Figure 2-1. NIST capacitance standard for SMM (a) top view, (b) side view, (c) equivalent electric circuit.

The capacitance of each MOS capacitor ( $C_{ox}$ ) was evaluated under the ideal parallel plate capacitor hypothesis using the gold pad area ( $A$ ) and SiO<sub>2</sub> layer thickness ( $d$ ) from AFM imaging. The depletion capacitance ( $C_d$ ) at the SiO<sub>2</sub>/Si interface was also implemented in the model (Figure 2-1.c). The capacitance of the structure is then defined by Equation 2-1.

$$\frac{1}{C} = \frac{1}{C_{ox}} + \frac{1}{C_d} \quad \text{Equation 2-1.a}$$

$$C_{ox} = \epsilon_0 \epsilon_{SiO_2} \frac{A}{d} \quad \text{Equation 2-1.b}$$

The capacitance standard was characterized by a scanning capacitance microscopy (SCM) for validation. The  $S_{11}$  map of the structure was acquired by the SMM. The instrument was calibrated using a single capacitor by applying Equation 2-2,

$$C_{tot} = \alpha^* |\Delta S_{11}| \quad \text{Equation 2-2.a}$$

$$\Delta S_{11} = S_{11}|_{gold\ pad} - S_{11}|_{SiO_2} \quad \text{Equation 2-2.b}$$

where  $\alpha^*$  is the calibration coefficient and  $\Delta S_{11}$  is the difference between the  $S_{11}$  on the gold pad and on the neighborhood SiO<sub>2</sub> layer. This difference is implemented to mitigate the impact of the depletion capacitance.

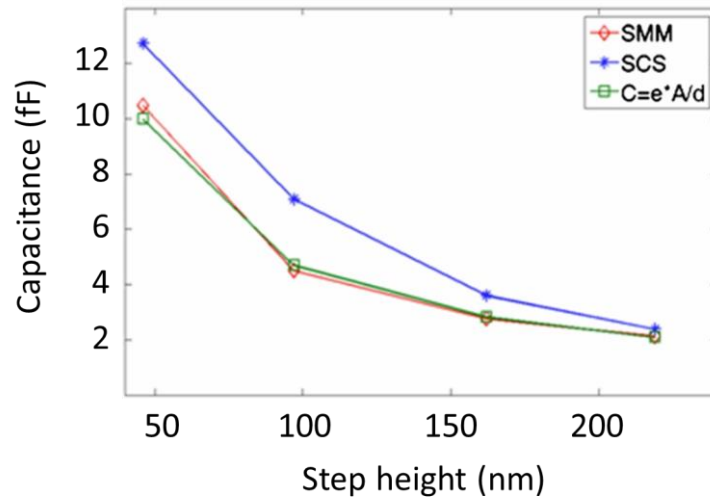


Figure 2-2. Comparison between the calculated and measured capacitance. SCS and calibrated SMM were used to measure the capacitances with a diameter of  $4\mu\text{m}$ . [5]

Figure 2-2 shows the measured capacitance with the SCS and calibrated SMM. Those values are to be compared with the computed capacitance values of the MOS capacitors. Only the gold pads of  $4\mu\text{m}$  diameter are represented. The uncertainty in the capacitance values measured by the calibrated SMM is estimated to be 20% [5], [6]. This uncertainty is mainly governed by the ones associated with the measurements of the terrace oxide's thickness, the top electrode's areas as well as the presence of a fringing field in the MOS capacitor (not taken into account by the parallel plate hypothesis), and of the depletion capacitance which is challenging to evaluate and can account for 10% of the total uncertainty while the fringing field counts for 30%. The study conducted in this chapter (sections 2 to 4) shows that, after careful measurements, the uncertainty associated with such capacitance can be reduced to the 3% level. An important of the uncertainty comes from the knowledge of the dielectric constant.

### 1.2.2 Membrane structure

T. Le Quang et al suggested to use of a free-standing dielectric membrane [11] to reduce combined uncertainty associated with the capacitance value by reducing the relative permittivity of the dielectric layer and depletion capacitance contribution to the global capacitance. By design, there is no depletion capacitance and the fringing field is accounted for by numerical simulation which significantly reduces their associated uncertainty. In this configuration, the capacitor is a combination of the capacitor due to the air gap between the central electrode and the guard electrode ( $C_{\text{gap}}$ ) and the capacitor between the central electrode and the back electrode ( $C_{\text{be}}$ ) as shown in Figure 2-3.

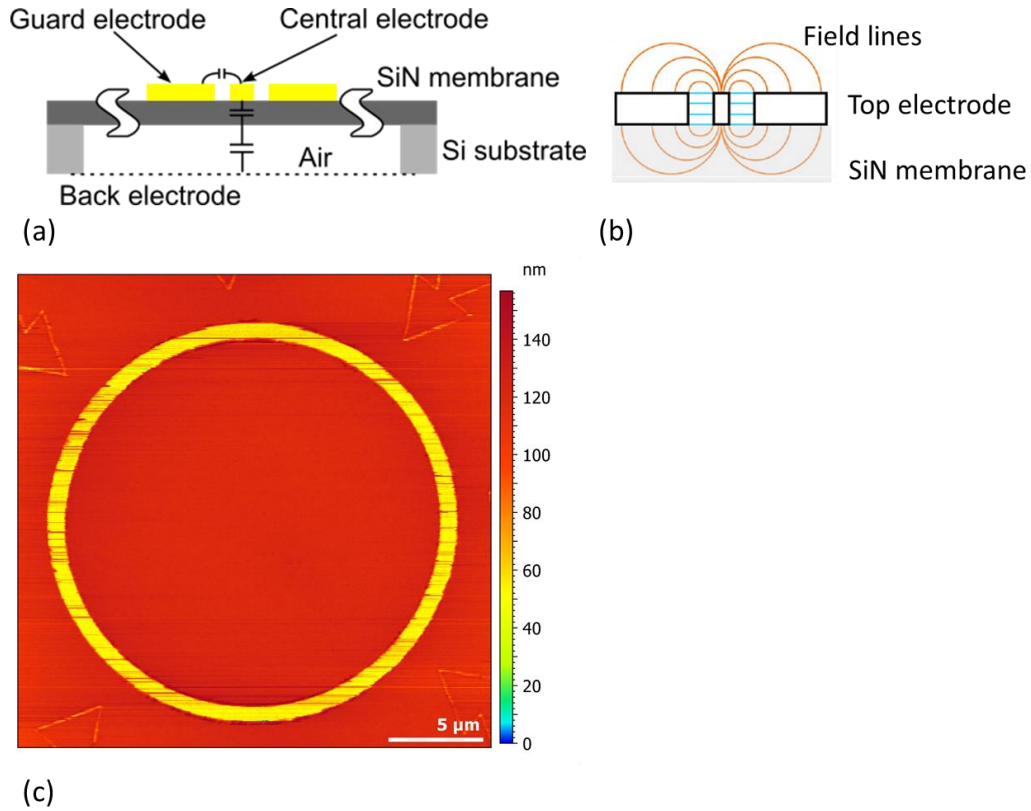


Figure 2-3. (a) Capacitor based on a membrane architecture as proposed by METAS, (b) field lines between the two top electrodes, (c) contact mode AFM image of a capacitive structure from METAS

The total capacitance value is then computed by Equation 2-3.

$$C_{\text{tot}} = C_{\text{gap}} + C_{\text{be}} \quad \text{Equation 2-3.a}$$

$$\frac{1}{C_{\text{be}}} = \frac{1}{C_{\text{SiN}}} + \frac{1}{C_{\text{air}}} \quad \text{Equation 2-3.b}$$

Due to the structure geometry,  $C_{\text{be}}$  is much smaller than  $C_{\text{gap}}$ . The dielectric constant of the air is known with an uncertainty of 1 ppm under standard condition for temperature, pressure and humidity and has the largest contribution to the total capacitance. The electric field lines in Figure 2-3.b encounter two different dielectric mediums, the air and the SiN membrane. Only the lines below the pads are passing through the SiN membrane. As the uncertainty associated with the dielectric constant of air is much lower than the one associated with the dielectric constant of SiN [12], this distribution of the field lines results in a reduction of the uncertainty associated with the capacitance calculation. Moreover, this architecture is believed to enable a lower capacitance range than its parallel plate counterpart. Evidence of this will be given in the simulation work (Section 5.2). Having capacitance as low as tens of attofarad will enable the study of fine parameters, such as water meniscus or impact on the calibration [13].

## 2 Structure characterization

In this thesis, the SMM was calibrated using either an EFM-based capacitance evaluation as described later (Chapter 4), or using a capacitance calibration standard. At the beginning of this work, the LNE used the only available MOS capacitance standard on the market to calibrate its SMM. It is a sample commercialized by MC2 technologies which had previous experience in manufacturing calibration samples for SMM [14]. The capacitance values are evaluated by measuring the dimensions of the top electrode and the dielectric layer, as well as the dielectric constant of the oxide layer. Those quantities ensure the traceability to the SI. The depletion capacitance estimation requires the knowledge of the dopant concentration of the silicon substrate.

## 2.1 Dimensional measurement

The thickness of the dielectric layer and top electrodes were measured with a calibrated AFM and well characterized in terms of uncertainties. The areas of the top electrodes were measured by scanning electron microscopy (SEM), for which a metrological qualification has also been carried out.

### 2.1.1 Thickness evaluation

To determine the height of the dielectric terraces and top electrode thickness, the structure was imaged using a calibrated AFM (Nanoman V from Veeco) operating in tapping mode with a tip velocity of  $6 \mu\text{m/s}$ . The used AFM tip (OTESPA-R3 from Bruker) has a nominal radius value of  $7 \text{ nm}$ , a front angle of  $(0 \pm 1)^\circ$ , and a side angle of  $(18 \pm 1)^\circ$ . The AFM dimensional calibration was carried out on an LNE-C2N surface topography standard (P900H60) with a pitch of  $(900.0 \pm 1.0) \text{ nm}$  and a height of  $(70.7 \pm 0.5) \text{ nm}$  [15]. This standard was initially calibrated directly on the LNE metrological AFM [16]. Four topographic images were acquired and the associated uncertainty budget was evaluated. Figure 2-4 shows a raw (a) and treated (b) topographic image acquired.

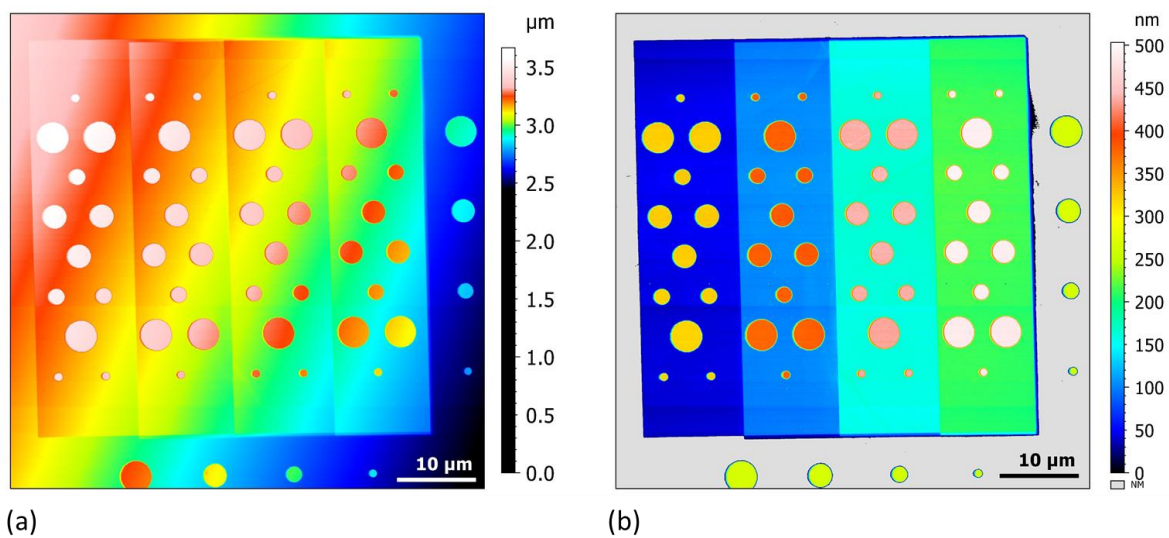


Figure 2-4. AFM image of the MC2 A61 sample. (a). Raw image; (b) Post-treatment image. Figure produced using MountainLab software.

After acquisition, the images were processed using the following procedure.

- Outlier point removal
- Filter to remove local pic
- Height segmentation of the structure
- Background leveling by rotation
- Terrace isolation by cropping
- Background and electrode separation by height segmentation for each terrace.

Then the average height of each feature (pad or terrace) was recorded. The thickness measurement and associated uncertainty budget are presented in Table 2-1.

Table 2-1. Uncertainty budget associated with thickness measurement by AFM for each terrace and pads

Uncertainty Budget (nm)	Type	1	2	3	4	Pads
Repeatability	A	0.6	0.4	0.4	0.3	0.2
Height AFM calibration	B	0.3	0.7	1.1	1.5	1.9
Combined $u_h$		0.7	0.8	1.2	1.5	1.9
$h$ (nm)		$49.8 \pm 0.7$	$100.8 \pm 0.8$	$160.2 \pm 1.2$	$214.8 \pm 1.5$	$275.1 \pm 1.9$

In all uncertainty budget presented in this work, the type A uncertainty are “extracted from the statistical distribution of the quantity values from series of measurements” while the type B uncertainty includes everything else [Ref VIM (JCGM)]. The height uncertainty contributes to the thickness measurement according to Equation 2-4.

$$u_{\text{height}} = \frac{u_{\text{height,cal}}}{\text{height cal}} \text{height sample} \quad \text{Equation 2-4.}$$

It can be challenging to further reduce the absolute uncertainty associated with the thickness measurement, except for the thinnest terrace, without using the metrological AFM, as an important part is due to the AFM calibration itself. Nevertheless, it is still possible to reduce the relative uncertainty by increasing the thickness of the terraces as explained in part 5.1.

### 2.1.2 Area of the electrodes

Images of the calibration sample were acquired with a field-emission SEM (Zeiss ULTRA-Plus) equipped with energy-dispersive X-ray spectroscopy (EDS, Ultim Max, Oxford). All the images were acquired using the in-lens detector. In fact, the In-Lens detector is particularly sensitive to the electrons coming from the surface. Two series of images were acquired with an acceleration voltage of 3 kV and 10 kV. A general view and two zoom-in on a top electrode of 1  $\mu\text{m}$  diameter are shown in Figure 2-5. In Figure 2-5.a, a bright corona is located around each pad. It was not expected and it motivated the acquisition of zoom-in images (Figure 2-5.b and c). In Figure 2-5.b, it is clear that the corona is surrounding the pad. As the image is top view, it is likely to correspond to a non-vertical flanked. A second darker corona is also spotted. Figure 2-5.c is a titled view of the same electrode. The two corona are still presented. It is now clear that the first one corresponds to a titled flank forming a cone angle of  $\theta = (19.5 \pm 1.5)^\circ$ . The second corona is located at the bottom of the electrode.

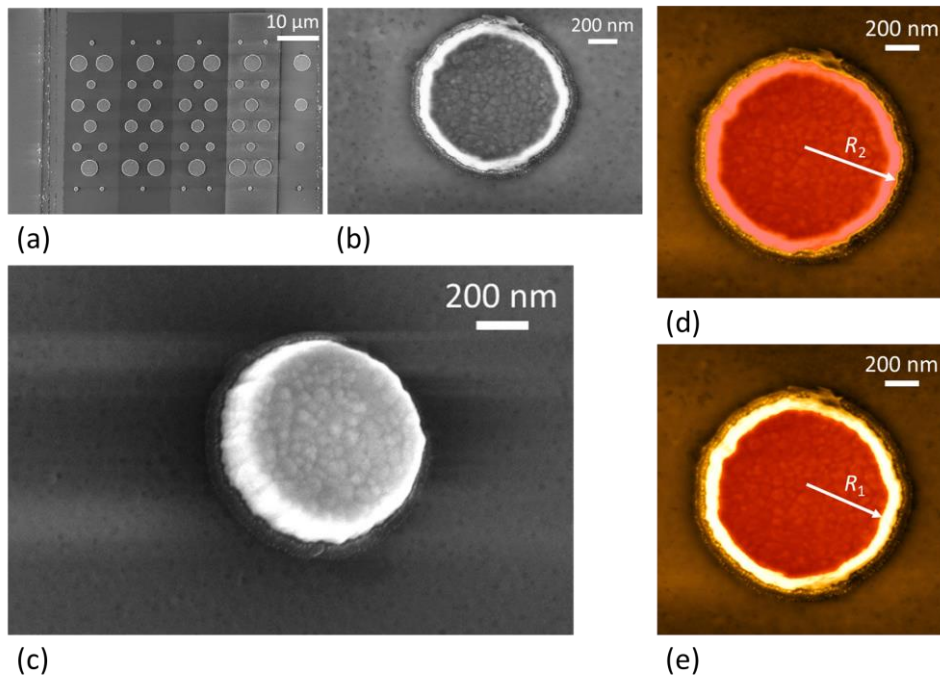


Figure 2-5. SE images of the MC2 capacitance standard (v1). (a): Global view, (b) zoom on a top electrode of 1  $\mu\text{m}$  diameter, (c) titled view of the same top electrode. A layer can be seen at the interface  $\text{SiO}_2/\text{Au}$ . The acceleration voltage is of 3 kV for image a and b and 10 kV for image c. The working distance is of 4 mm for image a and b and 6.3 mm for image c. Images d and e show the segmentation of image (b) at the lowest (highest) height of the pad.

An attempt to evaluate the electrodes area using SEM were conducted by height segmentation using Gwyddion free software [17]. Figure 2-5.d and e show the result of this segmentation at the bottom and summit of the electrode. Three images of this pad were considered leading to a type A uncertainty given by the standard deviation of the radius. The SEM image in Figure 2-5.b has a pixel size of 1.4 nm. Due to rectangular distribution [15], the pixel uncertainty on radius estimation is given by  $u_{\text{res}}(R_m) = \frac{t_{\text{pixel}}}{2\sqrt{3}}$ . The resolution contribution to uncertainty of area measurement is given Equation 2-5.

$$u_{\text{resolution}} = 2 \sqrt{\frac{\pi}{A_m}} \cdot u_{\text{res}}(R_m) \quad \text{Equation 2-5.}$$

Finally, an uncertainty of 11.5 nm is emerging from the SEM calibration. The corresponding equivalent radii  $R_1 = (425.1 \pm 11.8)$  nm and  $R_2 = (491.4 \pm 12.0)$  nm were evaluated using this segmentation.

Table 2-2. Uncertainty budget associated with the area measurement of MC2 capacitance standard (A61) performed by SEM

Uncertainty Budget	Type	$R_1$ (nm)	$R_2$ (nm)	$A_1$ ( $\mu\text{m}^2$ )	$A_2$ ( $\mu\text{m}^2$ )
Repeatability	A	2.5	3.6	0.007	0.011
Image resolution	B	0.04	0.04	0.000	0.000
SEM calibration	B	11.5	11.5	0.031	0.036
Combined $u_A$		11.8	12.0	0.031	0.037
Average values		425.1	491.4	0.568	0.759

The area of interest is located at the bottom of the electrodes. To be able to distinguish the bottom to the top area, zoom-in images need to be acquired on each pad. It can't be done in a reasonable time. Another strategy will be adopted by acquiring global images using the AFM setup described in the last section. The area of the electrodes will be evaluated at different heights and projected at the bottom using the cone angle.

To investigate the chemical composition of this additional corona visible at the interface between gold and silica, the EDS was used. Results are presented in Figure 6.

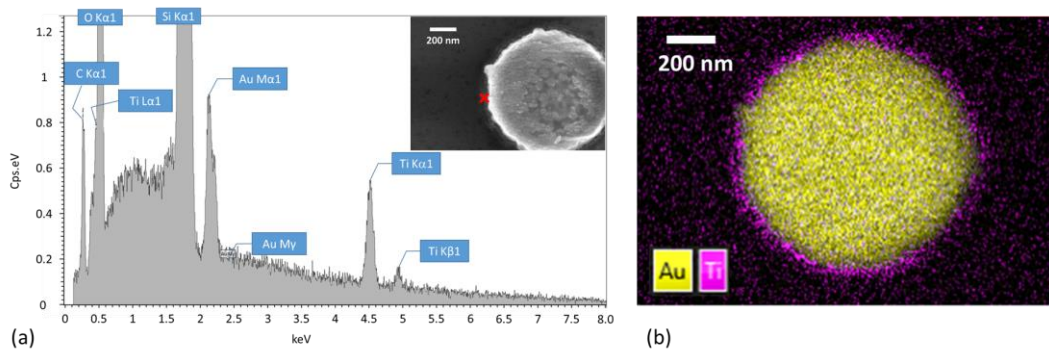


Figure 2-6. (a) EDS spectrum acquired at the bottom corona, (b) Superposition of Au and Ti component maps returned by EDS analysis over an SEM scan.

Figure 2-6.a presents the EDX spectrum acquired at the interface between gold and silica. Peaks associated with Carbon, Oxygen, Titanium, Silicon, and Gold are observed. For legibility purposes, only the maps associated with Au and Ti elements are shown in Figure 2-6.b. It underlines the Ti nature of the bottom corona localized between gold and silica. As mentioned before, Titanium is present in the fabrication process as an adhesion layer between the gold pad and the silicon oxide. Both layers (Au and Ti) underwent the same lithography process. It was expected that both would be etched to the same shape. To better understand what happened, High-resolution AFM images of the MC2 capacitance standards were acquired in tapping mode using the same setup as described in part 2.1.1. Zoom-in images on the Ti layer are presented for the different-size pads in Figure 2-7.



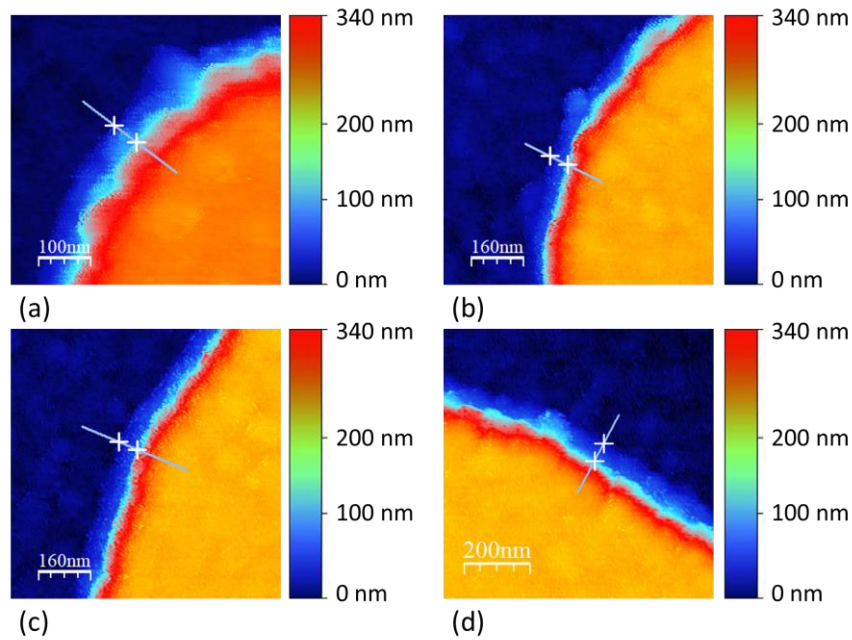


Figure 2-7. Tapping mode AFM image of the Ti layer for the different electrode radius: (a):  $R= 0.5 \mu\text{m}$ ; (b):  $R= 1 \mu\text{m}$ ; (c):  $R= 1.5 \mu\text{m}$ ; (d):  $R= 2 \mu\text{m}$

The Ti layer width was estimated using segmentation by height and averaged over the four images. Its value is found to be  $40.3 \text{ nm} \pm 3.6 \text{ nm}$ . This range is compatible with the two hypotheses. Either the resist used for the e-beam lithography (PMMA) was etched away by a step before the actual lithography or the Ti layer was enlarged due to stress existing at the PMMA and Ti interface. Then, additional images with a larger field of view were acquired in an attempt to increase the uncertainty of area measurements. Treated images are shown in Figure 2-8. To obtain the pads area at different heights, the following algorithm was applied to the topography images using Gwyddion software [17].

- All features were manually masked.
- The polynomial background was removed.
- The mean background was subtracted.
- All masks were deleted.
- Pads were masked by segmentation.
- The mask was dilated to encapsulate every pixel belonging to the pads.
- Each terrace was isolated by cropping.
- The terraces mean values were set to zero.
- Outsider values were identified by histogram and removed.
- Terraces were merged.
- All masks were removed.
- Mask 6.a to 6.e were applied by threshold ranging from 10% to 90%.

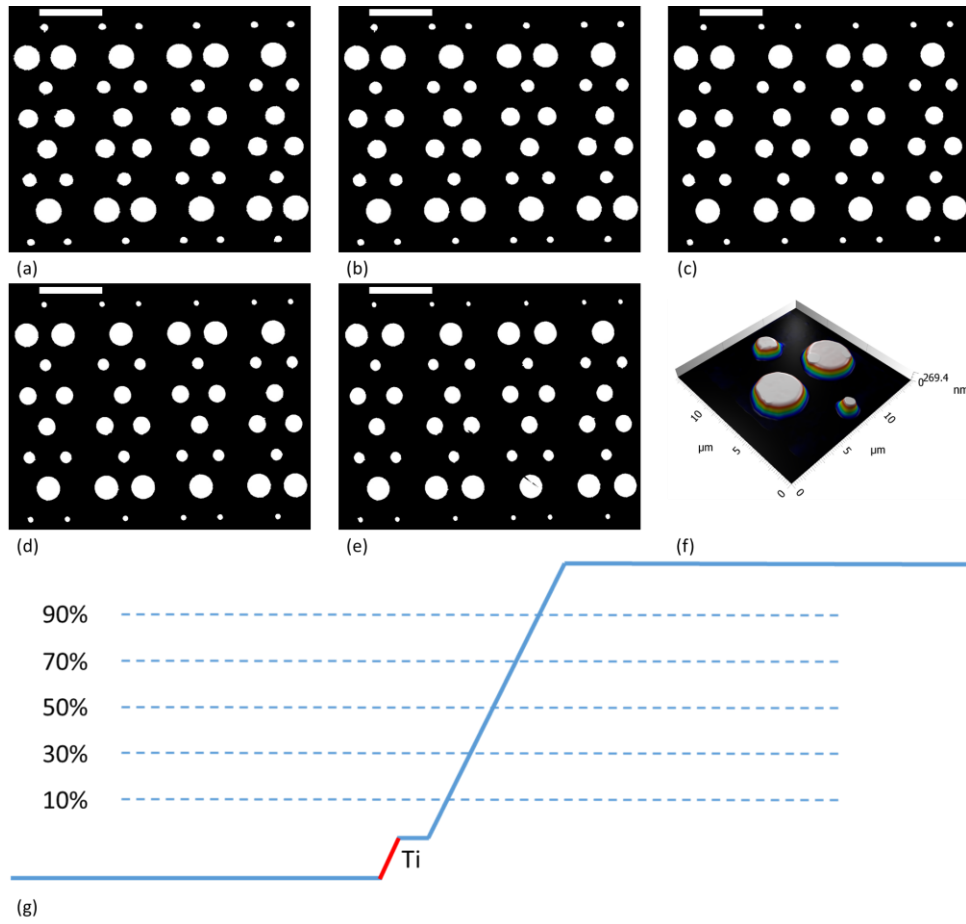


Figure 2-8. a to e: Top contact masked by z threshold ranging from 10% (a) to 90% (e) with a step size of 20%. All scale bars are 10  $\mu\text{m}$ . (f) 3D projection of a zoom-in on four pads. (g) Area determination scheme

Following the scheme presented in Figure 2-8.g, the area values were measured at five intermediate heights (10%, 30%, 50%, 70%, and 90%) before being extrapolated at full height ( $h_{pad} = (275.1 \pm 1.9) \text{ nm}$ ). This extrapolated area ( $A_m$ ) has been corrected by considering the cone angle  $\Theta$  measured by SEM on several pads,  $\Theta = (19.5 \pm 1.5)^\circ$  to obtain the area value at the bottom of the electrode ( $A_{eff}$ ). This approach to determining the area from the extrapolated value at 100% height allows one to avoid the correction due to the tip profile and thus to its corresponding uncertainty. The uncertainty budget of the area measurement by AFM is presented in Table 2-3.

Table 2-3. Uncertainty budget associated with the area measurement of MC2 capacitance standard (A61) performed by AFM

Uncertainty Budget ( $\mu\text{m}^2$ )	Type	$C_{13}$	$C_{02}$	$C_{19}$	$C_{40}$
Repeatability	A	$4.0 \cdot 10^{-3}$	$3.0 \cdot 10^{-3}$	$3.6 \cdot 10^{-3}$	$6.6 \cdot 10^{-3}$
Image resolution	B	$102.6 \cdot 10^{-3}$	$74.7 \cdot 10^{-3}$	$50.2 \cdot 10^{-3}$	$22.6 \cdot 10^{-3}$
Pitch AFM calibration	B	$28.0 \cdot 10^{-3}$	$14.9 \cdot 10^{-3}$	$6.9 \cdot 10^{-3}$	$1.7 \cdot 10^{-3}$
Ti layer area correction	B	$0.4 \cdot 10^{-3}$	$0.4 \cdot 10^{-3}$	$0.3 \cdot 10^{-3}$	$0.4 \cdot 10^{-3}$
Cone shape area correction	B	$30.7 \cdot 10^{-3}$	$23.2 \cdot 10^{-3}$	$15.9 \cdot 10^{-3}$	$28.1 \cdot 10^{-3}$
Combined $u_A$		$110.6 \cdot 10^{-3}$	$79.9 \cdot 10^{-3}$	$53.1 \cdot 10^{-3}$	$25.0 \cdot 10^{-3}$
Area ( $\mu\text{m}^2$ )		13.33	7.47	3.61	0.99
$R_{pad}$ ( $\mu\text{m}$ )		2.06	1.54	1.07	0.56

The repeatability was obtained by dividing the measured area standard deviation by its average value on a set of four images. For each AFM image,  $2048 \times 2048$  pixels were acquired over an area of  $60 \mu\text{m}^2$ . Each pixel has a lateral size ( $t_{pixel}$ ) of 29.3 nm. Due to rectangular distribution [15], the pixel uncertainty on radius estimation is given by  $u_{res}(R_m) = \frac{t_{pixel}}{2\sqrt{3}}$ . The resolution contribution to uncertainty of area measurement is given by Equation 2-5. The pitch uncertainty contributes to the  $A_{eff}$  estimation from  $A_m$  according to Equation 2-6.

$$u_{\text{pitch}} = 2 \frac{A_m}{A_{\text{eff}}} \frac{u_{\text{pitch,cal}}}{\text{pitch cal}} \quad \text{Equation 2-6.}$$

The last uncertainty comes from the titanium layer and the pad cone shape area correction. The uncertainty on area measurement from the Ti layer is of  $4.07 \cdot 10^{-5} \mu\text{m}^2$ . The cone shape contribution to the pad area is expressed by Equation 2-7.

$$A_{\text{eff}} = \pi \left( \frac{\sqrt{A_m}}{\pi} + h_{\text{Au}} \tan(\Theta) \right)^2 \quad \text{Equation 2-7.}$$

The uncertainty on the electrode thickness ( $h_{\text{Au}}$ ) and flank angle ( $\Theta$ ) can be propagated (Equation 2-8) [18].

$$u_{A_{\text{eff}}} = \sqrt{\frac{4\pi}{A_m} [\{h_{\text{Au}} \tan(\Theta)\}^2 u_{h_{\text{Au}}}^2 + \{h_{\text{Au}} \Theta (1 - \tan(\Theta)^2)\}^2 u_{\Theta}^2]} \quad \text{Equation 2-8.}$$

The total uncertainty is then given by a quadratic sum of the different components. The main contribution to the uncertainty on area measurement is the image resolution. Increasing this resolution can be done by subdividing the images. To ensure good repeatability, the AFM was operated with a scan speed of  $6 \mu\text{m/s}$  ( $0.1 \text{ line/s}$ ) leading to an acquisition time of 5 h 41 min. The repeatability was estimated over 4 images. A new tip was used to ensure that its apex radius is closed from the manufacturer value. If we wanted to increase the resolution by 2, it would require 4 sub-images. The overall acquisition time will be more than 3 days which is not desirable as it would lead to other perturbations (drift, change in environmental condition).

The second most important uncertainty component comes from the cone shape correction. Insuring a vertical flank of the electrode will improve the uncertainty of the measurement. It can be achieved by thinning down the electrode. Finally, the combined relative uncertainty can be reduced by using larger electrodes.

## 2.2 Electrical measurement

---

The electrical properties of the capacitor structure are measured using a CascadeMicrotech MPS150 probe station equipped with four DPP220 CascadeMicrotech micro positioners with a  $0.5 \mu\text{m}$  resolution. The PTT-06/4-25 probe from FormFactor with a nominal apex's radius of  $0.6 \mu\text{m}$  was used for all probe station measurements. The dopant concentration was extracted from resistance measurement performed by a Keysight 3458A multimeter in DC mode. The relative permittivity at low frequency of the dielectric layer was measured using a Keysight LCRmeter.

### 2.2.1 Dopant concentration

The depletion capacitance is computed from the dopant concentration of the Si substrate according to Equation 2-9 [19],

$$C_{\text{d,FB}} = \frac{\epsilon_0 \epsilon_{\text{r,Si}} A}{l_{\text{D}}} \quad \text{Equation 2-9.a}$$

$$l_{\text{D}} = \sqrt{\frac{kT \epsilon_0 \epsilon_{\text{r,Si}}}{e^2 N_{\text{a}}}} \quad \text{Equation 2-9.b}$$

where  $l_{\text{D}}$  is the Debye length,  $k$  is the Boltzmann constant,  $T$  is the temperature of the substrate,  $e$  is the elementary charge, and  $N_{\text{a}}$  is the doping concentration. In the Schottky diode, the difference in work function between the metal and the semiconductor results in a local potential drop and leads to

an inevitable band bending. Depletion capacitance is then reduced and its lowest value is bound by Equation 2-10

$$C_{d,\min} = \frac{C_{d,FB}}{2 \sqrt{\ln\left(\frac{N_a}{n_i}\right)}} \quad \text{Equation 2-10.}$$

where  $n_i$  is the intrinsic carrier concentration of the Si substrate. The doping concentration can be deduced from the resistivity of the Si substrate [20]. The electrical properties of the silicon substrate can be accessed by the Schottky diodes located near the SiO<sub>2</sub> terraces. Figure 2-9 shows the experimental setup to measure the resistivity of the silicon substrate.

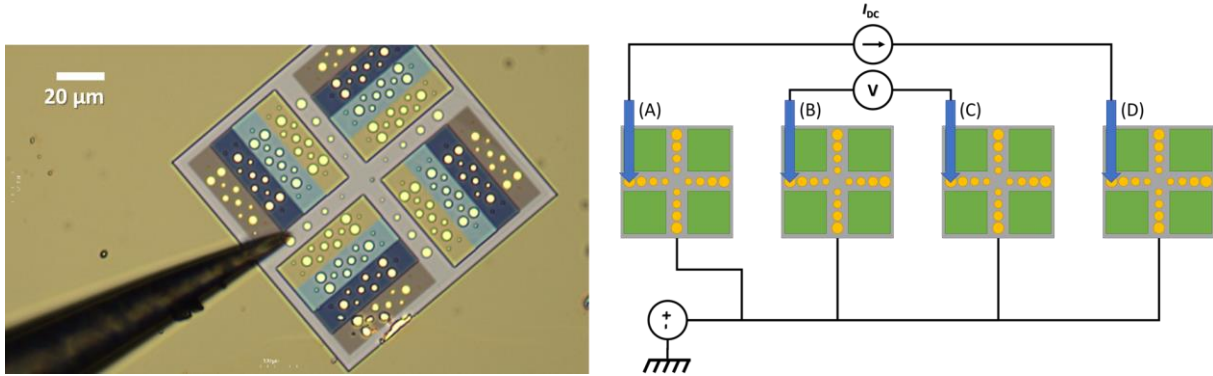


Figure 2-9. Experimental setup to measure the resistivity of the Si substrate on A61.

The calibration kit was mounted on the probe station and the back surface of the sample was biased at a given voltage  $V_B$  to ensure that the Schottky diodes show a conducting behavior. Four aligned Schottky diodes were connected to the probes. The latter is determined using Equation 2-11

$$\rho = R_{\text{sheet}} \cdot d = \frac{V}{I} \cdot CF \cdot d \quad \text{Equation 2-11.}$$

where  $d$  is the distance between the two inner Schottky diodes (arrows B and C) and  $CF$  is the correction factor to pass from the resistance to the sheet resistance [19]. A continuous current of 0.75 mA was applied between the two external Schottky diodes (arrows A and D) and the voltage drop was measured between the two inner electrodes. The  $CF$  is a function of the sample geometry and probe separation to sample length ratio [21]. In the case of this measurement, it is set to 4.22. It resulted in a sheet resistance of  $(10.41 \pm 0.10)$  mΩ.cm in good agreement with the manufacturer data ( $\rho = 10$  mΩ.cm). This corresponds to a dopant concentration  $N_a = (8.2 \pm 0.3) \cdot 10^{18}$  atoms/cm<sup>3</sup>. The depletion capacitance is then in the tens to hundreds of femtofarad range. Applying Equation 2-1, the depletion capacitance contributes to the capacitance of the structure at a level comprised between 0.25% to 8.64%. The highest contribution occurs for the large  $C_{ox}$  values.

### 2.2.2 Relative permittivity

Low-frequency capacitance measurements can be conducted on the structure by interfacing the probe station with an LCRmeter. To this end, one probe is set in contact with the top electrode of the DUT while a second is put in contact with the conductive Si substrate. Knowing the dimension of the capacitor, it is possible to adjust the dielectric constant in the simulation to equal the computed capacitance to the measured one. Unfortunately, even the largest available pads ( $R = 2$  μm) were too small to establish a satisfactory electrical contact using the probe. As this attempt to measure the in-situ dielectric constant of the SiO<sub>2</sub> layer failed, its value was extracted from the literature [22] with an uncertainty better than 0.03%. Nevertheless, it should be noted that this value was acquired over an area covered by a 38.1 mm diameter cylinder. It is expected to observe some local variation of the dielectric constant at the microscale [23]. Because the dielectric constant of materials can vary from one batch to another, a conservative uncertainty of 1% was considered from the dielectric constant. Future work will use a different probe geometry that will hopefully lead to the successful in-situ measurement of the dielectric constant.

## 3 Estimation of capacitance values

Once the dimensions of the capacitor (electrode shape and radius and dielectric thickness) and the electric properties of the dielectric ( $\epsilon_r$ ) have been measured, they can be used to evaluate the capacitance value of the MC2 structure.

### 3.1 Simulation

The capacitor parameters are implemented in a finite elements model (FEM) to determine the capacitance of the structure. The values returned are then used as a reference for the SMM calibration.

#### 3.1.1 Need for simulation

In section 1, the ideal parallel plate capacitor formula is given. It supposes an infinite length of the electrode which is not true in the actual configuration. Having finite-size electrodes creates a fringing field that influences the capacitance value and can no longer be neglected when the electrode radius ( $R$ ) to electrode separation distance ( $h$ ) ratio is below 20 [24]. Table 2-4 represents the relative deviation between the computed capacitance and the measured capacitance as a function of the  $R$  to  $d$  ratio using Maxwell's equations and the expression given in Sloggett's paper.

Table 2-4. Computed capacitance relative deviation to measured capacitance as a function of  $R$  to  $d$  ratio, from [24]

Relative deviation (%)		$R/h$					
		2	4	6	8	10	20
Model	Maxwell	-18	-14	-10	-6	-5	-1
	Sloggett	-8	-6	-3	-1	-0.5	+1

For the membrane architecture, having an analytical or even empirical expression to compute the capacitance for the dimensions and electric properties is challenging due to the presence of the membrane.

#### 3.1.2 Solving Poisson's equation by Comsol Multiphysics

Electrostatic simulations using a FEM were conducted to determine the capacitance of the structure. In FEM, the simulation box is divided into several small elements defined by a mesh. Due to the circular geometry of the top electrode, the MOS structure presents a revolution symmetry along the  $z$  axis allowing to reduce the simulation box to a 2D system with a revolution axis passing through the gold pad center, hence reducing significantly the computation cost. Typical simulation box geometry is shown in Figure 2-10. The top electrode's electric potential is set to 1 V while the back electrode has a 0 V potential. The objective is to compute the electrical potential over the whole simulation box. It is done by solving the Poisson's equation (Equation 2-12).

$$\nabla^2 V = -\frac{\rho}{\epsilon} \quad \text{Equation 2-12.}$$

The capacitance is then computed by integrating the second derivative of the electric potential over the top electrode of the capacitor as in Equation 2-13,

$$C = -\frac{\iint_{top\ electrode} \vec{\nabla}(\epsilon \vec{\nabla} V) \cdot d\vec{s}}{\Delta V} \quad \text{Equation 2-13.}$$

with  $\Delta V$  the potential difference between the two electrodes. In a 2D system, Equation 2-12 can be rewritten as in Equation 2-14.

$$\frac{\partial^2 V}{\partial x^2} + \frac{\partial^2 V}{\partial z^2} = -\frac{\rho}{\epsilon} \quad \text{Equation 2-14.}$$

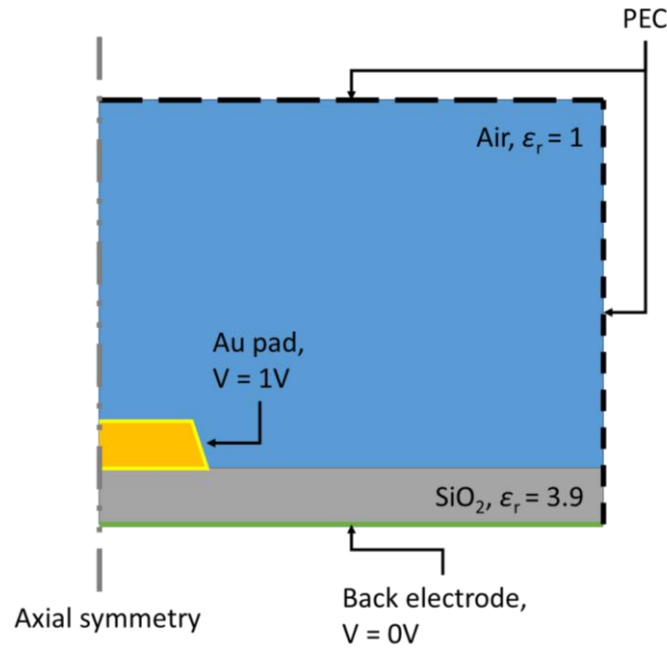


Figure 2-10. Simulation box geometry of a MOS capacitor. Axial symmetry is implemented at the center of the circular gold pad. A 1 V electrical potential was set on the top electrode while the back electrode potential was set to 0 V.

The boundary conditions set in the simulation box are described in Equation 2-15 where  $\vec{n}$  is the normal to the boundary.

$$\vec{n} \cdot -\vec{\nabla}V = \vec{n} \cdot \vec{E} = \vec{0} \quad \text{Equation 2-15.a}$$

$$\vec{n} \cdot \vec{\nabla}V = \vec{0} \quad \text{Equation 2-15.b}$$

$$V = 1 \quad \text{Equation 2-15.c}$$

$$V = 0 \quad \text{Equation 2-15.d}$$

In the top and right boundary of the simulation box, a perfect electric conductor (PEC) condition is set. It is equivalent to having zero charge which is transcribed by Equation 2-15.a. The axial symmetry means a null derivative along the normal to the boundary (Equation 2-15.b). The top (bottom) electrode is set to a 1 V (0 V) potential (Equation 2-15.c and 7.d). Due to its good electrical conductivity, the top conductor is supposed to be at equipotential. There is no need to mesh it, which saves computer time. The mesh is defined everywhere else.

To solve Poisson's equation by finite element analysis, it needs to be discretized over the mesh. Equation 2-16 is the central difference approximation that can be applied to a rectangular structured mesh [25].

$$\frac{V(x + \delta x) - 2V(x) + V(x - \delta x)}{\delta x^2} + \frac{V(z + \delta z) - 2V(z) + V(z - \delta z)}{\delta z^2} = \frac{\rho}{\epsilon} \quad \text{Equation 2-16.}$$

When using finite elements, the mesh rarely satisfies those conditions but this scheme is used in finite difference analysis and helps understand the mathematical principle behind discretization. The 2D finite element can be either triangular [26], [27] or rectangle [28]. Triangular elements were chosen as they fit the most the geometry. In the Comsol environment, two algorithms are available to generate the mesh, the Delaunay method [29], [30] and the advancing front method [30], [31]. To properly conduct the simulation, the mesh needs to be fine enough with elements as regular as possible. The regularity of the mesh element can be evaluated by looking at their skewness [32]. Figure 2-11 shows

the mesh resulting from the two algorithms applied to the simulation box with the following parameters:  $R_{el} = 667.5 \text{ nm}$ ,  $d_{diel} = 200 \text{ nm}$ ,  $\epsilon_r = 3.9$ . For the convenience of the reader, all the following figures will be in this configuration. It has been found that the advancing front method conducts to a higher quality factor than the Delaunay method in this particular setup.

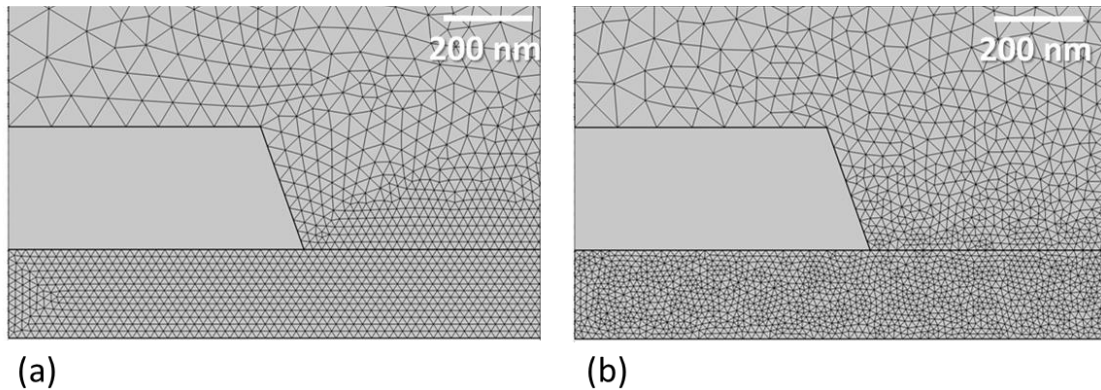


Figure 2-11. Mesh around the top electrode of the MOS capacitor. (a) using the advancing front method, average quality factor= 0.91; (b) using the Delaunay method, average quality factor= 0.82

Once the mesh, the equation governing the simulation box, and the boundary conditions have been defined, Poisson's equation can be solved. The capacitance of the structure is computed by applying Equation 2-13 to the electric potential distribution.

Here, the choice of the meshing algorithm is of prime importance. The capacitor presented in Figure 2-11 has a value of 353.4 aF for the advancing front method and a value of 355.7 aF for the Delaunay method. It results in a variation of 0.65% in the capacitance value. Figure 2-12 shows the electric potential and the field line across the structure.

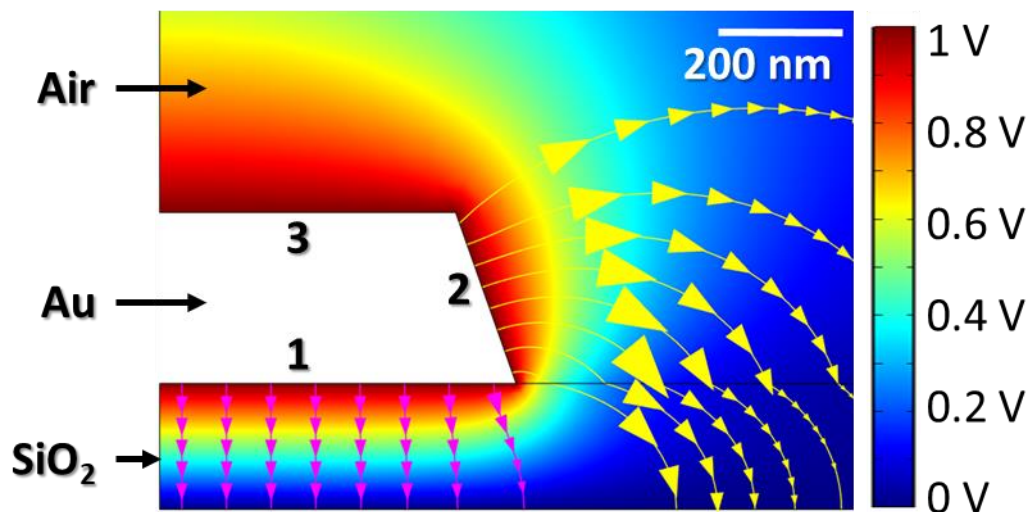


Figure 2-12. Electric potential (map color) and the field line (magenta and yellow arrows). A scale factor ( $\alpha$ ) is applied to the field lines arrow.  $\alpha = 2 \cdot 10^{-5}$  for the magenta lines and  $\alpha = 2 \cdot 10^{-4}$  for the yellow lines. The computations were done by Comsol Multiphysics 5.6.

The importance of the fringing field is highlighted by the field line proportion. When applying Equation 2-13, the computed capacitance value is found to be 0.35 fF. An analysis of the total capacitance by looking at the contribution of each part of the top electrode to the total electrode shows that part 1 of the top electrode contributes to 80.6% of the total capacitance value, part 2 contributes to 14.4 % and part 3 is responsible for 5.0%. The fringing field, which is not considered in the parallel plate capacitor equation, contributes to 19.4% of the total capacitance value. This illustrates the need for simulation to compute the capacitance. The reader must keep in mind that this particular capacitor configuration is further away from the parallel plate capacitor as it is the smallest electrode on the thickest dielectric layer. The fringing field contribution to the total capacitance value for the other capacitance ranges from 3.2% to 19.4%. The capacitance values of the different structures in the MC2 calibration sample are ranging from 0.28 fF to 9.16 fF.

### 3.1.3 Using an open-source solution – FeniCS python library

Evaluation of the capacitance of the structure can also be achieved using an open-source, free-to-use solution. The FEniCS FEM python library [33] and GMSH mesh generator using the Delaunay-Frontal generator[34] were used to complete this task. The mesh is presented in Figure 2-13 for the lowest capacitance value configuration.

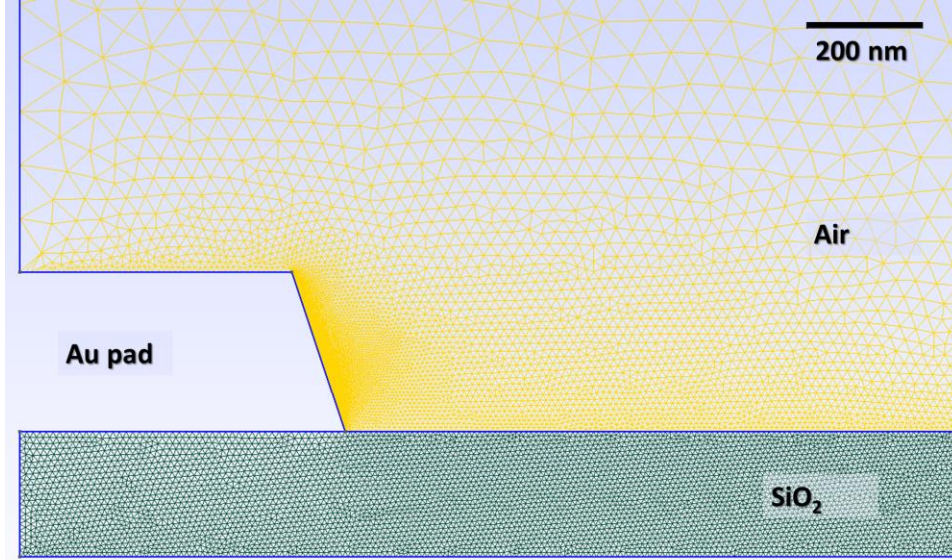


Figure 2-13. Mesh generated by GMSH for  $h_{SiO_2} = 214.8$  nm,  $h_{Au} = 275.1$  nm,  $R = 0.56$   $\mu$ m,  $\Theta = 19.5^\circ$ ,  $\epsilon_{r,SiO_2} = 3.9$

Dirichlet boundary conditions were implemented on the top electrode ( $V = 1$  V), bottom electrode ( $V = 0$  V), right and top edge of the simulation box ( $dV/dn = 0$  V/m) which is equivalent to the PEC. The Poisson's equation was solved over the whole simulation box. The capacitance is evaluated using Equation 2-13. An agreement below 0.1% is found between the solution computed by the open-source software and Comsol Multiphysics 5.6.

## 3.2 Empirical formula

For ease in the uncertainty propagation, it has been chosen to replace electrostatic simulation with an empirical formula. The starting point was the expression proposed by Sloggett et al. [24].

$$C_{sloggett} = C_{parallel\ plate} \left[ 1 + \frac{2h}{\pi R} \ln \left( \frac{8\pi R}{h} \right) + \left\{ \frac{h}{\pi R} \ln \left( \frac{h}{8\pi R} \right)^2 \right\} \right] \quad \text{Equation 2-17}$$

This equation is suited for circular plate capacitors with a top electrode surrounded by the same dielectric environment. The capacitors of the calibration kit have their top electrodes surrounded by two dielectrics, the dielectric layer of the sample at the bottom, and the dry nitrogen gas ( $N_2$ ) on the top of the sample. This is then the equivalent of two capacitors in series, leading to a negative term as correction. Moreover, the height of the top electrode has here a finite value not taken into account in Sloggett's expression. Equation 2-17 can be adapted to hold for this particular case (Equation 2-18).

$$C_{sloggett,m} = C_{parallel\ plate} \left( 1 + \gamma \times g \left( \frac{h}{R} \right) \right) \quad \text{Equation 2-18.a}$$

$$\gamma = 0.971 - 0.087i_r \quad \text{Equation 2-18.b}$$

$$g(k) = \frac{2h}{\pi R} \ln \left( \frac{8\pi}{\exp(1) \frac{h}{R}} \right) + \left[ \frac{h}{R\pi} \ln \left( \frac{h}{R} \frac{1}{8\pi} \right) \right]^2 \quad \text{Equation 2-18.c}$$



The relative deviation between the capacitance computed by the electrostatic simulation ( $C_{FEM}$ ) and the one computed by Equation 2-18 is shown in Figure 2-14

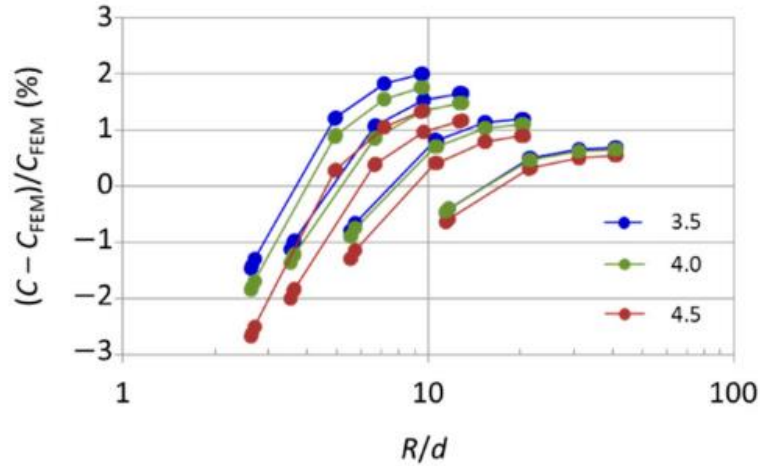


Figure 2-14. Relative deviation between  $C_{FEM}$  and  $C_{slogget,m}$  in function of the  $R$  to  $h$  ratio at three  $\epsilon_r$  values, [35]

Equation 2-18 works best for the thinner layers ( $h = 50$  nm and  $100$  nm) with a relative deviation at the level of 1%.

## 4 Evaluation of the uncertainty associated with capacitance

Using results from section 2 and the model described in section 3, the uncertainty budget of the MC2 capacitance standard sample is established in Table 2-5.

Table 2-5. Uncertainty budget associated with capacitance standard. [35]

Uncertainty budget	Type	$R=2\ \mu\text{m}$ $h_{\text{SiO}_2}=50\ \text{nm}$	$R=2\ \mu\text{m}$ $h_{\text{SiO}_2}=200\ \text{nm}$	$R=0.5\ \mu\text{m}$ $h_{\text{SiO}_2}=200\ \text{nm}$
$C_{\text{tot}}$ (fF)		9.472	2.528	0.272
$u_{\text{Cox}}$ $C_{\text{ox}}$ (aF)		181.9	37.7	7.4
$u_A$ ( $\mu\text{m}^2$ )	A, B	0.110	0.111	0.025
$u_h$ (nm)	A, B	0.7	1.5	1.5
$u_{\text{Permittivity}}$	B	0.039	0.039	0.039
$u_{\text{Cd}}$ (aF)	B	188.7	14.5	2.1
Numerical modeling (aF)	B	1.9	0.5	0.1
Combined uncertainty (aF)		262.6	63.1	9.2
Combined uncertainty (%)		2.77	1.60	2.84

The dimensional ( $u_A$  for the area,  $u_h$  for the thickness) and permittivity ( $u_{\text{Permittivity}}$ ) uncertainties contribution to the oxide capacitance uncertainty ( $u_{\text{Cox}}$ ) is computed using Equation 2-18 [18]. The major contributions to the combined uncertainty come from the area and thickness measurements as well as the uncertainty associated with the dielectric constant of the oxide and the depletion capacitance ( $u_{\text{Cd}}$ ). As mentioned before, the uncertainty associated with area measurement can be improved by ensuring the verticality of the electrode's flank. It will allow the area's evaluation by SEM image segmentation. One strategy to achieve this is to thin down the electrodes and replace the adhesion layer material to remove the bottom corona. Reducing the relative uncertainty associated with dielectric layer thickness can be done by increasing its absolute value. In-situ measurement of the dielectric constant was not successful on the existing standard. Having a larger pad will make possible its measurements by the probe station. Finally, the contribution of depletion capacitance can be further reduced by increasing the dopant concentration in the Si substrate.

# 5 Second version of the calibration structure

A second version of the capacitance standard was studied to address the issues mentioned in section 4 and to broaden the available range of capacitance present in the standard sample. The two existing capacitance designs (parallel plates and coplanar architectures) were considered. In the end, due to manufacturing cost considerations, the parallel plate architecture was chosen.

## 5.1 Parallel plate architecture

MC2 Technologies was entrusted with the fabrication of the reference sample with lower associated uncertainties. Simulation work was conducted to obtain the geometry responding to our need and satisfying the technological limitation (lateral dimension higher than 100 nm). To reduce the relative uncertainty associated with area and thickness measurements, the pad areas and dielectric thickness were set to larger values. The electrode thickness was reduced to 100 nm to ensure a vertical flank. The titanium adhesion layer between the dielectric and the top electrode was replaced by a chrome layer. This leads to the vanishing of the shouldering at the bottom of the electrode, allowing for area determination by SEM imaging. Figure 2-15 shows the geometry of the new design of the capacitance calibration kit. Due to the thicker dielectric layer, significant charging occurs during the SEM imaging. This leads to artifact formation in the image [36] that can be mitigated using the Zeiss ULTRA-Plus charge compensation system. An inert gas is locally injected to evacuate the charges in the dielectric layer [37]. A zoom-in image was acquired on a single electrode (Figure 2-15.b). It shows no corona around the electrode meaning that the verticality of the flank has been improved.

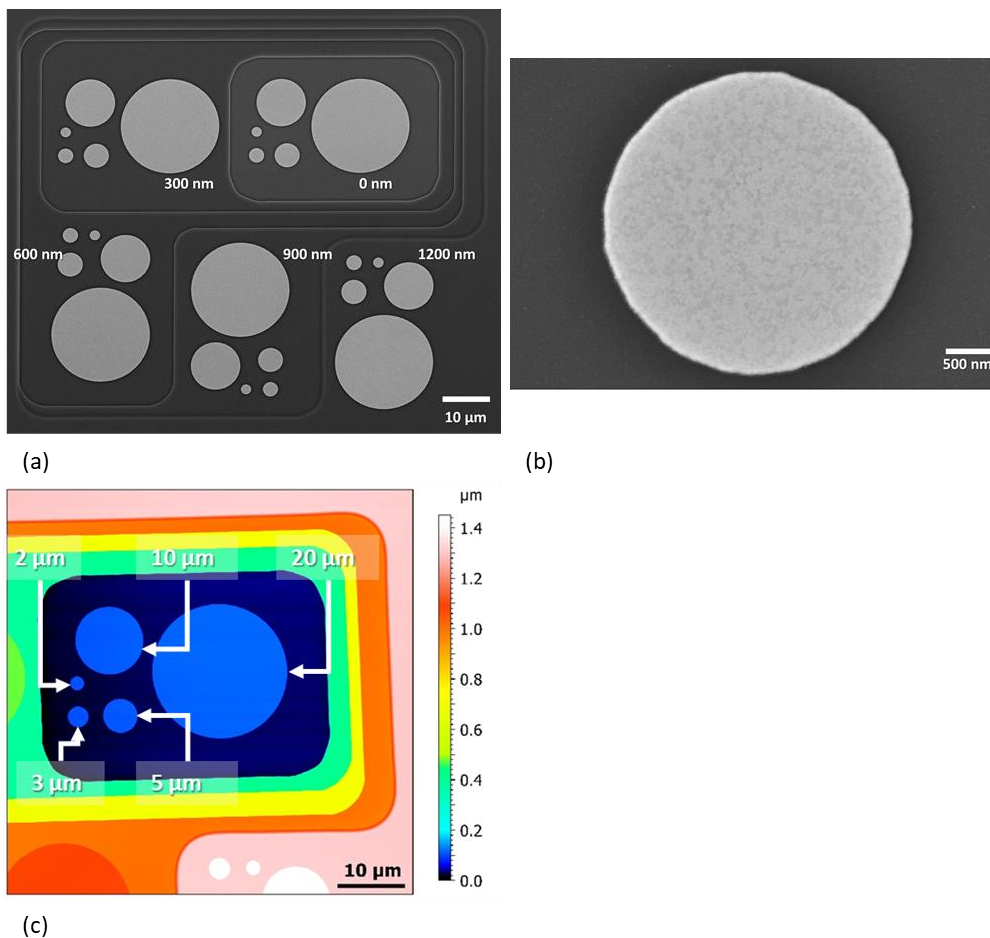


Figure 2-15. Capacitance standard v2, (a) SE image of the structure used for electrode's area determination, (b) Zoom-in SE image on an electrode of 3 μm diameter on the thinnest SiO<sub>2</sub> layer. All SE images were acquired with a 10 kV acceleration voltage and working distance of 4.5 mm (c) Post-treatment tapping mode AFM image. Figure produced using MountainLab software.

The lowest capacitance in this kit is 0.27fF. It was not possible to significantly reduce this value due to the large contribution of the fringing field. A lower value of capacitance may be achievable by use of coplanar capacitance and/or lower dielectric constant value. The choice to keep SiO<sub>2</sub> as the dielectric layer was motivated by its well-known dielectric constant and the fact that it is easier to grow on Si substrate. The Si substrate was chosen with a higher dopant concentration to reduce the contribution of the depletion capacitance. Based on the dimensional measurements performed with the same SEM and AFM setup described in section 2.1 and the dopant concentration estimation by the same method as described in 2.2.1 the uncertainty budget was established (Table 2-6).

Table 2-6. Uncertainty associated with capacitance standard v2.

Uncertainty budget	Type	$R = 10 \mu\text{m}$	$R = 10 \mu\text{m}$	$R = 1 \mu\text{m}$
		$h_{\text{SiO}_2} = 300 \text{ nm}$	$h_{\text{SiO}_2} = 1200 \text{ nm}$	$h_{\text{SiO}_2} = 1200 \text{ nm}$
$C_{\text{tot}}$ (fF)		39.381	11.112	0.298
$u_{\text{Cox}}$ (aF)		463.2	122.5	5.6
$u_A$ ( $\mu\text{m}^2$ )		$1.42 \cdot 10^{-3}$	$1.42 \cdot 10^{-3}$	$1.34 \cdot 10^{-3}$
Repeatability	A	$0.03 \cdot 10^{-3}$	$0.05 \cdot 10^{-3}$	$0.12 \cdot 10^{-3}$
Resolution	B	$1.42 \cdot 10^{-3}$	$1.42 \cdot 10^{-3}$	$1.34 \cdot 10^{-3}$
$u_h$ (nm)		4.6	11.2	11.2
Repeatability	A	3.7	6.6	6.6
Height calibration	B	2.8	9.1	9.1
$u_{\text{Permittivity}}$	B	0.039	0.039	0.039
$u_{\text{Cd}}$ (aF)	B	29.3	2.3	0.1
Numerical modeling (aF)	B	39.4	11.1	0.30
Combined uncert. (aF)		465.5	123.0	5.6
Combined uncertainty (%)		1.18	1.11	1.88

Thanks to the improved verticality of the electrode's flank and the absence of the corona at the bottom of the electrodes, the pad's areas are measured by SEM image segmentation. The pixel size of the beam is 25 nm and contributes to the uncertainty associated with area measurement according to Equation 2-5. A significant improvement in the uncertainty associated with the capacitance values has been achieved compared to the previous version. This has led MC2 to scale up the process in view of future commercialization.

The associated uncertainty associated with the capacitance value can be further improved by in-situ measurement of the dielectric constant. Coplanar waveguides have been deposited on SiO<sub>2</sub> sample made from the same Si substrate as the one used for the capacitance calibration sample. An optical microscopy view of this structure is shown in Figure 2-16.

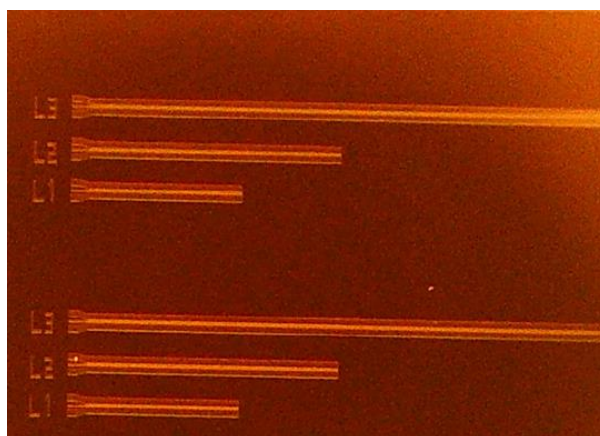


Figure 2-16. Coplanar waveguide for dielectric constant measurement of SiO<sub>2</sub>

Measurement of the SiO<sub>2</sub> dielectric constant was planned using the transmission line method described in Chapter 1.2.2.2. But, due to fabrication issues, those were unusable. Another way to access the dielectric constant of the SiO<sub>2</sub> layer is to use an LCRmeter interfaced with the probe station. The capacitance of the largest pad of each terrace of the second version of the calibration kit was measured. The LCRmeter short and open corrections were used. The simulation tool described in

section 3.1.2 was used to find the corresponding dielectric constant. The resulting dielectric constant ranges from 5.2 to 6.5 which is significantly different from the nominal value (3.9). This large deviation likely comes from the far-field contribution of the needle on the capacitance measurement. Future measurements of the capacitance will be done using a coaxial probe to remove this far-field contribution.

## 5.2 Membrane structure

During the design step, the coplanar capacitor structure was considered. Simulation work was conducted to achieve the geometry filling the requirement for the calibration of the SMM. All the results presented in this part are obtained with the following geometrical and electrical parameters: the electrode thickness is of 100 nm, the SiN membrane to back electrode distance is of 1.5  $\mu\text{m}$ , the SiN membrane thickness is of 500 nm and its dielectric constant is set at 7. Results of the simulation for a particular structure (radius of the central pad set at 400 nm, electrode separation distance of 200 nm) are presented in Figure 2-17. The mesh was generated using the extremely fine auto setting corresponding to element size ranging from 5 nm to 2.5  $\mu\text{m}$ .

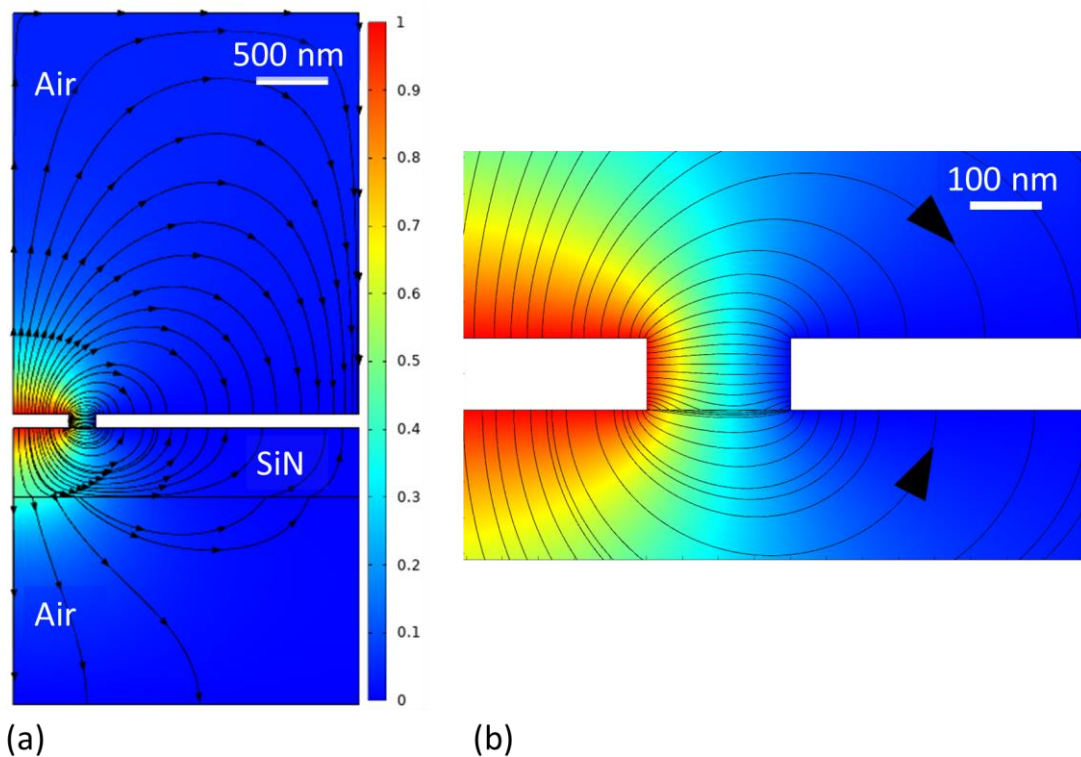


Figure 2-17. Electrostatic simulation of the coplanar capacitor structure. (a): a global view of the capacitor structure, (b) zoom in on the central electrode. The black arrows are the field lines. The computation is done by Comsol Multiphysics 5.6

By applying Equation 2-13 on the central electrode, the total capacitance of the structure is evaluated to be 166.3 aF. By a careful choice of geometry, the available capacitance can cover the 60 aF to 16 fF. The inner electrode radius ranges from 0.2  $\mu\text{m}$  to 20  $\mu\text{m}$  and the distance between the top electrodes is varied over the 0.2  $\mu\text{m}$  to 1  $\mu\text{m}$  range. The dimensional values satisfy the technological requirement mentioned in the last section (5.1).

After discussion with different manufacturers and economic considerations, the choice was made to not pursue the development of a coplanar capacitance calibration kit on our side. The simulation work conducted on this architecture is nevertheless presented as it highlights the possibility of reaching capacitance values as low as 58 aF with reasonable dimensions.

## 6 Conclusion

Two different architectures for capacitance standards are presented. The numerical simulation used to determine the capacitance value from dimensional and electrical properties of the structure was detailed as well as the use of an analytical formula to propagate the uncertainties. A comprehensive uncertainty budget associated with the capacitance value of the MOS structure was established from dimensional and electrical measurements. The error sources and corresponding uncertainties were analyzed for each contribution and strategies to reduce the overall uncertainty were explored. It was suggested to replace the titanium adhesion layer with chrome layer and to reduce the thickness of the electrode to ensure a vertical flank, allowing the segmentation of SEM images. Further progress was made by increasing the electrode's area to reduce the relative uncertainty. A similar strategy was applied to the dielectric layer, again to reduce the relative uncertainty. Finally, a Si substrate of higher dopant concentration was used to reduce the depletion capacitance contribution to the overall impedance. This new design was manufactured by MC2 technologies. It was characterized and an improvement on the uncertainty associated with the capacitance values by a factor of 2 or more was observed.

The second architecture for the capacitance calibration standard was also explored via numerical simulation. A design was proposed to extend the available capacitance to a lower value. But, due to cost considerations, the structure was not manufactured.

In the next chapter, the calibration of the SMM will be developed using the calibration structure exposed in this chapter. The performance of the different capacitance standards will be evaluated. An application case using the first calibration structure to measure the dielectric constant of high- $\kappa$  piezoelectric samples will be presented. Finally, an estimation of the impact of water meniscus on the instrument calibration will be developed.

- [1] C. Gao, T. Wei, F. Duewer, Y. Lu, and X. D. Xiang, "High spatial resolution quantitative microwave impedance microscopy by a scanning tip microwave near-field microscope," *Appl. Phys. Lett.*, vol. 71, no. 13, pp. 1872–1874, 1997, doi: 10.1063/1.120444.
- [2] C. Gao, F. Duewer, and X. D. Xiang, "Quantitative microwave evanescent microscopy," *Appl. Phys. Lett.*, vol. 75, no. 19, pp. 3005–3007, 1999, doi: 10.1063/1.125216.
- [3] G. Gramse, I. Casuso, J. Toset, L. Fumagalli, and G. Gomila, "Quantitative dielectric constant measurement of thin films by DC electrostatic force microscopy," *Nanotechnology*, vol. 20, no. 39, 2009, doi: 10.1088/0957-4484/20/39/395702.
- [4] G. Gramse, M. Kasper, L. Fumagalli, G. Gomila, P. Hinterdorfer, and F. Kienberger, "Calibrated complex impedance and permittivity measurements with scanning microwave microscopy," *Nanotechnology*, vol. 25, no. 14, 2014, doi: 10.1088/0957-4484/25/14/145703.
- [5] H. P. Huber *et al.*, "Calibrated nanoscale capacitance measurements using a scanning microwave microscope," *Rev. Sci. Instrum.*, vol. 81, no. 11, 2010, doi: 10.1063/1.3491926.
- [6] J. Hoffmann, M. Wollensack, M. Zeier, J. Niegemann, H. P. Huber, and F. Kienberger, "A calibration algorithm for nearfield scanning microwave microscopes," *Proc. IEEE Conf. Nanotechnol.*, pp. 1–4, 2012, doi: 10.1109/NANO.2012.6322116.
- [7] T. Le Quang, D. Vasyukov, J. Hoffmann, A. Buchter, and M. Zeier, "Fabrication and Measurements of Inductive Devices for Scanning Microwave Microscopy," pp. 1–5.
- [8] A. Buchter *et al.*, "Scanning microwave microscopy applied to semiconducting GaAs structures," *Rev. Sci. Instrum.*, vol. 89, no. 2, 2018, doi: 10.1063/1.5015966.
- [9] A. Karbassi, D. Ruf, A. D. Bettermann, C. A. Paulson, and D. W. Van Der Weide, "Quantitative scanning near-field microwave microscopy for thin film dielectric constant measurement," *Rev. Sci. Instrum.*, vol. 76, 2008, doi: 10.1063/1.2953095.
- [10] A. A. Volinsky, D. F. Bahr, M. D. Kriese, N. R. Moody, and W. Gerberich, "Nanoindentation Methods in Interfacial Fracture Testing," *Compr. Struct. Integr.*, pp. V8-3-V8-42, 2023, doi: 10.1016/B978-0-12-822944-6.00157-2.
- [11] T. Le Quang, A. C. Gungor, D. Vasyukov, J. Hoffmann, J. Smajic, and M. Zeier, "Advanced Calibration Kit For Scanning Microwave Microscope : Design , Fabrication and Measurement," 2020, doi: 10.1063/5.0032129.
- [12] S. Cular and D. Ph, "The Measurement and Uncertainty of Air Dielectric Capacitors from 1 kHz to 10 MHz," no. 2011, 2015.
- [13] F. Wang *et al.*, "Quantitative impedance characterization of sub-10 nm scale capacitors and tunnel junctions with an interferometric SMM," *Nanotechnology*, vol. 25, no. 40, 2014, doi: 10.1088/0957-4484/25/40/405703.
- [14] M. Kasper *et al.*, "Metal-oxide-semiconductor capacitors and Schottky diodes studied with scanning microwave microscopy at 18GHz," *J. Appl. Phys.*, vol. 116, no. 18, 2014, doi: 10.1063/1.4897922.
- [15] L. Crouzier *et al.*, "Development of a new hybrid approach combining AFM and SEM for the nanoparticle dimensional metrology," *Beilstein J. Nanotechnol.*, vol. 10, pp. 1523–1536, 2019, doi: 10.3762/bjnano.10.150.
- [16] S. Ducourtieux and B. Poyet, "Development of a metrological atomic force microscope with minimized Abbe error and differential interferometer-based real-time position control," *Meas. Sci. Technol.*, vol. 22, no. 9, 2011, doi: 10.1088/0957-0233/22/9/094010.
- [17] P. Klapetek, D. Nečas, and C. Anderson, "Gwyddion User Guide (gwyddion.net/documentation/user-guide-en)," 2021, [Online]. Available: [gwyddion.net/documentation/user-guide-en](http://gwyddion.net/documentation/user-guide-en).
- [18] JCGM, "Evaluation of measurement data — Guide to the expression of uncertainty in measurement," *JCGM 100*, 2008.
- [19] S. M. Sze and K. K. Ng, *Physics of Semiconductor Devices*, 3rd ed. John Wiley & Sons, Inc., 2007.
- [20] C. Bulucea, "Recalculation of Irvin's resistivity curves for diffused layers in silicon using updated bulk resistivity data," *Solid State Electron.*, vol. 36, no. 4, pp. 489–493, 1993, doi: 10.1016/0038-

- 1101(93)90257-Q.
- [21] F. M. Smits, "Measurement of Sheet resistivities with the Four-Point probe," *bell Syst. Tech. J.*, pp. 711–718, 1958.
- [22] M. D. Janezic, U. Arz', S. Begley, and P. Bartley, "Improved permittivity measurement of dielectric substrates by use of the TE<sub>111</sub> mode of a split-cylinder cavity," *73rd ARFTG Microw. Meas. Conf. Spring 2009 - Pract. Appl. Nonlinear Meas.*, pp. 1–3, 2009, doi: 10.1109/ARFTG.2009.5278066.
- [23] K. P. Mentor, *Defects in SiO<sub>2</sub> and related dielectrics: Science and Technology*. .
- [24] G. J. Sloggett, N. G. Barton, and S. J. Spencer, "Fringing fields in disc capacitors," *J. Phys. A. Math. Gen.*, vol. 19, no. 14, pp. 2725–2736, 1986, doi: 10.1088/0305-4470/19/14/012.
- [25] J. R. Nagel, "Numerical solutions to poisson equations using the finite-difference method [Education Column]," *IEEE Antennas Propag. Mag.*, vol. 56, no. 4, pp. 209–224, 2014, doi: 10.1109/MAP.2014.6931698.
- [26] E. Holzbecher and H. Si, "Accuracy Tests for COMSOL -and Delaunay Meshes Accuracy Tests for COMSOL - and Delaunay Meshes," no. January, 2015.
- [27] C. Geuzaine and J.-F. Remacle, "GMSH Reference Manual," 2020.
- [28] S. Weyer, H. Riesch-oppermann, and A. Fr, "Automatic finite element meshing of planar Voronoi tessellations," vol. 69, pp. 945–958, 2002.
- [29] S. W. Cheng, T. K. Dey, and J. R. Shewchuk, "Delaunay mesh generation," *Delaunay Mesh Gener.*, pp. 1–386, 2012, doi: 10.1201/b12987.
- [30] S. H. Lo, "Finite element mesh generation and adaptive meshing," *Prog. Struct. Eng. Mater.*, vol. 4, no. 4, pp. 381–399, 2002, doi: 10.1002/pse.135.
- [31] J. Schöberl, "An advancing front 2D/3D-mesh generator based on abstract rules," *Comput. Vis. Sci.*, vol. 1, no. 1, pp. 41–52, 1997, doi: 10.1007/s007910050004.
- [32] Multiphysics CO., "Comsol multiphysics reference manual. COMSOL." p. 1084, 2023.
- [33] A. Logg, K.-A. Mardal, and G. Wells, "Automated solution of differential equations by the finite element method. [electronic resource] : the FEniCS book," *Lect. notes Comput. Sci. Eng.* 84, 2012, [Online]. Available: <http://libezp.lib.lsu.edu/login?url=http://search.ebscohost.com/login.aspx?direct=true&db=c at00252a&AN=lalu.4056828&site=eds-live&scope=site&profile=eds-main%5Cnhttp://libezp.lib.lsu.edu/login?url=http://dx.doi.org/10.1007/978-3-642-23099-8>.
- [34] C. Geuzaine and J. F. Remacle, "Gmsh: A 3-D finite element mesh generator with built-in pre- and post-processing facilities," *Int. J. Numer. Methods Eng.*, vol. 79, no. 11, pp. 1309–1331, 2009, doi: 10.1002/nme.2579.
- [35] F. Piquemal, J. Morán-Meza, A. Delvallée, D. Richert, and K. Kaja, "Progress in Traceable Nanoscale Capacitance Measurements Using Scanning Microwave Microscopy," *Nanomaterials*, vol. 11, no. 820, 2021, doi: doi.org/10.3390/nano11030820.
- [36] J. Goldstein *et al.*, *Scanning Electron Microscopy and X-Ray Microanalysis*. 2003.
- [37] D. et al. Lange, "CNS STANDARD OPERATING PROCEDURE 055 Ultra55, Ultra Plus and Supra55VP FESEM," 2015.

---

## Chapter 3 Modified Short Open Load calibration

### Chapter 3 Modified Short Open Load calibration 79

1	<i>System description</i> .....	80
1.1	Probe holder .....	80
1.2	Interferometric system .....	81
1.3	VNA characterization .....	82
2	<i>Self-calibration</i> .....	83
2.1	Method description .....	83
2.2	Far parts contribution .....	86
2.3	Uncertainty budget.....	87
3	<i>Calibration robustness</i> .....	89
3.1	System of coordinate .....	89
3.2	Impact of location .....	90
3.3	Comparison between the two reference structures.....	91
3.4	Tip shape contribution .....	95
3.4.1	Shielded probe .....	95
3.4.2	Tip geometries .....	97
3.4.3	Tip coating .....	98
3.5	Simulation .....	98
3.5.1	Configuration .....	99
3.5.2	Self-calibration .....	101
3.5.3	Water meniscus evaluation .....	101
4	<i>Application – measurement on high-k sample</i> .....	104
4.1	Sample description .....	104
4.2	Dielectric constant evaluation .....	106
5	<i>Conclusion</i> .....	110



As mentioned before, techniques using the VNA for impedance measurements need to be calibrated. In this chapter, a modified Short Open Load (mSOL) calibration workflow is described.

# 1 System description

The SMM used at LNE is a Keysight Technologies 5600LS AFM interfaced with a N5230C VNA. The AFM is placed on an active anti-vibration table inside a glove box workstation (MBraun) under a nitrogen atmosphere at room temperature and dry conditions (relative humidity below 1 %) as shown in Figure 3-1.

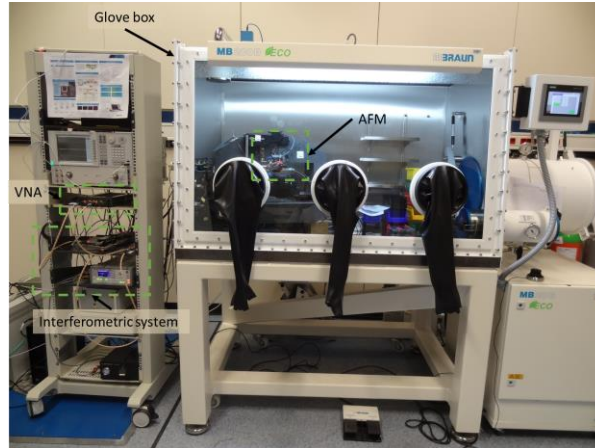


Figure 3-1. Experimental setup for SMM measurement at LNE

The whole set-up is installed in a shielded room fitted with a controlled air conditioning system. An interferometric system is implemented in the RF transmission line to increase the sensibility of the experiment.

## 1.1 Probe holder

The AFM probe is supported by the Keysight probe holder, thereafter referred to nose cone. It was designed to hold a conductive AFM tip. Figure 3-2 shows a full platinum AFM probe (300Pt12 B from Rocky Mountain Nanotechnology, USA) mounted on the Keysight nose cone. The chip shield (blue transparent element) has been made transparent on this picture to show the underneath RF contact between the transmission line and the SMM probe.

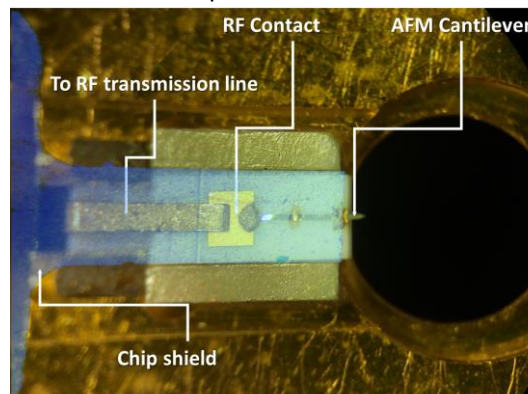


Figure 3-2. AFM probe 300Pt12B (Rocky Mountain Nanotechnology, USA) mounted on the Keysight nose cone.

This element has a shielding function as well as a mechanical support function. The AFM probe is inserted between the guide rails up until the point where the metallic tongue is centered on the probe RF contact. To ensure good mechanical holding, a 25  $\mu\text{m}$  thick layer of conductive steel was placed between the AFM probe and the nose cone. It also bring the chip closer to the RF metallic tongue,

ensuring good electric contact. Figure 3-3 shows a frequency sweep obtained with a tip-sample distance of 20  $\mu\text{m}$  and in contact with the sample. It can be noted that as the tip sample distance is decreased, the impedance between those two elements changes leading to a change in the frequency of resonance. To compensate this deviation, the excitation frequency of the VNA is shifted to lower value by 20 kHz below the one obtained in the frequency sweep above the sample.

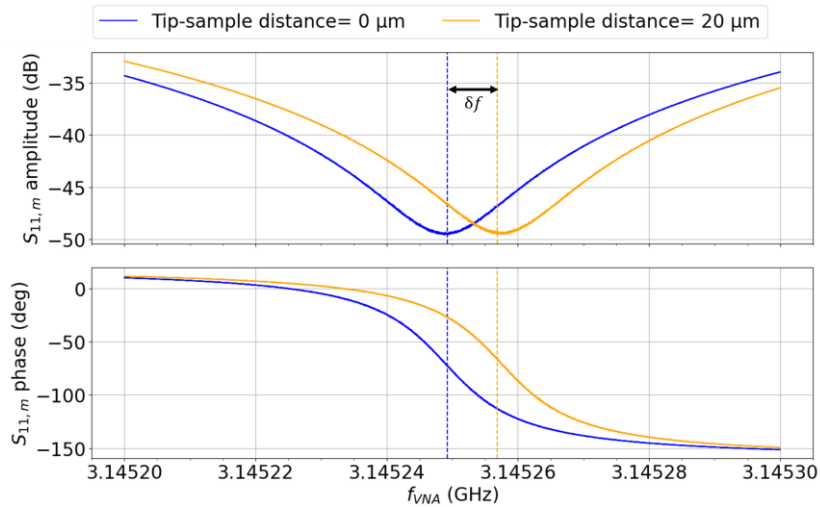


Figure 3-3. Frequency sweep obtained for the SMM tip in contact (blue curve) and 20  $\mu\text{m}$  (orange curve) above the thickest terrace on the MC2 calibration kit (v1, A64). A difference of 7.6 kHz is shown in the resonance frequency between the two configurations

A different nose cone was latter developed to manage a specific type of shielded SMM probe (PrimeNano) and is detailed in section 3.4.1.

## 1.2 Interferometric system

To improve the number of available adaptation peak and their associated quality factor, a Mach-Zehnder interferometric system is set in between the VNA and the AFM [1]. Having a higher quality factor improves the sensibility of the SMM measurement.

It is presented in Figure 3-4. The RF signal is split by a coaxial divider (model 11636B: DC – 26.5 GHz, power divider) in two part, one is kept as reference in two programmable step attenuators (model 84904K: DC – 26.5 GHz, 22 dB attenuation total range) in the attenuator, the other being send to the AFM tip by a coaxial cable. Then the reflected signal is coupled with the reference one by two directional couplers (model 87300C: 1 GHz – 26.5 GHz) forming an interferometric pattern that is amplified by a gain of 25 dB (model 83017A: 0 GHz – 26.5 GHz) before being read by the VNA. The attenuator parameters are adjusted to keep the interferometric pattern within the linear range of the VNA.

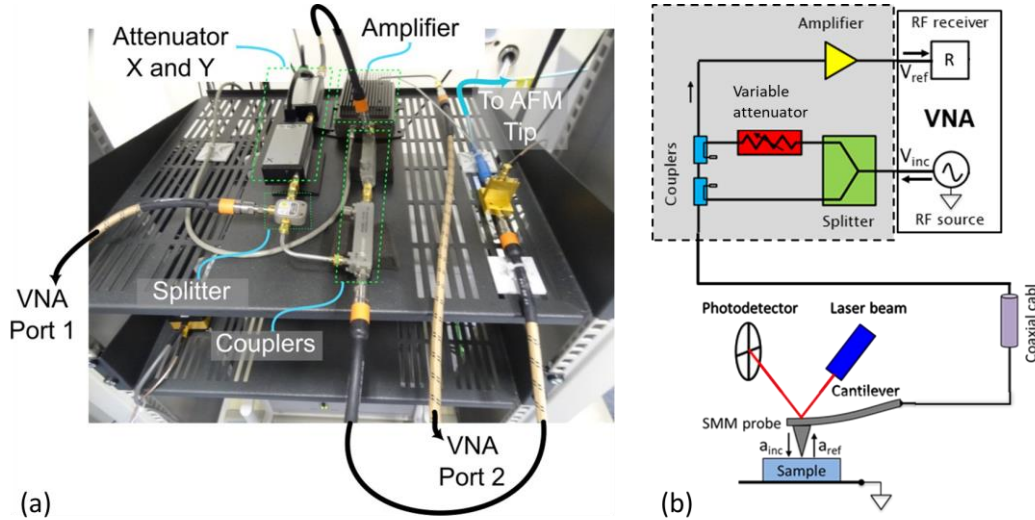


Figure 3-4. (a) Interferometric system implemented in the LNE's setup. (b): Schematic of the whole setup

In this configuration, the measured parameter is the transmitted signal between the port 1 and 2 ( $S_{21}$ ). Nevertheless, if we consider only the sample it corresponds to the reflection parameter as shown in Figure 3-4.b. Therefore, we will refer to the measured parameter as  $S_{11}$  parameter.

### 1.3 VNA characterization

In chapter 1, the VNA was presented as well as its key figure. The noise floor, trace noise of the VNA as well as the noise of the complete system (VNA and matching network) were measured [2]. The VNA Tools framework [3] with two short circuit standards (HP850552-60006 and MMC8047F F791) were used to measure the noise floor and trace noise. The matching network noise ( $N_M$ ) was computed using Equation 3-1.

$$N_M = \sqrt{N_C^2 - N_{VNA}^2} \quad \text{Equation 3-1.a}$$

$$N_{VNA} = \sqrt{N_F^2 + (N_{TA}^2 + N_{TP}^2)|S_m|^2} \quad \text{Equation 3-1.b}$$

where  $N_C$  is the noise of the complete setup (VNA and matching network) and  $N_{VNA}$  is the noise of the sole VNA. The resonance peak frequency ( $f_0$ ) of the  $S_{11}$  parameter is recorded as the tip-sample distance is increased (Figure 3-5).  $f_0$  increases with the tip-sample distance before reaching a plateau at a distance of 1 mm. To emancipate from the sample interaction, the noise of the complete setup is evaluated at this tip-sample distance of 1 mm.

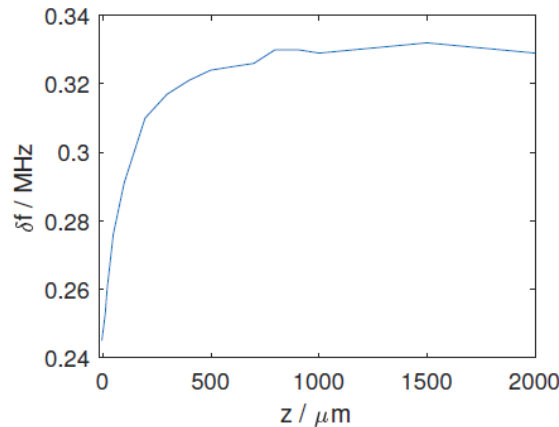


Figure 3-5. Resonance peak frequency of the  $S_{11}$  parameter as a function of the tip-sample distance

The gain of the setup is evaluated on a capacitive calibration sample (A64) by Equation 3-2.

$$G = \frac{|S_1 - S_2|}{|Y_1 - Y_2|} \quad \text{Equation 3-2}$$

where  $Y_n$  represents the two different measured admittances on the sample using the process detailed in section 2, whereas  $S_n$  stands for the  $S_{11}$  parameter measured at the respective standard. The different results are reported in Table 3-1.

Table 3-1. Measured noise and gain the matching network and noise of the VNA.

Frequency (GHz)	2.13	4.54	5.42	13.81	15.89	18.94
VNA noise (dB)	-94.77	-93.99	-94.70	-95.68	-95.92	-95.92
Matching network noise (dB)	-65.60	-59.67	-64.05	-65.34	-72.72	-67.69
Signal-to-noise ratio (dB)	152.4	162.3	189.5	123.5	152.0	135.3
Gain ( $S^{-1}$ )	310.8	736.6	897.1	4018.6	9504.7	7906.6

The higher the frequency, the higher the gain per Siemens allowing a better contrast in the  $S_{11,m}$  maps. In counterpart, the noise of the whole setup for  $S_{11}$  measurement is increased. Those results were compared to setup from different laboratories [2]. The key figures are presented in Table 3-2.

Table 3-2. Comparison between impedance matching network with and without interferometer [2]

Setup	Without interferometer (University of Lille)	With interferometer (LNE)
Price	Low	High
VNA Port	One-port	Two-port
Gain adjustable	No	Yes
Frequency adjustable	Single points	Whole frequency range of the VNA
Signal-to-noise ratio	127 dB	152 dB
Stability	-75 dB/h	-60 dB/h

Having an interferometric system in the transmission line allow for higher signal-to-noise ratio, more available frequency to probe the sample but it comes to the cost of higher price and degraded stability due to a more complex system.

## 2 Self-calibration

In chapter 2, the reference structures were described as well as the uncertainty budget associated with their capacitor evaluation. Here, a focus is shone on the SMM calibration method relying on those reference structure. In the next chapter, a second calibration method will be presented relying on the acquisition of  $dC/dz$  curve.

### 2.1 Method description

The SMM was calibrated on a capacitance standard sample using three different capacitance values by applying a method adapted from the Short Open Load method described in Chapter 1. An amplitude and phase image of the A64 calibration sample (MC2, v1) is shown on Figure 3-6.

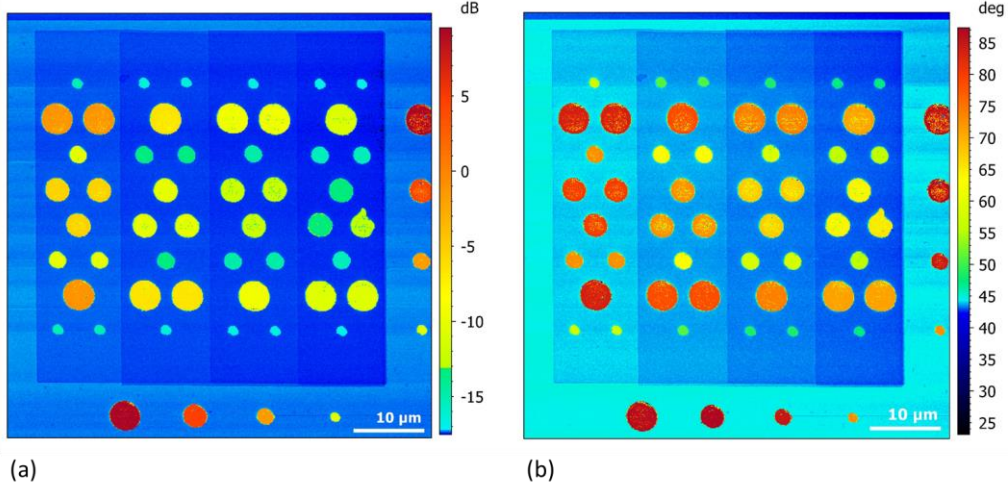


Figure 3-6. raw  $S_{11,m}$  amplitude (a) and phase (b) image acquired on A64 sample with the setup described in section 1

The image is then treated to remove the measurement artifacts. The following algorithm is applied to the  $S_{11,m}$  amplitude and phase by Gwyddion [4].

- All features were manually masked.
- The polynomial background was removed.
- The mean background was subtracted.
- All masks were deleted.
- Pads were masked by a watershed algorithm ([5]).
- Parts of the mask not belonging to the pads are removed by size filtering the grains.
- Mask was dilated to encapsulate every pixel belonging to the pads.
- Each terrace was isolated by cropping.
- The histogram of each terrace background (pads excluded) was produced.
- If multiple peaks are presented in the histogram, a polynomial align row algorithm is applied.
- The mean background was subtracted for each terrace (described in the next section).
- The average value of each terraces is set at zero.
- Terraces were merged.

Then, the  $S_{11,m}$  amplitude and phase as well as the mask associated with the different pads were saved. Three capacitors were selected for the calibration. As the used calibration method is inspired by the SOL method but uses three load reference instead of a Short, an Open and a Load reference, it is named modified Short-Open-Load calibration (mSOL) method. To proceed to the calibration, the ideal  $S_{11}$  associated to each reference capacitor were computed using Equation 3-3.a. The mapping function from the  $S_{11,m}$  to the calibrated  $S_{11}$  is described in Equation 3-3.b.

$$S_{11} = \frac{Z_S - Z_0}{Z_S + Z_0} \quad \text{Equation 3-3.a}$$

$$S_{11} = \frac{S_{11,m} - e_{00}}{e_{01} + e_{11}(S_{11,m} - e_{00})} \quad \text{Equation 3-3.b}$$

The error parameters ( $e_{ij}$ ) of the mSOL are computed by solving the Equation 3-4.

$$X = A^{-1}B \quad \text{Equation 3-4.a}$$

$$X = \begin{bmatrix} e_{00} \\ e_{01} - e_{00}e_{11} \\ e_{11} \end{bmatrix} \quad \text{Equation 3-4.b}$$

$$A = \begin{bmatrix} n_{cal} & \sum_{i \in [cal]} S_{11|i} & \sum_{i \in [cal]} S_{11|i} \cdot S_{11,m|i} \\ \sum_{i \in [cal]} S_{11|i} & \sum_{i \in [cal]} S_{11|i}^2 & \sum_{i \in [cal]} S_{11|i}^2 \cdot S_{11,m|i} \\ \sum_{i \in [cal]} S_{11|i} \cdot S_{11,m|i} & \sum_{i \in [cal]} S_{11|i}^2 \cdot S_{11,m|i} & \sum_{i \in [cal]} S_{11|i}^2 \cdot S_{11,m|i}^2 \end{bmatrix} \quad \text{Equation 3-4.c}$$

$$B = \begin{bmatrix} \sum S_{11,m|i} \\ \sum S_{11|i} \cdot S_{11,m|i} \\ \sum S_{11|i} \cdot S_{11,m|i}^2 \end{bmatrix} \quad \text{Equation 3-4.d}$$

where the  $S_{11}$  are summed over the ones considered for calibration. Then, using equation Equation 3-3.b, the calibrated  $S_{11}$  is evaluated for each capacitor of the image.

Having an xy image of the calibration structure means that the  $S_{11,m}$  is evaluated at each pixel of the image. Therefore, the  $S_{11,m}$  associated to each pad is not a single value but instead a distribution as shown in Figure 3-7. To select the most representative  $S_{11,m}$  value, an histogram is acquired for each pad with a 0.025 dB resolution for the amplitude and 0.025° resolution for the phase. Then, the  $S_{11,m}$  value associated with the pad is selected from a Gaussian fit performed by Matlab of the histogram.

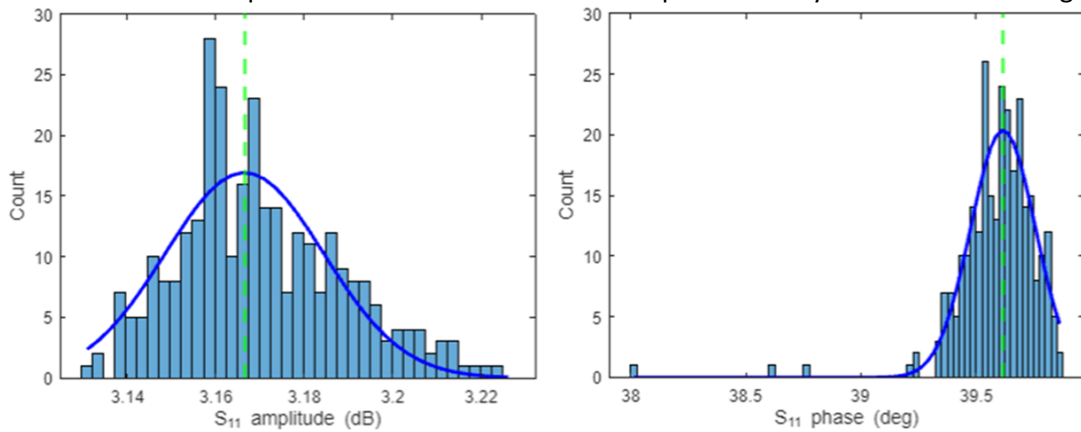


Figure 3-7.  $S_{11,m}$  amplitude and phase histograms associated with the pad 5

The outliers were removed by using the generalized extreme studentize deviate outlier removal procedure from Matlab [6]. Images of the capacitance obtained from the calibrated  $S_{11}$  is shown in Figure 3-8 as well as the relative deviation between the measured and simulated capacitance (Chapter 2) for each MOS capacitor.

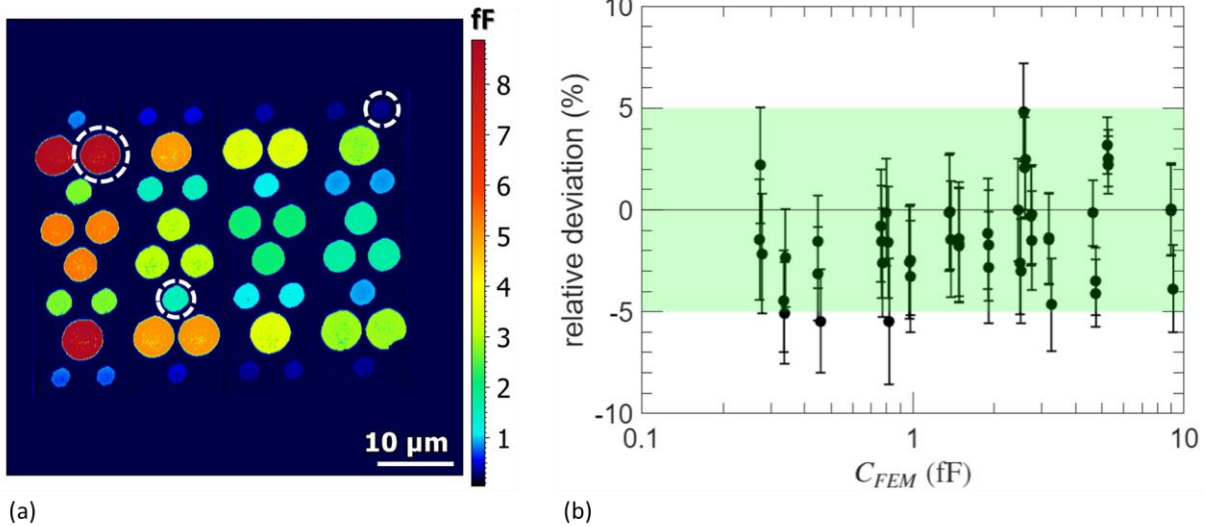


Figure 3-8. (a) Capacitance map of A64 calibration standard computed from the  $S_{11}$  map calibrated by the mSOL method applied to the circled pads. (b) Relative deviation between the measured and simulated value of the capacitance structure (in %)

In Figure 3-8.b, a good agreement is found at the 5% level. The evaluation of the uncertainty bars will be detailed in an upcoming part (2.3). The triplet of reference were choice to cover the whole range of capacitance present on the calibration sample. One of the reference capacitance is selected among the largest pad of the thinnest  $\text{SiO}_2$  terrace, another among the smallest pad on the thickest  $\text{SiO}_2$  layer and the last one on of the intermediate plateau. To minimize cross talk, the reference capacitance are selected as far as possible from each other.

## 2.2 Far parts contribution

The AFM probe used has a nominal apex radius ( $R$ ) below 100 nm, a nominal cone height ( $h_{\text{cone}}$ ) of 80  $\mu\text{m}$  with an opening angle of  $10.5^\circ$ . When projecting this cone on the sample surface, it forms a circle with a radius of 20  $\mu\text{m}$ . The projected area of the cantilever is even larger with a rectangle of 110  $\mu\text{m}$  by 300  $\mu\text{m}$  side. To ensure the sub-micrometric resolution of the instrument, precaution must be taken. Evidence will be shown that a substitution method can be used to deal with the cantilever and cone contribution to the capacitance. The ideal situation would be to use an AFM tip with a shielded cantilever and cone. A test has been conducted with a commercially available AFM tip with a shielded cantilever and is presented in Section 3.4.1.

The projected cone area on the MC2 A64 sample is shown Figure 3-9.a. A scheme of the capacitances between the different AFM parts and the sample is shown in the case where the tip is positioned at the center of an electrode (Figure 3-9.b) or lies outside the area of an electrode (Figure 3-9.c). For now on, the cantilever-sample and cone-sample capacitances in the configuration where the tip is located on top of an electrode will be noted  $C_{x,b}$  and  $C_{x,c}$  when the tip is in the neighborhood of the pad, where  $x$  can be cantilever or cone.

The total capacitance between the AFM tip and the back electrode of the sample in both configurations are given by Equation 3-5.

$$C_{\text{tot},b} = C_{\text{cantilever},b} + C_{\text{cone},b1} + C_{\text{cone},b2} + C_{\text{ox},b} \quad \text{Equation 3-5.a}$$

$$C_{\text{tot},c} = C_{\text{cantilever},c} + C_{\text{cone},c1} + C_{\text{cone},c2} + C_{\text{apex},c} \quad \text{Equation 3-5.b}$$

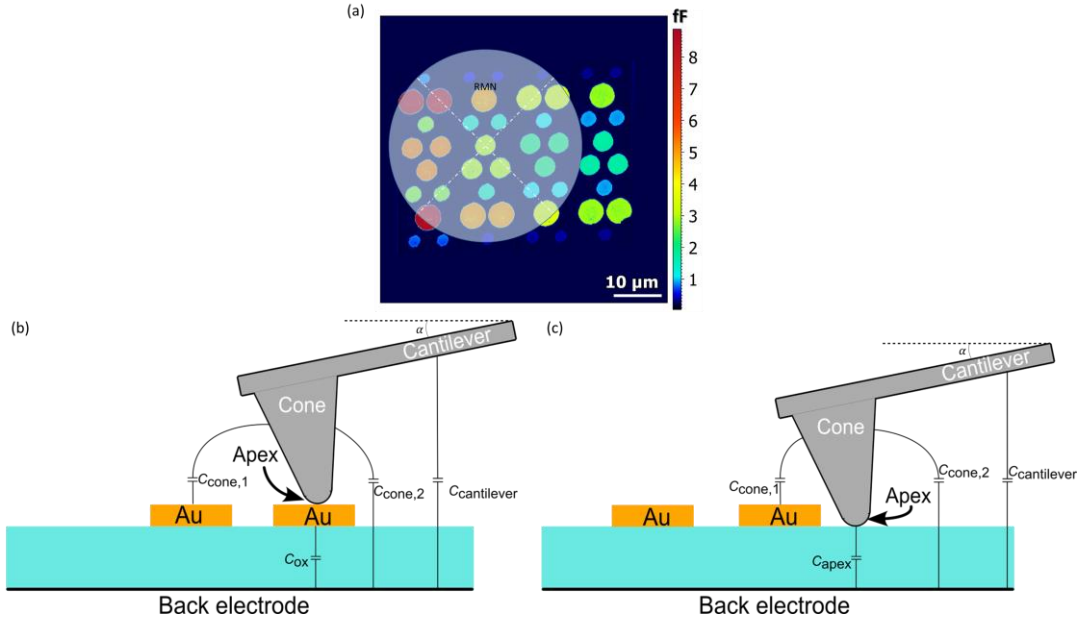


Figure 3-9. (a) Projection of the cone of the RMN AFM tip; Parasitic capacitances when the tip is centered (b) or off-centered (c) with respect to the top electrode.

The AFM probe cone's height is of 80  $\mu\text{m}$  while the one of the gold pad is of 270 nm. The ratio between those two quantities is about 300. The capacitance between the AFM tip cantilever and the sample can then be considered constant for the whole scan area ( $C_{\text{cantilever},b} = C_{\text{cantilever},c}$ ). The capacitance between the AFM tip cone and the sample is a function of the dielectric layer thickness and the presence of top electrode on its side. Those will shield the field lines between the cone and the sample back electrode. In first approximation, the parasitic capacitance ( $C_{\text{cone}}$ ) doesn't change significantly between the two configurations ( $C_{\text{cone},b1} \cong C_{\text{cone},c1}$ ;  $C_{\text{cone},b2} \cong C_{\text{cone},c2}$ ). The impedance being directly linked to the  $S_{11}$  by Equation 3-3.a, it is then possible to remove the parasitic capacitances by subtracting the  $S_{11,m}$  associated with the pad neighborhood to the  $S_{11,m}$  of the pad. Practically, it is done by the subtraction of mean background of each terrace as described in section 2.1. This substitution method was first reported in [7].

## 2.3 Uncertainty budget

Once the instrument is calibrated, the uncertainty budget associated with the capacitance measurement can be computed (Table 3-3). The uncertainty associated with the SMM calibration comes from the experimental conditions (histograms quality, repeatability, presence of water meniscus and parasitic capacitances) and from the definition of the calibration kit itself ( $u_{\text{SMM}}$ ). The uncertainty associated with the histogram ( $u_{\text{hist},i}$ ) is defined as the full-width at half maximum (FWHM) of the histogram Gaussian distribution of the capacitance  $C_i$ . The repeatability uncertainty is evaluated from three series of measurements. The uncertainty associated with the SMM calibration ( $u_{\text{SMM},i}$ ) is computed from the standard deviation of the capacitance returned by the instrument calibrated using 27 different values for the triplets of reference [ $C_{\text{calc},1}$ ,  $C_{\text{calc},2}$ ,  $C_{\text{calc},3}$ ].  $C_{\text{calc},j}$  can here take the value  $C_{\text{tot},j}$ ,  $C_{\text{tot},j} - u_{\text{Ctot},j}$ ,  $C_{\text{tot},j} + u_{\text{Ctot},j}$ . The uncertainty from the residual influence of long distance capacitance is evaluated using the analytical expression for  $C_{\text{cantilever}}$ ,  $C_{\text{cone}}$ , and  $C_{\text{apex}}$  from [8]–[10] (Equation 3-6).

$$C_{\text{cantilever}}(z) = \epsilon_0 \frac{w}{\tan(\alpha)} \ln \left( 1 + \frac{l \cdot \tan(\alpha)}{H + z} \right) \quad \text{Equation 3-6.a}$$



$$C_{cone}(z) = -\frac{2\pi\epsilon_0}{\ln\left[\tan\left(\frac{\theta}{2}\right)\right]^2} \left[ \left(z + \frac{h}{\epsilon_r} + \tilde{R}\right) \ln\left(\frac{H}{z + \frac{h}{\epsilon_r} + \tilde{R}}\right) + \tilde{R} + R \frac{\cos^2(\theta)}{\sin(\theta)} \ln\left(z + \frac{h}{\epsilon_r} + \tilde{R}\right) \right] + c_1 \quad \text{Equation 3-6.b}$$

$$C_{apex} = 2\pi\epsilon_0 R \cdot \ln\left(1 + \frac{\tilde{R}}{z + \frac{h}{\epsilon_r}}\right) \quad \text{Equation 3-6.c}$$

where  $\alpha$  ( $13^\circ$ ) is the tilt angle of the cantilever,  $w$  ( $110 \mu\text{m}$ ) its width,  $l$  ( $300 \mu\text{m}$ ) its length,  $z$  the apex to sample distance,  $\theta$  ( $15^\circ$ ) is the cone half-angle,  $H$  ( $80 \mu\text{m}$ ) its height,  $R$  is the apex radius and  $\tilde{R} = R(1 - \sin(\theta))$ .

Table 3-3. Uncertainty budget associated with the capacitance measurement on MC2 capacitance standard (A64) performed by the calibrated SMM, [11]. Here, a high, intermediate and low value of MOS capacitors are presented covering the whole capacitance range of the structure.

	$C_{05}$	$C_{23}$	$C_{32}$
Capacitance (fF)	$(8.79 \pm 0.19)$	$(1.36 \pm 0.04)$	$(0.33 \pm 0.01)$
Type A uncertainty (%)	0.5	1.3	2.1
$u_{\text{hist},i}$	0.1	0.6	2.1
$u_{\text{rep},i}$	0.5	1.1	0.2
Type B uncertainty (%)	2.1	2.9	2.6
$u_{\text{SMM},i}$	2.1	2.9	2.5
$u_{\text{parastic}}$	0.02	0.18	0.72
$u_{\text{humidity}}$	0.2	0.2	0.2
$u_{\text{combined}}$ (%)	2.2	3.2	3.3

Here the shielding from the electrodes in the neighborhood is neglected. The four different terraces form a slope that needs to be considered as reducing the cantilever tilt angle  $\alpha_{\text{corr}} = \alpha - \alpha'$  as shown in Figure 3-10.

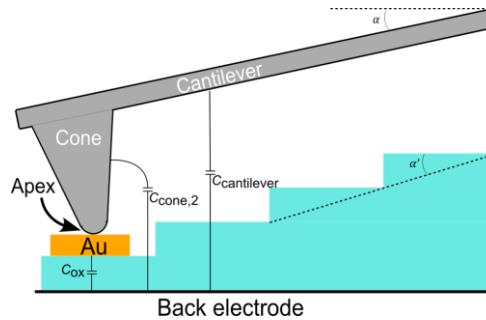


Figure 3-10. Tilt angle correction.

Finally, the water meniscus contribution was estimated by performing the calibration in four different experimental conditions corresponding to increasing  $RH$  starting at 0.9% up to 4%. The relative deviation between the measured and calculated capacitances is computed for each  $RH$  value. The average relative deviation for the whole structure is obtained for each relative humidity (Figure 3-11). It is of  $(0.17 \pm 0.46)\%$  for measurements at  $RH = 2\%$ ,  $(0.33 \pm 0.71)\%$  for  $RH = 2.9\%$  and  $(0.97 \pm 1.31)\%$  for  $RH = 4\%$ . In normal conditions, the SMM measurement is performed in the glove box with a relative humidity below 1%. A conservative uncertainty of 0.2% is considered for each pad. This value will be confirmed by numerical simulation (Section 3.5.3) and is in good agreement with the expected value of the capacitance generated by the water meniscus of a few attofarads [12]. Additional measurement on a capacitance standard showing smaller capacitor (below 100 aF) are planned to confirm those results.

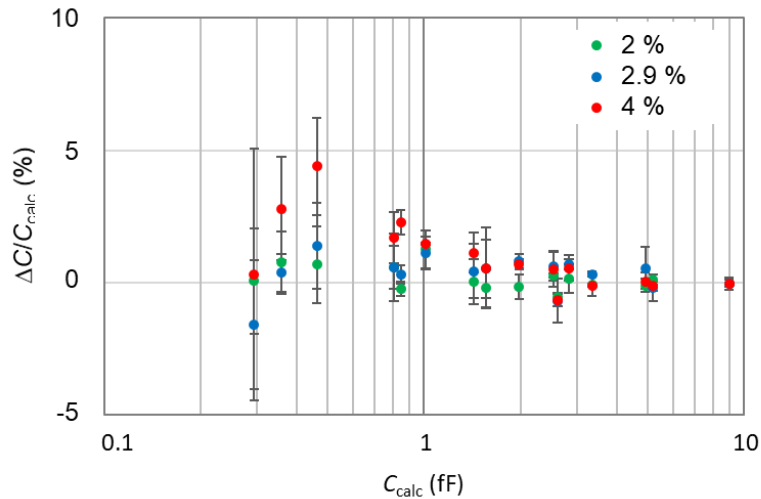


Figure 3-11. Relative differences between measured capacitances on the pattern A64-I05 at RH = 2%, 2.9% and 4% and capacitances measured at RH = 0.9%. Each marker represents the mean value of capacitances of 3 capacitors of same area and on same plateau. The error bars correspond to the standard deviation.

This demonstrates the possibility to calibrate the SMM for capacitance measurement with an associated uncertainty within 3.3 % without the use of a shielded probe.

## 3 Calibration robustness

The SMM calibration process has been described in the previous section. A study of its robustness to environmental electromagnetic noise will be conducted. Then the two versions of the calibration structure by MC2 will be compared, hence evaluating the validity of the substitution method. Finally, simulation work will be conducted to evaluate the sole impact of water meniscus on the calibration.

### 3.1 System of coordinate

In the following sections, a coordinate system is used to navigate the different calibration kit and is presented in Figure 3-12. In the first version, the MC2 calibration kits (A64, A61 and A45) are composed of 144 identical areas presenting 4 patterns (Figure 3-12.a) of 48 capacitors as reported in the Chapter 2. In this work, the upper left part of the area is scanned. The area is identified by its column (numbered from 1 to 12) and row (numbered A to L) as shown in Figure 3-12.b. For each pattern, the capacitors are labeled by number ranging from 1 to 48 (Figure 3-12.c)

In the second design, the calibration kit has 1600 identical patterns of 20 capacitors as presented in Chapter 2. The coordinate system for the area is the same as the first version with 40 columns (numbered from 1 to 20) and 40 lines (number from A to AN). The capacitors are label by number ranging from 1 to 20 (Figure 3-12.d).

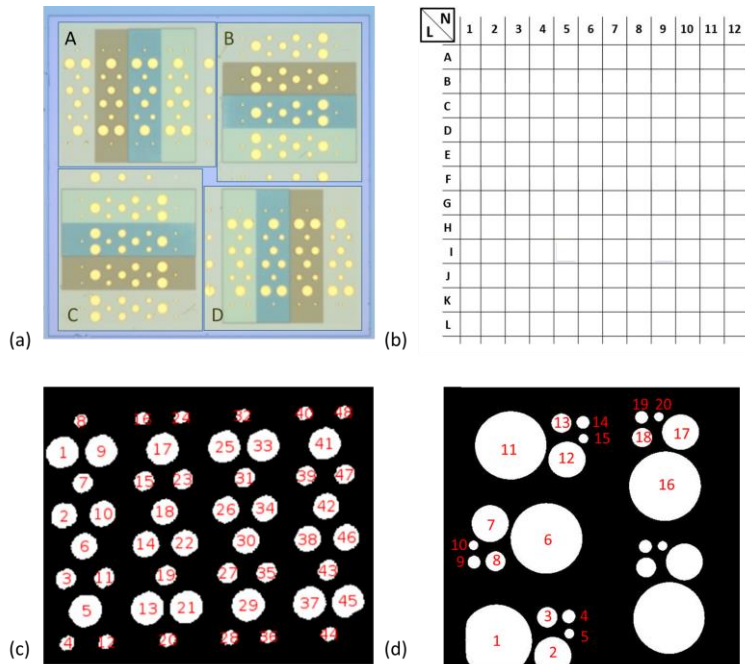


Figure 3-12. Coordinate system for MC2 calibration kit v1 (a) subdivision of area in pattern, (b) coordinate system for area, (c): capacitor label in MC2 calibration kit v1, (d): capacitor label in MC2 calibration kit v2

### 3.2 Impact of location

Five different patterns were measured with the SMM. The SMM was calibrated using a single pattern (G07) with the triplet (5; 13; 48) covering the whole capacitance range. The calibration was then applied to extract the capacitance of the other patterns. To ensure the stability of the calibration, the G07 pattern was measured before and after each test pattern. The relative difference between the computed and measured capacitances is computed (Figure 3-13.a).

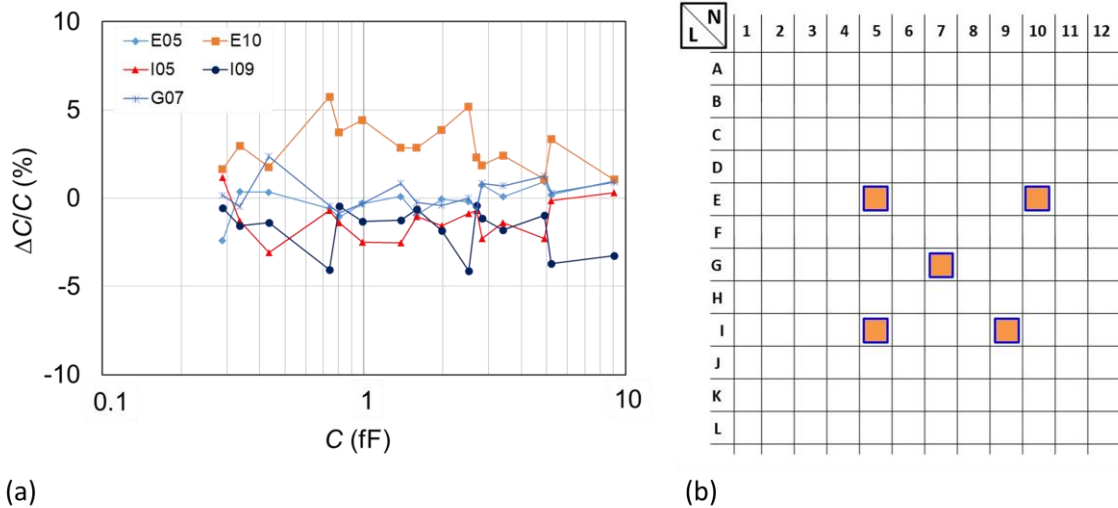


Figure 3-13. (a) Relative deviation between the computed and measured capacitance. SMM calibrated on the pattern G07. (b) Map of the A64 patterns.

A good agreement between the measured and expected values is found ( $\pm 2\%$ ) except for the E10 pattern ( $\pm 2.9\%$ ). These results tend to imply that the depletion capacitances and environmental electromagnetic noise are constant over the sample within a few percents.

### 3.3 Comparison between the two reference structures

Two different calibration samples of the first version were investigated. The instrument was calibrated on the first (A64 or A45) and used to measure the second (A61). The relative deviation between the measured capacitance between the two structures is computed by Equation 3-7.

$$\frac{\Delta C}{C_{FEM}} = \frac{C_{i,ref} - C_{i,A61}}{C_{i,FEM}} \quad \text{Equation 3-7.}$$

This relative deviation is evaluated for two different triplets of reference for the whole structure (Figure 3-14.a and b). This relative deviation increases almost linearly with  $C_{FEM}$  and its slope depends on the selected reference triplet (in bracket in the legend of Figure 3-14). For the 9 fF capacitances, a large deviation of 10% is found from the comparison between patterns A61F08 and A45E08.

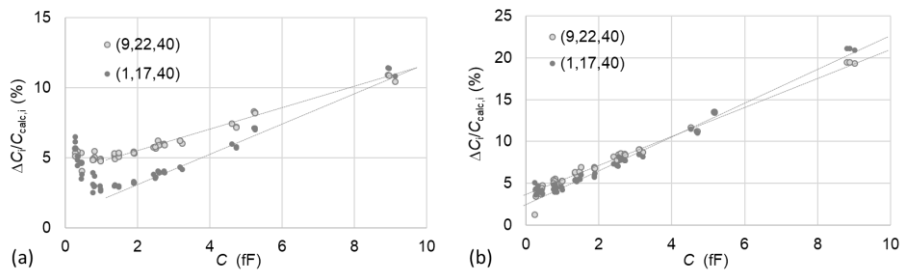


Figure 3-14. Difference  $\Delta C_i/C_{FEM,i}$  in percentage between the measured value on the calibration sample and the test sample. (a): Calibration sample: A45E08 test sample A61F08. (b): Calibration sample: A64F07 test sample A61E07.

The comparison between the patterns A61E07 and A64F07 shows an even larger deviation reaching 20%. It must be noted that the depletion capacitance values are again not considered here in the capacitance calculation since the p- doped Si substrates of samples A61, A45 and A64 present very close doping concentrations.

Another way to look at these data is to discriminate them by the thickness of the SiO<sub>2</sub> plateau (Figure 3-15). The calibration of the SMM is done on each plateau and then applied to the test sample. The triplet used for the calibration are the same for both calibration sample ([5,6,8]; [16,18,21]; [29,30,32]; [40,42,47]).

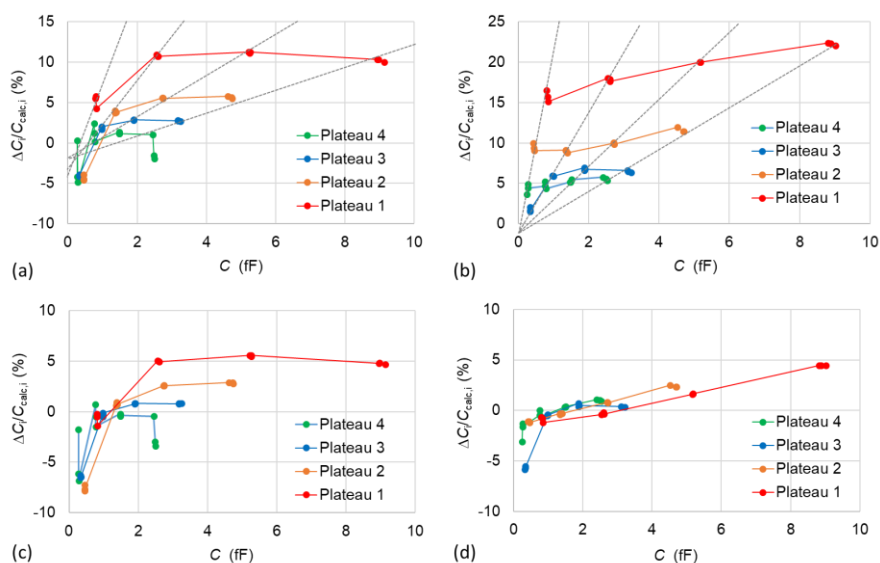


Figure 3-15. Difference  $\Delta C_i/C_{FEM,i}$  in percentage between the measured value on the calibration sample and the test sample treated per plateau. (a and c): Calibration sample: A45E08 test sample A61F08. (b and d): Calibration sample: A64F07 test sample A61E07. (a and b) raw difference, (c and d) difference corrected by a capacitance in serie  $C'$ .

On Figure 3-15. a and b, the raw deviation is presented. The highest deviation are observed for the thinnest plateau with maximal deviation above 10%. Such deviations cannot be explained by a difference of stray capacitances between the AFM tip and the samples due to different SiO<sub>2</sub> layer thicknesses. The stray capacitances do not create errors in the capacitance comparison at the level of 1%. By fitting linearly the capacitance values, which correspond to capacitors of same diameters, we find that the observed deviations can be explained by parasitic capacitors  $C'$  in series with the SiO<sub>2</sub> capacitors  $C$ . Their capacitances  $C'$  are given by Equation 3-8.

$$C' = \epsilon_0 \frac{A}{l} \quad \text{Equation 3-8.}$$

with  $A$  being the area of the top electrodes and a thickness  $l$  which differs between samples such that  $l_{A45} - l_{A61} = 0.67$  nm and  $l_{A64} - l_{A61} = 1.95$  nm. It must be noted that the fit on data for capacitors of the 1  $\mu$ m diameter in case of measurements on A61F08 has not been considered because of measurement uncertainties. The presence of native SiO<sub>2</sub> layers on the samples could cause such parasitic contributions. In these case, the afore-mentioned thickness differences would be multiplied by the value of the relative permittivity of SiO<sub>2</sub> ( $\epsilon_r = 3.9$ ) giving rise to thickness difference  $l_{A45} - l_{A61} = 2.61$  nm and  $l_{A64} - l_{A61} = 7.61$  nm. Typical native layer of SiO<sub>2</sub> are below 2 nm [13], well below the thickness needed to explain the deviation. Another explanation would be the difference in the dielectric constant of the SiO<sub>2</sub> layer for the two structures. Indeed, as described in Chapter 2, the dielectric constant was not measured but estimated from the literature with a 1% uncertainty.

Nevertheless, the native layer of SiO<sub>2</sub> layer is still present, to avoid this parasitic capacitances, the second version of calibration sample will be metalized on in back face.

A second comparison was latter conducted between the first (A64) and second (B03) version of calibration sample to validate the SMM calibration independence from geometry.  $S_{11,m}$  maps of two adjacent calibration samples were acquired. Due to the large area covered by the pattern of the second version, the  $S_{11,m}$  maps were acquired terrace by terrace with 35x35  $\mu$ m<sup>2</sup> scan area. The SMM calibration was performed on one of the calibration kit using four different triplets for the first version ([1,31,40]; [9,3,48]; [9,19,48]; [9,17,48]) and six for the second version ([1,2,5]; [1,3,5]; [1,4,5]; [2,3,5]; [2,4,5]; [3,4,5]). The calibration was then used to extract the capacitance on the test sample. The average relative deviation between the computed and measured value was then evaluated as shown in Figure 3-16.

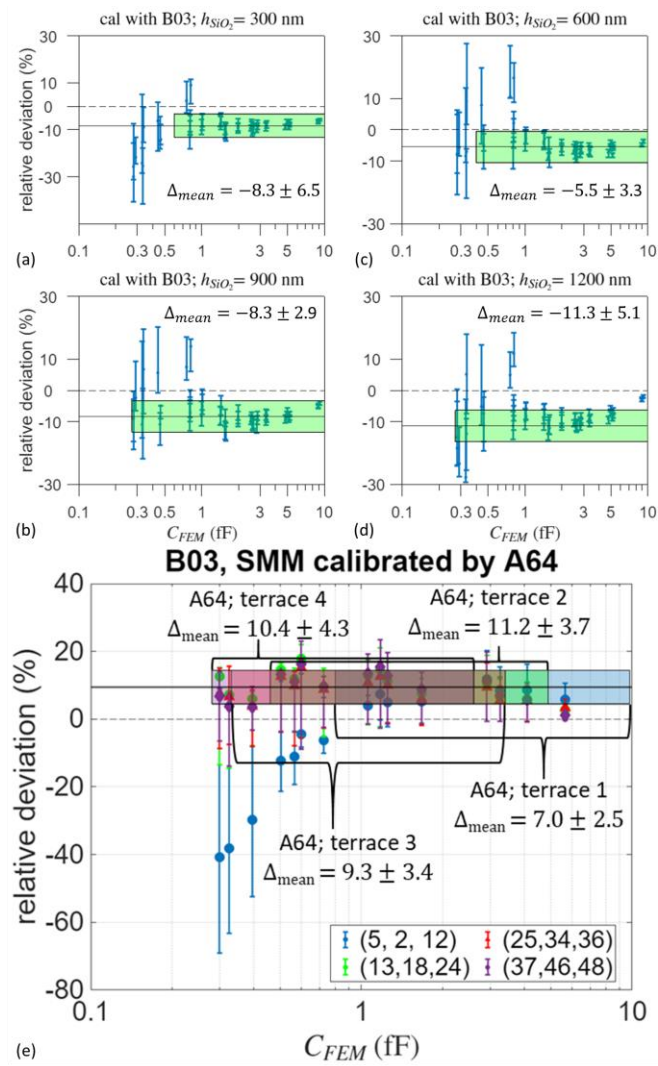


Figure 3-16. Difference  $\Delta C_i/C_{FEM,i}$  in percentage between the measured and calculated value on the test sample. Highlight area: validity range of the instrument calibration. (a to d): SMM calibrated on the different terraces of B03, (e): SMM calibrated on the different terraces of A64 sample.

The same operation was performed considering only the capacitance above and below 1 fF using the reference triplet [9; 29; 27] and [35; 20; 44] when A64 is used as reference and [1;2;3] and [3; 4; 5] when the reference is the thickest terrace on B03. The difference ( $\delta C$ ) between  $C_{FEM}$  and  $C_{exp}$  on the test sample is shown in Figure 3-17.

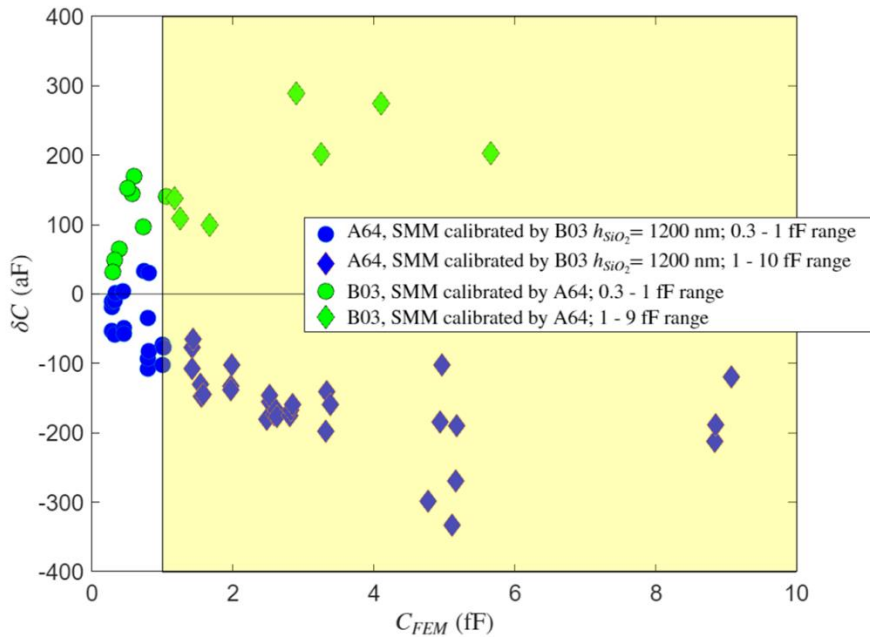


Figure 3-17. Difference between the computed and measured capacitance on the test sample.

A symmetry is visible between the two data sets, suggesting the existence of a parasitic capacitance. The absolute value of  $\delta C$  increases from 20 aF to 100 aF for the small capacitance and reaches a plateau at 200 aF for larger capacitance. It can be explained by the uncertainty on the dielectric constant between two  $SiO_2$  samples and a possible parasitic capacitance in series at the back of the structure. When considering only the capacitance above 1 fF, the averaged relative deviation is constant for the different terraces of the MC2, B03 standard (Figure 3-18).

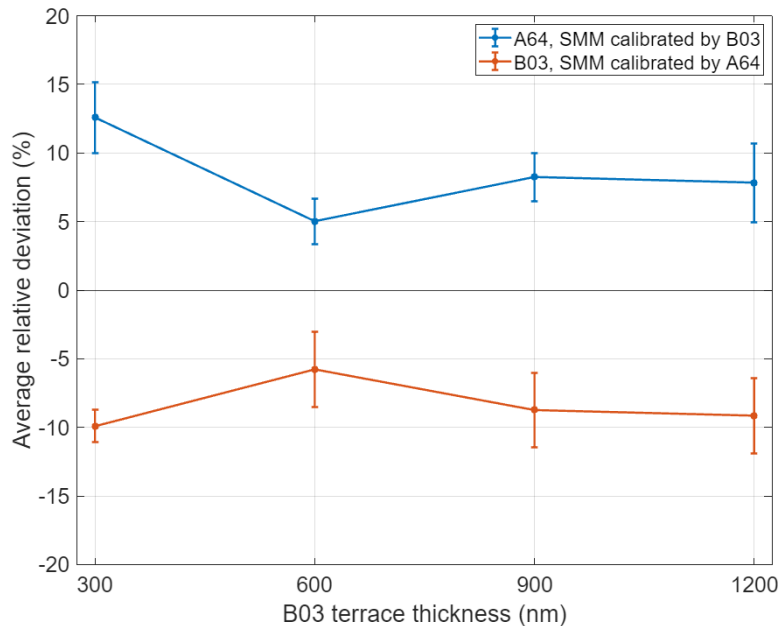


Figure 3-18. Averaged relative deviation between the computed and measured capacitance on the test sample as a function of the terrace of the B03 used for the calibration (blue curve) or the test (orange curve) measurement.

A symmetric pattern is visible in the relative deviation for the two test samples supporting the hypothesis of a systemic error.

Future work are planned to retake the measurement on those two sample after making sure they are in the same z-plane to minimize the scanner displacement. Measurement on the first reference standard will be acquired before and after scan on each terrace of the new calibration standard to

have a better control on the time deviation. Finally, in-situ measurement of the dielectric constant of the two reference standards will be done to affine the capacitance computation.

### 3.4 Tip shape contribution

The validity of the calibration method described in section 2 has been demonstrated for a tip geometry corresponding to the one of the RMN tip with a small cone opening angle and cantilever far of the surface due to high aspect ratio of the tip. Other conductive AFM tips are available and could be used to performed SMM measurement. A comparison between different available AFM tips is drawn in this section.

#### 3.4.1 Shielded probe

A commercial probe with a shielded cantilever [14] are produced by PrimeNano under the scanning microwave impedance microscopy (sMIM) denomination. A SEM image of the tip showing the cone and the shielded cantilever is presented in Figure 3-19.

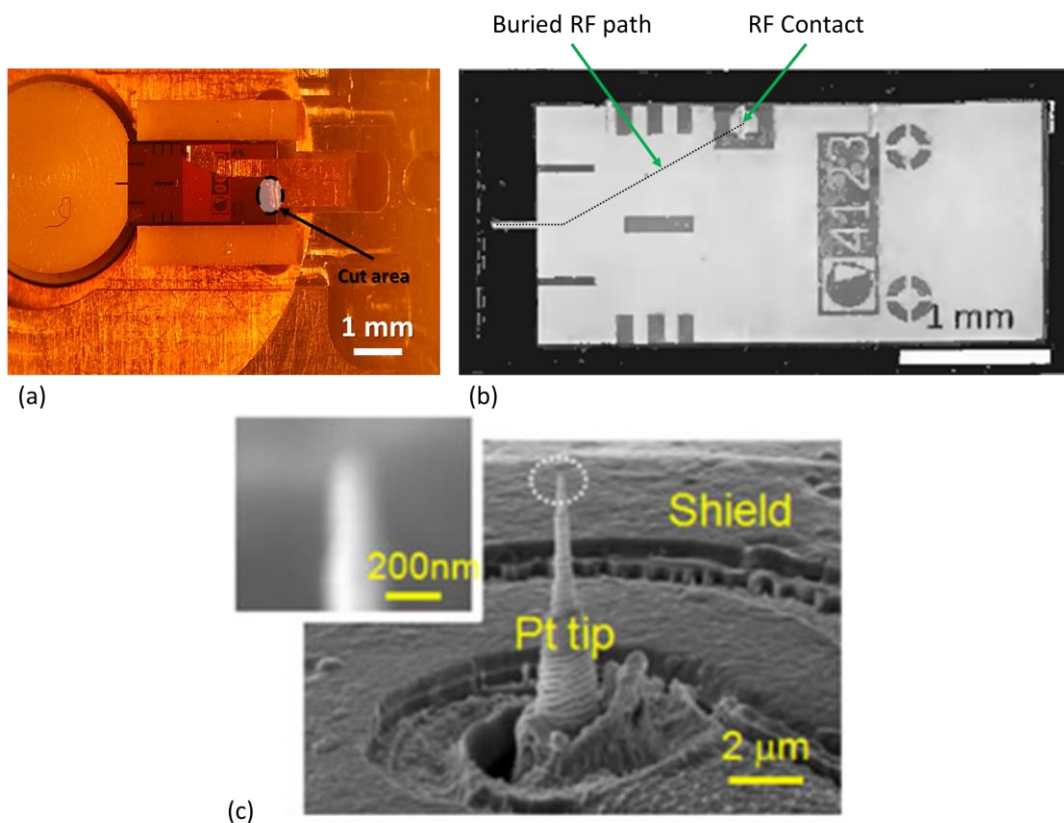


Figure 3-19. (a): Probe holder for sMIM configuration, (b) Optical microscope image of the sMIM probe. The RF signal is brought from the RF contact to the cone by a buried path (dashed black line). (c) SEM image of the shielded cantilever and cone of the AFM probe [14].

Due to the particular location of the RF contact on the side, the probe holder needs to be adapted. A second nose cone was manufactured by C&K Dole (Figure 3-19.a). The system had initially two tongues to ensure a good mechanical stability. One is connected to the RF contact of the AFM probe while the other is masked by an insulator to keep the cantilever shielded. This creates a parasitic capacitor within the probe holder generating an impedance mismatch. The issue was solved by cutting the second tongue as shown in Figure 3-19.a.

The sMIM probe was used to acquire a  $S_{11,m}$  map on the A64 calibration kit with an excitation frequency of 16.42 GHz. The mSOL calibration was conducted considering the raw  $S_{11,m}$  and treated by the



substitution method  $S_{11,m}$ . The relative deviation between the measured and computed capacitance for the two data set is shown in Figure 3-20.

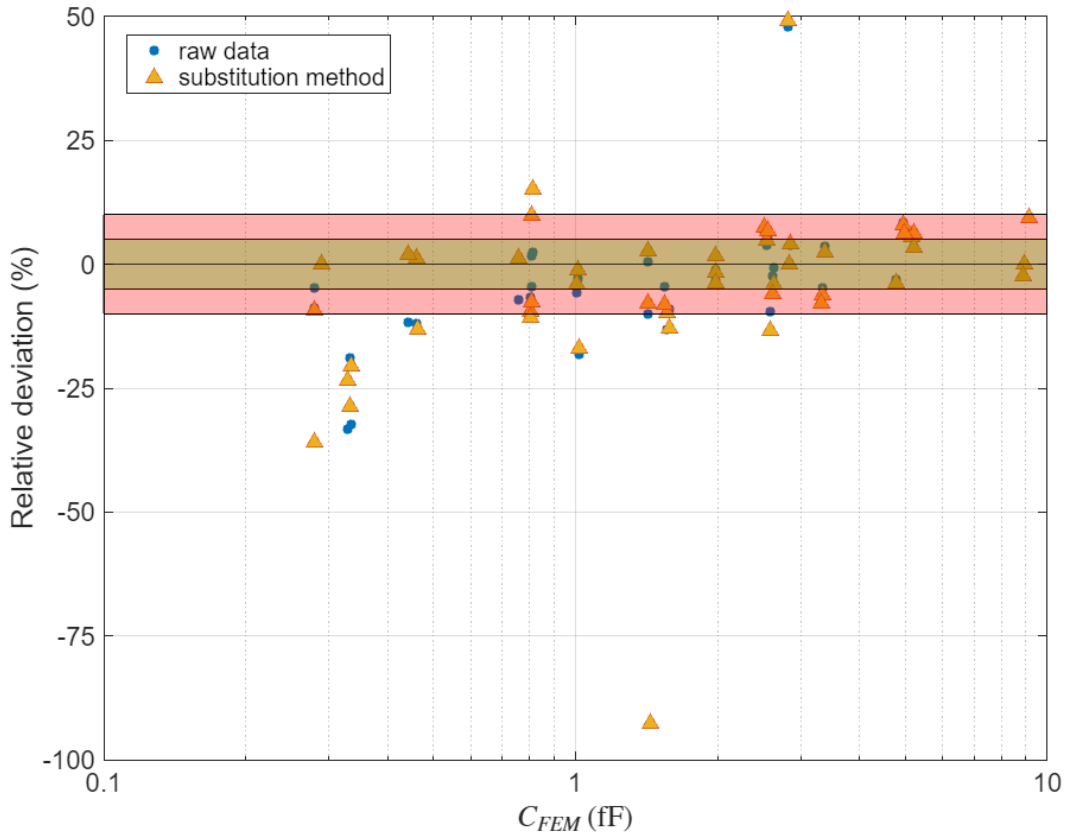


Figure 3-20. Relative deviation between the measured and computed capacitance as a function of the computed capacitance for the  $S_{11,m}$  raw (blue dots) and the  $S_{11,m}$  obtained after the substitution method (triangle).

No clear difference between the two data set is visible in this figure. This supports the efficiency of the cantilever shielding. A significant drop in performance is visible from previous measurement using the RMN probe. It can be explained by the non-perfect nose cone used. Fortified by this experience, a second version of the nose cone has been developed with better adaptation of the tongue. Nevertheless, the cone of the sMIM probe is left unshielded. While smaller than the one of the RMN tip ( $5\ \mu\text{m}$  instead of  $80\ \mu\text{m}$ ), its opening angle is larger ( $45^\circ$  instead of  $19.5^\circ$ ). This could lead to stronger cone-sample capacitance than the RMN tip originating from the MOS capacitor in the neighborhood. If it is the case, the RMN probe could show improved resolution while treated by the substitution method.

Another solution for shielding the cantilever would be to bring the RF signal to the cone by coplanar wave guide as proposed by Jonathan Weaver from the University of Glasgow.

A fully shielded probe could be foreseen taking precaution in the waveguide dimensions to match the characteristic impedance waveguide and minimize the reflection at the injection point of the RF signal. The development of such probe was not possible during the time of this thesis due to technological limitations and lack of time. A scheme describing the principle is nevertheless included (Figure 3-21).

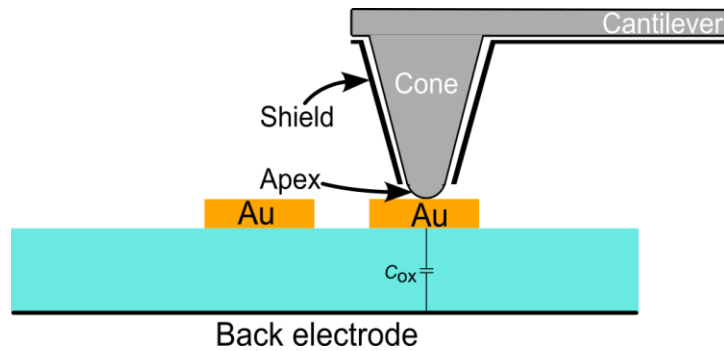


Figure 3-21. Scheme of the capacitance probed by a SMM tip with shielded cantilever and cone.

To fully adapt the measurement to this type of probe, the coaxial capacitor calibration sample as described in Chapter 2 could be used. In this way, the shield is in contact with the guard electrode, isolating the experiment from electromagnetic field variation from the environment.

### 3.4.2 Tip geometries

Five different probes were tried over a single pattern of the first version of the MC2 calibration kit (A64).

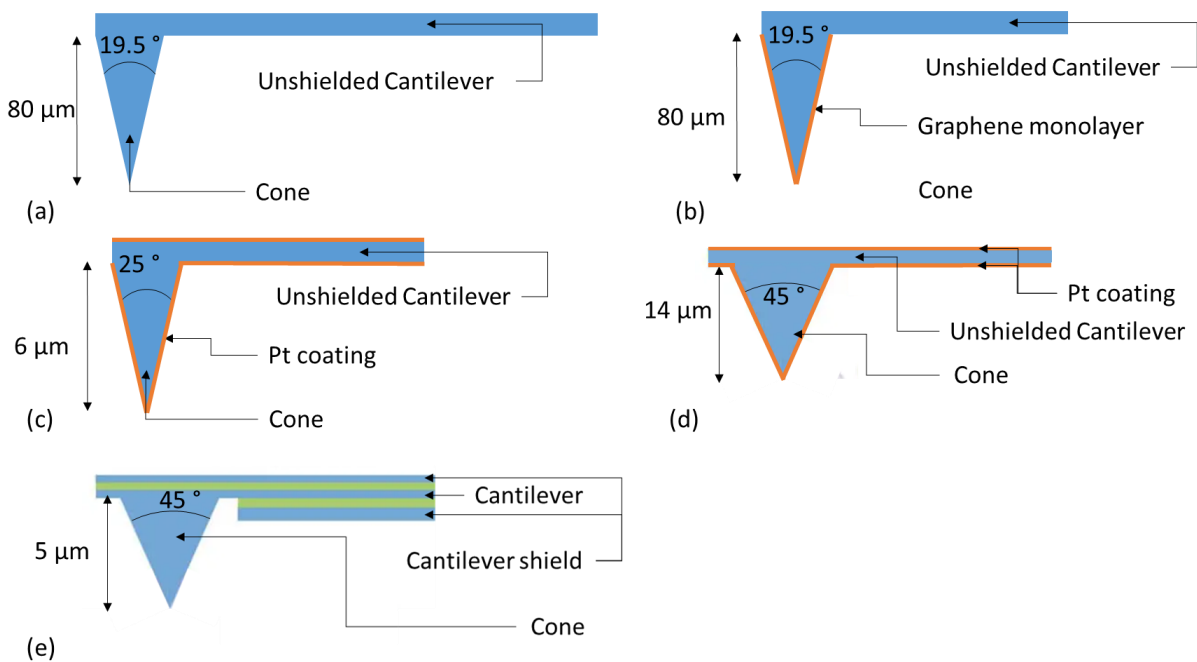


Figure 3-22. (a) Standard RMN probe, (b): RMN probe with a graphene layer, (c): Nu nano probe, (d): App nano probe (e): sMIM probe.

The probe described in Figure 3-22.a is a full platinum RMN probe commonly used in SMM experiment. A graphene coating was deposited on a RMN probe (b) by a Plasma Enhanced Chemical Vapor Deposition (PECVD) process [15]. Two platinum coated silicon probe are shown, a Nu nano probe (c) and an App nano probe (d). Finally, a sMIM shielded cantilever probe [16] is presented in (e). Each probe was used for acquiring  $S_{11,m}$  map on MC2 calibration kit first version (A64). The result of the self-calibration using the substitution method for each probe is presented in Table 3-4.

Table 3-4. Self-calibration performance of each probe

	RMN	RMN-g	Nu nano	App nano	sMIM
mean( $\delta C$ ) (aF)	$-14 \pm 80$	$-34 \pm 61$	$-36 \pm 143$	$-8 \pm 157$	$-48 \pm 110$

Number of capacitors within 5%	38	31	29	16	28
Area of the pattern covered by the cone projection (%)	62.7	62.7	1.1	26.7	3.4

The experiments performed with RMN and RMN-g probes return a standard deviation of the difference between the computed and measured capacitance values below 80 aF. The sMIM probe's experiment is associated with a standard deviation of 110 aF while the last two probes (Nu nano and App nano) are associated with a standard deviation above 140 aF. This disparity in performance can be explained by the geometry of each probe. The cone of the RMM tip has a projection of a radius of 21  $\mu\text{m}$  covering up to 62.7% of the pattern. Therefore, the capacitance of the cone doesn't change significantly from one location to another leading to good performances of the substitution method. The Nu nano's and App nano's cones cover respectively 1.1% and 26.7% of the pattern. The cone capacitance is a function of the location of the probe. When applying the substitution method, the left-out capacitance is then given by Equation 3-9.

$$C = C_{\text{pad}} - C_{\text{neighbor}} = (C_{\text{ox}} + C_{\text{cone}}(\text{pad})) - (C_{\text{apex}} + C_{\text{cone}}(\text{neighbor})) \quad \text{Equation 3-9.}$$

As the cantilever of those probes is not shielded, the substitution method is still required to eliminate its contribution and ensure the local nature of the measurement. It is not the case for the sMIM probe which shows a shielded cantilever. The substitution method is then optional for this probe explaining its good performance despite of the low percentage of coverage of its cone's projection.

### 3.4.3 Tip coating

On Table 3-4, the  $\delta C$  distribution is tighter for the RMN-g probe than for the RMN probe. Two hypothesis were formulated to explain this increase in performance. The graphene layer could act as a casing improving its mechanical stability. As the tip is scanned over the sample, the cone bending and apex blunting will be reduced compared to the configuration without graphene layer. This leads to smaller variation  $z$  of parasitic capacitance over the whole scan area. The full width at half maximal of the  $S_{11,m}$  amplitude and phase histograms associated with each pad would then be reduced. The other hypothesis is on the hydrophobic nature of the graphene layer. Additional measurement are planned to test those hypothesis by acquiring adhesion force curve as a function of the relative humidity and acquisition of image at higher scanning speed.

If the adhesion force of the graphene coated tip is smaller than the uncoated tip, it could be a sign of the hydrophobic nature of the coated tip.

Acquiring images with higher scanning speed will induce more friction between the probe and the sample's surface. If the graphene layer adds mechanical stability, a slight improvement in the standard deviation associated with the  $S_{11,m}$  histograms could be noted.

To compare the results between the two probes, the geometry of the AFM probe should be taken in account. SEM images of both probe will be acquired before and after the experiments.

## 3.5 Simulation

In section 2.3, it was mentioned that the relative humidity plays a role on the uncertainty associated with the mSOL calibration of the instrument. The typical workflow to evaluate the impact of a single parameter on the measurement is to perform three times the experiment: the first time with the parameter set at the default value, then with the parameter set at the test value and finally with the parameter returned to the default value. In this way, a comparison before and after the change can be done to make sure that only the parameter of interest has been changed. For environmental

parameter such as relative humidity, returning to the original configuration can be time consuming and challenging. The choice was made to use numerical method to simulate the instrument calibration process and to implement a water meniscus to study its sole impact on the calibration.

### 3.5.1 Configuration

Comsol Multiphysics 5.6 was used with the RF module to simulate the microwave propagation in the SMM setup. The simulation box comprises an AFM tip on top of a MOS capacitor. The AFM tip was positioned at the center of the simulation box to exploit the rotational symmetry. The geometry of the AFM tip was based on the RMN tip used in the experiment. The cone height is set to 80  $\mu\text{m}$ , its opening angle ( $\theta$ ) is set at 15°, the apex radius ( $R$ ) is set at 80 nm. The contact between the probe's apex and the sample surface is modeled by a blunt the tip on the surface which is considered non deformable. It is translate by a contact of radius ( $\xi$ ) set at 48 nm. The simulation box and a zoom-in image of the AFM tip in contact with the sample surface is shown Figure 3-23.

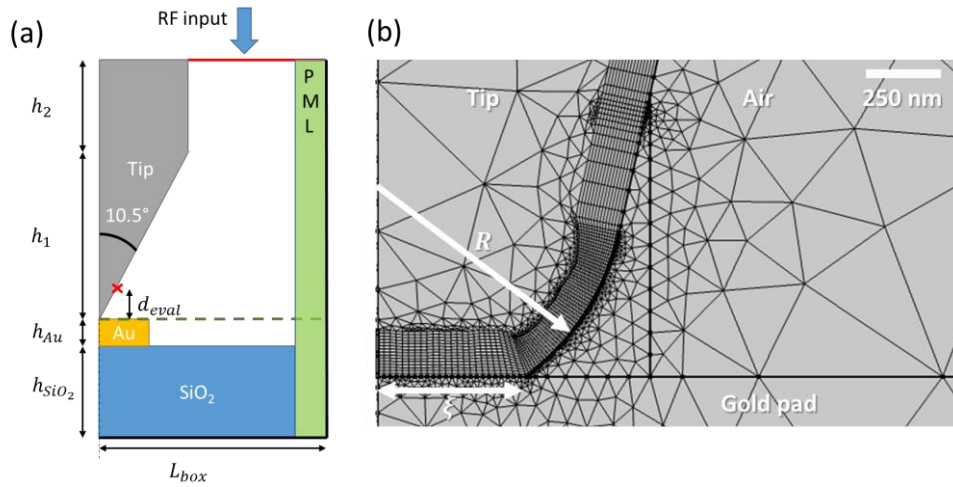


Figure 3-23. Simulation box configuration (not to scale). Green dashed line: Control integral for potential evaluation; Red cross: Control point for current evaluation; Green rectangle: Perfectly Matched Layer (PML); Bold black boundary line: perfect electric conductor (PEC). (b) Zoom on the mesh at the tip apex.

The microwave is injected in the simulation box using a coaxial port condition (Equation 3-10.a) at the top of the simulation box (Figure 3-23.a red line) between the probe and the right edge of the simulation box. The right and bottom edges of the simulation box are set to perfect electric conductor boundary condition (PEC) where the normal component of the electric field is null corresponding to zero charges on these edge. The microwave is then propagated inside the simulation box by solving the Maxwell's equation of wave propagation (Equation 3-10.b):

$$\hat{n} \times (\vec{\nabla} \times \vec{E}) + j\vec{k}_0 \hat{n} \times (\vec{n} \times \vec{E}) = \vec{0} \quad \text{Equation 3-10.a}$$

$$\vec{\nabla} \times \mu_r^{-1} (\vec{\nabla} \times \vec{E}) - k_0^2 \left( \epsilon_r - \frac{j\sigma}{\omega\epsilon_0} \right) \vec{E} = \vec{0} \quad \text{Equation 3-10.b}$$

where  $\mu_r$  is the relative magnetic permeability,  $\vec{E}$  is the electric field,  $\vec{k}_0$  is the wave vector,  $\hat{n}$  is the normal element oriented outside the element, and  $\omega$  is the angular frequency. When the microwave reaches the gold pad, it is reflected according to Equation 3-3. The reflection coefficient is evaluated at the port condition at the top of the simulation box. In everyday experiment, the VNA operates in the range between 0.5 GHz and 20 GHz corresponding to a wavelength of 14 mm. To properly mesh the apex of the probe, the mesh size in this region was set below 1 nm. This leads to a low-frequency breakdown problem [17]. To solve the wave propagation equation (Equation 3-10) in finite element method, the matrix equation (Equation 3-11) is solved.

$$(S - \omega^2 T + j\omega R)\{x(\omega)\} = \{b(\omega)\} \quad \text{Equation 3-11}$$

where  $x(\omega)$  is the solution of the electric field,  $b(\omega)$  is the null vector,  $S$  is the stiffness matrix,  $T$  is the mass matrix and  $R$  is related to the conductivity and boundary condition matrix. The ratio between the elements of  $S$  and  $\omega^2 T$  is approximately  $(\lambda/6l)^2$  where  $l$  is the minimal mesh size. For the tip considered,  $l$  was set at 0.5 nm. For a wavelength of 20 GHz, the element of  $\omega^2 T$  is  $2 \cdot 10^{13}$  times smaller than those of  $S$ . Due to rounding error, the contribution of  $\omega^2 T$  are treated as zero in Equation 3-11 leading to a singular  $A$  matrix. Techniques have been developed to overcome this breakdown [17], [18] but turned out to be difficult to implement in the simulation environment (Comsol 5.6). Instead, the choice was made to increase the excitation frequency up to 300 GHz while keeping the material properties at their 20 GHz values.

In the SMM experiment, the AFM tip is composed of platinum. To simplify the physics of the problem, the 0.120 V surface potential difference between the gold pad and Pt tip [19] was not considered. Those two materials were set to gold with a high electrical conductivity ( $0.456 \cdot 10^{12}$  S/m), resulting in a skin depth of 1.4 nm for an excitation frequency of 300 GHz.

In Figure 3-23.a, the capacitance of the structure is estimated by taking the complex potential to current ratio. The potential is computed by Equation 3-12.a over the green dashed line while the current is computed by Equation 3-12.b at the red cross.

$$\Delta V = \int \vec{E} \cdot d\vec{l} \quad \text{Equation 3-12.a}$$

$$I = \oint \vec{B} \cdot d\vec{l} \quad \text{Equation 3-12.b}$$

The capacitance value associated with a gold pad of 2  $\mu\text{m}$  diameter on a  $\text{SiO}_2$  layer of 200 nm is shown in Figure 3-24 as a function of the location of the point for current evaluation.

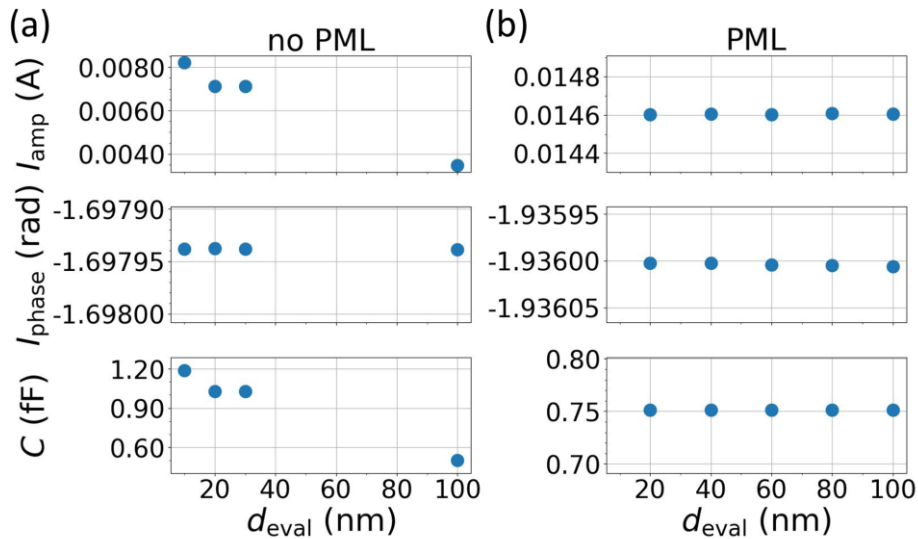


Figure 3-24. Capacitance evaluated on a 2  $\mu\text{m}$  diameter pad on a  $\text{SiO}_2$  layer of thickness of 200 nm as a function of the  $d_{\text{eval}}$  parameter. (a) Without implementation of the PML, (b) with the PML implemented.

In the naïve situation where the simulation box is in direct contact to the right PEC, the current intensity amplitude and, therefore the capacitance, are decreasing when  $d_{\text{eval}}$  is increasing. It can be explained by the contribution of the signal reflected at the right PEC boundary which reaches this location. This problem can be solved by implementing a perfectly matched layer (PML) (Figure 20) [20] between the simulation box and the right PEC boundary. This layer absorbs, without any reflection, the signal before it reaches the right PEC boundary. The current intensity amplitude is then constant as well as the capacitance. Now that the simulation box has been properly set, its performance will be evaluated by a self-calibration of the setup.

### 3.5.2 Self-calibration

A series of simulations was conducted by varying the gold pad radius and dielectric layer thickness to cover the whole range of capacitances in the reference sample used in SMM experiments. The  $S_{11}$  parameter evaluated at the port condition differs from the one estimated at the tip-sample interface due to the impedance of the SMM tip [21]. The calibration was done using three reference capacitances ( $C_z$ ) values from the evaluation described in section 3.5.1.

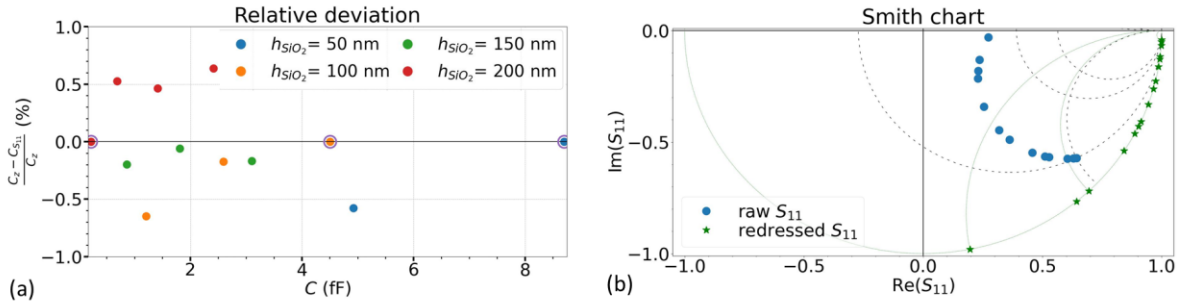


Figure 3-25. Self-calibration of a tip on top of a capacitive MOS structure. a) Relative deviation between the capacitance estimated at the calibrated reference plane ( $C_z$ ) and the capacitance ( $C_{S_{11}}$ ). b) Smith chart, where the impedances used for the calibration are marked by dashed lines.

Figure 3-25.a shows the relative deviation between the reference and calibrated capacitances. The capacitances used to compute the error parameters of the mSOL calibration are encircled in blue. The relative deviation is below 0.8% for all capacitances, and below  $4 \cdot 10^{-12}$  for the three capacitances used as references. The Smith chart of the raw (blue point) and calibrated (green points)  $S_{11}$  is shown in Figure 3-25.b. The capacitance values used for the calibration are located at the intersection of the constant resistive and capacitive circles (dashed line). We notice that the  $S_{11}$  parameter is associated with a null resistance after calibration, which is expected as the simulated calibration device is set with a perfect dielectric. This level of precision could be increased by refining the mesh or making use of higher order of the Nédélec's element [22]. Nédélec's element is a category of FEM edge element belonging to the Hilbert space  $H(\text{curl})$  with a vector field defined per element. The first order of Nédélec's element has degree of freedom on the edge only while the higher order has additional degree of freedom inside the element [23].

Nevertheless, these results were considered satisfying and a water meniscus was implemented at the interface tip-sample to evaluate its impact on the mSOL calibration.

### 3.5.3 Water meniscus evaluation

Several groups have investigated the formation [24], [25], shape [24], [26], [27], and impact of the water meniscus on electrical measurements [24], [28]. The expected parasitic capacitance from the water meniscus is in the range of a few aF. The geometry of the implemented water meniscus is shown Figure 3-26.

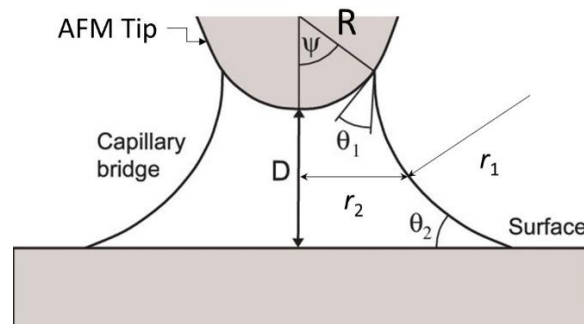


Figure 3-26. Water meniscus implemented at the tip sample interface, [24]

Here,  $\psi$  is the fill angle,  $\theta_1$  and  $\theta_2$  are the contact angle at the Pt tip and at the Au pad, respectively, and  $r_1$ , and  $r_2$  define the water meniscus. The relative dielectric constant of the water is 80 but when one dimension of the water layer is lower than 100 nm, its dielectric constant is reduced and can reach

values as low as 2 [29]. It is due to the vanishing of the out of plane component of the dielectric constant. As the thickness of the water layer is reduced, so their polarizability due to the loss of the normal component of  $\epsilon_r$  [29], [30]. In consequence, the relative dielectric of the water meniscus was set to 10. Its conductivity is of 5.5 S·m as it is the standard value in Comsol multiphysics.

The geometry depends on the volume of the water meniscus and the angle of contact between platinum (at the apex surface) and gold (at the sample's electrode). From literature,  $\theta_1$  is set at 32° [31] and  $\theta_2$  is set at 40° [32], the only missing parameter is  $\psi$ . This parameter can be extracted from adhesion force measurement. In Equation 3-13 the relationship between  $\psi$  and the adhesion force is given.

$$F_{adh} = F_{stv} + \frac{F_t + F_p}{1 + e^{\frac{RH - RH'}{m}}} \quad \text{Equation 3-13.a}$$

$$F_t = 2\pi\gamma_w R_t \sin(\psi) \sin(\psi + \theta_1) \quad \text{Equation 3-13.b}$$

$$F_p = -2\pi\gamma_w R_t^2 \sin(\psi)^2 H(\theta_1, \theta_2, \psi). \quad \text{Equation 3-13.c}$$

where  $F_{adh}$  is the adhesion force,  $F_{stv}$  is the contribution from vapor water,  $F_t$  and  $F_p$  are the contributions to the capillary force due to the surface tension and pressure difference, respectively.  $\gamma_w$  is the surface tension of water set at 72 mN·m<sup>-1</sup> [33],  $RH$  and  $RH'$  are the relative humidities of the current experiment and the transition from ice-like to bulk water behavior, respectively,  $m$  is the slope of this transition, as defined in [27].  $H$  is the local mean curvature of the meniscus, as defined in [34]. A scan over a tip characterizer sample (Supracon, Germany) was acquired with a contact force of 35 nN ± 15 nN to extract the apex radius [35]. The obtained tip radius is 289 nm ± 14 nm, which is large compared to the nominal value of 20 nm. This significant deviation can be explained by the large number of scans acquired with the used AFM tip prior to the measurement campaign. It has been done with the purpose of reducing the uncertainty on the apex radius by increasing its absolute value.

A series of approach retract curves above a gold surface were recorded at different humidity levels using a platinum tip (12Pt300A, RMN), with a nominal spring constant of 0.8 N/m ± 0.3 N/m. The relative humidity was increased in the glovebox by opening the large load lock for 30 seconds. Then, the glove box atmosphere was homogenized by circulation of nitrogen for 2 minutes. The temperature, pressure and relative humidity was recorded in the glove box during the entire time of the experiment. When opening the glove box, a peak in pressure was detected before a return to the nominal value. The RH started increasing after a significant delay compared to the glove box opening due to the large volume of the glove box. During the circulation, the rate at which the RH increases is accelerated before reaching a plateau. Due to the purification reactor involve in the gas circulation, the temperature of the glove box is increased during the circulation [36]. It is then needed to wait for 10 minutes after the circulation ended for the temperature to return to its default value. After this process, the relative humidity is stable within 0.1 % for one hour before it starts increasing again due to leak in the glove themselves.

The adhesion force is estimated from the snap out of contact in the retract portion of the curve force as shown in Figure 3-27.a. The deflection ( $D$ ) is measured by the photodetector array with a reading in V. To obtain the adhesion force in nN, Equation 3-14 can be applied

$$F = D \cdot S \cdot k \quad \text{Equation 3-14}$$

where  $S$  is the photodetector sensibility in m/V ( $S = 148.9 \pm 1.1 \cdot 10^{-9}$  m/V) evaluated on the deflection raw data (Photodetector array reading in V as a function of tip displacement in  $\mu$ m). The variations in the adhesion force as a function of the relative humidity are reported in Figure 3-27.b

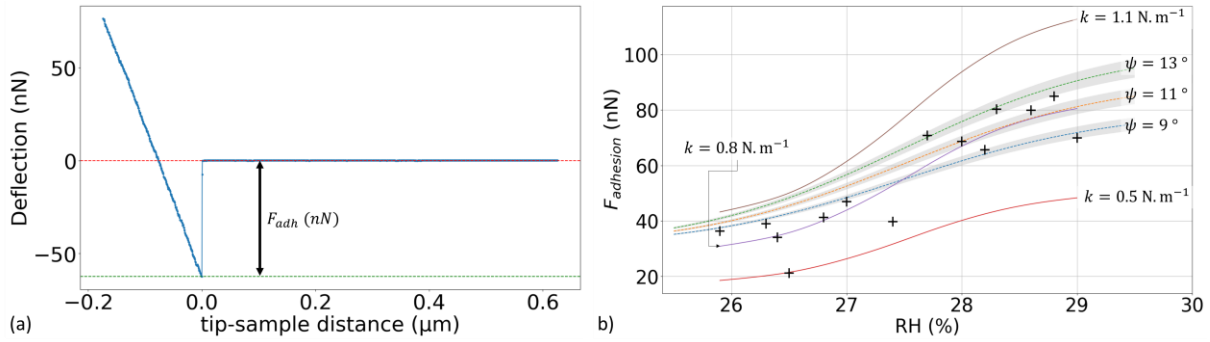


Figure 3-27. (a) Evaluation of the adhesion force by curve force (b) Evolution of the adhesion force as a function of the relative humidity. Black cross: Experimental values with nominal  $k = 0.8 \text{ N/m}$ , solid lines: fit of experimental data with spring constant varying within the uncertainty range, dashed line: adhesion model (from Equation 3-13) with uncertainty associated with the apex radius.

The  $RH'$  and  $m$  parameters were extracted for the fit of experimental curve in Figure 3-27.b. When injecting those parameters in Equation 3-13, it was found that a filling angle of  $(11 \pm 2)^\circ$  corresponds to the measured evolution of the adhesion force.

This meniscus was then implemented in the simulation box, at the interface between the tip's apex and the sample. The thickness of the absorbed layer of water was set to 1 nm and the filling angle of the meniscus was set to  $15^\circ$ . The impact of this meniscus on the wave propagation and the calibration is shown in Figure 3-28, where the  $\log_{10}$  of the electric field and the electric field vector inside the water meniscus are shown in (a). In this particular example, the SMM tip was located on top of a gold pad of radius 500 nm on a 50 nm  $\text{SiO}_2$  terrace. Figure 3-28.b shows the relative deviation between the calibrated capacitance ( $C_{S_{11}}$ ) without and with water meniscus attached to the apex of the tip. The calibration was done only in absence of the water meniscus. The obtained parameters were then applied to both configurations. The presence of water meniscus results in a deviation in the calibrated capacitance up to 0.3%. This value is in good agreement with previous experimental data (2.3). It should be noted that, in reality, calibration and measurement are done with a water meniscus present. Thus, observable discrepancies due to the water meniscus between measured value and calibrated value are even smaller.

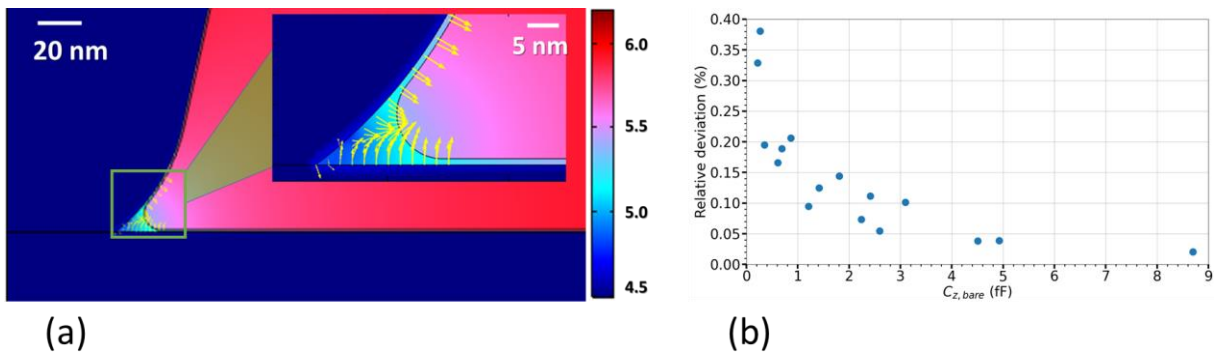


Figure 3-28. (a)  $\log_{10}(E)$  at the tip sample interface for a water meniscus ( $h=1 \text{ nm}$ ,  $r_1= 20 \text{ nm}$ ), inset: zoom on the water meniscus. (b) relative deviation between the  $C_z$  (evaluated without water meniscus) and  $C_{S_{11}}$  calibrated with the errors parameters obtained without water meniscus.

In future work, the simulation will be run again with the experimental water meniscus parameters ( $\psi = 11^\circ \pm 2^\circ$ ). A comparison with experimental value acquired on a calibration sample extend to lower value (sub 100 aF) will also be conducted to study more deeply the contribution of water meniscus.



## 4 Application – measurement on high- $\kappa$ sample

An application case of SMM is found in measuring the dielectric constant of material with the sub micrometer resolution. The instrument was calibrated for capacitance measurement on the 0.3 fF to 9 fF range using the first version of MC2 calibration kit (A64). Measurements were then performed on a test sample located next to the calibration sample. After the measurement was done,  $S_{11,m}$  maps on A64 were acquired to check if any change occurred in the calibration.

### 4.1 Sample description

The dielectric constant of two high- $\kappa$  materials, lead zirconate titanate (PZT) and lead magnesium niobate-lead titanate (PMN-PT) were quantified using the calibrated SMM. Both samples were provided by Electrosiences LTD. The multilayer structure of each sample as well as a cross section SEM view of the high- $\kappa$  layer is given in Figure 3-29.

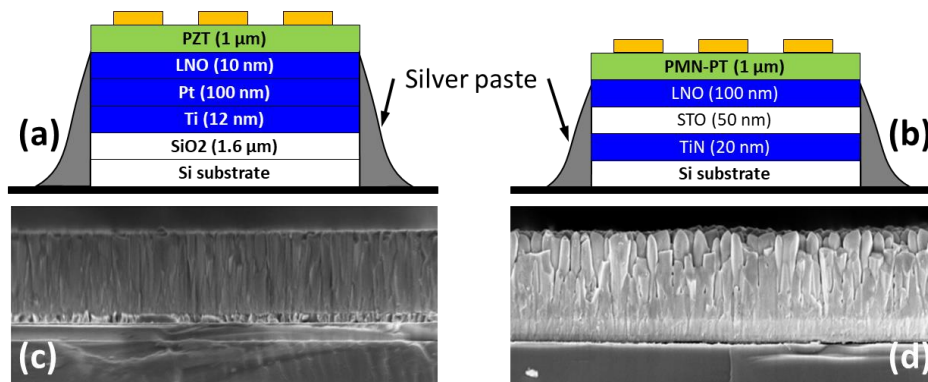


Figure 3-29. Schematic representations of the multilayer structure of the PZT (a) and PMN-PT (b) sample. (c,d) Corresponding cross-section SEM secondary electron images using the In-Lens detector. The acceleration voltage is of 3 kV and the working distance is of 4 mm.

The sample described in Figure 3-29.a starts with SiO<sub>2</sub> layer on the silicon substrate. Then a 12 nm Ti adhesion layer is deposited followed by a 100 nm Pt layer acting as the bottom electrode. Finally, a Lanthanum Nickel Oxide (LNO) layer of 10 nm was grown as a buffer layer for the PZT. On Figure 3-29.b, a TiN layer is grown on the silicon substrate to have a high quality crystalline layer on which to grow the other layer. Then, a Strontium Titanium oxide (STO) layer is grown as a buffer layer for the PMN-PT. As the STO is not conductive, a LNO layer is added with a back electrode function. Finally, the PMN-PT layer is grown on top of this multilayer structure. After growth, 16 gold pads of radius ranging from 50 nm to 1000 nm were processed on top of the structure to form micro capacitors by Renatech. The dimensional parameters of the sample were then measured by SEM secondary electrons mode and tapping mode AFM images. Using the same methodology as the one described in Chapter 2, the area of the top electrodes of the PZT sample are ranging from  $(0.020 \pm 0.002) \mu\text{m}^2$  to  $(3.560 \pm 0.018) \mu\text{m}^2$ . The SEM image used for the top electrodes area measurement on the PZT sample is shown in Figure 3-30.c.

It was not possible to evaluate the top electrode area on the PMN-PT sample due to low contrast. Latter AFM image acquired in tapping mode (Figure 3-30.a and c) show an important surface roughness of the PMN-PT sample ( $S_q = 37.4$  nm) compared to the pads thickness (50 nm). The segmentation of the top electrodes is then challenging on this image. The last option available to determine the electrodes area of this sample is by use of the  $S_{11,m}$  contrast (Figure 3-30.b and d).

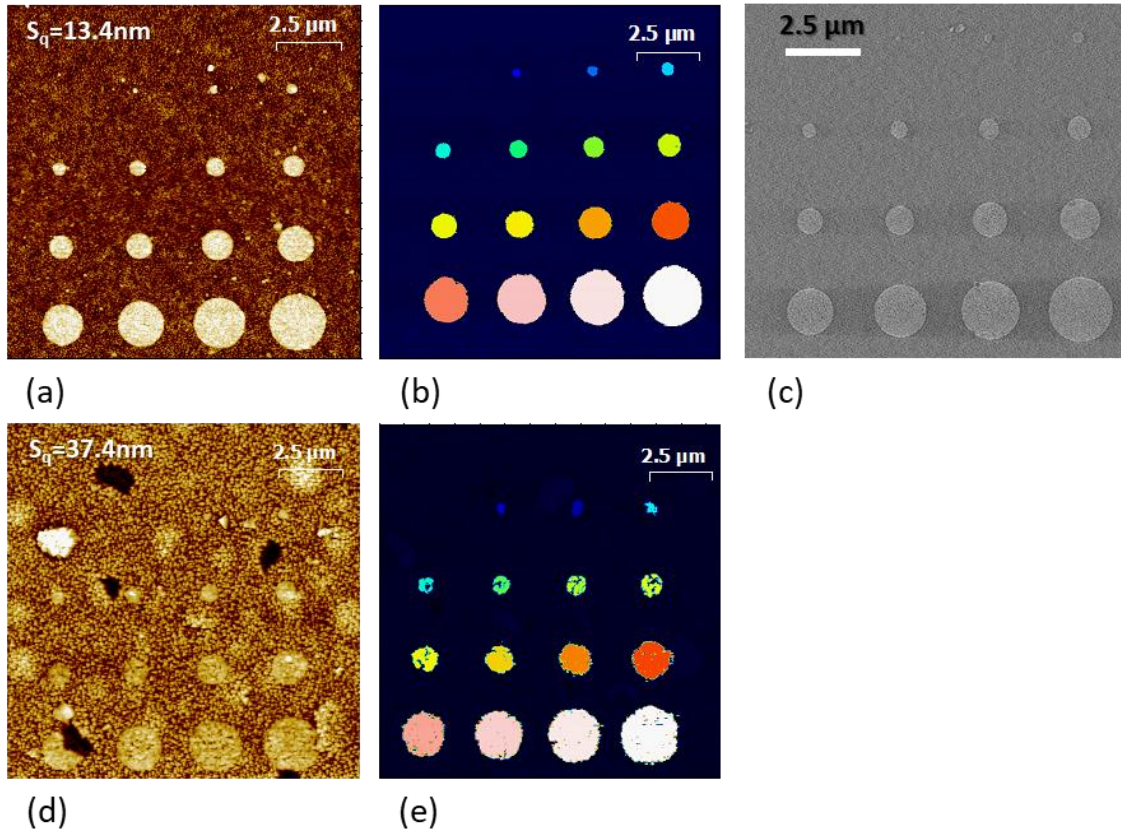


Figure 3-30. AFM Tapping mode images of top electrodes on PZT (a) and PMN-PT (d) samples;  $S_{11,m}$  amplitude map of top electrodes on PZT (b) and PMN-PT (e) samples; (c) SEM secondary electron image of top electrodes on PZT.

The electrical area of the top electrodes defined by the  $S_{11,m}$  image are compared to the topographical one obtained by the topographical data from the AFM image in tapping mode. The correlation fraction  $N$  between those two quantities is computed by taking the electrical to dimensional area ratio. Those values are reported in Table 3-5.

Table 3-5. Electrical and dimensional area of the pads on PZT and PMN-PT sample

# pad	1	2	3	4	5	6	7	8
$A_{\text{topo}}$ (PZT)	0.02	0.05	0.10	0.16	0.24	0.35	0.45	0.56
$N$	0.75	0.84	0.89	0.91	0.88	0.86	0.88	0.90
$A_{\text{elec}}$ (PMN-PT)	0.05	0.11	0.17	0.24	0.27	0.46	0.59	0.67
$A_{\text{corr}}$ (PMN-PT)	0.04	0.09	0.15	0.22	0.24	0.39	0.53	0.61
$u_{\text{area}}$	0.01	0.01	0.03	0.02	0.02	0.04	0.04	0.03
# pad	9	10	11	12	13	14	15	
$A_{\text{topo}}$ (PZT)	0.70	1.02	1.40	1.83	2.34	2.92	3.56	
$N$	0.90	0.90	0.92	0.90	0.90	0.90	0.91	
$A_{\text{elec}}$ (PMN-PT)	0.81	1.15	1.52	2.06	2.54	3.06	3.80	
$A_{\text{corr}}$ (PMN-PT)	0.73	1.03	1.40	1.85	2.29	2.77	3.45	
$u_{\text{area}}$	0.04	0.06	0.06	0.06	0.07	0.07	0.08	

Due to the acquisition condition (contact mode, 0.7 line/sec, 512×512 pixels), the uncertainty associated with this area measurement is quite high (up to 20% of the area value for the smallest pads). The PZT and PMN-PT layer thickness were evaluated to respectively  $(950 \pm 10)$  nm and  $(964 \pm 26)$  nm from the SEM cross section image shown in Figure 3-29.

## 4.2 Dielectric constant evaluation

The PZT, MC2 calibration kit (A64) and PMN-PT samples were located next to each other. The SMM was calibrated on the A64 sample, used for measuring one of the test samples, and measuring again the A64 sample to check for any change. Then the second test sample was measured following the same process. The experiment was repeated at 14 different frequencies ranging from 1.49 GHz to 5.53 GHz.

Typical capacitance maps on A64, PZT, and PMN-PT acquired with the calibrated SMM with an excitation frequency of 3.67 GHz are shown Figure 3-31.

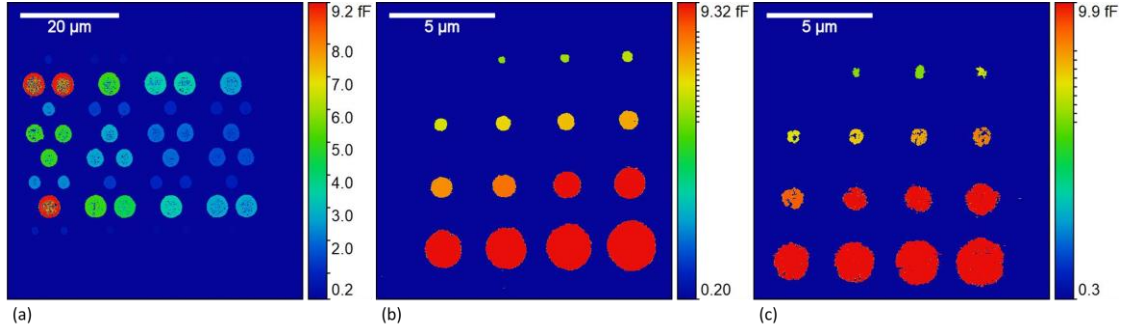


Figure 3-31. Capacitance map on A64 (a), PZT (b) and PMN-PT (c) sample at  $f_{VNA} = 3.67$  GHz

For each pad, the Poisson's equation was solved by numerical simulation (FEM, Comsol) taking as input the dimensions of the structure and a guess dielectric constant and returning the computed capacitance. The dielectric constant was then adjusted to equalize the computed capacitance ( $C_{FEM}$ ) to the measured capacitance ( $C_{exp}$ ) at the 1% level. Different values of  $\epsilon_r$  were found for each sample depending on the area of the gold pad, as shown in Figure 3-32.

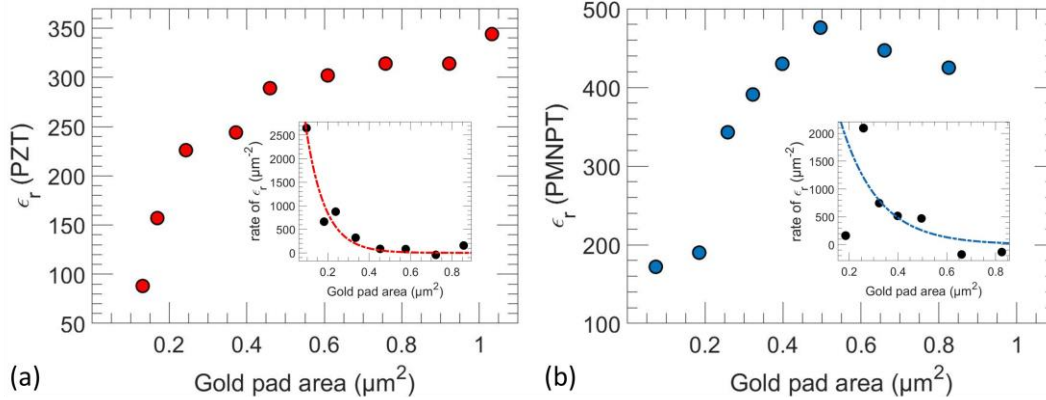


Figure 3-32. Dielectric constant of the high- $\kappa$  layer as a function of the gold pad area on PZT (a) and PMN-PT (b) sample. Inset: variation of  $\epsilon_r$  as a function of the pads' area.

The dielectric constant of the high- $\kappa$  layer increases significantly as a function of the pads' area (changing rates above 2000 per  $\mu\text{m}^2$ ) before reaching a plateau for the largest pads. These changes cannot be attributed to local changes in the dielectric films since the layers are homogenous from a dielectric point of view. The existence of an additional parasitic capacitance in series with the capacitance of the high- $\kappa$  layer can be assumed from this behavior. The global capacitance of the structure will then be given by Equation 3-15

$$\frac{1}{C_{exp}} = \frac{1}{C_{high-\kappa}} + \frac{1}{C_{par}} = \frac{1}{C_{high-\kappa}} + \frac{d_{par}}{\epsilon_0 \epsilon_{r,par} A} \quad \text{Equation 3-15.}$$

where  $d_{par}$  is the thickness of the parasitic layer and  $\epsilon_{r,par}$  its dielectric constant. The deviation between the capacitance of the whole structure and the capacitance of the sole high- $\kappa$  layer is decreasing with the gold pad area, resulting in a stabilization of the dielectric constant evaluated by the previously

mentioned method. To evaluate the dielectric constant of the high- $\kappa$  layer, its value was empirically adjusted in the model until the difference between the measured and calculated capacitance is constant with the pads' area. Then the parasitic capacitance ( $C_{par}$ ) in series with the high- $\kappa$  layer is evaluated until the computed capacitance is equal to the measured one. The results of this analysis is shown Figure 3-33.

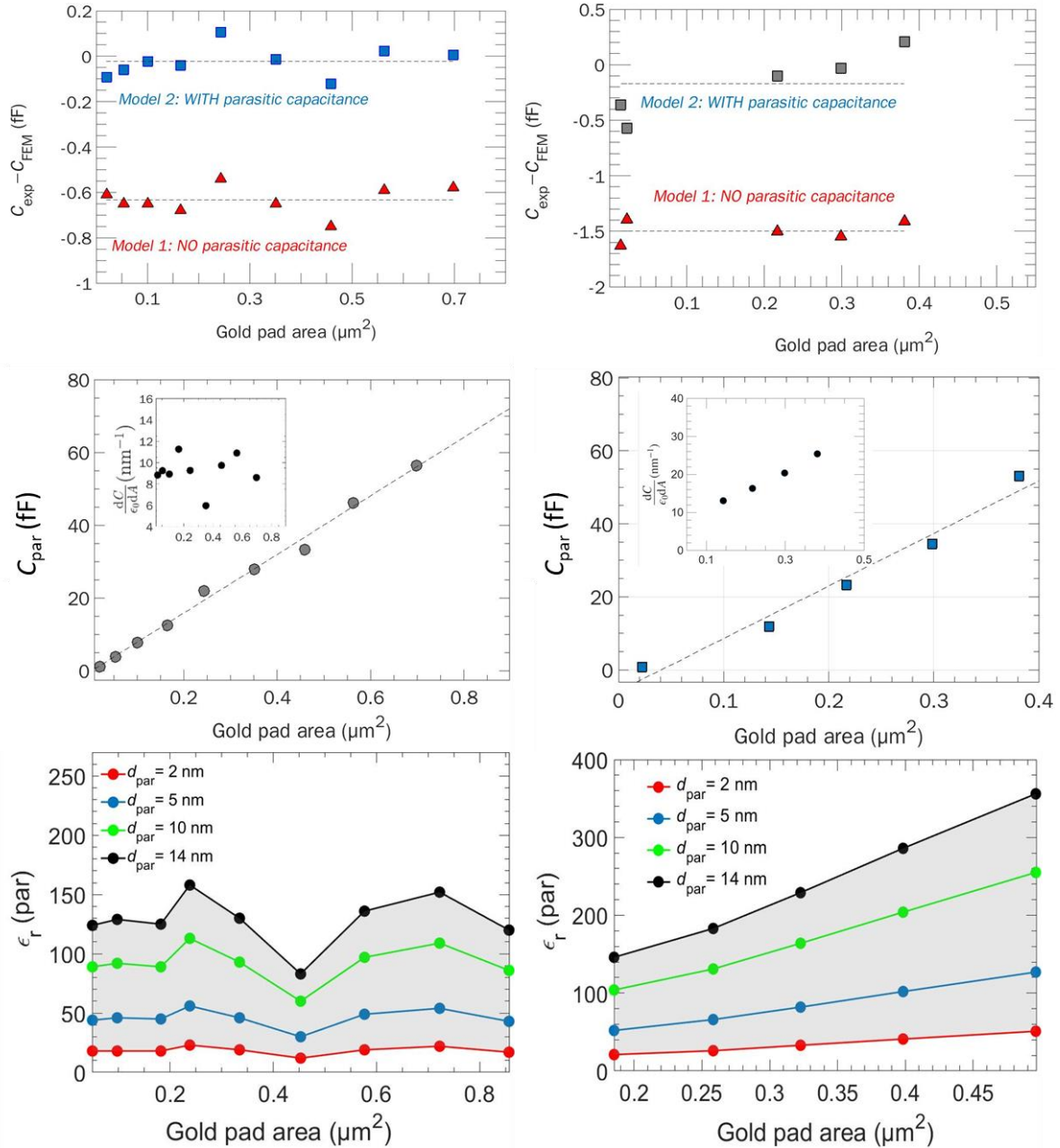


Figure 3-33. Result on PZT and PMN-PT samples at a frequency of 3.67 GHz. (a,d): Difference between  $C_{exp}$  and  $C_{FEM}$  as a function of the gold pad area on PZT (PMN-PT). (b,e): Corresponding parasitic capacitances, dashed line: linear fit, red area: not considered for the fit. (c,f): Corresponding dielectric constants of the parasitic capacitances as a function of the layer thickness.

In Figure 3-33.b and e, the parasitic capacitance is plotted as a function of the pads area. A linear evolution was found, in agreement with a parallel plate capacitor. The slope of the evolution of the parasitic capacitance with pad area can be used to extract the product of the thickness of the parasitic capacitance's layer and the dielectric constant of parasitic layer. The dielectric constant of the parasitic layer is plotted for the different pads' area as a function of the parasitic layer in Figure 3-33.c and f. High resolution SEM images were acquired on the top electrodes as well as cross section images of the PZT sample across the top electrodes (Figure 3-34). The voids and pillar-like bulk structure in the PZT

layer are marked by red arrows. The location of the gold pad was confirmed by acquiring a map of energy-dispersive X-ray spectroscopy (EDS) spectrum [37]. On Figure 3-34.e and h, the presence of grain is visible and can be a clue of the polycrystalline nature of the PZT [38]. Future analysis using diffraction method such as electron back-scattering diffraction (EBSD) or X-ray diffraction (XRD) could dispel doubt on the crystalline nature of PZT and PMN-PT. It could explain the linear increase of the parasitic capacitance first derivative with respect to the area.

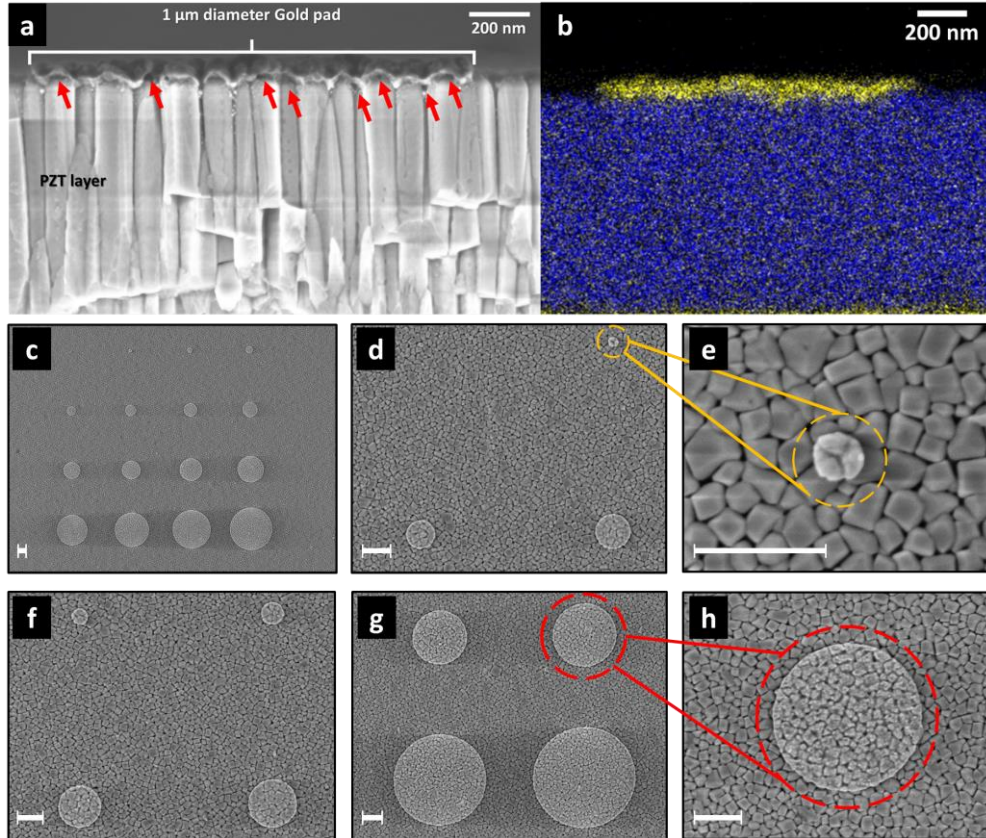


Figure 3-34. Cross section SEM (a) and EDS (b) images of a 1  $\mu\text{m}$  diameter gold pad. The red arrows mark discontinuity between the gold pad and PZT layer. On b, the blue points are associated with the Pb signature and yellow points with the Au signature. (c-h): Secondary electron SEM images of a pattern formed by 15 gold pads. All scale bars correspond to 400 nm. All images were acquired with a 4.6 mm working distance and an acceleration voltage of 3 kV.

The quality of the interfacial layer under the gold pads is directly dependent on the surface roughness of the high- $\kappa$  samples. The measurement of the actual interface roughness under the gold electrodes is not accessible. Nonetheless, the higher the roughness, the higher the equivalent thickness of the parasitic layer would be. For this, a range of different values for the parasitic capacitance thickness  $d_{\text{par}}$  between 2 nm and 14 nm was considered. While the lowest value reflects low local roughness under a gold pad, the highest value of 14 nm corresponds to the average peak-to-valley value calculated over the entire surface excluding the circular gold pads. For the PZT sample, the equivalent parasitic permittivity  $\epsilon_{r,\text{par}}$  remains mostly below 80, except for the higher values of  $d_{\text{par}}$ . These values are well below the extracted dielectric constant for the PZT film (i.e.,  $\epsilon_{r,\text{PZT}} = 445 \pm 16$ ). This suggests that the equivalent parasitic layer is mostly formed by air voids and potentially confined water. Indeed, recent results report abnormally low permittivity of confined water ( $\epsilon_r$  below 80) [29], [30].

The variations in  $\epsilon_{r,\text{par}}$  for the PMN-PT sample show a similar behavior for the case of a low roughness interface represented by small values of  $d_{\text{par}}$ . However, the AFM analysis in Figure 3-30 clearly indicates a much higher surface roughness for the PMN-PT sample. Thus, the higher values of  $d_{\text{par}}$  (i.e.,  $d_{\text{par}} = 10$  and 14 nm) constitute a better representation of the variations in the dielectric constant of the

parasitic capacitance for the case of PMN-PT. It is noticeable in this case that  $\epsilon_{r,par}$  is mostly higher than 80 (dielectric constant of bulk water), practically for all gold pad areas, as shown in Figure 3-33.f.  $\epsilon_{r,par}$  increases as the area of the gold electrodes increases, reaching values comparable to that extracted for the PMN-PT film (i.e.,  $\epsilon_{r,PMN-PT} = 641 \pm 44$ ). This points towards the fact that the rough PMN-PT surface leads to a parasitic layer under the gold pads mostly incorporating peaks of the ferroelectric material with a lower density of voids, especially for larger gold pads.

This analysis highlights the crucial role of the interfacial surface roughness between the gold top electrodes and the surface of the high- $\kappa$  sample. As pointed out in a theoretical study in [39] on the effect of the electrode's roughness on the capacitance of a parallel-plate capacitor, the higher the surface irregularities and roughness of the electrode are, the higher is the capacitance. The interface roughness under the gold pads in the case of our samples increases the effective area of the top electrode for the different micro-capacitor structures. It therefore naturally follows that the larger gold pad areas incorporate a stronger contribution of the parasitic capacitance as observed experimentally in Figure 3-33.b,e.

This study was conducted at different frequency ranging from 1.49 GHz to 5.53 GHz. The dielectric constant of the PZT and PMN-PT layer is evaluated by the aforesaid method for each frequency and reported in Figure 3-35.

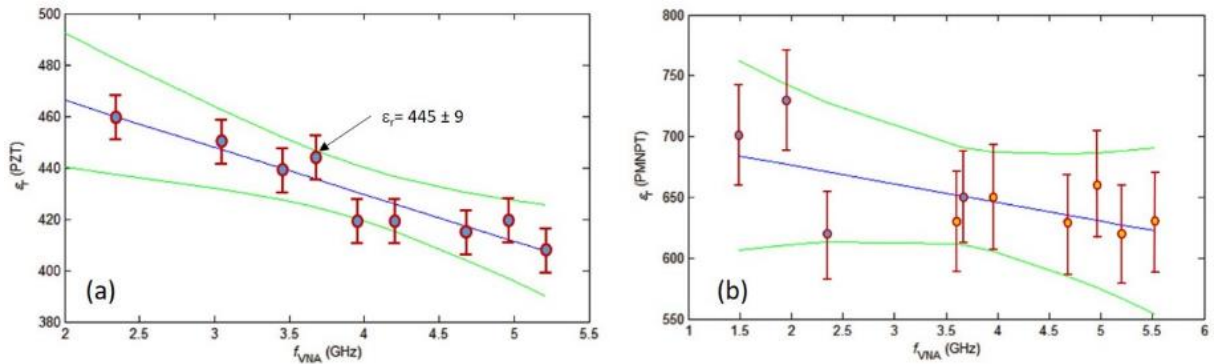


Figure 3-35. Dielectric constant of (a) PZT and (b) PMN-PT samples as a function of the VNA frequency. Error bars correspond to the combined uncertainty. Green continuous envelope: lower and upper limit of the dielectric constant in the [1.49; 5.53] GHz range according to the uncertainty of the measured points.

The green envelope corresponds to the lower and upper limit of the dielectric constant in the 1.49 GHz to 5.53 GHz according to the uncertainty of the measured points. This envelope was computed by Generalized Least-Square Generalized Gauss Markov Regression (GLS GGMR) to account for the uncertainty in dielectric constant and VNA's frequency with the RegPoly software [40]. For the PZT sample, a slight decrease in the dielectric constant is observed with a slope of  $\Delta\epsilon_r/\Delta f = (18.4 \pm 1.6)$  GHz which is in agreement with results reported elsewhere [41]. The uncertainty on the dielectric constant measurement for the PMN-PT sample make difficult to draw a conclusion from these results. In addition, the multiple scan has worn the capacitive pattern away causing deterioration in the contrast of the pattern. At the middle of the measurement campaign, it was not possible to pursue on the same pattern and the decision was taken to pursue on a different area of the same sample. This change of location is marked by two different colors in Figure 3-35.b. The global uncertainty budget on the capacitance measurement for PZT and PMN-PT sample are reported in Table 3-6.

Table 3-6. Uncertainty budget associated with the capacitance constant measurement by SMM of PZT and PMN-PT samples

Uncertainty sources	PZT	PMN-PT (1 <sup>st</sup> area)	PMN-PT (2 <sup>nd</sup> area)
Capacitance calculation	(2.5; 9.7)	(6.5; 20.5)	(6.5; 23.6)
Area ( $u_A$ )	(1.3; 9.5)	(3.5; 19.7)	(3.4; 22.9)
Thickness ( $u_d$ )	2.1	5.5	5.5
Capacitance measurements	3.2	3.3	3.2
Type A (histogram, repeatability)	(0.1; 0.2)	(0.2; 0.6)	(0.2; 0.6)
SMM calibration	3.1	3.1	3.1
Other	<1.8	<1.8	<1.8
Combined uncertainty ( $u_c$ )	3.5	9.1	10.6

The other contributions include the water meniscus and residual influence of parasitic capacitance between the probe and the sample. The corresponding uncertainty on the dielectric constant extraction is of 3.5% for the PZT sample and 6.9% for the PMN-PT sample. Finally, attempt to auto calibrate the SMM on the PZT sample was conducted (Figure 3-36).

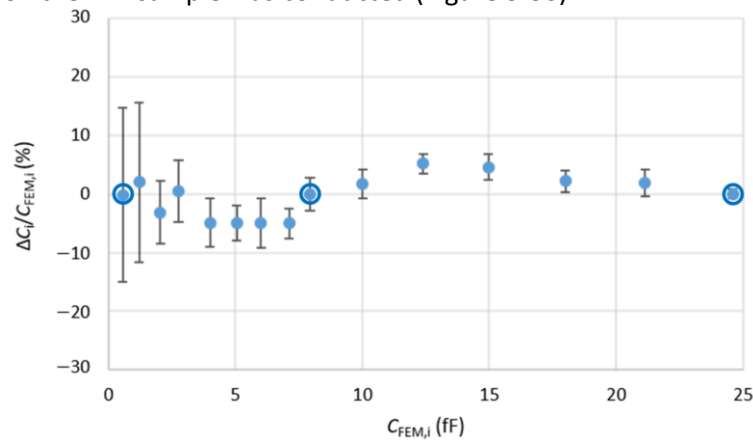


Figure 3-36. Relative differences  $\Delta C_i/C_{FEM,i}$  (in %) between measured  $C_{exp,i}$  and calculated  $C_{FEM,i}$  capacitance values for 15 capacitors  $C_i$  of the PZT sample at 3.67 GHz. The SMM has been calibrated using the three capacitors of calculated capacitances 0.56, 7.93, and 24.69 fF

The dielectric constant measured on the 9 smallest pads are generalized to the whole structure for capacitance computation. The relative error is within the 5% range over the whole calibration range supporting the stability of the method to extract the dielectric constant.

## 5 Conclusion

In this chapter, the SMM setup was described and the mSOL calibration is detailed. It was shown that the capacitance standard sample introduced in Chapter 2 can be used to calibrate the SMM within the 3.3%. This calibration was done with an unshielded tip thanks to a substitution method where the  $S_{11,m}$  associated with the neighborhood of the capacitor is subtracted from the  $S_{11,m}$  of the capacitor. The objective is to get rid of the parasitic impedance between the cone and cantilever of the AFM probe and the sample. The major uncertainty contribution are the capacitance values themselves followed by the repeatability and the remaining parasitic capacitances.

The robustness of the calibration method was put to the test by applying the error parameter obtained in one area to another area of the same sample or of other calibration sample. The impact of location on the calibration was found below 2% for most location and up to 2.9% for one location. This suggests a constant depletion capacitance and trapped charges at the semiconductor oxide interface over the sample as well as a homogeneous electromagnetic noise. When comparing the two versions of the calibration kit, a systematic error of about 200 aF on the largest capacitance is visible. This deviation can be explained by a combination of parasitic capacitance in series and variation of  $\epsilon_r$  value between

the two samples. A same behavior was found when comparing two samples of the first calibration kit. Finally, a simulation work was conducted to better investigate the role of water meniscus on the calibration. It was shown that a water meniscus under everyday condition generates a relative deviation increasing when the capacitance value decreases. This relative deviation is below 0.05% for capacitance above 4 fF and up to 0.38% for capacitance of 0.3 fF which is coherent with the experimental data.

The performance of a SMM probe with shielded cantilever is investigated by mean of a home-made nose cone to adapt our SMM to the tip geometry. Most of the relative deviation are within the 10% limit. The substitution method doesn't change significantly the performance of the calibration compared to raw data. Other tip geometries are investigated and required additional measurement to compare them. Finally the role of coating of the RMN tip is investigated. Primarily results tend to show a better performance of the calibration when a graphene coating is present. Future experiments are planned to further investigate this behavior.

An application case was explored by measuring the dielectric constant of PZT and PMN-PT samples. It was found to be in agreement with previously reported results. The associated uncertainty are of 3.5% for the PZT sample and in the 10.6 % range for the PMN-PT sample.



- [1] T. Dargent *et al.*, “An interferometric scanning microwave microscope and calibration method for sub-fF microwave measurements,” *Rev. Sci. Instrum.*, vol. 84, no. 12, 2013, doi: 10.1063/1.4848995.
- [2] J. Hoffmann *et al.*, “Comparison of Impedance Matching Networks for Scanning Microwave Microscopy,” *IEEE Trans. Instrum. Meas.*, 2024, doi: 10.1109/TIM.2024.3378310.
- [3] M. Wollensack and J. Hoffmann, “METAS VNA Tools - Math Reference V2 . 4 . 3,” no. December, pp. 1–83, 2020.
- [4] P. Klapetek, D. Nečas, and C. Anderson, “Gwyddion User Guide (gwyddion.net/documentation/user-guide-en),” 2021, [Online]. Available: gwyddion.net/documentation/user-guide-en.
- [5] L. Vincent and P. Soile, “Watersheds in digital spaces: an efficient algorithm based on immersion simulations,” *IEEE Trans. Pattern Anal. Mach. Intell.*, vol. 13, pp. 583–598, 1991, doi: doi:10.1109/34.87344.
- [6] B. Rosner, “Percentage points for a generalized esd many-outlier procedure,” *Technometrics*, vol. 25, no. 2, pp. 165–172, 1983, doi: 10.1080/00401706.1983.10487848.
- [7] H. P. Huber *et al.*, “Calibrated nanoscale capacitance measurements using a scanning microwave microscope,” *Rev. Sci. Instrum.*, vol. 81, no. 11, 2010, doi: 10.1063/1.3491926.
- [8] L. Fumagalli *et al.*, “Nanoscale capacitance imaging with attofarad resolution using ac current sensing atomic force microscopy,” *Nanotechnology*, vol. 17, no. 18, pp. 4581–4587, 2006, doi: 10.1088/0957-4484/17/18/009.
- [9] L. Fumagalli, G. Ferrari, M. Sampietro, and G. Gomila, “Dielectric-constant measurement of thin insulating films at low frequency by nanoscale capacitance microscopy,” *Appl. Phys. Lett.*, vol. 91, no. 24, 2007, doi: 10.1063/1.2821119.
- [10] G. Gomila, G. Gramse, and L. Fumagalli, “Finite-size effects and analytical modeling of electrostatic force microscopy applied to dielectric films,” *Nanotechnology*, vol. 25, no. 25, 2014, doi: 10.1088/0957-4484/25/25/255702.
- [11] F. Piquemal, J. Morán-Meza, A. Delvallée, D. Richert, and K. Kaja, “Progress in Traceable Nanoscale Capacitance Measurements Using Scanning Microwave Microscopy,” *Nanomaterials*, vol. 11, no. 820, 2021, doi: doi.org/10.3390/nano11030820.
- [12] F. Wang *et al.*, “Quantitative impedance characterization of sub-10 nm scale capacitors and tunnel junctions with an interferometric SMM,” *Nanotechnology*, vol. 25, no. 40, 2014, doi: 10.1088/0957-4484/25/40/405703.
- [13] M. Morita, T. Ohmi, E. Hasegawa, M. Kawakami, and M. Ohwada, “Growth of native oxide on a silicon surface,” *J. Appl. Phys.*, vol. 68, no. 3, pp. 1272–1281, 1990, doi: 10.1063/1.347181.
- [14] K. Lai, W. Kundhikanjana, M. A. Kelly, and Z. X. Shen, “Nanoscale microwave microscopy using shielded cantilever probes,” *Appl. Nanosci.*, vol. 1, no. 1, pp. 13–18, 2011, doi: 10.1007/s13204-011-0002-7.
- [15] M. Joud, M. El Marssi, and M. Lejeun, “Process for direct deposition of graphene or graphene oxide onto a substrate of interest,” 2023.
- [16] Y. Yang *et al.*, “Batch-fabricated cantilever probes with electrical shielding for nanoscale dielectric and conductivity imaging,” *J. Micromechanics Microengineering*, vol. 22, no. 11, 2012, doi: 10.1088/0960-1317/22/11/115040.
- [17] B. Y. Wu, X. Q. Sheng, R. Fabregas, and Y. Hao, “Full-wave modeling of broadband near field scanning microwave microscopy,” *Sci. Rep.*, vol. 7, no. 1, pp. 1–10, 2017, doi: 10.1038/s41598-017-13937-5.
- [18] F. Vico, Z. Gimbutas, L. Greengard, and M. Ferrando-Bataller, “Overcoming low-frequency breakdown of the magnetic field integral equation,” *IEEE Trans. Antennas Propag.*, vol. 61, no. 3, pp. 1285–1290, 2013, doi: 10.1109/TAP.2012.2230232.
- [19] S. Mugo and J. Yuan, “Influence of Surface Adsorption on Work Function Measurements on Gold-Platinum Interface Using Scanning Kelvin Probe Microscopy Influence of Surface Adsorption on Work Function Measurements on Gold-Platinum Interface Using Scanning Kelvin Probe Microscopy,” *J. Phys. Conf. Ser.*, 2012, doi: 10.1088/1742-6596/371/1/012030.

- [20] S. G. Johnson, "Notes on Perfectly Matched Layers (PMLs)," pp. 1–16, 2021, [Online]. Available: <http://arxiv.org/abs/2108.05348>.
- [21] M. Azizi, "CMOS-MEMS Scanning Microwave Microscopy," 2017.
- [22] R. B. Wehrspohn, H. Kitzerow, and K. Busch, *Nanophotonic Materials: Photonic Crystals, Plasmonics and Metamaterials*, vol. 204, no. 11. 2007.
- [23] J.-M. Jin, *The finite element method in electromagnetics*, 3rd ed. 2014.
- [24] Z. Wei and Y. P. Zhao, "Growth of liquid bridge in AFM," *J. Phys. D. Appl. Phys.*, vol. 40, no. 14, pp. 4368–4375, 2007, doi: 10.1088/0022-3727/40/14/036.
- [25] E. Charlaix and M. Ciccotti, "Capillary Condensation in Confined Media," *Handb. Nanophysics*, no. October 2009, pp. 219–236, 2020, doi: 10.1201/9781420075410-19.
- [26] A. Assy, S. Lefèvre, P. O. Chapuis, and S. Gomès, "Analysis of heat transfer in the water meniscus at the tip-sample contact in scanning thermal microscopy," *J. Phys. D. Appl. Phys.*, vol. 47, no. 44, 2014, doi: 10.1088/0022-3727/47/44/442001.
- [27] D. L. Sedin and K. L. Rowlen, "Adhesion forces measured by atomic force microscopy in humid air," *Anal. Chem.*, vol. 72, no. 10, pp. 2183–2189, 2000, doi: 10.1021/ac991198c.
- [28] F. Wang *et al.*, "Quantitative impedance characterization of sub-10 nm scale capacitors and tunnel junctions with an interferometric SMM \_ Supp info," *Nanotechnology*, vol. 25, no. 40, 2014, doi: 10.1088/0957-4484/25/40/405703.
- [29] L. Fumagalli *et al.*, "Anomalously low dielectric constant of confined water," *Science (80-. )*, vol. 360, no. 6395, pp. 1339–1342, 2018, doi: 10.1126/science.aat4191.
- [30] T. Dufils, C. Schran, J. Chen, A. K. Geim, L. Fumagalli, and A. Michaelides, "Origin of dielectric polarization suppression in confined water from first principles," *Chem. Sci.*, vol. 15, no. 2, pp. 516–527, 2023, doi: 10.1039/d3sc04740g.
- [31] Z. Li, P. Beck, D. A. A. Ohlberg, D. R. Stewart, and R. S. Williams, "Surface properties of platinum thin films as a function of plasma treatment conditions," *Surf. Sci.*, vol. 529, no. 3, pp. 410–418, 2003, doi: 10.1016/S0039-6028(03)00015-3.
- [32] C. T. Nguyen, M. Barisik, and B. Kim, "Wetting of chemically heterogeneous striped surfaces: Molecular dynamics simulations," *AIP Adv.*, vol. 8, no. 6, 2018, doi: 10.1063/1.5031133.
- [33] N. B. Vargaftik, B. N. Volkov, and L. D. Voljak, "International Tables of the Surface Tension of Water," *Journal of Physical and Chemical Reference Data*, vol. 12, no. 3. pp. 817–820, 1983, doi: 10.1063/1.555688.
- [34] F. M. Orr, L. E. Scriven, and A. P. Rivas, "Pendular rings between solids: Meniscus properties and capillary force," *J. Fluid Mech.*, vol. 67, no. 4, pp. 723–742, 1975, doi: 10.1017/S0022112075000572.
- [35] G. Y. Kwak *et al.*, "Calibration of high magnification in the measurement of critical dimension by AFM and SEM," *Appl. Surf. Sci.*, vol. 565, no. April, p. 150481, 2021, doi: 10.1016/j.apsusc.2021.150481.
- [36] MBraun, "Glove Box Systems - Gas purification platform MB20/MB200 and Labmaster SP/DP," 2008.
- [37] J. Goldstein *et al.*, *Scanning Electron Microscopy and X-Ray Microanalysis*. 2003.
- [38] D. Tierno *et al.*, "Microwave Characterization of Ba-substituted PZT and ZnO Thin Films," 2017.
- [39] Y. P. Zhao, G. C. Wang, T. M. Lu, G. Palasantzas, and J. T. M. De Hosson, "Surface-roughness effect on capacitance and leakage current of an insulating film," *Phys. Rev. B - Condens. Matter Mater. Phys.*, vol. 60, no. 12, pp. 9157–9164, 1999, doi: 10.1103/PhysRevB.60.9157.
- [40] C. Yardin, "REGPOLY: A software to estimate the calibration function and to compute experimental result," in *International Congress of Metrology*, 2013, vol. 04009, doi: 10.1051/metrology/201304009.
- [41] L. Jin, "Broadband Dielectric Response in Hard and Soft PZT: Understanding Softening and Hardening Mechanisms," vol. 4988, 2011.

---

## Chapter 4 Electrostatic Force Microscopy based calibration

<b>Chapter 4</b>	<b>Electrostatic Force Microscopy based calibration</b>	<b>114</b>
1	<i>Principle</i> .....	115
1.1	Operating mode far from the resonance frequency.....	117
2	<i>Comparison with the mSOL calibration</i> .....	117
2.1	Capacitance gradient on the dielectric.....	118
3	<i>Estimation of the cantilever spring constant</i> .....	120
3.1	Common methods for spring constant evaluation .....	120
3.1.1	Thermal noise.....	120
3.1.2	Sader method.....	121
3.1.3	Ion milling method .....	122
3.1.4	Force sensor.....	123
3.2	Electrostatic method .....	124
4	<i>Conclusion</i> .....	128

The principle of electrostatic force microscopy (EFM) was briefly described in Chapter 1. An extended description is given here. Then, the method was used to obtain an approach curve while acquiring the  $S_{11,m}$  parameter. A calibration of the SMM using three points on the  $dC/dz$  curve was done for the case where the approach curve is acquired over the bare dielectric of the calibration kit from MC2 (A64) to compare the two calibration methods. Finally, the  $dC/dz$  curve are used to perform a traceable measurement of the spring constant of the cantilever.

# 1 Principle

An AC voltage ( $V_{AC}$ ) is applied in addition to the DC voltage ( $V_{DC}$ ) between the conductive AFM probe and the back electrode of the sample. The potential difference between the sample and the AFM probe can be seen as the contribution of the local contact potential ( $V_{cp}$ ),  $V_{DC}$  and  $V_{AC}$  (Equation 4-1) [1].

$$V = (V_{cp} + V_{DC}) + V_0 \sin(\omega t) \quad \text{Equation 4-1}$$

where  $V_0$  is the magnitude and  $\omega$  the angular frequency of  $V_{AC}$ .

This potential difference generates an electrostatic force containing with two harmonics (Equation 4-2).

$$F_{es} = F_{DC} + F_{\omega} + F_{2\omega} \quad \text{Equation 4-2.a}$$

$$F_{DC} = \left( \frac{(V_{cp} + V_{DC})^2}{2} + \frac{V_0}{4} \right) \frac{dC}{dz} \quad \text{Equation 4-2.b}$$

$$F_{\omega} = (V_{cp} + V_{DC}) V_0 \sin(\omega t) \frac{dC}{dz} \quad \text{Equation 4-2.c}$$

$$F_{2\omega} = -\frac{V_0^2 \cos(2\omega t)}{4} \frac{dC}{dz} \quad \text{Equation 4-2.d}$$

Due to the presence of contamination, the contact potential between the probe and the sample can be difficult to know without in-situ measurement [2]. In Equation 4-2.d, the  $dC/dz$  quantity can be extracted with the sole knowledge of the alternating applied potential and the second harmonic of the electrostatic force. The electrostatic force's second harmonic can be accessed by a lock-in amplifier. Typical capacitance evolution as a function of the tip-sample distance is shown in Figure 4-1.

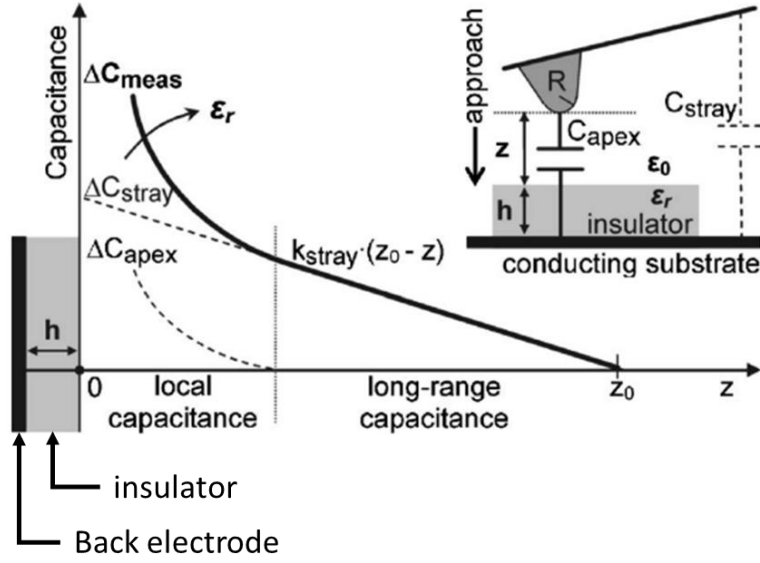


Figure 4-1. Tip-sample capacitance as a function of the separation distance, [3]

When the tip is far away from the sample surface, the capacitance shows a linear decrease with the tip-sample distance leading to a constant electrostatic force and therefore a constant oscillation movement. But as the separation distance is reduced, the  $|dC/dz|$  quantity increases. This translates as a change in the electrostatic force. Another way to look at the system is to consider it as a forced damped oscillator. Newton's second law solution for this problem is given in Equation 4-3.

$$-kz - b \frac{dz}{dt} + F_{2\omega} = m \frac{d^2z}{dt^2} \quad \text{Equation 4-3.a}$$

$$z(t) = A \cos(2\omega t + \varphi) \quad \text{Equation 4-3.b}$$

$$A = \frac{V_0^2}{4} \frac{dC}{dz} \sqrt{m(4\omega^2 - \omega_0^2)^2 + (2b\omega)^2}^{-1} \quad \text{Equation 4-3.c}$$

where  $z$  is the tip-sample distance,  $b$  is the damping,  $m$  is the mass of the oscillator,  $A$  is the oscillation amplitude at  $2\omega$ ,  $\omega_0$  is the resonant pulsation and  $\varphi$  is the phase shift due to the damping. Here when  $d$  is large, the  $2\omega$  mode of oscillation is free of damping. When the tip-sample distance is reduced, the probe starts sensing the underneath sample, damping the oscillator and creating a shift in the oscillation amplitude and frequency. The second harmonic is detected in the experiment by a lock-in amplifier analyzing the oscillation while keeping its amplitude (AM-EFM) or its frequency (FM-EFM) constant. Those two operating modes are detailed in this part.

Independently of the chosen mode, the resolution in the force sensing is limited by the thermal noise generating an oscillating movement of the AFM probe (Equation 4-4) [4],

$$\left. \frac{dF}{dz} \right|_{min} = \frac{1}{A_0} \sqrt{\frac{27k_B T B k}{\omega Q}} \quad \text{Equation 4-4}$$

where  $A_0$  is the amplitude of oscillation,  $k$  is the cantilever stiffness,  $B$  is the bandwidth of the detection system, and  $Q$  is the quality factor of the oscillation. Hence, the softer the cantilever, the higher the achievable resolution force.

## 1.1 Operating mode far from the resonance frequency

In this operating mode, the applied AC potential is adjusted by the lock-in to keep the amplitude of the cantilever's oscillation constant. There exists a relationship between the lock-in signal ( $A_{p,2\omega}$ ) and  $F_{2\omega}$ ,

$$F_{2\omega} = A_{p,2\omega} \frac{kS}{G} \quad \text{Equation 4-5.}$$

where  $S$  is the sensibility of the photodetector (in nm/V), and  $G$  is the gain of the lock-in. The sensibility is measured by acquiring a force curve on a hard surface. When the probe hits the surface, the cantilever bends by the known displacement of the piezo actuator. The sensibility of the photodetector is then given by the  $z$  piezo displacement to deflection ratio. Using Equation 4-2 and Equation 4-5, the  $dC/dz$  is expressed by Equation 4-6.

$$\frac{dC}{dz} = 4A_{p,2\omega} \frac{k \cdot S}{G \cdot V_{AC}^2} \quad \text{Equation 4-6.}$$

In 2011, Schwart *et al.* [5] evaluated the phase shift ( $\varphi$ ) evolution with the tip-sample distance for a PVAc film of 250 nm thickness with a driving frequency of 1 kHz (

Figure 4-2). They used a SCM-PIT coated tip with 4 N/m stiffness and a resonant frequency of 75 kHz.

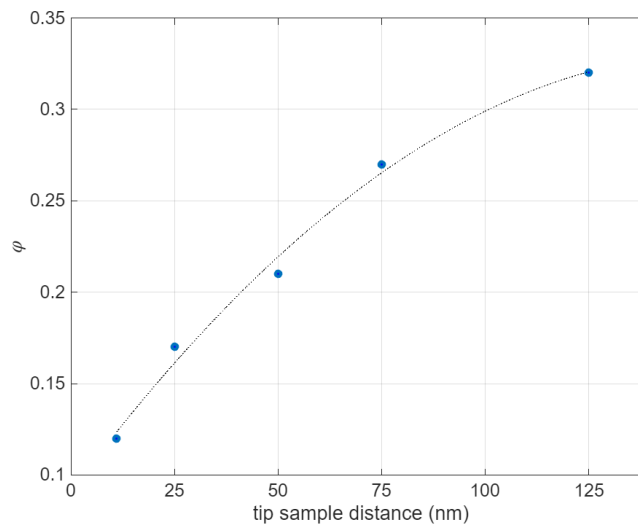


Figure 4-2. Calculated phase shift (in °) as a function of the tip-sample distance, from [5]

This phase shift can give information on the dielectric constant of the underneath sample. In the experiments detailed in this work, only the amplitude of the lock-in output was used.

To avoid the contribution of the jump to contact (see Chapter 1), only the retraction part of the curve was considered. The adhesion was minimized by acquiring all the curves at a relative humidity below 0.1%.

## 2 Comparison with the mSOL calibration

It is possible to use this technique to access the  $dC/dz$  quantity occurring between the AFM probe and the back electrode during an approach retract curve. As shown in Figure 4-1, the  $dC/dz$  can be separated into two contributions, the far part contribution coming from the cantilever and the near part contribution originating from the AFM probe cone and apex.

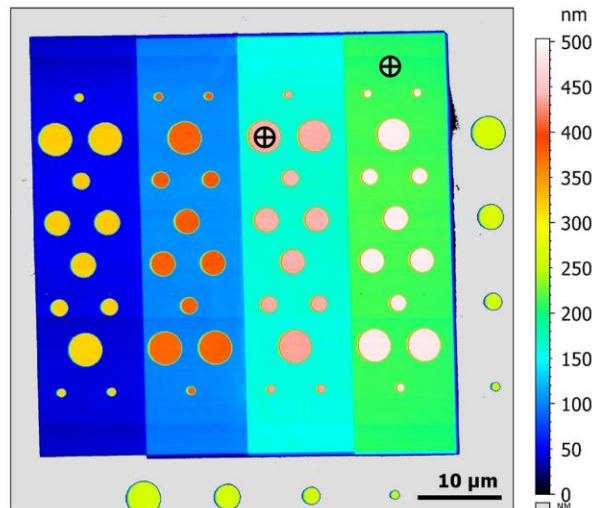


Figure 4-3. A64 MC2 calibration kit, black cross are the location of acquisition of the spectroscopy curve

In this section, the acquisition of the capacitance gradient on a bare dielectric part and above a capacitor of the MC2 calibration kit (A64) is presented (Figure 4-3). The  $S_{11,m}$  parameter was simultaneously acquired with a bandwidth of 100 Hz. The z-displacement covered a 1  $\mu\text{m}$  range with a speed of 16.7 nm/s. The objective was to use three points of the  $dC/dz$  curve as the reference points for the SMM mSOL calibration and to compare its performance with the case detailed in Chapter 3.

## 2.1 Capacitance gradient on the dielectric

After a scan of the A64 sample, the probe was moved toward the 100 nm terrace of  $\text{SiO}_2$  on the A64 calibration kit. Three series of 5 approach retract curves were acquired. The first two were unstable due to the non-linearity of the z-piezo actuator. Repeating 10 times the same experiment allows for the vanishing of the creep and non-linearity in the displacement of the z-actuator. The last series of approach-retract curves were used to extract the sensibility of the photodetector and the  $dC/dz$  quantity and its analysis is shown in Figure 4-4.

Considering a zero deformation at the tip-sample interaction, the photodetector's sensibility was extracted using the deflection signal as a function of tip-sample distance (Figure 4-4.a). After the tip enters in contact with the sample's surface, the cantilever starts to bend. The displacement in z is known from the piezoelectric actuator displacement.  $S$  is then given by the inverse of the slope of the curve in the red area. The data points which are too close from the "snap out of contact" are excluded to avoid the instability due to the large position change. Using Equation 4-6, the nominal  $k$  of the cantilever ( $18 \text{ N/m} \pm 7.2 \text{ N/m}$ ) and the  $S$  previously found, the lock-in signal is used to obtain the raw  $dC/dz$  signal (Figure 4-4.b). The  $dC/dz$  signal is then integrated to obtain the tip-sample capacitance ( $\Delta C$ ) relative to the far capacitance (Figure 4-4.c). Finally, the contribution of the cantilever is corrected by subtracting the projected slope computed in the red area to the raw  $\Delta C$ . Indeed, as shown in Figure 4-1, this slope correspond to long range capacitance. The corrected  $\Delta C$  is reported in Figure 4-4.d.

There is quite an important jump in the  $\Delta C$  curve during the "snap out of contact" (red vertical line). It is due to the large spring constant of the cantilever that translate in a large displacement on the probe during the snap out of contact. This important discontinuity made impossible the calibration of the instrument over the whole  $\Delta C$  range. The maximal  $\Delta C$  value available for the SMM calibration is of 0.07 fF. The calibrated  $S_{11}$  is shown in Figure 4-4.d (orange points). Three different  $\Delta C$  values are selected as reference for the mSOL calibration.

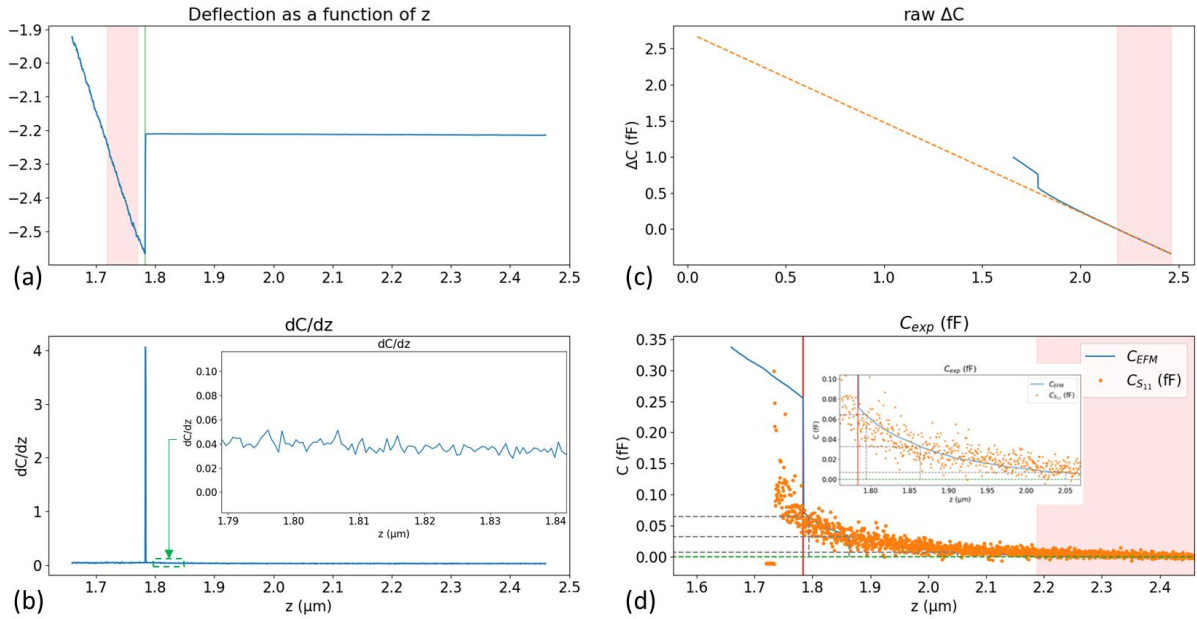


Figure 4-4. Interpretation of the retract curve over a capacitive pad ( $C_{07}$ ). (a): Deflection as a function of the tip-sample distance, (b): raw  $dC/dz$  considering the nominal spring constant ( $k = 18$  N/m). (c): raw  $\Delta C$  obtained by integrating the data from b. (d): Redressed  $\Delta C$  obtained by subtraction of the linear slope in the red area from (c) containing the long-range capacitance contribution.

To compare the two calibration methods, their application ranges must overlap. Although it is possible to access to the highest value of capacitance by using a softer cantilever to smooth the discontinuity, the maximal  $\Delta C$  value is of a few hundreds of aF. Another option would be to acquire the approach-retract curve over a MOS capacitor of the structure.

In Figure 4-5, the different capacitances in play are shown as well as the field lines. The tip sample capacitance is a combination of multiple capacitance. The apex-sample capacitance is a serie of  $C_{air}$  and  $C_{ox}$ . The capacitance defined by the capacitive structure is two to three order of magnitude larger than the one due to the air layer between the apex and the top electrode. The combined capacitance is then dominated by  $C_{air}$  (Equation 4-7).

$$\frac{1}{C_{apex}} = \frac{1}{C_{ox}} + \frac{1}{C_{air}} \approx \frac{1}{C_{air}} \quad \text{Equation 4-7}$$

The proposed method is therefore insensible to the  $C_{ox}$  quantity.

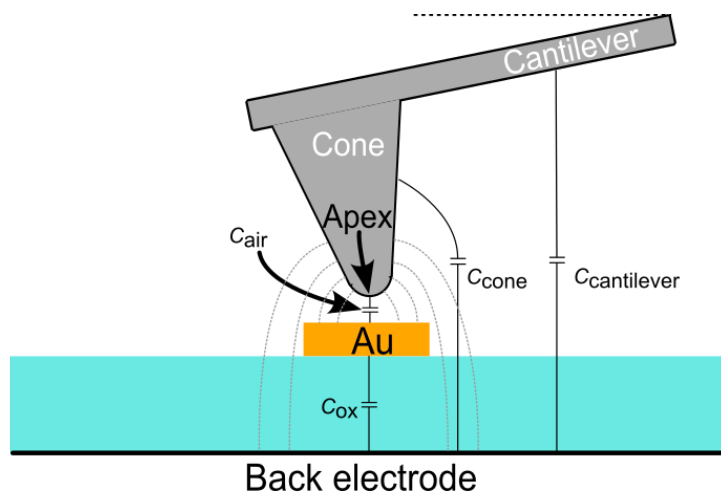
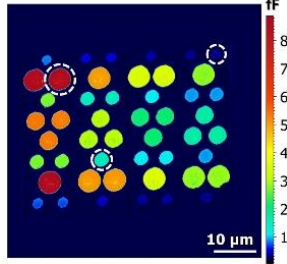
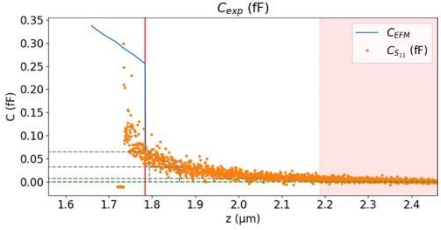


Figure 4-5. Configuration of the capacitance in play during the approach-curve experiment. Gray dashed line: Filed line between the AFM probe and the sample.



Future work will include measurement of  $dC/dz$  curve over a new calibration sample presenting MOS capacitors of lower value developed by the University of Lille. An overlap in the range of the two calibration methods can be expected. The experiment will be performed with a softer AFM tip ( $k = 0.8$  N/m or  $k = 0.6$  N/m). In the meantime, a take-home table of the difference between the two calibration methods is shown Table 4-1.

Table 4-1. Comparison between the two calibration methods

	Calibration standard	$dC/dz$
Principle		
Load	3 capacitances from calibration standard	3 Capacitances at different height from the studied sample
Advantages	Large range of capacitance Less sensible to tip geometry change.	No need for a calibration sample
Cons	Need for a calibration sample	Need to calibrate the spring constant of the cantilever Need an unchanged dielectric constant at kHz and GHz frequencies

### 3 Estimation of the cantilever spring constant

When acquiring an approach retract curve, the main uncertainty contribution comes from the spring constant of the cantilever according to Equation 4-5. The spring constant of the cantilever is given by the manufacturer with 40% uncertainty. In this section, a stage-of-the-art of the different methods for spring constant evaluation is presented. Then, a novel measurement method to access the spring constant of the cantilever from  $dC/dz$  curve is presented.

#### 3.1 Common methods for spring constant evaluation

The thermal noise [6] and Sader [7], [8] methods are used in everyday operations to measure the spring constant of the cantilever. Those methods are simple to implement but are associated with a quite large uncertainty (10% – 20%). Other methods such as ions milling [9] and added mass [10], and method based on force standards [11]–[13] are reported in the literature but the complexity of their setup made it difficult to generalize for everyday operation.

##### 3.1.1 Thermal noise

This method was first introduced in 1993 by Hutter and Bechhoefer [6]. Using the equipartition theorem, it is possible to link the cantilever’s displacement generated by the thermal fluctuation to the spring constant of the cantilever as shown in Equation 4-8,

$$\langle \frac{1}{2} m \omega_0^2 q^2 \rangle = \frac{1}{2} k_B T \tag{Equation 4-8.}$$

where  $q$  is the displacement of the cantilever. For AFM probes used in everyday operation (RMN 25Pt300B and 12Pt300B), the nominal spring constant is respectively 18 N/m and 0.8 N/m. Applying Equation 4-8, the cantilever displacement is below 0.1 nm which is not reasonably detectable. Instead, the thermal noise measurement focuses on the frequency domain. The spring constant is then linked to the area below the resonance peak ( $P$ , shown in Figure 4-6) by Equation 4-9.

$$k = \frac{k_B T}{P} \quad \text{Equation 4-9.}$$

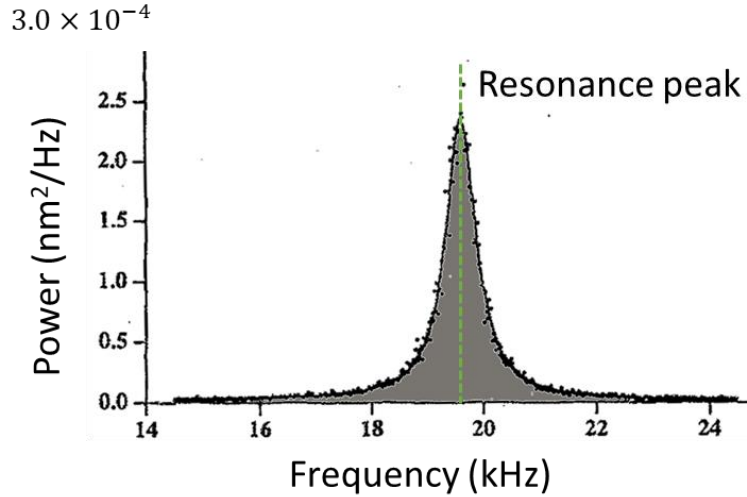


Figure 4-6. Power spectral density plot of fluctuations in the output of the cantilever deflection detector. The resonant peak is fit to a Lorentzian spectrum [6]

This power spectral density plot was measured by acquiring multiple time series experiments. They are then switched to frequency series by Fourier transform and averaged together [14]. The typical uncertainty of this method is in the 10% – 30% range [15], [16]. The main contributions to this uncertainty are the laser spot size, the z-displacement of the piezo calibration, and the determination of the photodetector sensitivity. This uncertainty can be lowered by reducing the white noise by putting the system in a vacuum and using of interferometric system to emancipate from the sensitivity measurement [17]. The uncertainty reported by such a system is in the 3% range.

### 3.1.2 Sader method

Noticing the absence of standardization in spring constant measurement between laboratories, Sader and his group proposed a centralized application on which the users can input the measured resonance frequency ( $f_R$ ) and quality factor ( $Q$ ) as well as the AFM probe used which is translated by the coefficient  $A$  (Equation 4-10.a) [7]:

$$k_{\text{sader}} = A Q f_R^{1.3} \quad \text{Equation 4-10.a}$$

$$k_{\text{sader,rect}} = 0.1906 \rho b^2 L Q \Gamma_i(\omega_R) \omega_R^2 \quad \text{Equation 4-10.b}$$

where  $\rho$  is the density of the fluid surrounding the AFM probe,  $b$  and  $L$  are the width and length of the cantilever and  $\Gamma_i(\omega_R)$  is the imaginary part of the hydrodynamic function of the cantilever. Equation 4-10.a was derived from Equation 4-10.b [8] used to extract the cantilever spring constant of a rectangular cantilever from the resonance frequency and quality factor.

In its general expression, the coefficient  $A$  is computed from the average of the community-based measurement (Equation 4-11) [7], [8].

$$A = \frac{1}{N} \sum_{i=1}^N \frac{k_{\text{ref},i}}{f_{R,\text{ref},i}^{1.3} Q_{\text{ref},i}} \quad \text{Equation 4-11.}$$

This method allows compensation of the instrument and operator uncertainty in the spring constant measurement by the thermal noise method. Indeed, Sader et al. [7] reported an inter-laboratory comparison of the measurement of the spring constant of the same AFM cantilever by thermal noise (Figure 4-7) and showed an important disparity from one group and one user to another.

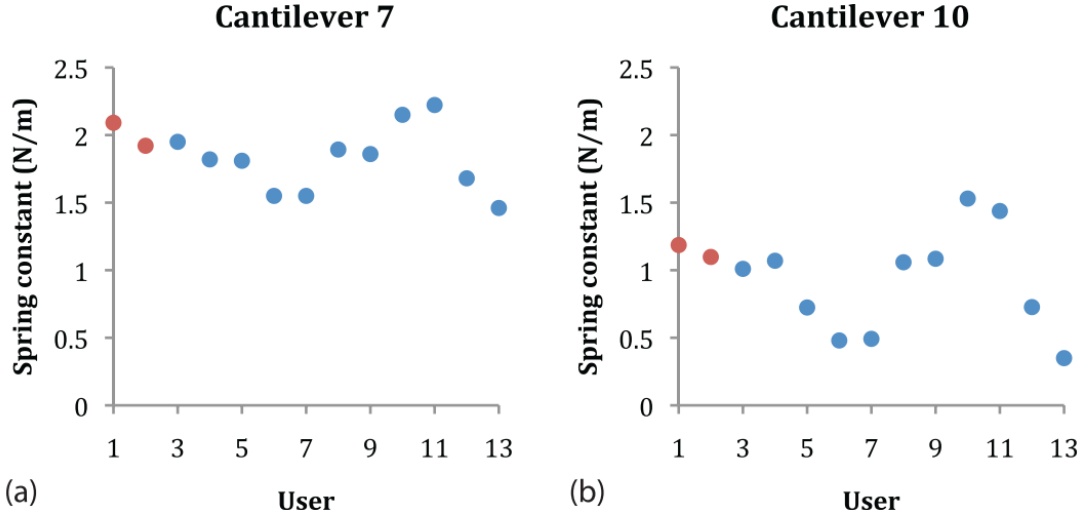


Figure 4-7. Measured spring constant for two cantilevers using by thermal noise using laser Doppler vibrometer (LDV) (red points) and the native thermal noise measurement (blue points) [7]

Averaging the  $A$  parameter over multiple measurements performed on the same type of AFM probe can help to reduce the uncertainty associated with the spring constant as reported in [16]. Nevertheless, due to the manufacturing process, there is a large disparity in RMN probe geometry making the Sader method ill-adapted to this application case.

### 3.1.3 Ion milling method

This method allows for spring constant measurement with an associated uncertainty between 7% and 10 %, with possible reduction to less than 5% [9]. A given volume of material is removed from the cantilever of the AFM tip by the focused ion beam (FIB). The resonance frequency is evaluated for the AFM tip before and after the milling. The spring constant of the cantilever can be linked to the shift in resonance frequency by Equation 4-12.

$$k = \frac{4\pi^2 M}{\omega_0^{-2} - \omega_1^{-2}} \quad \text{Equation 4-12.}$$

where  $M$  is the mass of the removed material, and  $\omega_0$  ( $\omega_1$ ) is the resonance frequency of the cantilever before (after) milling. The location of the removal area impacts differently the frequency shift. This is taken in account by considering an effective removed mass ( $M_{\text{effective}}$ ). The relationship between the effective mass and spring constant ( $k_{\text{effective}}$ ) is then given by Equation 4-13.

$$M_{\text{effective}} = \frac{k_{\text{effective}}}{\omega^2} - M^* \quad \text{Equation 4-13.}$$

where  $M^*$  is the effective mass of the cantilever before milling. They acquired the resonance frequency of the AFM probe after removal of increasingly larger mass. By plotting  $M_{\text{effective}}$  as a function of  $\omega$ , they obtained a linear plot of slope equal to  $k_{\text{effective}}$  according to Equation 4-13. The milled cantilever and results are shown in Figure 4-8.

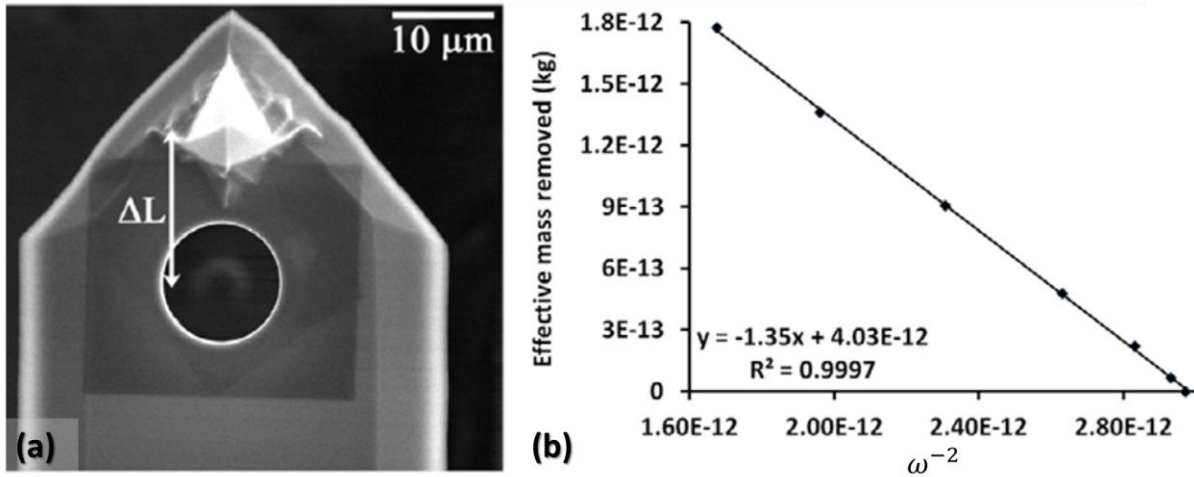


Figure 4-8. (a) Milled cantilever of an AFM tip (F1),  $\Delta L$  is the location of the center of removed volume compared to the apex. (b)  $M_{\text{effective}}$  as a function of  $\omega^{-2}$ . [9]

To preserve the structural integrity of the cantilever, the hole's diameter to cantilever's width ratio is set below 0.5. The cantilever's spring constant is extracted with uncertainty of 7.1%. An uncertainty budget is presented by Slattery. The largest contribution comes from dimensional measurement of the cantilever's and hole's geometries. They proposed additional precaution in the milling and SEM imaging steps to reduce the uncertainty below 5%.

This method is similar to the method of added mass presented by [10]. It shows improved associated uncertainty at the cost of the destruction of parts of the probe.

### 3.1.4 Force sensor

In 2007, Langlois et al. [16] made use of the NIST electrostatic force balance to perform traceable measurements of the spring constant of the AFM probe's cantilever. Other groups have performed calibration of the cantilever's spring constant using force sensor:

- Triskelion piezoelectric force sensor [11]
- Test bench relying on MEMS [12]
- Photoelestatic force sensor [13]
- Electrostatic force experiment [18].

Nevertheless, those method is quite demanding in instruments and cannot reasonably be generalized to industrial and academic laboratories. In this section, the method used by Langlois is detailed. The electrostatic force balance (EFB) is a force standard that is primarily used to realize the milligram unit as defined in the 2018 revision of the SI [19]. It can also be used to apply a known force to an object. In their paper, Langlois et al. [16] suggested using the EFB to apply a force to a piezoresistive cantilever to calibrate its stiffness. The calibrated piezoresistive cantilever acts as a sensor for the mechanical force ( $F$ ) applied by the test cantilever. As presented in Figure 4-9.b, the test AFM probe is located above the piezoresistive cantilever and moved down. The spring constant of the test cantilever is given by Equation 4-14,

$$F \cdot \cos(\theta) = k \frac{\delta_c}{\cos(\theta)} \quad \text{Equation 4-14.}$$

where  $\delta_c$  is the deflection of the test cantilever measured by the photodetector array and  $\theta$  is the tilt angle of the test cantilever. For the same applied force, the deflection of the reference cantilever and therefore the piezoresistive response change as a function of the location of the contact between the reference cantilever and the element applying the force (EFB or test cantilever). This location differs between the two configurations. The change in the piezoresistive response needs to be compensated

by a tip location coefficient. For a perfectly rectangular reference cantilever, this coefficient can be computed from the length of the cantilever and the location of the point of application. This generated an uncertainty in the force measurement originating from the cantilever shape and dimensions.

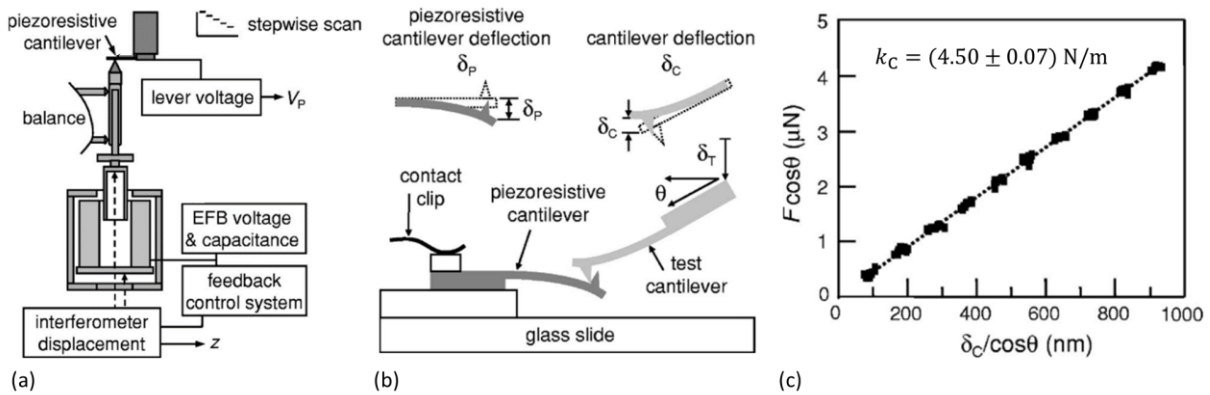


Figure 4-9. (a). Experimental setup for calibration of the piezoresistive cantilever. (b). Schematic of the experimental setup for spring constant measurement of AFM probe's cantilever. (c). Experimental data: force applied by the test cantilever as a function of the test cantilever's deflection

Langlois and his group reported the nominal and measured spring constant for different cantilevers (Table 4-2). They used the EFB to directly measure the spring constant (case Figure 4-9.a), the measurement using the piezoresistive reference cantilever (case Figure 4-9.b), and the thermal noise and Sader methods.

Table 4-2. Measured cantilever spring constant (in N/m) obtained by 4 different methods with associated uncertainty, [16]

Cantilever #	1	3	4
$k_{\text{nom}}$	$0.2 \pm 0.4$	$3.5 \pm 0.8$	$15 \pm 16$
$k_{\text{EFB}}$	$0.0634 \pm 0.0007$	$4.38 \pm 0.02$	$11.2 \pm 0.3$
$k_{\text{piezo}}$	$0.0667 \pm 0.0010$	$4.86 \pm 0.07$	$12.2 \pm 0.6$
$k_{\text{therm}}$	$0.0652 \pm 0.0027$	$4.81 \pm 0.15$	$9.2 \pm 0.2$
$k_{\text{Sader}}$	$0.0694 \pm 0.0011$	$4.24 \pm 0.16$	$11.5 \pm 0.1$

The uncertainty of the piezoresistive method is in the 1.5% to 5% range over the 0.06 N/m to 12 N/m span. It needs to be compared with other commonly used methods returning uncertainty in the 2.2% to 4.2% range for the same spring constant span.

### 3.2 Electrostatic method

In this work, another method based on the electrostatic force microscopy procedure presented at the beginning of this chapter is developed.

The method presented in the above section are either difficult to implement, either shows unsatisfying uncertainty on the spring constant measurement. Another method would be to use the EFM-based method presented at the beginning of this chapter. Approach retract curve on dielectric sample of known dielectric constant can be used to obtain a traceable measurement of the cantilever's spring constant provided the AFM probe geometry is known. The process is reported in Figure 4-10.

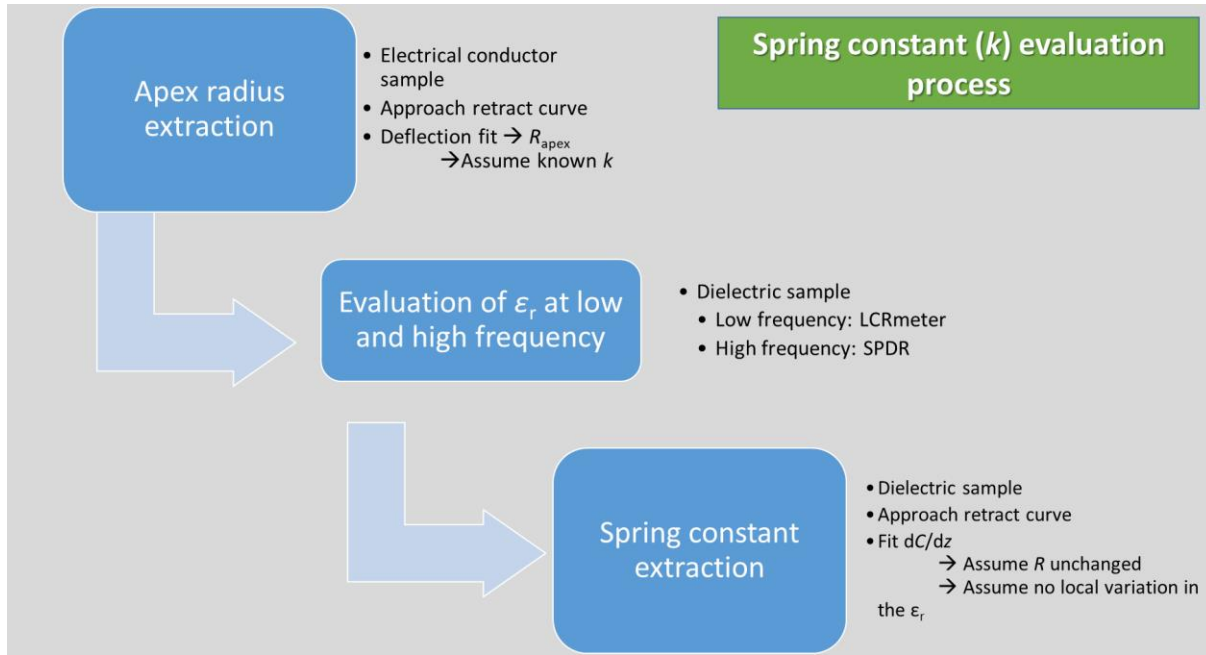


Figure 4-10. Experimental process to extract the spring constant of the cantilever from  $dC/dz$  curve

First, the radius of the apex of the AFM probe is measured by acquiring the  $dC/dz$  above a conductive sample. There exists a relationship between the probe geometry and electrostatic force between the AFM probe and the conductive sample [20],

$$F_{tot} = \pi\epsilon_0 V^2 \left[ \frac{R\tilde{R}}{z(z+\tilde{R})} + A^2 \left( \ln\left(\frac{z+\tilde{R}}{H}\right) - 1 + \frac{R \cos^2 \theta_0 / \sin \theta_0}{z+\tilde{R}} \right) \right] \quad \text{Equation 4-15.a}$$

$$\tilde{R} = R(1 - \sin(\theta_0)) \quad \text{Equation 4-15.b}$$

$$A^2 = \left[ \ln\left(\tan\left(\frac{\theta_0}{2}\right)\right) \right]^{-2} \quad \text{Equation 4-15.c}$$

where  $V$  is the applied voltage to the AFM tip,  $z$  is the tip-sample distance,  $R$  is the radius of the apex,  $H$  is the cone height, and  $\theta_0$  is the cone angle opening. The electrostatic force can be converted in  $dC/dz$  quantities by Equation 4-16.

$$\frac{dC}{dz} = -\frac{2F_{tot}}{V^2} + \frac{dC}{dz} \Big|_{\text{far from surface}} \quad \text{Equation 4-16.}$$

The contribution of the cantilever to the  $dC/dz$  quantity is corrected by subtracting the  $dC/dz$  quantity far from the surface as explained in Section 2.

Using an RMN tip with a nominal spring constant of 0.8 N/m, four series of 10 approach retract curves were acquired over a gold sample of surface roughness (RMS) below 17 nm. The experimental  $dC/dz$  quantity is reported in Figure 4-11.

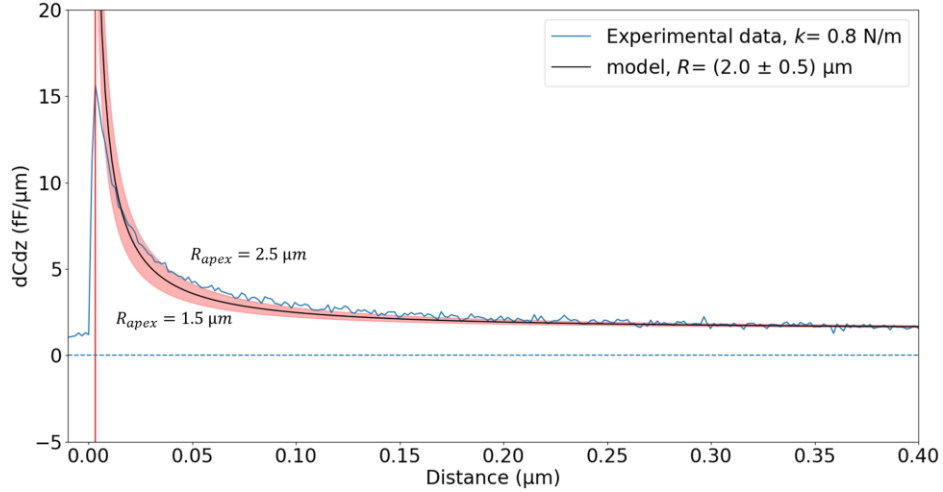


Figure 4-11. Fit using Equation 4-15 and Equation 4-16 of the experimental  $dC/dz$  quantity over a gold sample acquired with an RMN tip ( $k_{nom}=0.8$  N/m). The blue area covers the  $dC/dz$  values returned by the model for  $R_{apex}$  ranging from 1.5 to 2.5  $\mu\text{m}$ .

Using Equation 4-15 and Equation 4-16, the superposition of experimental data with a model tip with a radius ranging from 10 nm to 50 nm shows good agreement considering the nominal spring constant of the cantilever. Then, a series of approach retract curves were done over a dielectric sample previously characterized at low (few kHz) and high (3.36 GHz and 14.93 GHz) frequencies. The dielectric constant of this sample was macroscopically measured by an LCRmeter and a split post-dielectric resonator as described in Chapter 1. Results of the LCRmeter experiment are reported in Figure 4-12 with combined uncertainty below 0.3%.

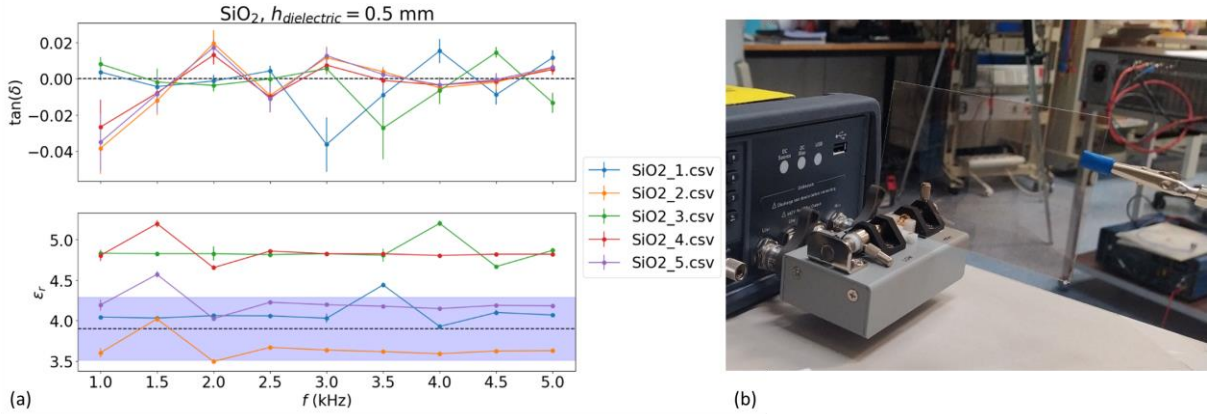


Figure 4-12. (a) Loss tangent and dielectric constant of the  $\text{SiO}_2$  sample obtained from capacitance measurement by LCRmeter. (b) Picture of the test bench used with the two electrodes forming the measured capacitor ( $R_{electrode} = 0.19$  mm)

The considered uncertainty contribution in this measurement is the electrode radius and the repeatability over 3 successive measurements. Once the dielectric sample has been characterized, a series of  $dC/dz$  curves can be acquired with the AFM probe under test (Figure 4-13). Repeatability was evaluated by taking the last three curves of the last series of 10 approach-retract curves (green area in Figure 4-13). The expected tip-sample capacitance is computed from Equation 4-17 [21].

$$\frac{dC_{apex}}{dz} = 2\pi\epsilon_0 \frac{R\tilde{R}}{B(z + h/\epsilon_r)} \quad \text{Equation 4-17.a}$$

$$\frac{dC_{cone}}{dz} = \frac{2\pi\epsilon_0}{\ln(\tan(\theta_0/2))^2} \left[ \ln\left(\frac{H}{B}\right) - 1 + \frac{R \cos(\theta)^2}{B \sin(\theta)} \right] \quad \text{Equation 4-17.b}$$

$$B = z + \frac{h}{\epsilon_r} + \tilde{R}$$

Equation 4-17.c

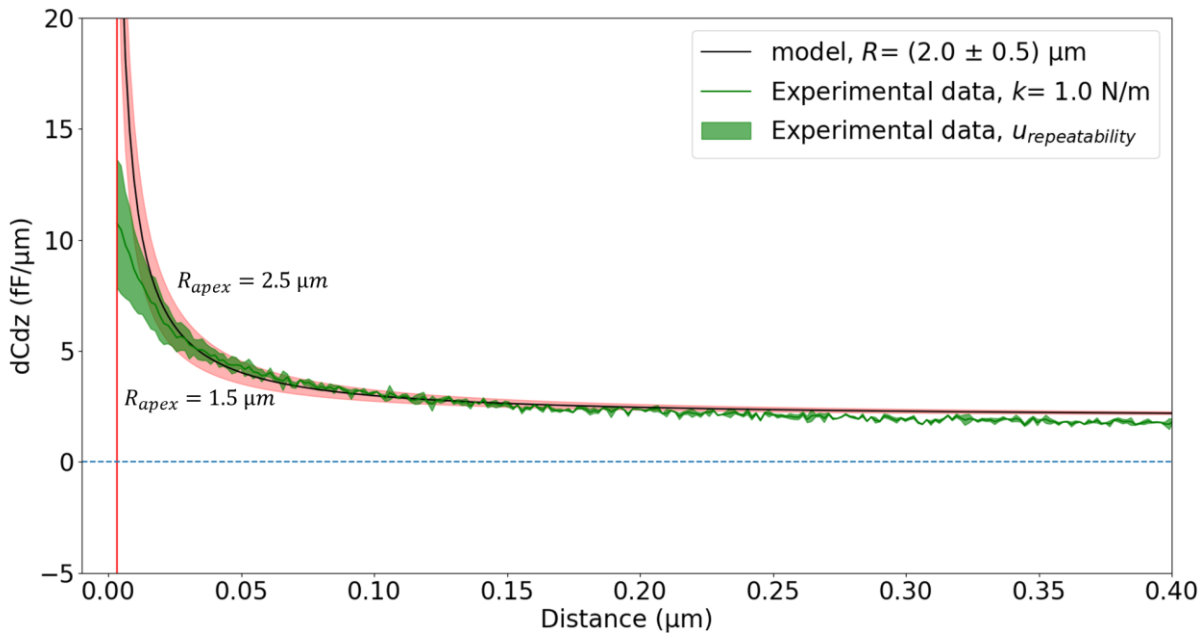


Figure 4-13. Experimental  $dC/dz$  quantity over a  $\text{SiO}_2$  sample ( $\epsilon_r=3.80$ ), repeatability over 3 successive approach-retract curves obtained by the same probe than the one used in Figure 4-11.

A spring constant of 1.0 N/m is a good fit to the expected data for an AFM probe with  $R = 2 \mu\text{m}$  as found in the previous experiment over the gold sample. The nominal spring constant of this tip is 0.8 N/m which is coherent with this measurement. Future experiments should include a thermal noise experiment on the same AFM tip before and after the  $dC/dz$  experiment to allow for comparison with the known method.

Equation 4-17 is valid for thin films. The dielectric sample used for the experiment in Figure 4-13 has a thickness of 0.5 mm which doesn't satisfy this condition. It is planned to repeat the experiment over a dielectric area of the capacitance calibration kit (MC2, v1, A64) to satisfy the thin film condition. The following procedure is proposed for the second set of experiments.

- Capacitance measurement of a MOS structure of the 50 nm  $\text{SiO}_2$  layer of A64 for dielectric constant extraction
- SEM image of the AFM tip to gain knowledge of its specific geometrical properties
- Spring constant evaluation by thermal noise
- Acquisition of the  $dC/dz$  curve over the gold sample for evaluation of the apex radius
- Acquisition of the  $dC/dz$  curve over the 50 nm  $\text{SiO}_2$  layer of the A64 sample for evaluation of the spring constant
- Spring constant evaluation by thermal noise
- Scan over the tip characterizer sample (Supracon) [22] with limited contact force to extract the apex radius.

This protocol will provide a well-known geometry of the AFM tip, bringing closer the model from the actual experiment and improving the uncertainty evaluation process. It will also improve the metrology of the experiment by providing a controlled evaluation of the spring constant by another method (thermal noise) before and after the tip is brought into contact with samples.

During the experiment, the static bending of the cantilever changes with the tip-sample distance. This static bending adds uncertainty to the tip-sample distance. A solution to this issue was recently proposed by Georg Gramse from Johannes Kepler University (JKU). It is to acquire the  $2\omega$  oscillation of the cantilever as a function of the static bending of the cantilever at a constant tip-sample distance for



different amplitudes of the AC voltage. As the AC amplitude is increased, so is the  $2\omega$  oscillation amplitude and static bending of the cantilever (Figure 4-14). The evolution rate of these quantities is linked to the cantilever stiffness. This experiment could be conducted by the tapping mode in the Keysight AFM. The static bending and  $2\omega$  oscillation amplitude would be measured by the photodetector array.

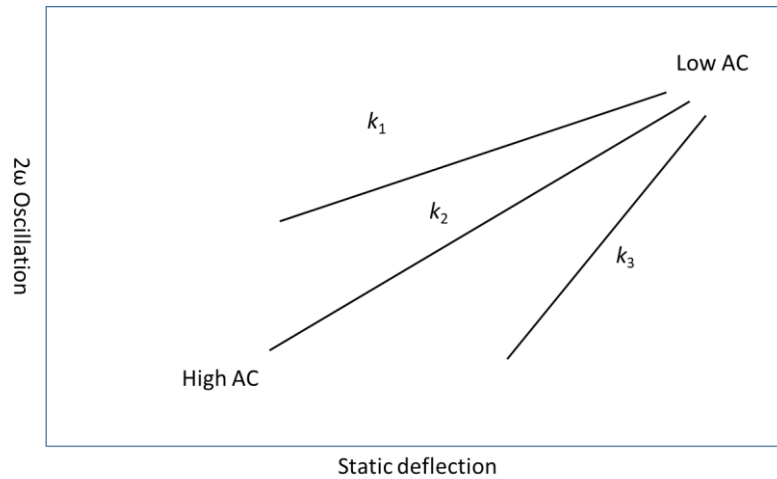


Figure 4-14. Expected behavior of the  $2\omega$  oscillation as a function of the static deflection.

## 4 Conclusion

In this chapter, the  $dC/dz$  approach retract curve acquisition is detailed. A tentative comparison between this method and the calibration method from Chapter 3 was conducted. The experiment was conducted on the bare dielectric with a satisfying calibration of the  $S_{11}$  parameter. Nevertheless, the comparison with the method using the calibration method was not possible due to a lack of overlap between the two ranges of validity for the two methods. Perspectives are presented to solve this issue. By its nature, the  $dC/dz$  method is highly sensitive to the spring constant of the cantilever. A method is presented to perform a traceable measurement of the cantilever's spring constant in the second part of this chapter. Although well established in the community, spring constant measurement methods suffer from a lack of traceability to the SI. NIST has shown a method involving electrostatic force balance and a calibrated piezoresistive cantilever to apply a known force on the test cantilever and gain access to its spring constant. Nevertheless, this technique requires access to an electrostatic force balance or, at the very least to a calibrated cantilever to act as a transfer instrument to measure the force applied by the test cantilever. Here, a new calibration method based on the  $dC/dz$  approach retract is presented. It required the knowledge of the AFM probe geometry and a dielectric standard of known permittivity. Primary results are promising. A comparison with the thermal noise method or other well-established spring constant characterization techniques is required to better evaluate the accuracy of this technique. A protocol is proposed for future experiments to complete the analysis and establish a metrology of this measurement technique.

Limitations in this technique can be seen in the modification of the static bending of the cantilever as the tip-sample distance is changed adding uncertainty on  $z$ . One way to compensate for it would be to operate at a given tip-sample distance and to vary the amplitude of the AC potential using the native tapping mode in the AFM. The quantities of interest are then the static deflection and the amplitude of the  $2\omega$  oscillation of the cantilever. By plotting those two quantities, the spring constant of the cantilever can be extracted.

Having a method to measure the spring constant of the cantilever in a traceable fashion is key to improve the uncertainty associated with the  $dC/dz$  approach retract curve. Acquiring such a curve can

allow for electrical properties measurement on a sample without any deposition of gold pads with improved spatial resolution.

- [1] P. Girard, "Electrostatic force microscopy: Principles and some applications to semiconductors," *Nanotechnology*, vol. 12, no. 4, pp. 485–490, 2001, doi: 10.1088/0957-4484/12/4/321.
- [2] S. Lilliu *et al.*, "EFM data mapped into 2D images of tip-sample contact potential difference and capacitance second derivative," *Sci. Rep.*, vol. 3, pp. 17–19, 2013, doi: 10.1038/srep03352.
- [3] L. Fumagalli, G. Ferrari, M. Sampietro, and G. Gomila, "Dielectric-constant measurement of thin insulating films at low frequency by nanoscale capacitance microscopy," *Appl. Phys. Lett.*, vol. 91, no. 24, 2007, doi: 10.1063/1.2821119.
- [4] F. Marchi, R. Dianoux, H. J. H. Smilde, P. Mur, F. Comin, and J. Chevrier, "Characterisation of trapped electric charge carriers behaviour at nanometer scale by electrostatic force microscopy," *J. Electrostat.*, vol. 66, no. 9–10, pp. 538–547, 2008, doi: 10.1016/j.elstat.2008.06.006.
- [5] G. A. Schwartz, C. Riedel, R. Arinero, P. Tordjeman, A. Alegría, and J. Colmenero, "Broadband nanodielectric spectroscopy by means of amplitude modulation electrostatic force microscopy (AM-EFM)," *Ultramicroscopy*, vol. 111, no. 8, pp. 1366–1369, 2011, doi: 10.1016/j.ultramic.2011.05.001.
- [6] J. L. Hutter and J. Bechhoefer, "Calibration of atomic-force microscope tips," *Rev. Sci. Instrum.*, vol. 64, no. 7, pp. 1868–1873, 1993, doi: 10.1063/1.1143970.
- [7] J. E. Sader *et al.*, "A virtual instrument to standardise the calibration of atomic force microscope cantilevers," *Rev. Sci. Instrum.*, vol. 87, 2016.
- [8] J. E. Sader *et al.*, "Spring constant calibration of atomic force microscope cantilevers of arbitrary shape," *Rev. Sci. Instrum.*, vol. 83, 2012, doi: 10.1063/1.4757398.
- [9] A. D. Slattery, J. S. Quinton, and C. T. Gibson, "Atomic force microscope cantilever calibration using a focused ion beam," *Nanotechnology*, vol. 23, no. 28, 2012, doi: 10.1088/0957-4484/23/28/285704.
- [10] J. P. Cleveland, S. Manne, D. Bocek, and P. K. Hansma, "A nondestructive method for determining the spring constant of cantilevers for scanning force microscopy," *Rev. Sci. Instrum.*, vol. 64, no. 2, pp. 403–405, 1993, doi: 10.1063/1.1144209.
- [11] R. K. Leach *et al.*, "Advances in engineering nanometrology at the National Physical Laboratory," *Meas. Sci. Technol.*, vol. 23, no. 7, 2012, doi: 10.1088/0957-0233/23/7/074002.
- [12] U. Brand *et al.*, "Small Force Metrology for AFM, Stylus Instruments, CMM and Nanoindenter," *CPEM 2018 - Conf. Precis. Electromagn. Meas.*, no. Cmm, pp. 14–15, 2018, doi: 10.1109/CPEM.2018.8500987.
- [13] N. E. Khelifa, "Miniaturized Nd-YAG laser as photoelastic transducer for small forces sensing," *17th Int. Congr. Metrol. CIM 2015*, vol. 2, pp. 1–6, 2015, doi: 10.1051/metrology/20150004002.
- [14] J. E. Sader, M. Yousefi, and J. Friend, "Uncertainty in least-squares fits to the thermal noise spectra of nanomechanical resonators with applications to the atomic force microscope," no. February 2014, 2014, doi: 10.1063/1.4864086.
- [15] Y. Song, S. Wu, L. Xu, and X. Fu, "Accurate Calibration and Uncertainty Estimation of the Normal Spring Constant of Various AFM Cantilevers," pp. 5865–5883, 2015, doi: 10.3390/s150305865.
- [16] E. D. Langlois, G. A. Shaw, J. A. Kramar, J. R. Pratt, and D. C. Hurley, "Spring constant calibration of atomic force microscopy cantilevers with a piezosensor transfer standard," *Rev. Sci. Instrum.*, vol. 78, no. 9, pp. 1–10, 2007, doi: 10.1063/1.2785413.
- [17] P. Paolino, B. Tiribilli, and L. Bellon, "Direct measurement of spatial modes of a micro-cantilever from thermal noise To cite this version : HAL Id : ensi-00379365 Direct measurement of spatial modes of a micro-cantilever from thermal noise," 2009.
- [18] E. Bonaccorso, F. Schönfeld, and H. J. Butt, "Electrostatic forces acting on tip and cantilever in atomic force microscopy," *Phys. Rev. B - Condens. Matter Mater. Phys.*, vol. 74, no. 8, pp. 1–8, 2006, doi: 10.1103/PhysRevB.74.085413.
- [19] "Mise en pratique for the definition of the kilogram in the SI," 2019.
- [20] S. Hudlet, M. Saint Jean, C. Guthmann, and J. Berger, "Evaluation of the capacitive force between an atomic force microscopy tip and a metallic surface," *Eur. Phys. J. B*, vol. 2, no. 1, pp. 5–10, 1998, doi: 10.1007/s100510050219.

- [21] G. Gramse, M. Kasper, L. Fumagalli, G. Gomila, P. Hinterdorfer, and F. Kienberger, "Corrigendum: Calibrated complex impedance and permittivity measurements with scanning microwave microscopy (2014 Nanotechnology)," *Nanotechnology*, vol. 26, no. 14, 2015, doi: 10.1088/0957-4484/26/14/149501.
- [22] Supracon, "Tip characterizer."

# Conclusion

This thesis work focuses on the development of a metrology for sub-micrometric measurement of electrical properties. The scanning microwave microscopy (SMM) can fit those specifications. It is an atomic force microscope (AFM) interfaced with a vector network analyzer (VNA). If the metrology for VNA measurement is well established, it is not the case for the SMM.

In this thesis, it was demonstrated the possibility of producing capacitance standards for SMM calibration with associated uncertainty below 2.9%. After taking the output of this uncertainty budget, another calibration structure was put in production and characterized with uncertainty below 1.9%. In both cases, the main contributions to the uncertainty are the dimensional measurements (top electrodes area, dielectric and electrodes thickness) and electrical properties of the dielectric layer (depletion capacitance and dielectric constant). Further improvement in the uncertainty of both structures can be foreseen if in-situ measurement of the dielectric constant can be performed.

Then the modified Short Open Load calibration method was evaluated over the two calibration structures. A relative deviation within 5% is found between the expected and measured capacitances over the whole structure. The associated uncertainty was found below 3% with major contribution originating from the capacitance definition, the repeatability of the measurement and the  $S_{11,m}$  histogram defined on each pads. Improvement could be foreseen by acquiring the image on smaller area. The impact of relative humidity, location on the sample and used AFM tip was studied. The impact of water meniscus on the calibration was further investigated by numerical simulation. The error parameters associated with a bare SMM tip were applied to the same SMM tip with a water meniscus. The relative deviation between the expected and computed capacitance is found negligible for capacitances above 4 fF and tops at 0.4% for 0.3 fF capacitances. The substitution method was used to ensure sub-micrometric resolution. The performance of the method was tested by comparing results to a shielded SMM tip. No significant difference could be seen between the two processing methods. A comparison between the two different versions of the calibration structure was started but requires additional work to be completed. Finally, a case study is presented with the extraction of the dielectric constant of a PZT and PMN-PT samples using the calibrated SMM. The dielectric constant was found with uncertainties of 3.5% for the PZT sample and 6.9% for the PMN-PT sample. This difference can be explained by the roughness of the PMN-PT sample which made the characterization of pads' area more difficult.

Finally, the last chapter focuses on  $dC/dz$  curve by EFM. The  $S_{11,m}$  were recorded while performing the  $dC/dz$  curve. After calibration using three points on the curve, a good agreement was founded between the capacitance measured by the EFM method and by the SMM. A comparison with the method relying on the capacitance standard was unsuccessful due to the lack of overlap between the two capacitance range covered by the two methods. As the capacitance value returned by the EFM depends strongly on the spring constant of the cantilever, a focus was shined on the methods used to evaluate it. A state of the art of measurement techniques for the evaluation of spring constant of AFM probes is presented. Then, the  $dC/dz$  curve was also used to establish a traceable measurement technique for the spring constant of the AFM's cantilever.

# Future work and perspective

To complete the uncertainty budget associated with the capacitance values of the two versions of the MC2 standards, the dielectric constant of the SiO<sub>2</sub> layer will be evaluated by capacitance measurement using an LCRmeter interfaced with the four-probe station. After adaptation of the existing system, coaxial probe will be used to perform the measurement. Numerical simulation will be done to estimate the dielectric constant from the MOS capacitor dimension in a similar way as for the PZT and PMN-PT dielectric constant extraction. Having the in-situ value of dielectric constant of the SiO<sub>2</sub> layer of each structure will remove doubt on the origin of the systemic error observed in the comparison of the SMM measurement between the two reference structures.

A new comparison between the two versions of the capacitance standards will be performed after making sure that they are in the same z-plane to minimize the scanner displacement. The measurement on the sample used for calibration will be done before and after the measurement on the test sample and will be repeated at different frequencies to investigate the effect of the depletion capacitance. With actualized values of the dielectric constant, the new values of the capacitance of the standards will be more accurate and a reduction in the deviation between computed and measured capacitances on the test sample could be expected.

The improvement in SMM measurement observed when the probe (RMN tip) is coated with a graphene layer will be further investigated. Two hypothesis were proposed to explain the reduction in the standard deviation associated with the values: the hydrophobic property of the graphene layer or an improved mechanical stability of the cone and apex. The hydrophobic property could be confirmed by the acquisition of adhesion force curves as a function of relative humidity for both probes. The measured values of adhesion force will then be corrected by the geometry of the probe. Finally,  $S_{11,m}$  maps will be acquired at high scan speed and the histograms associated with each MOS capacitor will be studied. If a smaller FWHM is observed for the graphene-coated tip compared to the non-coated one, it could indicate an improved mechanical stability of the probe.

The water meniscus impacts on the calibration will be further investigated by acquiring  $S_{11,m}$  maps on capacitance standard exhibiting smaller capacitance values (below 100 aF) proposed by Kamel Haddadi from the University of Lille.

Using the second version of the capacitance calibration kit with higher capacitance values, the PZT and PMN-PT samples will be measured again. This will enable the capacitance measurements of all the capacitors presented on the test structures. The larger ones could be used to check the validity of the dielectric constant previously extracted by comparing the computed capacitances to the measured one. By considering the conductance measured by the SMM on a suitable calibration standards, it could be possible to calibrate the SMM not only in capacitance but also in resistance. This could enable the extraction of the complex permittivity of the test sample. An application could be found in the evaluation of the loss tangent of material with similar spatial resolution as the capacitance measurement.

The  $dC/dz$  calibration method will be done on a new capacitance standard presenting lower capacitances values. Then, a  $S_{11,m}$  map of the pattern is acquired and the instrument is calibrated using the first method and the  $dC/dz$  curve previously acquired. A comparison between the two methods will be conducted by taking advantage of the smallest capacitances.

A comprehensive uncertainty budget associated with the  $dC/dz$  method will be established. A special attention will be given to the role of relative humidity which is expected to be important. The shape of the probe will be measured by SEM before and after the experiment to check for the erosion of the tip in an effort to quantify the time deviation.

The result of the proposed method to characterize the spring constant of the cantilever will be compared to thermal noise measurement. The tip under study will be characterized by SEM before and after the experiments. The goal here is to complete the uncertainty budget associated with the measurement as it

is strongly dependent on the probe geometry. The major uncertainty contributions could be identified and precaution could be suggested to improve the accuracy of the method.

For the mid and long-term development, progress could be foreseen in the shielded tip. The tips presenting a coplanar waveguide on the cantilever to bring the RF signal would show a higher form factor than existing shield tip leading to local measurement. The centered location of the RF contact will required little or no adaptation of the probe holder. Similar test as the ones performed for the performance evaluation of the sMIM probe will be done on a reference sample to evaluate the shielding of the cantilever. The development of a fully shielded SMM probe, while allowing for true local measurements, represents an important technical challenge.

To prevent early tip blunting, it could be interesting to operate the SMM in intermittent contact mode such as peak force microscopy. This will allow for the minimization of the lateral force during the displacement of the probe while applying the same contact force while acquiring the  $S_{11,m}$  parameter. Using this type of mode will enable the acquisition of SMM images at a higher scan speed which could help enlarge the community of SMM users.

FOLIO ADMINISTRATIF

THESE DE L'INSA LYON, MEMBRE DE L'UNIVERSITE DE LYON

NOM : RICHERT  
(avec précision du nom de jeune fille, le cas échéant)

DATE de SOUTENANCE : 08/07/2024

Prénoms : Damien

TITRE : Métrologie des techniques de microscopie à sonde locale micro-onde appliquées aux mesures de transport dans le domaine des semiconducteurs

NATURE : Doctorat

Numéro d'ordre : AAAAISALXXXX

Ecole doctorale : ED160 Electronique, Electrotechnique, Automatique

Spécialité : Electronique, micro et nanoélectronique, optique et laser

RESUME : Cette thèse se focalise sur l'établissement d'une métrologie des mesures de propriétés électrique à l'échelle submicrométrique. Le Scanning Microwave Microscopy (SMM), qui permet d'accéder aux propriétés électriques d'un échantillon (impédance, permittivité électrique, tangente d'angle de perte et concentration de dopant), répond à ces critères. Il s'agit d'un microscope à force atomique interfacé à un analyseur de réseaux vectoriel (VNA). Si la métrologie de la mesure électrique utilisant un VNA est bien établie, ce n'est pas le cas pour les configurations SMM. Un VNA permet, s'il est calibré, d'extraire des propriétés électriques à partir de la mesure du paramètre de réflexion. Pour une configuration SMM, la méthode la plus commune est dérivée de la calibration Short-Open-Load utilisant trois impédances connues sur un échantillon de référence. L'un des résultats clé de cette thèse est l'établissement du bilan d'incertitude associé à la mesure d'impédance par SMM. Pour ce faire, une caractérisation de l'échantillon de référence démontra que l'incertitude associée aux valeurs des impédances présentes (0.3; 9.8 fF) est inférieure à 2.8 %. Fort de ce bilan d'incertitude, un second échantillon de référence fut proposé et caractérisé avec une incertitude associée inférieure à 1.9 %. L'incertitude sur la mesure des capacités de référence par le SMM calibré est inférieure à 3 %. Un cas d'application est l'extraction de la permittivité d'échantillons piézoélectriques avec une incertitude inférieure à 10.6 %. L'incertitude due à l'humidité relative (RH) sur la calibration du SMM fut étudiée empiriquement et par simulation numérique. Le RH impacte la calibration à hauteur de 0.4 % pour les capacités de 0.3 fF et devient négligeable pour les capacités au-dessus de 4 fF. Enfin, des courbes  $dC/dz$  furent acquise par microscopie à force électrostatique (EFM) sur un diélectrique connu afin d'assurer la traçabilité de la mesure de constante de raideur de la sonde employé.

MOTS-CLÉS : Microscopie à force atomique ; Mesure électrique à l'échelle submicrométrique ; Métrologie électrique ; Structure de référence capacitive

Laboratoire (s) de recherche :

INL

Directeur de thèse:

Brice Gautier  
François Piquemal

Président de jury :

Composition du jury :



